

## Power Quality of Electric Vehicle Charging

Wang, L.

**DOI**

[10.4233/uuid:bffec116-cc8f-41c6-a869-13f368f9891c](https://doi.org/10.4233/uuid:bffec116-cc8f-41c6-a869-13f368f9891c)

**Publication date**

2024

**Document Version**

Final published version

**Citation (APA)**

Wang, L. (2024). *Power Quality of Electric Vehicle Charging*. [Dissertation (TU Delft), Delft University of Technology]. <https://doi.org/10.4233/uuid:bffec116-cc8f-41c6-a869-13f368f9891c>

**Important note**

To cite this publication, please use the final published version (if applicable). Please check the document version above.

**Copyright**

Other than for strictly personal use, it is not permitted to download, forward or distribute the text or part of it, without the consent of the author(s) and/or copyright holder(s), unless the work is under an open content license such as Creative Commons.

**Takedown policy**

Please contact us and provide details if you believe this document breaches copyrights. We will remove access to the work immediately and investigate your claim.

# **POWER QUALITY OF ELECTRIC VEHICLE CHARGING**





# **POWER QUALITY OF ELECTRIC VEHICLE CHARGING**

## **Dissertation**

for the purpose of obtaining the degree of doctor  
at Delft University of Technology  
by the authority of the Rector Magnificus, Prof.dr.ir. T.H.J.J. van der Hagen;  
Chair of the Board for Doctorates  
to be defended publicly on  
Wednesday 18, December 2024 at 12:30 o'clock

by

**Lu WANG**

Master of Science in Electrical Engineering,  
Delft University of Technology, The Netherlands  
born in Sichuan, China

This dissertation has been approved by the promotor.

Composition of the doctoral committee:

Rector Magnificus,	chairperson
Prof. dr. ir. P. Bauer,	Delft University of Technology, promotor
Dr. Z. Qin,	Delft University of Technology, promotor

*Independent members:*

Prof. dr. ir. M. Popov,	Delft University of Technology
Prof. dr. T. Thiringer,	Chalmers University of Technology, Sweden
Prof. ir. P.T.M. Vaessen,	Delft University of Technology
Prof. dr. ir. J.A. La Poutré,	Delft University of Technology
Dr. ir. T. Slangen,	Stedin

The work in the thesis has been carried out under the sponsorship of the project PROGRESSUS, which received funding from the Electronic Components and Systems for European Leadership Joint Undertaking under grant agreement No 876868. This Joint Undertaking receives support from the European Union's Horizon 2020 research and innovation programme and Germany, Slovakia, Netherlands, Spain, Italy.



Cover Design: Lu Wang

ISBN 978-94-6366-980-1

An electronic version of this dissertation is available at  
<http://repository.tudelft.nl/>.

## SUMMARY

Electric vehicle (EV) charging plays a crucial role in paving the way for zero-emission vehicle markets, which require massive installations of EV chargers. However, that causes degraded power quality of the power grid, which may lead to non-compliance issues. To prepare for massive installations, a comprehensive understanding of EV chargers' potential power quality impacts is essential. Furthermore, mitigation measures for potential power quality issues should be prepared beforehand to prevent catastrophic power quality issues from happening. Therefore, the thesis aims to clarify the potential power quality issues caused by EV chargers, prepare modelling methods to understand the root cause of the power quality issues and develop mitigation measures to alleviate chargers' power quality impacts.

### **POWER QUALITY ISSUES AND STANDARDS**

The concept of power quality is quite broad, which basically quantifies what the nominal grid voltage is and how the grid users should behave to maintain the nominal grid voltage. Before diving into the details, it is therefore important to clarify the expected power quality impacts of EV chargers and which standards should be applied to quantify if the impacts are problematic or not. To that end, the thesis starts with a comprehensive review. It summarizes the international grid codes from IEEE and IEC to clarify which standards are suitable for evaluating EV chargers' power quality impacts and how to apply them. Besides, after reviewing the technical trends of EV charging, the thesis concludes all the possible power quality issues brought by it but puts a focus on the harmonic non-compliance issue because of its importance and difficulty.

### **GRAY-BOX IMPEDANCE MODELLING**

A promising method to study the harmonic and resonance of a grid-charger system is the impedance-based approach. Although the impedance-based approach is well established in the literature, the problem of how to extract the input impedance of a power converter is always encountered in practice. On the one hand, the analytical approach developed in the literature requires knowing the design information, e.g., controller parameter values and circuit parameter values that are in many cases unknown because of, for example, industrial confidentiality. On the other hand, purely relying on the measured results is also not preferred because it is sensitive to measurement noise and very time-consuming.

To tackle this challenge, a gradient-descent (GD) optimization based gray-box modeling approach is proposed. The proposed method requires sparse measurement results to identify the unknown parameters. Then, the impedance can be obtained by substituting the estimated parameter value into the analytical model. To achieve high estimation accuracy, a sensitivity study on the analytical impedance model of an EV charger to identify in which frequency range that each controller and circuit parameter can influence the input

impedance. The analysis reveals that each parameter has a different influential frequency range, which greatly decreases the difficulty of multiple parameter estimation since they can be decoupled. Compared to pure frequency sweep, the proposed approach achieves a higher accuracy for the coupling impedance and a comparable accuracy for the diagonal elements in the two-by-two impedance matrix.

### **LONG-TERM HARMONIC MODELLING**

To accurately simulate chargers' harmonic emission, a small time step, i.e., typically smaller than  $10\ \mu\text{s}$ , is required due to switching dynamics. However, in practice, harmonics should be continuously assessed for a long period of time, e.g., a day. A trade-off between accuracy and time efficiency thus exists. To address this issue, a multi-time scale modeling framework is proposed. In the presented framework, the chargers' input impedance and harmonic current emission in the ideal grid condition, that is, zero grid impedance and no background harmonic voltage, are obtained based on a converter switching model with a small timescale simulation. Thereafter, they are used in fast-charging charging station modelling, where the chargers are simplified as Norton equivalent circuits. In the station-level simulation, a large time step, i.e., one minute, is used because the chargers' operating power can be assumed as a constant over a minute. With this co-simulation, a charging station's day-long harmonic emission can be assessed in about two hours with the same accuracy as a circuit-level simulation.

### **DESIGN RECOMMENDATIONS TO PREVENT SMALL SIGNAL INSTABILITY**

The control design can shape the input impedance of a charger and thereby influence its harmonic emission. In the worst case, small signal instability can be caused by the under-damped resonances between the grid and the charger. Therefore, an analytic approach to design the typical power factor correction (PFC) control of an EV charger to ensure small signal stability in weak grid conditions is discussed. Compared to the previous works, the proposed method considers the dynamics of all the control loops, i.e., phase-locked loop (PLL), voltage loop (VL), and current loop (CL). The impacts of key influential parameters on stability are analyzed. Furthermore, the upper limits of the PLL and voltage loop bandwidth to ensure small signal stability are derived. Accordingly, the influences of the CL bandwidth, short circuit ratio (SCR), and the filter inductance on the upper limit of the PLL bandwidth and the VL bandwidth are quantified. Consequently, a design procedure that eliminates the need to model the input impedance for tuning the controller to prevent small signal instability is proposed.

### **QUANTIFICATION OF SYNTHETIC INERTIA**

The last point discussed in the thesis is about how to quantify the synthetic inertia provided by grid-tied converters. Considering the highly pulsating load profile of EV charging, installing battery energy storage systems (BESSs) in a fast charging station is highly expected. To maximize the usage of the installed BESS, enabling its multi-functionalities is crucial. As one of the important functionalities, BESS can be used to provide synthetic inertia. However, how to evaluate how much synthetic inertia is provided is still unclear. In the thesis, a method to quantify the synthetic inertia of converter-based resources is proposed from a power and energy perspective.

---

# SAMENVATTING

Opladen van elektrische voertuigen (EV) speelt een cruciale rol bij het leiden van de weg voor markten met uitstootvrije voertuigen, waarvoor massale installaties van EV-laders nodig zijn. Dit veroorzaakt echter een verminderde stroomkwaliteit van het elektriciteitsnet, wat kan leiden tot niet-nalevingsproblemen. Om voorbereid te zijn op massale installaties, is een uitgebreid begrip van de potentiële invloed op de spanningskwaliteit van EV-laders essentieel. Daarnaast moeten voorafgaande maatregelen worden voorbereid om mogelijke spanningskwaliteit problemen te verlichten, om catastrofale spanningskwaliteit problemen te voorkomen. Daarom heeft deze scriptie tot doel de potentiële spanningskwaliteit problemen veroorzaakt door EV-laders te verduidelijken, modelleringsmethoden voor te bereiden om de oorzaak van de spanningskwaliteit problemen te begrijpen en verlichtende maatregelen te ontwikkelen om het effect van laders op de spanningskwaliteit te verminderen.

## **PROBLEMEN EN NORMEN VOOR SPANNINGSKWALITEIT**

Het concept van spanningskwaliteit is vrij breed, wat in principe kwantificeert wat de nominale netspanning is en hoe de netgebruikers zich moeten gedragen om de nominale netspanning te behouden. Voordat we in de details duiken, is het daarom belangrijk om de verwachte invloed van EV-laders op de spanningskwaliteit te verduidelijken en welke normen moeten worden toegepast om te kwantificeren of het effect problematisch is of niet. Om die reden begint het proefschrift met een uitgebreide review. Het vat de internationale netcodes van IEEE en IEC samen om te verduidelijken welke normen geschikt zijn voor het evalueren van de impact van EV-laders op de spanningskwaliteit en hoe deze moeten worden toegepast. Bovendien concludeert het proefschrift, na het bekijken van de technische trends van EV-laden, alle mogelijke problemen met de spanningskwaliteit die het met zich meebrengt, maar legt de nadruk op het probleem van harmonische non-conformiteit vanwege het belang en de moeilijkheid ervan.

## **GRAY-BOX IMPEDANTIEMODELLERING**

Een veelbelovende methode om de harmonischen en resonantie van een grid-ladersysteem te bestuderen is de impedantie-gebaseerde benadering. Hoewel de impedantie-gebaseerde benadering goed is gevestigd in de literatuur, wordt in de praktijk altijd het probleem ondervonden hoe de ingangsimpedantie van een vermogensomvormer kan worden geëxtraheerd. Enerzijds vereist de analytische benadering ontwikkeld in de literatuur kennis van ontwerpgegevens, zoals controllerparameterwaarden en circuitparameterwaarden, die in veel gevallen onbekend zijn vanwege bijvoorbeeld industriële vertrouwelijkheid. Anderzijds is het ook niet gewenst om uitsluitend op de gemeten resultaten te vertrouwen, omdat dit gevoelig is voor meetruis en zeer tijdrovend is.

Om deze uitdaging aan te gaan, wordt een op gradient-descent (GD) optimalisatie gebaseerd op de gray-box modellering benadering voorgesteld. De voorgestelde methode vereist

alleen een schaarse hoeveelheid meetresultaten om de onbekende parameters te identificeren. Vervolgens kan de impedantie worden verkregen door de geschatte parameterwaarde in het analytische model te substitueren. Om een hoge schattingsnauwkeurigheid te bereiken, wordt een gevoeligheidsstudie uitgevoerd op het analytische impedantiemodel van een EV-lader om het invloedrijke frequentiebereik per controller- en circuitparameter te identificeren. De analyse onthult dat elke parameter een ander invloedrijk frequentiebereik heeft, wat de moeilijkheid van meervoudige parameterschatting aanzienlijk vermindert, aangezien ze kunnen worden ontkoppeld. In vergelijking met een pure frequentiesweep, bereikt de voorgestelde benadering een hogere nauwkeurigheid voor de koppeling impedantie en een vergelijkbare nauwkeurigheid voor de diagonale impedantie.

### **LANGETERMIJN HARMONISCHE MODELLERING**

Om de harmonische emissie van laders nauwkeurig te simuleren, is een kleine tijdstap nodig, d.w.z. typisch kleiner dan  $10 \mu\text{s}$ , vanwege de schakelingsdynamiek. In de praktijk moeten harmonischen echter continu voor een lange duur worden geëvalueerd, bijvoorbeeld een dag. Er bestaat dus een afweging tussen nauwkeurigheid en tijdsefficiëntie. Om dit probleem aan te pakken, wordt een multi-tijd schaal modellering kader voorgesteld. In het voorgestelde kader worden deingangsimpedantie van de laders en de harmonische stroomemissie in de ideale netconditie, dat wil zeggen nul netimpedantie en geen achtergrond harmonische spanning, verkregen op basis van een omzetter schakelmodel met een kleine tijdschaalsimulatie. Daarna worden deze gebruikt in het modelleren van snellaadstations, waarbij de laders worden vereenvoudigd als Norton equivalente circuits. In de simulatie op station niveau wordt een grote tijdstap, d.w.z. één minuut, gebruikt omdat het vermogen van de laders als constant kan worden verondersteld over een minuut. Met deze co-simulatie kan de daglengte harmonische emissie van een laadstation in ongeveer twee uur worden beoordeeld met dezelfde nauwkeurigheid als een circuitsimulatie.

### **ONTWERPAANBEVELINGEN OM KLEINE SIGNAALINSTABILITEIT TE VOORKOMEN**

Het regelsysteemontwerp kan deingangsimpedantie van een lader vormgeven en daarmee de harmonische emissie beïnvloeden. In het slechtste geval kan kleine signaalinstabiliteit worden veroorzaakt door ondergedempte resonanties tussen het net en de lader. Daarom wordt een analytische benadering besproken voor het ontwerpen van de typische vermogensfactorcorrectie regeling van een EV-lader om kleine signaalstabiliteit te waarborgen onder zwakke netomstandigheden. In vergelijking met eerdere werken houdt de voorgestelde methode rekening met de dynamiek van alle regelcircuits, d.w.z. de phase-locked loop (PLL), spanningslus (VL) en stroomlus (CL). De impact van belangrijke beïnvloedende parameters op de stabiliteit wordt geanalyseerd. Verder worden de bovengrenzen van de PLL en spanningslusbandbreedte afgeleid om kleine signaalstabiliteit te waarborgen. Verder, worden de invloeden van de stroomlus-bandbreedte, kortsluitverhouding en de filterinductantie op de bovengrens van de faselocklus-bandbreedte en de spanningslus-bandbreedte gekwantificeerd. Vervolgens wordt een ontwerpprocedure voorgesteld die de noodzaak om deingangsimpedantie te modelleren voor het afstemmen van de regelaar om kleine signaalinstabiliteit te voorkomen, elimineert.

## **KWANTIFICERING VAN SYNTHETISCHE INERTIE**

Het laatste punt dat in de thesis wordt besproken, betreft hoe de synthetische inertie die door netgekoppelde omvormers wordt geleverd, gekwantificeerd kan worden. Gezien het sterk pulserende laadprofiel van EV-opladen, wordt het installeren van batterij-energieopslagsystemen (BESS) in een snellaadstation zeer verwacht. Om het gebruik van de geïnstalleerde BESS te maximaliseren, is het cruciaal om de multifunctionaliteiten van de BESS mogelijk te maken. Als een van de belangrijke functionaliteiten kan de BESS worden gebruikt om synthetische inertie te leveren. Hoeveel synthetische inertie daadwerkelijk wordt geleverd, is echter nog onduidelijk. In de thesis wordt een methode voorgesteld om de synthetische inertie van omvormer-gebaseerde bronnen te kwantificeren, vanuit een power- en energieperspectief.





# CONTENTS

<b>Summary</b>	<b>v</b>
<b>Samenvatting</b>	<b>vii</b>
<b>Abbreviations</b>	<b>xv</b>
<b>1 Introduction</b>	<b>1</b>
1.1 Motivation . . . . .	1
1.2 Thesis Objective and Research Questions. . . . .	2
1.3 Contributions . . . . .	5
1.4 Thesis Outline . . . . .	6
<b>2 Power Quality Impact of Electric Vehicle Charging: An Overview</b>	<b>9</b>
2.1 Introduction . . . . .	10
2.2 Trends of fast charging. . . . .	12
2.2.1 Ultra-fast charging is coming. . . . .	12
2.2.2 Batteries are going high power. . . . .	14
2.2.3 Architecture of ultra-fast charging station . . . . .	15
2.3 Power quality issues . . . . .	18
2.3.1 Voltage fluctuation . . . . .	19
2.3.2 Harmonic stability . . . . .	20
2.3.3 Harmonic emission. . . . .	22
2.3.4 Supraharmonics . . . . .	22
2.4 Power quality standards . . . . .	25
2.4.1 RMS voltage tolerance . . . . .	27
2.4.2 Voltage fluctuation . . . . .	27
2.4.3 Harmonic current distortion . . . . .	28
2.4.4 Harmonic voltage distortion . . . . .	29
2.4.5 Voltage unbalance . . . . .	29
2.4.6 Emission level allocation . . . . .	29
2.5 Mitigation measures . . . . .	32
2.5.1 Smart charging. . . . .	32
2.5.2 Integration of energy storage. . . . .	32
2.5.3 Impedance based approach. . . . .	34
2.5.4 Design of DC fast chargers. . . . .	37
2.6 Conclusion. . . . .	39

<b>3</b>	<b>Modelling of Electric Vehicle Charger for Power Quality Study</b>	<b>41</b>
3.1	Introduction . . . . .	42
3.2	Overview and Impedance Modeling . . . . .	44
3.2.1	System Description. . . . .	44
3.2.2	Overview of the proposed approach . . . . .	46
3.2.3	Small-signal modeling . . . . .	47
3.2.4	Elements in the impedance matrix . . . . .	49
3.3	Impedance sensitivity study . . . . .	50
3.3.1	Pre-conditioning . . . . .	50
3.3.2	Influential frequency range per parameter . . . . .	51
3.4	Multiple Parameter Estimation. . . . .	54
3.4.1	Challenges in a normal gradient descent optimization based approach . . . . .	54
3.4.2	Proposed estimation approach . . . . .	55
3.5	Experimental Results. . . . .	59
3.5.1	Experiments and measurement setup. . . . .	59
3.5.2	Analytical model verification. . . . .	60
3.5.3	Estimation results . . . . .	61
3.6	Conclusion. . . . .	68
<b>4</b>	<b>Modelling of Electric Vehicle Charging Station for Power Quality Study</b>	<b>69</b>
4.1	Introduction . . . . .	70
4.2	Modelling of the DC fast charger. . . . .	72
4.2.1	Design of the DC fast charger . . . . .	72
4.2.2	Input impedance modeling . . . . .	73
4.3	Modelling of the fast-charging station . . . . .	74
4.3.1	Configuration of the fast-charging station . . . . .	74
4.3.2	Modeling of the external grid. . . . .	75
4.3.3	Modelling of the charging load profile . . . . .	75
4.4	Simulation results and discussion . . . . .	76
4.4.1	Input impedance of the DCFC . . . . .	76
4.4.2	Harmonic current source of the DCFC . . . . .	77
4.4.3	Daily harmonic emission of the DCFCs. . . . .	78
4.5	Conclusion. . . . .	79
<b>5</b>	<b>Design Guidelines of Charger Control for Power Quality Impact Mitigation</b>	<b>81</b>
5.1	Introduction . . . . .	82
5.2	Fundamentals . . . . .	83
5.2.1	System Description. . . . .	83
5.2.2	Small signal stability criterion for a charging system. . . . .	83
5.3	Stability criterion breakdown. . . . .	86
5.3.1	Full-order model . . . . .	86
5.3.2	Reduced-order model. . . . .	86
5.3.3	Expressions of the maximum NPR frequencies . . . . .	89
5.3.4	Expressions of the resonant frequencies . . . . .	89

5.3.5	Impact of influential parameters on stability . . . . .	91
5.4	Analytic design of the controller . . . . .	92
5.4.1	Upper limit of the PLL and VL bandwidth . . . . .	92
5.4.2	Discussion . . . . .	93
5.4.3	Design steps . . . . .	94
5.4.4	Influences of neglecting the coupling effects . . . . .	95
5.4.5	Comparison with the existing methods. . . . .	97
5.5	Validations . . . . .	98
5.6	Conclusion . . . . .	101
<b>6</b>	<b>Onsite BESS for enhancing system inertia</b>	<b>103</b>
6.1	Introduction . . . . .	104
6.2	Revisit synchronous generator inertia . . . . .	105
6.2.1	Model of a synchronous generator . . . . .	105
6.2.2	Frequency response of synchronous generators . . . . .	106
6.2.3	Approaches to estimating the inertia of a synchronous generator . . . . .	111
6.3	Proposed synthetic inertia estimation approach . . . . .	114
6.3.1	Approximate inertia power without measuring mechanical power . . . . .	114
6.3.2	Proposed approach to estimating synthetic inertia . . . . .	115
6.3.3	Discussion over fast frequency response power . . . . .	118
6.4	Case study . . . . .	122
6.5	Rethinking VSM control for providing synthetic inertia . . . . .	123
6.6	Conclusion . . . . .	125
<b>7</b>	<b>Conclusion</b>	<b>127</b>
	<b>Bibliography</b>	<b>133</b>
	<b>Acknowledgments</b>	<b>147</b>
	<b>Curriculum Vitæ</b>	<b>149</b>
	<b>List of Publications</b>	<b>151</b>



# ABBREVIATIONS

<b>AC</b>	Alternating Current
<b>AFE</b>	Active Front End
<b>BESS</b>	Battery Energy Storage System
<b>CBR</b>	Converter Based Resource
<b>CC</b>	Current Control
<b>CL</b>	Current Loop
<b>COI</b>	Center of Inertia
<b>DC</b>	Direct Current
<b>DCFC</b>	Direct Current Fast Charger
<b>DVC</b>	Direct Voltage Control
<b>EMI</b>	Electromagnetic Interference
<b>EV</b>	Electric Vehicle
<b>FC</b>	Fast Charging
<b>FCR</b>	Frequency Containment Reserve
<b>FCS</b>	Fast Charging Station
<b>FFR</b>	Fast Frequency Response
<b>GD</b>	Gradient Descent
<b>GNC</b>	General Nyquist Criterion
<b>LV</b>	Low Voltage
<b>NPR</b>	Non-Passive Region
<b>ICEV</b>	Internal Combustion Engine Vehicle
<b>IEC</b>	International Electrotechnical Commission
<b>IEEE</b>	Institute of Electrical and Electronics Engineers
<b>MV</b>	Medium Voltage

---

<b>PCC</b>	Point of Common Coupling
<b>PFC</b>	Power Factor Correction
<b>PFR</b>	Primary Frequency Response
<b>PI</b>	Proportional Integral
<b>PLL</b>	Phase Lock Loop
<b>PQ</b>	Power Quality
<b>PV</b>	Photovoltaics
<b>PWM</b>	Pulse Waveform Modulation
<b>RMS</b>	Root Mean Square
<b>RoCoF</b>	Rate of Change of Frequency
<b>RVC</b>	Rapid Voltage Change
<b>SAE</b>	Society of Automotive Engineers
<b>SC</b>	Synchronous Condenser
<b>SCR</b>	Short Circuit Ratio
<b>SG</b>	Synchronous Generator
<b>SI</b>	Synthetic Inertia
<b>SST</b>	Solid State Transformer
<b>TDD</b>	Total Demand Distortion
<b>THD</b>	Total Harmonic Distortion
<b>UFC</b>	Ultra Fast Charging
<b>VL</b>	Voltage Loop
<b>VSC</b>	Voltage Source Converter
<b>VSM</b>	Virtual Synchronous Machine
<b>V2G</b>	Vehicle to Grid

# 1

## INTRODUCTION

### 1.1 MOTIVATION

Transportation electrification plays a crucial role in climate change mitigation and the transition towards a more sustainable society. Since 1990, the carbon dioxide (CO<sub>2</sub>) emissions from road transport increased despite the combustion engines becoming more fuel efficient [1]. Currently, the emissions from road transport are one of the main sources of greenhouse gas emissions. For example, for the European Union, the CO<sub>2</sub> emissions from road transport make up 24% of the total emissions in 2020 [2]. To reduce road transport emissions, electric vehicles (EVs) are deemed a promising alternative to conventional fossil-fuel vehicles. Therefore, although the early human-carrying EVs were already invented by the end of the nineteenth century, they once again attracted interest in the recent two decades. With the policy push and daily improving EV technologies, the recent decade witnessed a dramatic growth of the EV market, as shown in Fig. 1.1 [3].

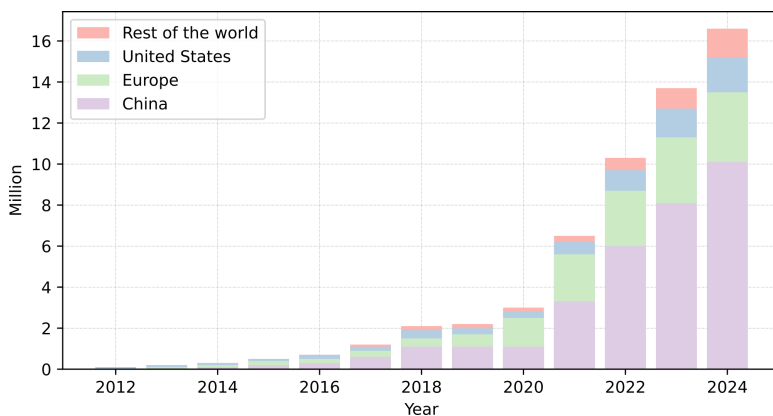


Figure 1.1: Electric vehicle sales from 2012 to 2024 [3].

Despite the recent successes of EVs, there are still many obstacles on the way to achieving a zero-emission vehicle market. One of the obstacles is the range anxiety of



EV customers. Therefore, EV battery technologies developed fast in these years, which greatly increases the range of EVs without recharging. Currently, some battery EVs can go 690 km on a single charge [4]. However, only increasing EVs' battery capacity is not sufficient to address range anxiety especially for very long-range trips. Therefore, providing convenient recharging services is also crucial to pave the way to a more flourishing EV market. Being used to driving fossil-fuel vehicles, customers want to have equivalently convenient and fast recharging services when changing to EVs. Such requires enough EV charging infrastructures and fast charging technologies. Therefore, both the number of charging infrastructures and charging power increased significantly in recent years. For example, the maximum charging power of some EV fast chargers can reach 400 kW [5] whereas some EV models can be charged by 200 kW [4]. With this charging power, some EVs can be recharged for the next 400 km in half an hour.

However, massive installations of charging infrastructures and increased charging power both bring huge pressures for power grids. On the one hand, the congestion issues faced by grids become more severe because recharging EVs brings additional load demand to grids and the charging power profiles of EVs are highly pulsating [6]. On the other hand, EV chargers are essentially power-electronics converters which are non-linear loads. The power quality issues brought by the power-electronic converters are already found in some other applications such as PV inverters [7] and wind turbine inverters [8]. Similarly, an EV charger will bring power quality disturbances emissions, such as harmonics emissions [9–12], supraharmonics emissions [13, 14], and flicker emissions [15, 16]. These power quality disturbances emissions distort the grid voltages and can lead to deteriorated grid compatibility, which will further increase the power quality disturbance emissions of the other grid-connected devices and might lead to malfunction of protection devices [13]. In the worst case, when connecting EV chargers to grids, instability of grid-tied devices, including the charger itself, can happen. The promising solutions to the issue of insufficient grid capacity for EV charging consist of upgrading grid infrastructures, improving system operation planning, smart charging, etc., which are more power-system level related. On the contrary, the issue related to the impacts of EV charging on PQ is brought by the power-electronics converters and can be solved by improving the designs, including control and hardware design, of the power-electronics converters. Given the rapidly growing EV market, it becomes very urgent to prepare tools and solutions for the two issues faced by power grids.

The research focus of the thesis is on studying the power quality disturbance emissions of EV chargers to prepare for their massive installations. Specifically, the study aims to prepare methods and models for evaluating the power quality impacts of EV chargers and to prepare mitigation measures for EV chargers' power quality impacts. Briefly, it starts with the modelling of an EV charger and a fast charging station (FCS) that consists of several EV chargers for power quality evaluation. On top of the modelling, mitigation measures, namely design recommendations and modified control algorithms for power electronics converters inside EV chargers, are developed accordingly.

## 1.2 THESIS OBJECTIVE AND RESEARCH QUESTIONS

As indicated previously, the research objective of this thesis is as follows.

*"To model electric vehicle chargers for evaluating their impacts on power quality and de-*

*velop mitigation measures including design recommendations and improved control algorithm to reduce their impacts on power quality."*

More specifically, due to the time limit, the focus is on modelling EV chargers for harmonic study and small-signal stability study. Mitigation measures are proposed to reduce the harmonic emissions of EV chargers and prevent small-signal instability arising from connecting chargers to grids. Besides, how to enable the ability of BESSs to provide synthetic inertia and reduce the impact of the massive load demand of charging EVs on the grid frequency is also discussed. A breakdown of the research objective leads to several research questions that are as follows.

**Q1** *What power quality issues do EV chargers potentially have and what standards should be used to evaluate their power quality?*

Like the other loads connected to power grids, EV chargers emit disturbances contaminating power quality. Nevertheless, having power quality impacts does not necessarily mean EV chargers will bring power quality issues. It becomes problematic when the disturbance emissions from EV chargers exceed the limits standardized in grid codes, which results in grid code non-compliance issues and might cause abnormal functions or malfunctions of grid-tied devices. To have a quantified study on the power quality impacts of EV chargers, investigations on the state-of-the-art EV charging technologies, including battery technologies and power-electronics technologies for EV chargers, are essential. Besides, unlike, for example, IEC 61400 series to wind turbine inverters and IEEE 1547 to distributed energy resources inverters, there are currently no dedicated grid codes that specify the emission compliance requirements for EV chargers. Therefore, based on the potential power quality impacts of EV chargers, the existing power quality compliance codes used for general loads or other power-electronics-based devices might be suitable. However, in the literature, information about which existing standards can be used to evaluate EV chargers' power quality compliance is opaque. Hence, a comprehensive review is needed to clarify the standards for EV chargers' power quality compliance study and the potential non-compliance issues of EV chargers.

**Q2** *Without knowing design details, how to model EV chargers to analyze their harmonic emission considering their interactions with grids?*

Harmonic emissions are expected to be important disturbance emissions of EV chargers. These disturbance emissions are not only determined by an EV charger itself but also by the interactions between the charger and the grid to which it is connected. Different from passive devices such as resistive load, EV chargers are power electronic converters that belong to the class of active switching devices. Their control and switching dynamics also influence their interaction with the grid. The interaction between a device and a grid can lead to resonances between the device and the grid, which might amplify the harmonic emissions. In the worst-case scenario, the device can become unstable due to the interactions. Compared to the primary harmonic emissions of an EV charger, namely the charger's emissions without interactions with a grid, the emissions caused by grid interactions are more problematic. The reasons are twofold. First, primary emissions can be greatly reduced in laboratories with ideal test conditions during the product development stage. However, the emissions caused by grid interactions are highly dependent on grid conditions, e.g.,

grid voltage harmonics and grid impedance. Therefore, due to the amplification by grid interactions, qualified EV chargers might also cause harmonic emission non-compliance issues after being installed in the field. Second, the grid conditions are time-varying even for the same connection point. Therefore, emissions of EV chargers caused by grid interactions are time-varying, further complicating their evaluation. In this context, modelling EV chargers' harmonic emissions caused by grid interactions becomes crucial. Moreover, modelling requires design information, which is, however, normally confidential for those who need to carry out EV chargers' compliance study, e.g., charging station operators. Therefore, how to establish EV chargers' models for harmonic compliance study without knowing the confidential information is of practical interest.

**Q3** *How to model a fast charging station that has several EV chargers for a long-term harmonic study?*

Except for evaluating the harmonic emissions of a single EV charger, the harmonic emissions of an FCS that has several EV chargers also need to be evaluated. Compared to the modelling of a single device, system-level modelling is more difficult because of three reasons. First, an EV charger's harmonic emission is dependent on its charging power. However, each EV charger has its charging power profile which is not necessarily the same as the others. Because of the differences, it becomes challenging to aggregate the model of a single EV charger to the model of an FCS. Second, it is difficult to balance the trade-off between accuracy and time cost for a system-level simulation. It is important to know how to properly simplify the model without significantly sacrificing the accuracy of the simulation of harmonic emission of an FCS. Finally, a harmonic compliance study is typically based on a long-term, e.g., a day. Such further increases the pressure on balancing the trade-off between simulation accuracy and time cost. A method to address the aforementioned challenges is needed.

**Q4** *How to design an EV charger to prevent small-signal instability caused by its interactions with a grid?*

The interactions between an EV charger and a grid lead to resonances that might amplify the harmonic emissions of the charger. In the worst-case scenario, the resonances can make the EV charger unstable. The instability happens when the EV charger operates at a steady state and is thereby small-signal instability. Both of the two phenomena can be analyzed with an impedance-based approach. Specifically, the EV charger's dynamics influencing its interactions with the grid can be modeled as its input impedance. The resonances between the charger and the grid are equivalent to the resonances between the grid impedance and the charger's input impedance. After answering the previous research question, how to extract a charger's input impedance model should be clear. On top of that, how a charger's input impedance is shaped by its design parameters can and should be clarified. The answer to this question can give design recommendations for EV chargers so that the risk of having small-signal instability and harmonic emission amplification can be reduced. Hence, the power quality impacts of EV chargers can be mitigated by following the design recommendations.

**Q5** *How to quantify the synthetic inertia provided by inverter-based resources and how to control inverters to provide synthetic inertia better?*

The charging profile is highly pulsating, especially for high-power chargers. Therefore, a battery energy storage system (BESS) is typically installed inside an FCS to shave the charging profile. Meanwhile, as a type of converter-based resource (CBR), a BESS can provide ancillary service for the grid to which it is connected, which helps to balance the load and source and maintain the stability of the grid. However, with the increasing uses of renewable energy, power grids are changing towards being a power-electronics dominant system. With fewer synchronous generators (SGs), less rotating mass is in the grid leading to decreased system inertia. Such is problematic since enough system inertia is crucial for maintaining system frequency during contingency events. Given the fast response speed of inverters, the inverter of a BESS can be controlled to provide synthetic inertia. For example, the virtual synchronous machine (VSM) control is one control method that enables the ability of an inverter to provide synthetic inertia. Due to the mathematical similarity, the controller parameter that mimics the inertia of an SG is normally deemed as the synthetic inertia provided by the inverter. However, this is not a trustworthy result because of two reasons. First, the controller parameter values can be a time-variant value. In literature, some attempt to make the controller parameter adaptive to solve active power oscillations encountered by VSM control. Consequently, it becomes problematic to quantify the synthetic inertia of the inverter. Second, the synthetic inertia of an inverter needed to be quantified for the external behavior of the inverter instead of the internal parameters. This is important for system operators for evaluations, which helps to establish a market for inertia services, if any, in the future. Since the inertia of an SG releases power and energy to reduce the rate of change of frequency (RoCoF) and increase frequency nadir, the synthetic inertia should have the same functionality, which gives rise to a method to quantify the synthetic inertia of an inverter from a power and energy perspective.

## 1.3 CONTRIBUTIONS

Targeting to give answers to the aforementioned research questions, the thesis has the contributions as follows.

1. A comprehensive review of EV-charging-related technologies and standards, which clarifies EV chargers' potential power quality impacts and the grid codes suitable for compliance evaluation of EV chargers' power quality disturbance emissions (**Chapter 2**). The publication related to this contribution is as follows:
  - **J1:** "Grid Impact of Electric Vehicle Fast Charging Stations: Trends, Standards, Issues, and Mitigation Measures - An Overview", *IEEE Open J. Power Electron.*, 2021. (Highly Cited)
2. A gray-box approach to extract an EV charger's input impedance without knowing its design information is developed (**Chapter 3**). Case studies demonstrate an accuracy of about 3% of the estimated input impedance by the proposed approach. The publication related to this contribution is as follows:
  - **J2:** "A Gradient-Descent Optimization Assisted Gray-Box Impedance Modeling of EV Chargers", *IEEE Trans. Power Electron.*, 2023.

3. A multi-timescale co-simulation approach is proposed to simulate the harmonic emissions of an FCS for the long term, which balances the trade-off between accuracy and time cost. With the proposed approach, a day-long harmonic simulation of a fast charging station can be finished in about two hours with the same accuracy as a circuit-level simulation (**Chapter 4**). The publications related to this contribution are as follows:
  - **J3**: "Python supervised co-simulation for a day-long harmonic evaluation of EV charging", *Chinese J. Elec. Eng.*, 2021.
  - **C1**: "Multi-timescale Modeling of Fast Charging Stations for Power Quality Analysis", in *EPE'21 ECCE Europe*, 2021.
4. Design recommendations for EV chargers to shape their input impedance to prevent small-signal instability are developed with analytic approaches (**Chapter 5**). The publications related to this contribution are as follows:
  - **J4**: "Analytic Design of an EV Charger Controller for Weak Grid Connection", *IEEE Trans. Ind. Electron.*, 2024.
  - **C2**: "Critical Short Circuit Ratio of an EV Charging System", in *EPE'23 ECCE Europe*, 2023.
  - **C3**: "Stability Enhanced Design of EV Chargers for Weak Grid Connection", in *2023 ECCE*, 2023.
5. A method to quantify the synthetic inertia of a CBR from a power and energy perspective is proposed (**Chapter 6**). This part of the work has not been published yet but it will be published in:
  - **J5**: "Quantification of Synthetic Inertia", *Draft*, 2024.

## 1.4 THESIS OUTLINE

The outline of the remainder of this thesis and the interrelations between the chapters are schematically shown in Fig. 1.2. Starting with Chapter 2, the thesis first presents a review of the state-of-the-art EV charging-related technologies. On top of that, the potential power quality issues, the grid codes to evaluate EV chargers' power quality compliance, and the promising solutions to mitigating EV chargers' power quality impacts are also comprehensively reviewed. After setting the foundation in Chapter 2, Chapter 3 presents the input impedance modelling of EV chargers for their harmonic emission analysis. The focus is on extracting an EV charger's input impedance, which can be used for harmonic emission analysis, without knowing the confidential design information. In Chapter 4, a multi-timescale co-simulation approach is presented, which is used to simulate the long-term harmonic emission of an FCS in a time-efficient way. After clarifying the modelling of EV chargers and FCSs for their harmonic emission study in Chapter 3 and Chapter 4, Chapter 5 presents how to design the control of an EV charger properly to attenuate their harmonic resonances with the grid and prevent small-signal instabilities due to the interactions with grids. Beyond mitigating EV chargers' power quality impacts by improving the design of an individual EV charger, Chapter 6 studies how to use the BESS

installed inside an FCS to provide synthetic inertia to mitigate the influences of reduced system inertia due to increasing uses of renewable energies. Finally, the thesis is concluded in Chapter 7.

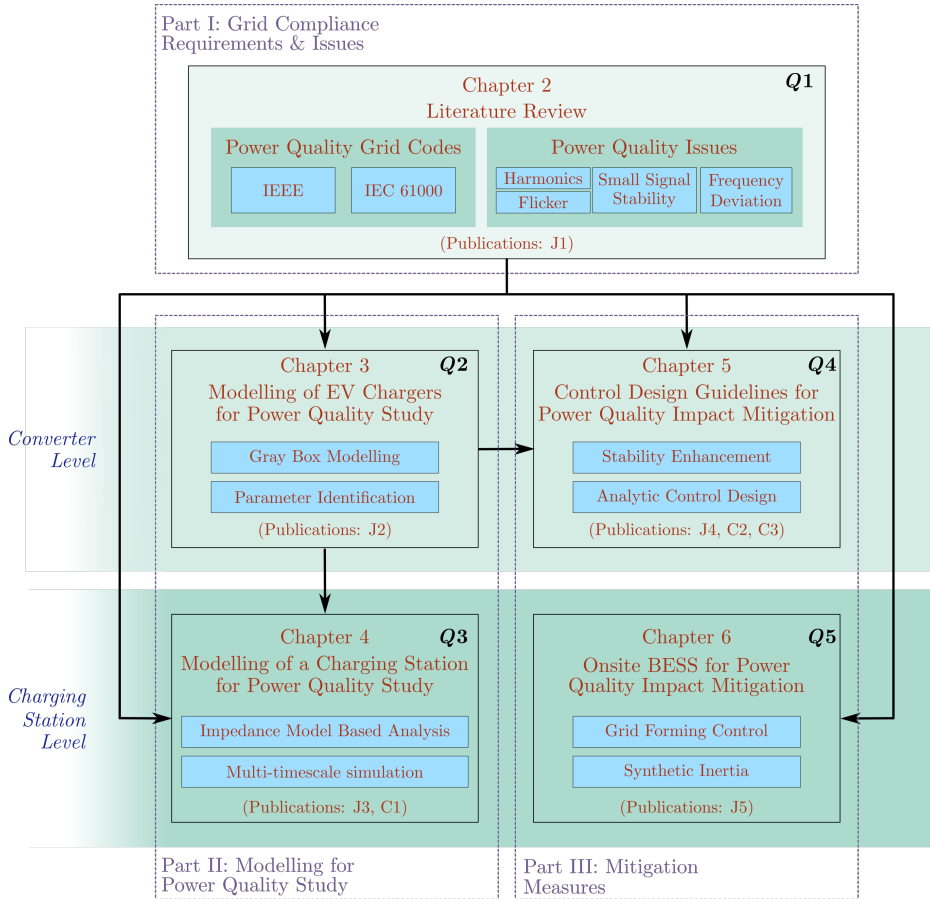


Figure 1.2: Outline of this thesis and the interrelation between the chapters.



## 2

# POWER QUALITY IMPACT OF ELECTRIC VEHICLE CHARGING: AN OVERVIEW

*Transportation electrification is coming to us. One of the main barriers to widespread electric vehicle (EV) adoption is range anxiety, which can be alleviated by fast charging (FC). The main technology constraints for enabling fast charging consist of high-charging-rate batteries, high-power-charging infrastructure, and grid impacts. Although these technical aspects have been studied in literature individually, there is no comprehensive review on FC involving all the perspectives. Moreover, the power quality (PQ) impacts of fast charging stations (FCSs) on power grids and the mitigation of these impacts are not clearly summarized in the literature. This chapter comprehensively reviews the techniques of FC, the standards to evaluate the grid impacts of FCSs, the reported or estimated PQ impact in the literature, and the existing mitigation measures to address these PQ issues.*



## 2.1 INTRODUCTION

Growing concern about climate change intensifies the trend towards decarbonization and interest in clean technology. As a substitute for internal combustion engine vehicles (ICEVs), EVs powered by renewable electricity, can reduce petroleum usage and greenhouse emission [17, 18]. Besides, new technologies on the powertrain of EVs, e.g., wide-band-gap-component based motor drive that improves battery-to-wheel efficiency [19], make EVs more competitive in energy saving.

The convenience of EV recharging significantly influences EV adoption and utilization. The charging power level is generally categorized into two classes - the slow charging and the FC. Typically, the former signifies the distributed charging at home, and public destinations, with the power rated lower than the maximum household power (e.g., 22 kW in the European Union and 19 kW in the United States [20]). On the contrary, fast chargers have a higher power rating and are typically used in FCSs. The charging modes are standardized in IEC 61851-1 [21] and SAE J1772 [17], according to the type of the input current (AC or DC) and the power level. In IEC 61851-1, four charging modes are defined, where Mode 1, 2, and 3 are the AC charging mode, and Mode 4 is the DC charging mode. Moreover, only Mode 3 and 4 support the FC. In SAE J1772, the EV charging is classified into three levels, where Level 1 and 2 are the slow charging via AC on-board chargers, and Level 3 is the FC via DC off-board charger. Due to the space and weight constraints of the on-board chargers, it has a limited maximum power rating, e.g., 43 kW for Mode 3 in IEC 61851-1. Thus, the mainstream FC is through the DC off-board charger that potentially offers higher charging power. For simplicity, the DCFC is referred to when FC is mentioned in this chapter.

For most daily charging events, the energy demand can be satisfied by the overnight slow charging, whose grid impact is well studied [22–24]. Besides, slow charging also shows the features of an extended charging period and a wide distribution area, allowing for distribution system operators to plan and regulation. With the topologies allowing bi-directional energy flow [25, 26], the vehicle-to-grid (V2G) function is developed to not only minimize the grid impacts of EV charging but also provide grid support, e.g. load balancing, frequency and voltage regulation [27–30].

For a better recharging experience for the EV drivers, the recharging time of EVs at FCSs needs to be comparable to the refueling time of ICEVs. Hence, the power of FC has kept increasing in the past years. To distinguish from FC (rated at 50 kW), the state-of-the-art multi-hundred-kilowatt charging is named ultra-fast charging (UFC), which is gaining more attention in recent years [31]. Meanwhile, the FCSs also bring challenges to the grid. An FCS is essentially a power electronics-based grid. Like other counterparts, e.g., wind farms [32] and PV farms [7], FCSs' power quality and stability issues might occur. A few power quality issues in terms of voltage imbalance that once, flicker, harmonics, supraharmonics, etc. [9, 15, 16], have been reported, where the influences of FCSs are seen as prime suspects. Considering the fast increase in both their power level and installation number, it is expected that their influences on grids will become more and more significant.

As a larger system interconnecting many devices, a power grid should be compatible with all agreed users to ensure the proper operation of all grid-tied equipment. To that end, the concept of power quality is established, which defines quantified parameters to restrict the behavior of both system operators and grid users. On one hand, system operators

Table 2.1: Power quality parameters and their descriptions

Power Quality Disturbances		Description
Voltage Sag		Under voltage exceeding the threshold (e.g., 90% of the nominal grid voltage) in short term
Voltage Swell		Over voltage exceeding the threshold (e.g., 110% of the nominal grid voltage) in short term
Voltage Imbalance		RMS values of the line or phase voltages are not equal)
Voltage fluctuation	Rapid Voltage Change	A quick transition in RMS voltage between two steady-state conditions
	Flicker	Fluctuation of the grid voltage's RMS value which leads to the unsteadiness of light stimulus
Voltage Interruption		Reduction of the grid voltage below the interruption threshold
Frequency Deviation		Grid voltage frequency variation exceeds the tolerance limit in long term
Voltage Deviation		Grid voltage level variation exceeds the tolerance limit in long term
Harmonics		Components in the grid voltage or current with a frequency of an integer multiple of the fundamental frequency and below 2 kHz
Interharmonics		Components in the grid voltage or current with a frequency of a non-integer multiple of the fundamental frequency and below 2 kHz
Supraharmonics		Components in the grid voltage or current with a frequency between 2 kHz and 150 kHz

are responsible for maintaining the compatibility level of grids and ensuring fairness between different grid users. On the other hand, grid users are responsible for limiting their disturbance emissions that deteriorate the grid compatibility [14]. The parameters used to quantify that have influences on power quality and their descriptions from the international standards IEC 61000-4-30 [33] are summarised in Table 2.1.

Although the installation of FCS has increased dramatically, it is still an emerging load to the power grid. The power quality standards specific to the FCS do not exist yet. For example, the IEC 61400 series for wind turbine inverters and IEEE 1547 for distributed energy resource inverters. Nonetheless, referring to the IEEE power quality standards [34–37] and IEC 61000 series [38–46], which are widely used, can be a feasible approach.

To fulfill these PQ standards, a few mitigation measures have been proposed or even applied in the industry. Tan *et al.* [47] proposes a real-time charging navigation framework to overcome the impact of FCSs on voltage stability. Zhao *et al.* [48] proposes a management method for FCS operators to regulate the EV's charging behavior. BESSs can also be integrated into FCS to compensate for the pulsating charging load and reduce the required FCSs' grid connection capacity. A few studies have been done regarding the BESS sizing [49], and the power flow control of the BESS [50, 51]. For harmonic mitigation, the

methods mainly include filter design with various damping methods [52, 53] and control. For the latter, the impedance-based approach is one of the very promising ones [32, 54–61], especially if several converters are connected in parallel in a weak grid, which is likely the FCS scenario. Much research has been done regarding the impedance modeling [57, 59] and shaping [55, 60, 61] for the fast charger’s front-end converter.

The rest of the chapter is organized as follows. In Section 2.2, the trend of FC, the state-of-the-art standards, and batteries and infrastructures for FC are investigated. Then, a survey on the measured and estimated PQ problems brought by FCSs is presented in Section 2.3. The PQ standards, with which the performance of FCSs can be assessed, from IEEE and the IEC are reviewed and summarized in Section 2.4. The PQ issues’ mitigation measures are then presented in Section 2.5. The chapter is concluded in Section 2.6.

## 2.2 TRENDS OF FAST CHARGING

A survey [62] was done in 2017, revealing that most EVs only travel short distances and mainly rely on home charging. However, the survey also reflects a positive correlation between EV’s daily driving distance and the number of FC events, as illustrated in Fig. 2.1. The same conclusion remains when the scope is per week. Such a positive correlation indicates that FC is needed for EV drivers for long-distance trips. To alleviate the users’ range anxiety and encourage them to use EVs for long-distance trips, many FC facilities have been installed in the past years, by EV manufacturers (e.g., Tesla) or energy companies (e.g., Shell).

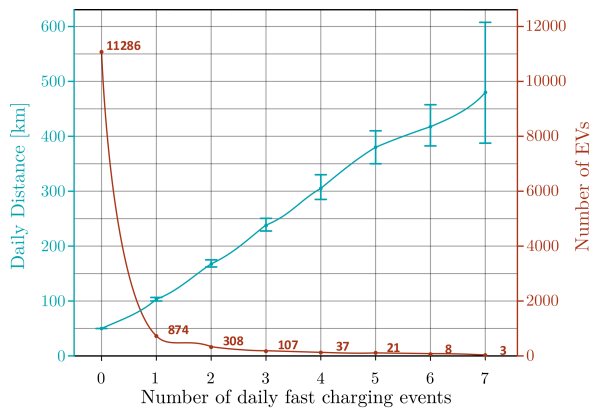









Figure 2.1: The relation between the daily distance traveled and the number of the FC events [62]

### 2.2.1 ULTRA-FAST CHARGING IS COMING

With the rollout of EVs, the total energy demand for EVs is expected to grow dramatically. The trend of energy demand for EVs in the three primary markets is shown in Fig. 2.2a [65]. More specifically, although the slow AC charging will keep its dominant share through 2030, the penetration of DCFC will increase very significantly, as seen in Fig. 2.2b.

These years witnessed a fast increase in the charging power of DCFCs. In 2020, the DCFC typically rates at 50 kW [66]. Four years later, more than half of the DCFCs can

Table 2.2: Status of FC standards in 2020 [18, 63, 64]

Standard	CHAdeMO	GB/T	CCS Type 1	MCS
Compliant Standards	IEEE 2030.1.1 IEC 62916-3	IEC 62916-3	SAE J1772 IEC 62916-3	N.A.
Connector Inlet				
Maximum Voltage (V)	1000	750	600	1250
Maximum Current (A)	400	250	400	3000
Maximum Power (kW)	400	185	200	3750
Maximum Market Power (kW)	150	125	150	1000-1500
Communication Protocol	CAN		PLC	
V2X Function	Yes		No	
Start year	2009	2013	2014	2022
Standard	CCS Type 2	Tesla	ChaoJi	
Compliant Standards	IEC 62916-3	SAE J3400 (NACS)	CHAdeMO and GB/T (IEC and CCS not yet but is ongoing)	
Connector Inlet				
Maximum Voltage (V)	900	1000	1500	
Maximum Current (A)	400	500	600	
Maximum Power (kW)	350	500	900	
Maximum Market Power (kW)	350	250	N.A.	
Communication Protocol	PLC	PLC	CAN	
V2X Function	No	YES	Yes	
Start year	2013	2023	2020	

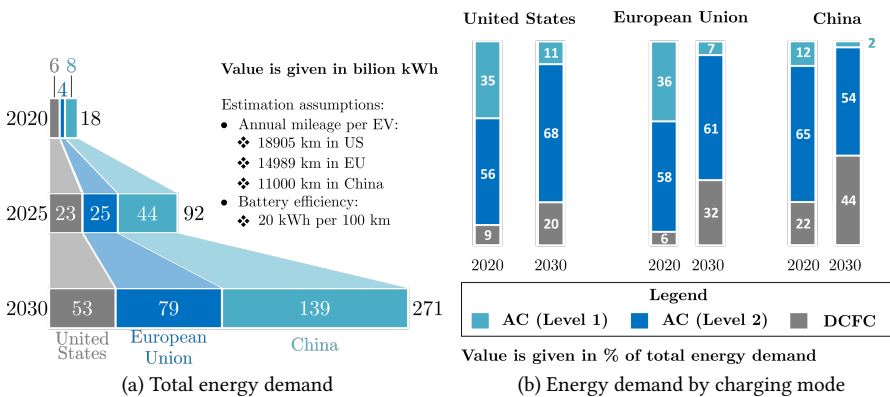


Figure 2.2: The energy demand for EVs [65]

deliver more than 150 kW charging power in Europe [67]. Unlike overnight-slow charging, a 15-minute charging time is the maximum acceptable to most drivers during traveling [68]. To charge EVs in 15 minutes, the required power for EV models with high battery capacity [69] in the market is listed in Table II. As seen, the desired charging power for the long-range EV can reach up to more than 300 kW. Compared to the results in 2020 [70], the battery capacity increased a lot which makes high charging power more necessary.

Table 2.3: Statistics of the EVs on the market in 2024 [69]

Model	Battery Capacity (kWh)	Range (km)	Required Charging Power (kW)*	Actual Maximum Charging Power (kW)
VinFast VF 9	123	520	344	130
Mercedes-Benz EQS SUV 500	118	530	330	160
Mercedes-Benz EQS 450+	118	690	330	160
Lucid Air Grand Touring	112	665	314	184
Porsche Taycan Turbo S	97	505	271	240
Tesla Model S	95	560	266	140

Note \*: Required average charging power to recharge the EV's battery from SoC = 10% to SoC = 80% in 15 minutes, where SoC means state of charge

Meanwhile, the FC standards are also being developed quickly to support UFC. The widely adopted FC standards comprise CCS, CHAdeMO, GB/T, and NACS (i.e., SAE J3400). The CCS has Type 1 for the North American market and Type 2 for Europe and Australia market [18]. The maximum operating specifications of different DC charging standards are summarized in Table 2.2. Besides, the compatibility of the FC standards with international standards (i.e., IEC 62916, IEEE 2030.1.1, and SAE J1772) for both the AC and DC charging modes are also shown. As an example to show the fast development in this field, the standard ChaoJi was co-developed by the CHAdeMO association and China Electricity Council in 2020 and was the one defining the highest charging power by then [63]. Only two years later, in 2022, the association CharIN released its MCS standards and brought the charging power to the megawatt level. However, it is worth mentioning that MCS is developed mainly to fulfill the gap in standards for charging heavy-duty vehicles instead of light-duty vehicles.

## 2.2.2 BATTERIES ARE GOING HIGH POWER

The battery technology also limits the maximum charging power. Besides, the high energy capacity of batteries is desired by customers as well so the demand for long-range is satisfied.

The lithium-ion battery is the most popular one in the EV market because of its relatively higher energy and power density than other mobile battery technologies. The lithium-ion battery cell's energy and power density are significantly affected by the material used for the electrodes. By applying the state of art material, there are already commercial battery cells that can be charged with 4C (15-min charging time) while keeping the energy density acceptable (i.e., > 150 Wh/kg), as listed in Table 2.4 [71–74].

The battery's maximum charging power also depends on the thermal performance of the cell and the cooling in the cell and pack level. In [75], four battery packs' thermal performance with different battery cells and cooling conditions are simulated under the

Table 2.4: Battery cells capable of fast charging [71–74]

Company	Material of anode/cathod	Charging rate (Max.)	Energy density
CATL	Graphite/NMC	4 C	215 Wh/kg
Kokam	Graphite/NMC	4 C	152 Wh/kg
Microvast	PC/LMO	4 C	190 Wh/kg
Enevate	Si/NMC	9 C	350 Wh/kg

Note:

- NMC: Lithium Nickel Manganese Cobalt Oxide
- PC: Porous Carbon
- LMO: Lithium Manganese Oxide

350 kW charging power. It denotes that the batteries’ temperature under UFC stays in the safe region if the low energy density (175 Wh/kg) battery cell is used. However, the cooling system in the study is substantially oversized. There are already EVs in the market rated at 200 kW and 60 kWh [76], a good balance between power and energy density. Besides, the battery pack’s voltage level is rising from 400 V to 800 V for UFC, which can reduce the weight of the cable and design challenges of its cooling system.

However, battery technology still needs to be improved to get a long lifespan. The capacity degradation of batteries can be significantly influenced by UFC, among other factors, including the operating temperature of the cell, the characteristics of the active material, the anode design, and the charging protocol (e.g., constant-current-constant-voltage charging) [77]. Thus, more research on these aspects of batteries is needed before they can be reliably applied for UFC.

**2.2.3 ARCHITECTURE OF ULTRA-FAST CHARGING STATION**

Most FCSs are expected to be constructed along the expressway to offer FC service for long-distance trips. According to the configuration of Tesla’s FCSs [78], an FCS comprises 10-12 150 kW DCFCs resulting in a total power capacity of 1.5-1.8 MW is normal. For such an FCS, the direct connection to the medium-voltage (MV) distribution network is preferred to avoid overloading of the low-voltage (LV) grid. In [18, 79–81], several approaches are proposed for the direct connection to the MV grid for FCS.

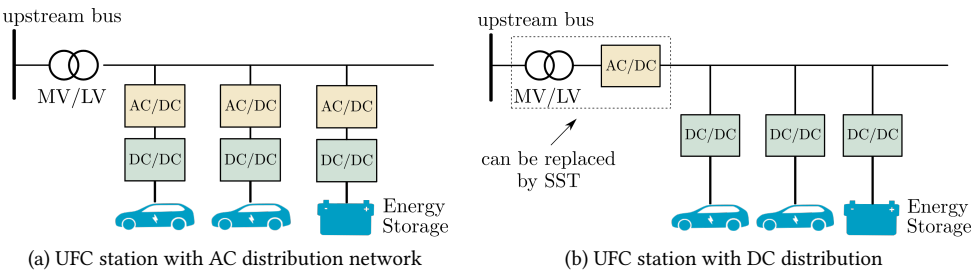


Figure 2.3: The structure of UFC station [18, 79]

The LV distribution network inside the FCS can be either AC or DC, as shown in Fig.

2.3[18]. Compared with its DC counterpart, the AC distribution network is mature and adopted by most state-of-the-art FCSs [18, 79]. Nevertheless, the DC network configuration shows advantages on fewer conversion stages and simpler integration of chargers. Besides, as the rectifier is centralized, it, together with the MV/LV line frequency transformer, can be replaced by a solid-state transformer (SST), which can significantly reduce the space, power losses, and cost of FCSs compared with the AC-coupled station [79]. As a promising concept, there is already a manufacturer planning to develop an SST-based FCS [82]. Despite this, this chapter will focus on the AC-coupled FCS, which is still the mainstream solution for now and near future.

As shown in Fig. 2.4, the DCFC consists typically of two stages of conversion. The first stage is usually a step-up PFC to match the EV battery voltage (400 V - 800 V). The typical topologies for this stage include Vienna rectifier, conventional 2-level voltage source rectifier, and multi-pulse rectifier [83, 84] because of their features: a) low complexity, b) high reliability, c) low input current harmonics [88, 89].

Compared with the other two, the Vienna rectifier has three voltage levels. Hence, it requires less inductance for the input filter to fulfill the grid code regarding harmonics. Besides, as illustrated in Fig. 2.4, the voltage stress on the switches was reduced by half. These two factors lead to improved efficiency and increased power density. However, the Vienna rectifier only allows unidirectional power flow. Another active front-end converter among the three is the conventional 2-level voltage source rectifier. Due to two-level switching, it is less competitive regarding power density. However, it allows for bi-directional power flow. So, it is also widely used for on-board chargers on which the V2G functions are implemented. As for the last one, the multi-pulse rectifier, it is used mainly because of its simplicity. It is less attractive than the other two because it has severe distortion in the current draw from the grid.

For the second stage, typically used topologies are the half-bridge LLC, dual active bridge [25, 26], and interleaved buck [85–87]. The galvanic isolation is needed in either the this stage or the first stage to provide the isolation between the EV and the grid, required by IEC 61851-23.

Also, DCFCs generally use modular design [90] because a) the voltage and current stresses on components can be reduced, b) the DCFC can be compatible for the EVs with a wide range of voltage level in the market, c) the high efficiency can be maintained in the broad operation range of the charger, d) the cooling is easier as the heat source is spread [31], e) the charging power capacity of the DCFC can be fully utilized by charging several EVs with proper control despite the charging power for single EV has a wide range in the whole charging cycle. Especially for b) and c), as the battery voltage has a wide range regarding the battery's SoC and different EV models might have 400 V system or 800 V systems, the DCFC is usually designed for the output voltage range from 200 V to 1000 V. With proper control strategy[91], modular design allows the submodules to switch between parallel and series connections to keep high efficiency in a wide output voltage range.

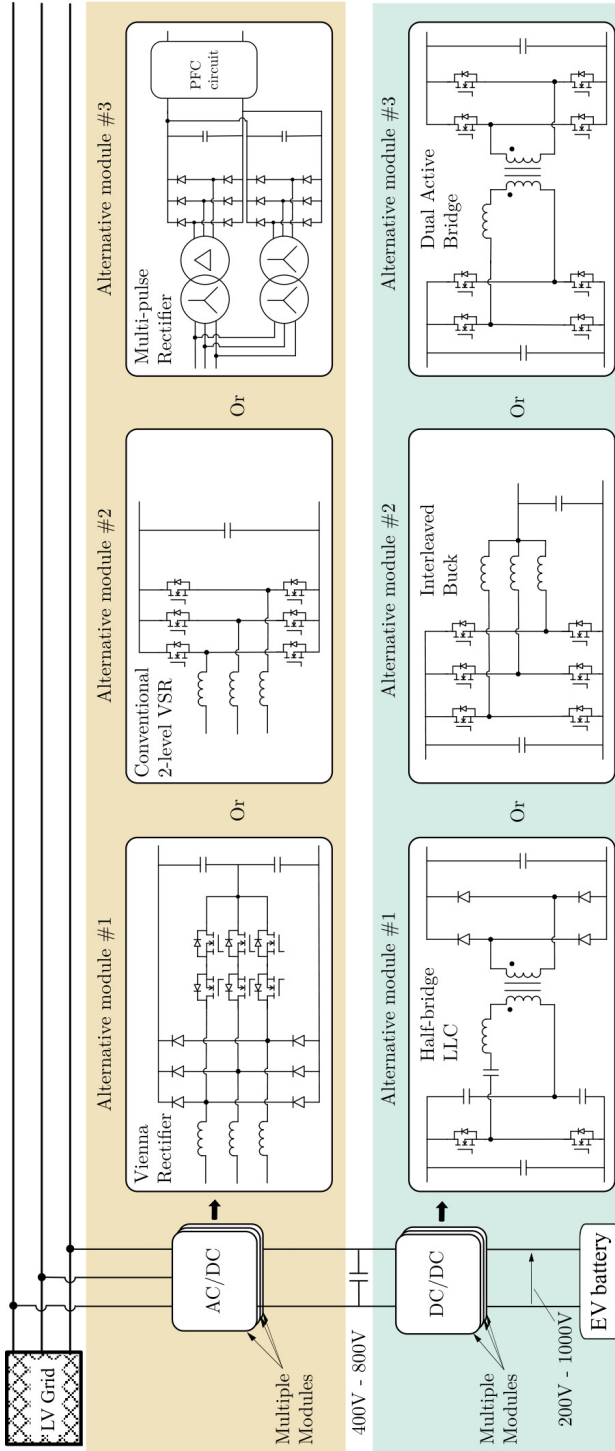


Figure 2.4: Typical topologies of DC fast charger [83–87]



## 2.3 POWER QUALITY ISSUES

Compared with the overnight slow charging, FCS shows some different characteristics as follows:

- the charging power is high
- the load demand is centralised at the FCS
- the charging is mainly during daytime
- the load is more pulsating because of shorter charging time and higher power demand

Due to these features, FCS might create more severe issues in power quality. As mentioned in the previous section, FCS is usually connected to the MV distribution grid due to its high-power capacity. Thus, the scope of this chapter is limited to the PQ inside and at the point of common coupling (PCC) of the FCS, which can be summarized as follows as reported or predicted in the literature: [7, 9–13, 15, 16, 92, 93]:

- Voltage fluctuation
- Harmonic stability
- Harmonic emission
- Supraharmonic emission

The PQ at the FCS's PCC is influenced not only by the FCS itself but also by the grid condition and the behavior of the other loads/sources connected to the grid. For instance, the harmonic voltage at the FCS's PCC is determined by the FCS's harmonic emission, the harmonic voltage in the background voltage, and the grid impedance at FCS's PCC, which is discussed in details in Subsection 2.3.3.

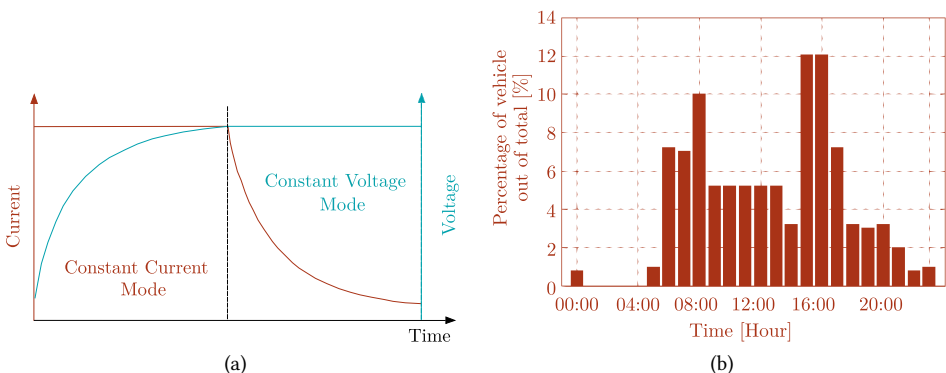


Figure 2.5: (a) The charging profile of an EV [94] and (b) the equivalent of the arrival time distribution of EVs at an FCS, which is adapted from the arrival time distribution of ICEVs at a petrol fuelling station [95]

Besides, the voltage fluctuation measured at the PCC is influenced by both the FCS's load profile and the other loads' behavior (e.g., the start-up and shut-down of a motor)

and how does the voltage fluctuation propagate from the point where the load cause the voltage fluctuation is connected to the FCS's PCC. The uncertainties on the grid condition, e.g., the harmonic voltage in the background voltage and impedance at the FCS's PCC, and FCS's load profile, make it difficult to discuss the FCS's impact on the distribution grid in general. However, the methodology for assessing the FCS's grid impact using some typical data (e.g., IEEE test feeder cases and representative load profile of FCS) can still be established. A typical load charging profile of EV is shown in Fig. 2.5a [94]. Based on the single EV load profile, the FCS's load profile can be estimated with a typical arrival time distribution of EVs at the FCS. As shown in Fig. 2.5b, the arrival time distribution of EVs at an FCS can be assumed equivalent to the arrival time distribution of ICEVs at a petrol fuelling station [95].

### 2.3.1 VOLTAGE FLUCTUATION

The voltage fluctuation issues includes rapid voltage change (RVC) and flicker. To analyze the flicker problems brought by the FCS, a case study is carried out in [15]. The assumption used in the case study comprises: a) the typical arrival time distribution at the FCS [95], b) the Monte Carlo method for probabilistic analysis, c) the IEEE 4 bus test feeders which is illustrated in Fig. 2.6. According to the results, the magnitude of the voltage fluctuation on Bus 4 is much higher when the DCFC's maximum charging power increases from 60 kW to 350 kW.

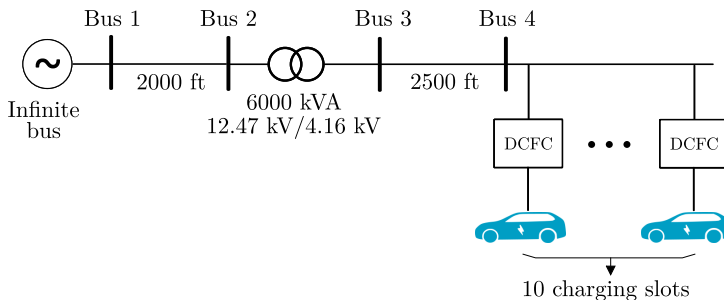


Figure 2.6: IEEE 4 bus test feeder used in [15] to simulate the voltage fluctuation induced by the EV charging with DCFCs

The flicker issue is also found at a bus station with a 120 kW charger [16], as seen in Fig. 2.7 where the short term flicker severity  $P_{st}$  exceeds the standard limit 1.0 on some days. In this specific case, the topology of the charger's front-end is the six-pulse diode rectifier. However, as the charging station is implemented with a wind generator, it is not clear that the measured flicker issue is mainly induced by either the variable wind generation or the charging.

However, it can be expected that high-power DCFC will induce voltage fluctuation in the LV grid inside the FCS. When a DCFC starts and stops charging the EV, it causes a change in the load current. The LV network's grid voltage will fluctuate when the load current changes because of the cable resistance. Hence, the severity of the voltage fluctuation will increase when the DCFC's power grows.

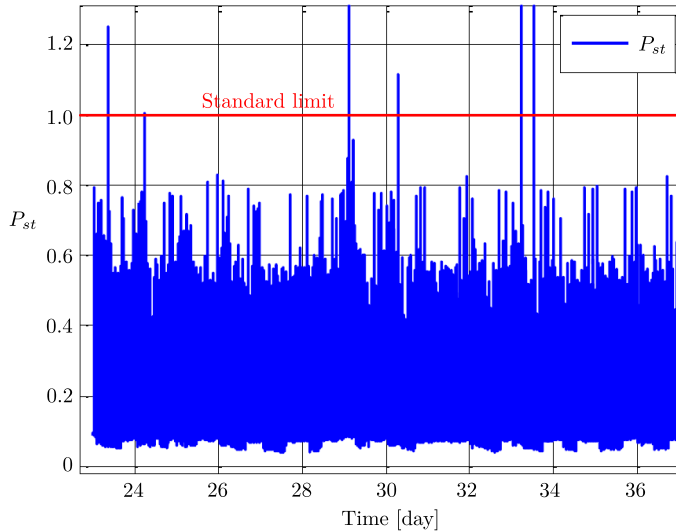


Figure 2.7: The flicker emission of a 120kW charger at a bus station during April [16]

### 2.3.2 HARMONIC STABILITY

Essentially, a DCFC is an active power converter with feedback control. The front-end converter of a DCFC is a voltage-source converter (VSC), which is connected to a voltage source on either DC side for inverter or AC side for rectifier. The output or input impedance of such a converter will behave like a negative resistance at some frequencies. If there is a resonant point in the same frequency range, instability will happen, which is the root cause of the instability of the power electronics-based system. As DCFC is also a power electronics-based system, stability issues can be expected. To analyze such problems, an impedance model-based approach, shown in Fig.2.8 is often used [54].

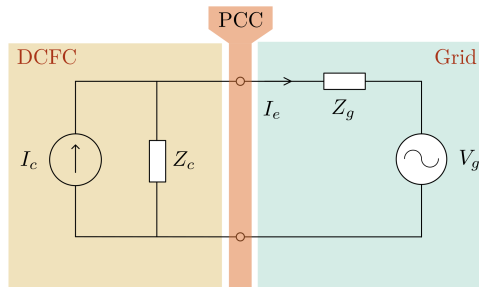


Figure 2.8: Impedance model of charger-grid system

The impedance model is a small-signal model in which the grid is simplified as the background voltage source  $V_g$  and the grid impedance  $Z_g$  at the PCC of the DCFC. On the other side, the DCFC is modeled as the harmonic current source  $I_c$  with the converter input impedance  $Z_c$  in parallel. The harmonic current source is used instead of the harmonic

voltage source because DCFCs' input current is controlled to meet the charging demand. According to the impedance model, the harmonic current emission  $I_e$  can be calculated as (2.1)

$$I_e(s) = \left( I_c(s) - \frac{V_g(s)}{Z_c(s)} \right) \frac{1}{1 + \frac{Z_g(s)}{Z_c(s)}} \quad (2.1)$$

As seen,  $Z_g/Z_c$  is like an open-loop transfer function of a feedback control system. So it determines the stability of the system, and Nyquist stability criteria can be applied here. It also shows that the system's stability is a matter of matching between the grid impedance and the DCFC's input impedance. That's why, under the weak grid condition (i.e.,  $Z_g$  is high), the converter input impedance  $Z_c$  plays a crucial role for system stability since the Nyquist plot of  $Z_g/Z_c$  has a chance to encircle  $(-1, 0)$ .

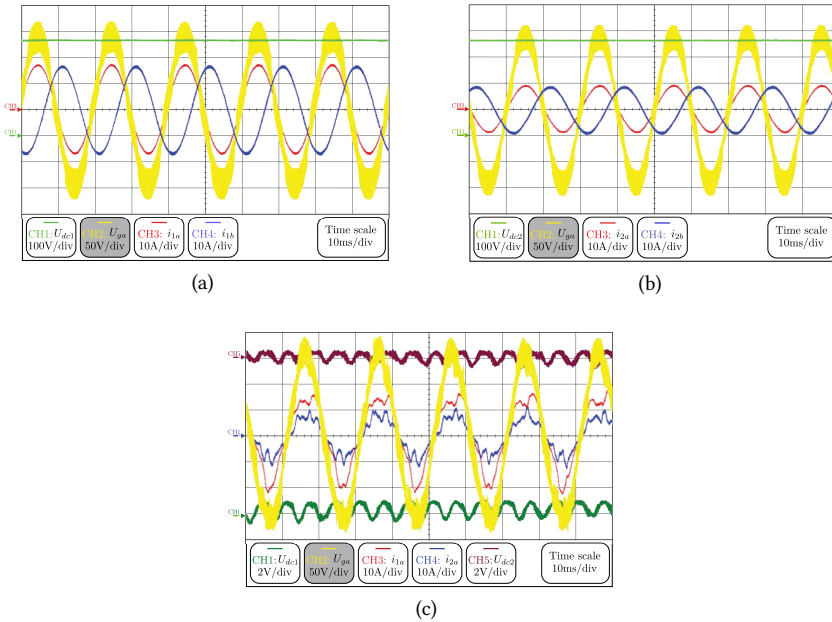


Figure 2.9: Waveform of two VSCs when: (a) the converter 1 is connected to the non-ideal power grid solely, (b) the converter 2 is connected to the non-ideal power grid solely and (c) the two converters are connected to the non-ideal power grid in parallel, where for example the  $U_{dc1}$ ,  $U_{ga}$ ,  $i_{1a}$  and  $i_{1b}$  is the dc bus voltage, phase a input voltage, phase a input current and phase b input current of the converter 1 respectively [92]

Furthermore, the properly tuned single VSC, which is stable when solely connected to the grid, might become unstable when connected to the grid with several units in parallel, as reported in [92] and shown in Fig. 2.9. The parameters of the nonideal power grid and the VSCs is listed in Table 2.5.

Besides, due to the interaction between the  $Z_c$  and  $Z_g$ , a grid-tied VSC operates well when the  $V_{PCC}$  is clean and with 3% total harmonic distortion (THD), but it trips when the  $V_{PCC}$  is distorted with the maximum allowed THD set in EN 50160 [7].

Table 2.5: Parameters of the nonideal power grid and converter in [92]

Nonideal power grid					
$V_a, V_b, V_c$	$f_1$	$L_s$	$L_L$		
110 Vrms	50 Hz	1.2 mH	180 $\mu$ H		
Converter 1					
$U_{dc,ref}$	$C_{dc}$	$L$	$R_L$	$r$	$f_s$
360 V	1000 $\mu$ F	3 mH	37 $\Omega$	0.01 $\Omega$	10 kHz
Converter 2					
$U_{dc,ref}$	$C_{dc2}$	$L$	$R_L$	$r$	$f_s$
360 V	1000 $\mu$ F	3 mH	72 $\Omega$	0.01 $\Omega$	10 kHz

Note:

- $V_a, V_b, V_c$ : Line to neutral voltage of phase a, b, and c, respectively
- $f_1$ : line frequency
- $L_s$ : grid impedance
- $L_L$ : Inductance between the two converters
- $U_{dc,ref}$ : DC bus voltage
- $L$ : filter inductance
- $C_{dc}$ : Capacitance of the DC bus capacitor
- $R_L$ : Resistance of the load resistor
- $r$ : filter resistance
- $f_s$ : switching frequency

2

### 2.3.3 HARMONIC EMISSION

The harmonic current emission in (2.1) can be rewritten as

$$I_e(s) = \frac{Z_c(s)I_c(s)}{Z_c(s) + Z_g(s)} - \frac{V_g(s)}{Z_c(s) + Z_g(s)} \quad (2.2)$$

where the left-hand side term indicates the harmonic current generated by the harmonic current source, i.e., the VSC, while the right-side term indicates the harmonic current emanated from the distorted background voltage  $V_g$ .

The harmonic current of a commercial 50 kW DCFC, when the input power is 11 kW and 50 kW respectively, is measured in [10] and shown in Fig. 2.10. Due to the lack of grid voltage measurement, it is difficult to identify the harmonic current's primary source. The result is shown with the percentage of the fundamental current, making it challenging to evaluate the absolute harmonic emission (in Ampere) since the fundamental current keeps changing during a whole charging cycle.

Alternatively, the total demand distortion (TDD) of the current, which is calculated using the root-mean-square (RMS) value of the maximum demand current as the base, is a better metric for assessing the harmonic current emission rather than the THD of the current [12, 96]. In a measurement [11], the TDD and the percentile of the main individual harmonic current to the rated DC output current in the whole charging cycle are recorded, as seen in Fig. 2.11. The result shows that the maximum harmonic current emission does not appear at the peak load.

### 2.3.4 SUPRAHARMONICS

The harmonic analysis in a conventional power system is normally performed on the harmonics with a frequency below 2 kHz. In the standards [34, 41, 43, 46, 97], the emission

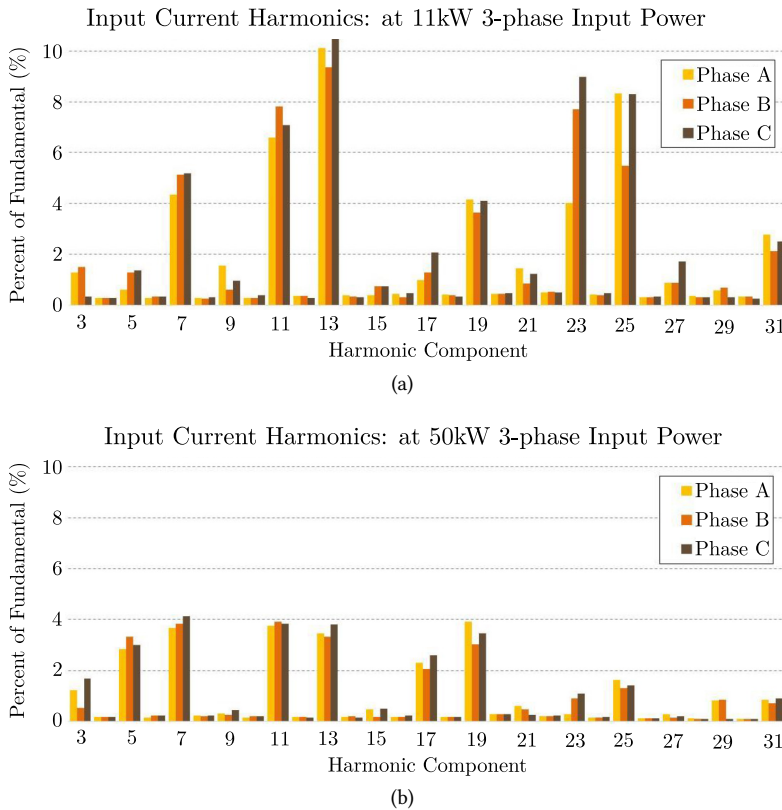


Figure 2.10: The individual harmonic current of the 50kW DCFC when: (a) the input power is 11kW (b) the input power is 50kW [10]

limits are given for up to 50<sup>th</sup> harmonic (2.0 or 2.4 kHz for a 50 or 60 Hz system respectively) for equipment rated < 16A [97] and > 16 A [41]. However, due to more integration of the power electronic-based system (e.g., DCFC and wind turbine), research interest on the supraharmatics (components within the frequency range 2 to 150 kHz) [98] is increasing, and to standard IEC 61000-4-30 [99] an informative annex about this topic is added. The chargers, or more specifically converters, can be a source of supraharmatic distortions, as switching frequencies in the supraharmatic range are often used as efficiency- cost- and weight-effective solutions. Especially for on-board chargers in electric vehicles, where low weight and small size is even of more importance, the converters mostly use switching frequencies in the supraharmatic range as shown previously [100][101].

As electric vehicles charge with relatively high power and a higher chance of more supraharmatic disturbances than other household equipment, their effect on a low-voltage installation can be tremendous. Supraharmatics can lead to different impacts on the LV grid and equipment connected to it. If a supraharmatic component with a significant amplitude is present in a weaker grid (with a higher impedance) this can also lead to a higher distortion of the voltage. This voltage distortion will then propagate additional

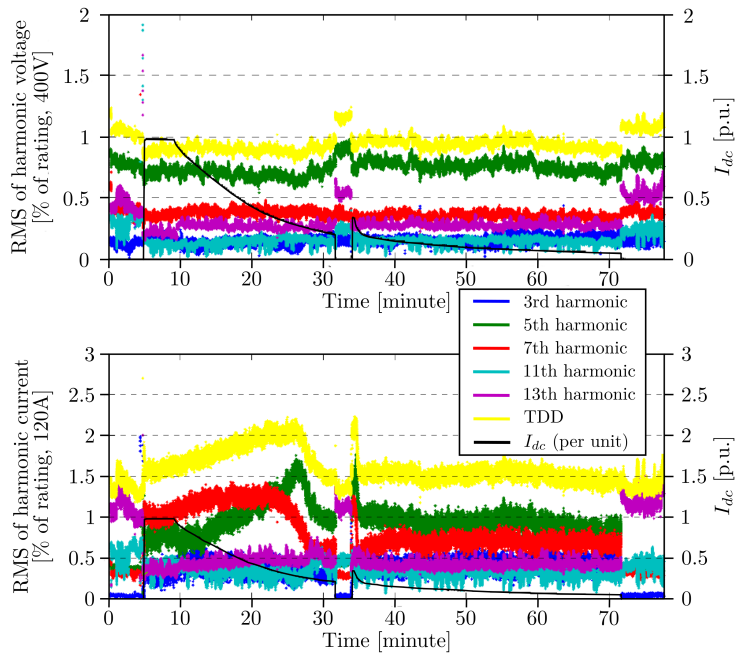


Figure 2.11: Main harmonic emission in the charging course of the 50 kW DCFC [11]

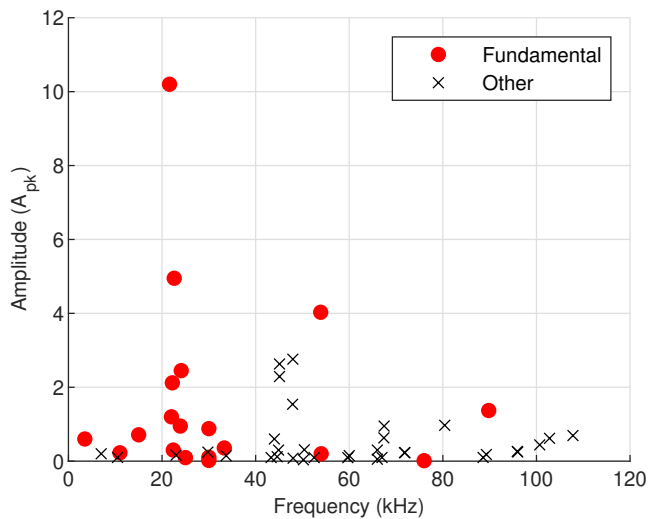


Figure 2.12: Supraharmonic emission of 22 DCFCs, showing the first (fundamental) switching component and multiples or unrelated (other) components

supraharmonic currents through the installation, exposing more components and devices to it. Mainly because supraharmonic emission is still only partly standardized, devices are often not immune to disturbances in this frequency range. This can lead to additional heating of those and a reduced lifetime. Furthermore, audible noise (2 - 20 kHz falls into the human hearing range), malfunction of equipment (e.g., charging interruptions and high errors in energy metering), malfunction of power-line communication (PLC) and possibly tripping of residual current devices have been reported [13, 93].

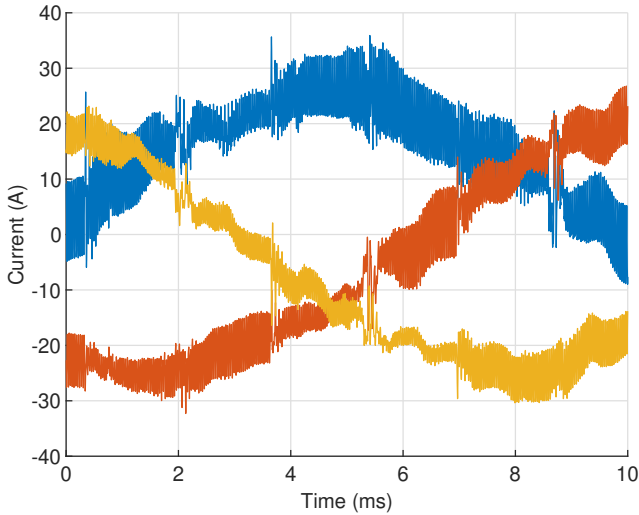


Figure 2.13: Supraharmonics in the 3-phase currents measured at the input of a DCFC

Regarding DCFCs, which mostly have higher power than the on-board chargers and sometimes a different converter type, it is unknown if similar or other effects can be expected. Indicative measurements (by ElaadNL) of 22 DCFCs from 18 manufacturers at reduced power showed that DCFCs could also be a very significant source of supraharmonic currents, with amplitudes higher than the on-board chargers, as seen in Fig. 2.12. Side note here is that DCFCs are often installed in another grid situation than AC chargers, making a smaller impact on the consumer installation. Nevertheless, this can lead to interaction between the DCFCs and impact the grid, which is still under investigation. Also, for these kinds of distortions from DCFCs, no standard exists yet. An example of currents from a DCFC at reduced power with supraharmonic components is shown in Fig. 2.13.

## 2.4 POWER QUALITY STANDARDS

As an emerging installation to the grid, FCS does not have dedicated PQ standards. Nonetheless, the general PQ standards can be used for assessment. Internationally, the most adopted PQ standards include IEEE PQ standards [34–37] and IEC 61000 series [38–46], whose content related to the aforementioned PQ issues of FCSs are summarized in Table 2.6. For simplicity, the national grid codes are not compared here.



Table 2.6: Comparison of IEEE PQ standards and IEC 61000 series within the scope of the FCS related[34–46]

Voltage level for MV and LV grid		IEEE PQ standards		IEC 61000 series			
		LV grid: $V \leq 1\text{kV}$ MV grid: $1\text{kV} < V \leq 69\text{kV}$		LV grid: $V \leq 1\text{kV}$ MV grid: $1\text{kV} < V \leq 35\text{kV}$			
		Level		Compatibility level		Emission (E) and Planning (P) level	
		Value	In IEEE	Value	In IEC 61000-	Value	In IEC 61000-
Voltage Level	MV grid	$\pm 10\%$ tolerance	1159	$\pm 10\%$ tolerance	2-4	N.A.	
	LV grid	$\pm 10\%$ tolerance	1159	$\pm 10\%$ tolerance	2-4		
Voltage Fluctuation	MV grid	Same as IEC 61000 series	1453	RVC $\leq 3\%$ Flicker: N.A.	2-12	RVC (Indicative): • 2.5% - 6% (P) Flicker (Indicative): • $P_{st} = 0.9$ (P) • $P_{lt} = 0.7$ (P) • Guidelines for setting emission level are given	3-7
	LV grid		1453	RVC $\leq 3\%$ Flicker: • $P_{st} = 1$ • $P_{lt} = 0.8$	2-2	RVC: • 3% - 6% (E) Flicker: • $P_{st} = (S_L/S_{TR})^{1/3}$ (E) • $P_{lt} = 0.65(S_L/S_{TR})^{1/3}$ (E)	3-5
Voltage unbalance	MV grid	N.A.		$V_n \leq 2\%V_p$	2-12	• $V_n \leq 1.8\%V_p$ (P) • Guidelines for setting emission level are given	3-13
	LV grid	$V_n \leq 2\%V_p$	141	$V_n \leq 2\%V_p$	2-2	• Planning level can equal to the compatibility level • Guidelines for setting emission level are given	3-14
Harmonic Current	MV grid	Table 2.7	519	Compatibility level is given only for harmonic voltage		Guidelines for setting emission level are given	3-6
	LV grid	Table 2.7	519			Guidelines are given for setting emission level	3-4 3-14
Harmonic Voltage	MV grid	Fig 2.14	519	Fig 2.14	2-12	• Planning level is shown in Fig 2.14 • Guidelines for setting emission level are given	3-6
	LV grid	Fig 2.14	519	Fig 2.14	2-2	• Planning level can equal to the compatibility level • Guidelines for setting emission level are given	3-14

Note:

- $S_{TR}$ : Apparent power of the service transformer
- RVC : Rapid Voltage Change
- $S_L$ : Apparent power of the load
- $I_{eqp}$ : Rating phase current of the equipment
- $V_n$ : Negative sequence voltage
- $V_p$ : Positive sequence voltage

In general, both the IEEE PQ standards and IEC 61000 series provide the limits or the guidelines on setting limits for the PQ items, which can be assessed at the PCC. In detail, the IEC 61000 series mostly gives only system compatibility and planning level. The equipment emission level is then calculated based on the system planning level and specifications. In

this way, the emission level adapts to the specific system and more room for the normal operation of the system is reserved. On the contrary, IEEE PQ standards, which set fixed values as the limits, are much simpler, but also easier to use. Apart from the mentioned standards, it is worth mentioning that IEC 61000-3-16 gives a good reference for harmonic current emission limits for inverter and inverter-type energy supplying equipment, which can be applied to chargers with V2G functionality. Regarding the network characteristics, IEC 61000-2-15, CISPR 16-1-2, and IEC 60725 give more references and are helpful for allocating suitable local emission level.

Additionally, although it is not shown in Table 2.6, the compatibility level for supraharmonics is added into IEC 61000-2-2 amendment 1 and 2. Regarding the rest power quality disturbances, a more detailed comparison of IEEE PQ standards and the IEC 61000 series is given as follows.

### 2.4.1 RMS VOLTAGE TOLERANCE

The RMS voltage tolerance in normal operation for different voltage levels is specified in IEEE 1159 and IEC 61000-2-4. As shown in Table 2.6, in both of the standards,  $\pm 10\%$  tolerance is allowed for the long-term (i.e.,  $> 1$  min) RMS voltage.

### 2.4.2 VOLTAGE FLUCTUATION

The voltage fluctuation consists of the RVC of the fundamental voltage and flicker. It is worth noting that RVC and flicker are sometimes overlapped on each other in assessment, but there is no clear correlation between the two [102]. Thus, in Table 2.6, the two limits are separated.

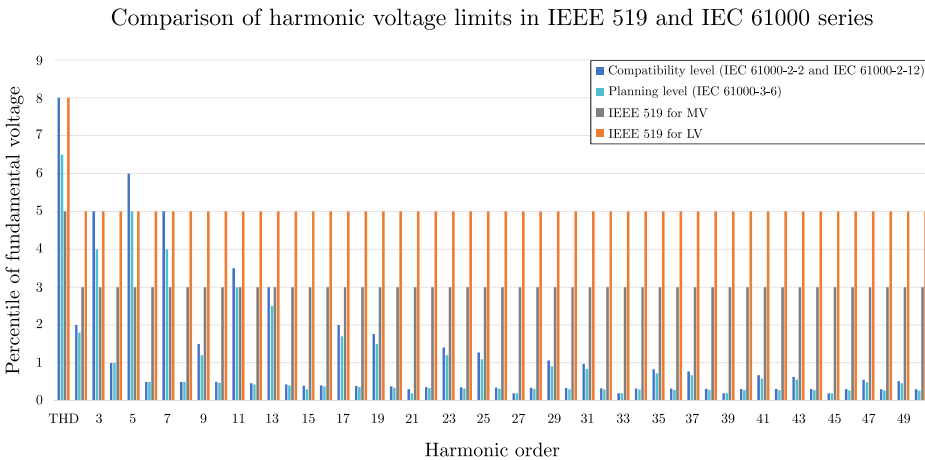


Figure 2.14: Limits set for harmonic voltage in IEEE 519 and IEC 61000 series [34, 38, 40, 43]

In the IEC 61000 series, only the compatibility level and planning level are given where the emission level is decided by the system operator or owner, according to the planning level and the system circumstance. In IEEE PQ standards, the content regarding the limit for voltage fluctuation is the same as that in the IEC 61000 series.

Table 2.7: Harmonic current limits in IEEE-519[34]

$I_{sc}/I_L$	Maximum harmonic distortion of the individual harmonic order in percent of $I_L$					TDD
	$3 \leq h < 11$	$11 \leq h < 17$	$17 \leq h < 23$	$23 \leq h < 35$	$35 \leq h < 50$	
< 20	4.0	2.0	1.5	0.6	0.3	5.0
20 < 50	7.0	3.5	2.5	1.0	0.5	8.0
50 < 100	10.0	4.5	4.0	1.5	0.7	12.0
100 < 1000	12.0	5.5	5.0	2.0	1.0	15.0
> 1000	15.0	7.0	6.0	2.5	1.4	20.0

Note:

- Limits for even harmonics are 25% of the odd harmonic limits
- DC offset in current is not allowed
- $I_L$ : maximum demand load current
- $I_{sc}$ : maximum short circuit current at PCC

### 2.4.3 HARMONIC CURRENT DISTORTION

In the IEC 61000 series, the THD, which is the ratio of the RMS value of the sum of all the harmonic components up to 50th order to the RMS value of the fundamental component, is used for standardization. For installations with a phase current rating higher than 16 A connected to the LV grid, the emission level at the PCC is limited in IEC 61000-3-4 [41]. However, the limits are determined based on some assumptions that are representative of small residential loads [46], which might not be applicable for a high power, e.g., 350 kW, DCFC. IEC 61000-3-14 [46] provides guidelines on how to develop emission limits to prevent excessive voltage distortion in the LV grid. As for the emission level for installations connected to the MV grid, the recommended emission limits are not given in IEC 61000-3-6[43]. Instead, guidelines on how to set the emission level according to the situation in practice are provided.

In IEEE 519, the TDD, which is the ratio of the RMS value of the sum of all the harmonic components up to 50th order to the RMS value of the maximum demand current, is used for the standardization. The maximum demand current is a summation of the DC component, fundamental component, and all harmonic components. Besides, the recommended harmonic current emission is given in specific values for five different short-circuit ratio (SCR) values. A low SCR indicates a high grid impedance for a particular load whose load capacity is specified. In the weak grid scenario, the grid impedance is high. The grid voltage at PCC is more sensitive to the harmonic current emission from the load, so a lower harmonic current emission is allowed.

Compared with the IEC 61000 series, IEEE 519 is less complicated to be applied. Although the IEC 61000 series provides enough flexibility, it might be difficult when applying them because, for instance, it requires network data and calculation of many factors as shown in Fig. 2.15. However, by following the IEC 61000 series guidelines, the system's normal operation tends to be maintained more easily without compromising the fairness between the customers. As aforementioned, IEEE 519 set harmonic current emission limits for five different SCR values regardless of, for instance, the system voltage level and supply system's capacity, which might lead to failing to keep the harmonic voltage limit set by its own [103]. However, compared with the counterpart, IEEE 519 might be more successful when assessing the harmonic current emission of DCFCs since it uses TDD as the metric for the assessment, which is, as aforementioned, preferred to reflect the harmonic emission level of chargers.

### 2.4.4 HARMONIC VOLTAGE DISTORTION

For harmonic voltage distortion, its compatibility level in the MV grid is interpreted in the IEC 61000-2-12, whereas the indicative planning level is introduced in IEC 61000-3-6. Similarly, the guidelines for setting the harmonic voltage emission level are given instead of any specific values. In the LV environment, its compatibility level is introduced in IEC 61000-2-2, whereas the guidelines for setting harmonic voltage emission levels is provided in IEC 61000-3-14. With a known impedance of the grid at PCC, the current and voltage emission levels can be converted to each other.

In IEEE 519, the maximum THD of the grid voltage is given for the LV and MV grid respectively, which is illustrated in Fig. 2.14

### 2.4.5 VOLTAGE UNBALANCE

In LV grid, the negative sequence voltage should be lower than 2% of the positive sequence voltage, which is set in IEEE 141 and IEC 61000-3-14. As for large installations like the high-power DCFC, the guidelines for deriving the device's emission level in the LV and MV grid are introduced in IEC 61000-3-14 and IEC 61000-3-13, respectively. Moreover, an indicative planning level of voltage unbalance in the MV grid is given in IEC 61000-3-13. In contrast, no suggestion is given for the planning level of voltage unbalance in the LV grid. No IEEE standards exist regarding the voltage unbalance in the MV grid.

### 2.4.6 EMISSION LEVEL ALLOCATION

In the IEC 61000 series [43–46], guidelines for allocating the installations' emission levels in the MV and LV environment are introduced. Overall, three stages are provided for the allocation. Among the three stages, Stage 2 is suitable for the installation that is the same as the FCS whose power capacity is high (e.g., 2-3 MW) and high power DCFC. Thus, Stage 2 is briefly summarized hereafter.

As shown in Fig.2.15, to allocate the emission level of the FCS in the MV distribution network at Node i and the emission level of the DCFC in the LV distribution network at Node c, the critical four steps are as follows,

#### STEP 1: ACQUIRING SYSTEM PARAMETERS

To plan the emission that can be allocated to the FCS and the specific DCFC, the necessary system parameters are:

- The planning level of the emission to be assessed in different voltage levels (i.e.  $L_{xLV}$ ,  $L_{xMV}$  and  $L_{xUS}$ ), where the subscript  $x$  denotes the type of the emission, i.e.  $h$  for harmonics,  $u$  for voltage unbalance,  $Pst$  for short-term flicker and  $Plt$  for long-term flicker. For simplicity, the denotations afterward are always the same and explained otherwise.
- The grid harmonic impedance  $X_h$  at the MV busbar, the grid harmonic impedance  $X_{hi}$  at the PCC of the FCS in the MV distribution grid, the grid harmonic impedance  $X_{hB}$  at the LV busbar of the FCS and the grid harmonic impedance  $X_{hc}$  at the PCC of the DCFC in the LV distribution grid inside the FCS. The subscript  $h$  denotes the harmonic order.

- The maximum power capacity  $S_{iMV}$  of the MV distribution network, the maximum power capacity  $S_{iLV}$  of the FCS, the agreed power  $S_i$  of the FCS, and the agreed power of the DCFCs (e.g.,  $S_c$  for the DCFC at Node c in Fig. 2.15).

## 2

### STEP 2: CALCULATING THE GLOBAL EMISSION LEVEL

To derive the emission level allocated to the FCS in the MV grid and DCFC in the LV grid, the global emission levels  $G_{xMV+LV}$ ,  $G_{xMV}$  and  $G_{xLV}$ , which signify the emission can be shared by all the MV and LV installations, only the MV installations and only the LV installations respectively, are derived on beforehand. Based on the system parameters acquired in Step 1, these global emission levels can be derived considering the contribution of the disturbance transmitted from the upstream and downstream systems.

The equations used for the derivation are shown in Fig. 2.15 in Step 2 block, where the summation law with the exponent  $\alpha$ , the transfer coefficient  $T_{xML}$  for the disturbance transferred from the MV grid to the LV grid and the transfer coefficient  $T_{xUM}$  for the disturbance transferred from the upstream grid to the MV grid, are applied. The typical value of the  $T_{xUM}$ ,  $T_{xML}$  and  $\alpha$  for the different types of emission is given, which is shown at the bottom of Fig. 2.15.

It is worth noting that to derive the  $G_{xMV}$ , the disturbance,  $E_{xLV}$ , transmitted from the LV grid to the MV grid is needed. For flicker emission, the  $E_{PstLV}$  and  $E_{PltLV}$  are neglected because of the LV installations' small power capacity relative to the power capacity of the MV grid. As for the voltage unbalance, the  $G_{uMV}$  is not needed as  $G_{uMV+LV}$  is used instead. However, the LV grid's harmonic voltage can propagate to the MV grid, and the  $E_{hLV}$  needs to be estimated. The estimation method is not elaborate here for simplicity.

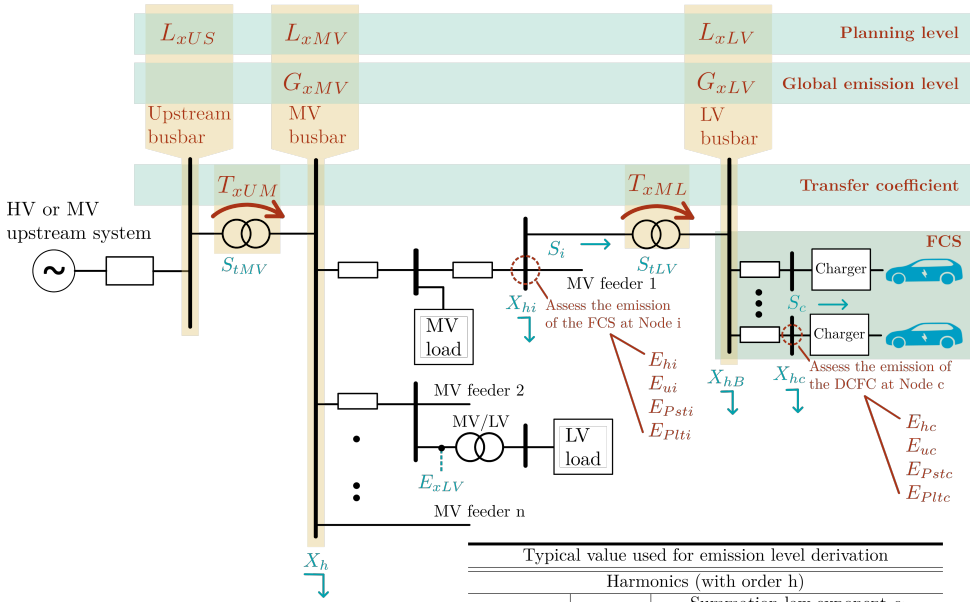
### STEP 3: DERIVING THE CHARACTERISTIC PARAMETERS OF THE POWER SYSTEM

In this step, the reduction factor  $K_{xB}$  of the LV grid, the allocation coefficient  $A_{xMV}$  of the installations in the MV grid, and the inherent unbalance coefficient  $K_{uE}$  of the whole MV and LV distribution grid are derived. The methods for derivation are introduced in the IEC 61000 series, which is not elaborated here for simplicity.

### STEP 4: DERIVING THE EMISSION LEVEL

Finally, the emission level can be derived with the equations shown in Fig. 2.15 in Step 4 block. In the equations, the  $U_{NLV}$  is the nominal phase-to-phase voltage of the LV grid, and the  $S_{LV}$  signifies the power capacity of the installations supplied directly by the other LV distribution grid except FCS. The allocated emission to the installation is dependent on the position of the PCC in the system and the agreed power of the installation.

To maintain the disturbance within the planning level, the emission  $E_{xi}$  at Node i where is the PCC of the FCS, and emission  $E_{xc}$  at Node c where is the PCC of the DCFC need to be maintained below the allocated emission level.



Typical value used for emission level derivation			
Harmonics (with order h)			
$T_{hUM}$	$T_{hML}$	Summation law exponent $\alpha$	
		$h < 5$	$5 \leq h < 10$
$< 1 - 3$	$< 1 - 3$	1	1.4
Flicker			
$T_{PstUM}$	$T_{PstML}$	Summation law exponent $\alpha$	
		3	
0.82 - 0.91	0.98 - 1		
Voltage unbalance			
$T_{uUM}$	$T_{uML}$	Summation law exponent $\alpha$	
		1.4	
0.8 - 1	0.8 - 1		

**Step 1: Planning level**

Acquiring the planning level

↓

**Step 2: Global emission level**

Calculate the global emission level of the MV and LV grid.

LV grid:  

$$G_{xLV} = \sqrt[\alpha]{L_{xLV}^\alpha - (T_{xML} \cdot L_{xMV})^\alpha}$$

MV grid and LV grid:  

$$G_{xMV+LV} = \sqrt[\alpha]{L_{xMV}^\alpha - (T_{xUM} \cdot L_{xUS})^\alpha}$$

MV grid:  

$$G_{xMV} = \sqrt[\alpha]{L_{xMV}^\alpha - (T_{xUM} \cdot L_{xUS})^\alpha - E_{xLV}^\alpha}$$

↓

**Step 3: Characteristics of the system**

Estimating the reduction factor  $K_{xB}$  of the LV grid

Estimating the allocation factor  $A_{xMV}$  for all the emission pertaining to the FCS

Estimating the unbalance factor  $K_{uE}$  accounting for the system inherent unbalance

**Step 4: Emission level**

Emission allocated to the DCFC at Node c:  

$$E_{xc} = \frac{U_{NLV}^2}{S_c} \cdot G_{xLV} \cdot \sqrt{\frac{S_c}{S_{LV}}} \cdot \min\left(\frac{K_{xB}}{X_{hB}}, \frac{1}{X_{hc}}\right)$$

Harmonic emission allocated to the FCS at Node i:  

$$E_{hi} = \frac{A_{hMV} \cdot S_i}{\sqrt{X_{hi}}}$$

Voltage unbalance emission allocated to the FCS at Node i:  

$$E_{ui} = \sqrt[\alpha]{K_{uE} \cdot G_{uMV+LV}} \cdot \sqrt{\frac{S_i}{S_{LMV}}}$$

Flicker emission allocated to the FCS at Node i:  

$$E_{Pxti} = G_{PxtMV} \cdot \sqrt{\frac{S_i}{S_{tMV} - S_{LV}}}$$

Figure 2.15: The procedure for allocating the emission level of the FCS and DCFC. The FCS is connected to the MV distribution grid at Node i where the disturbance emission of the FCS needs to be evaluated. The disturbance emission of DCFCs should be assessed at their PCC e.g. Node c [43–46]

## 2.5 MITIGATION MEASURES

To fulfill these PQ standards, mitigation measures have been proposed or already applied in the industry. More details are as follows,

### 2

#### 2.5.1 SMART CHARGING

Conventional smart charging strategy is effective for 6-8 hour overnight low-power charging but not for FCSs, which happen randomly in a day and lasts for a short period (typically 15 mins).

To overcome the impact of FCSs on voltage stability, a real-time charging navigation framework, as seen in Fig. 2.16, is proposed [47] to attract EV drivers to recharge at off-peak hours to decrease the stress on the grid. The navigation framework also reduces the stress on the transportation system by guiding EV drivers to the closest FCS offering the desired charging price and charging power. With this framework, the distribution system operator can influence the EV drivers' charging behavior by manipulating the electricity price. A simulation is performed to investigate the effectiveness of the proposed approach. The simulation is based on a distribution system whose topology is the IEEE 34-node test feeder. The results reveal that the proposed approach can reduce the burden of the peak load.

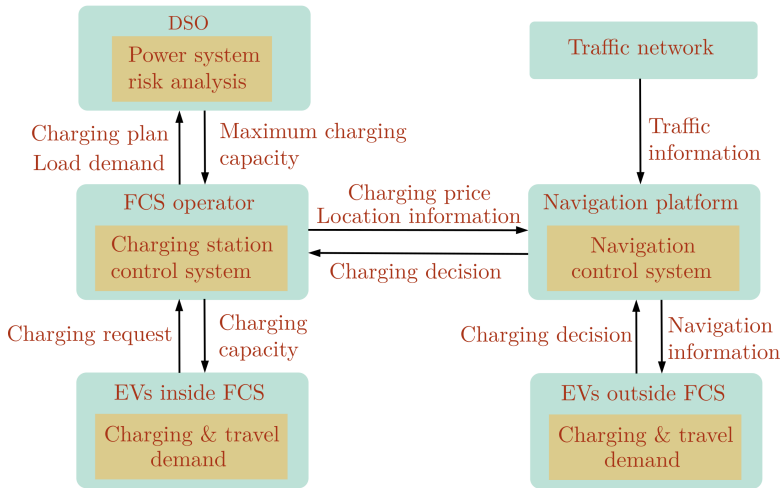


Figure 2.16: A EV charging navigation framework and FCS control system to decrease the risk of voltage sag and instability [47, 48]

Moreover, the FCS operator can coordinate the chargers according to the grid condition by altering the charging power. In [48], a management method is proposed to regulate the EVs' charging behavior to decrease the FCS's impact on the power grid voltage. Simultaneously, the financial benefits of FCS operators and customers are also increased.

#### 2.5.2 INTEGRATION OF ENERGY STORAGE

The application of BESSs in the power system is an emerging topic, as it can provide different ancillary services. The BESSs can be categorized into different types [104]. Typically, there

are power and energy types, where the former has a higher power rating, and the latter has higher energy capacity [50].

Integrating a BESS into an FCS can mitigate the influence of the large-pulsating load of the FCS. As shown in Fig.2.17, by integrating BESS, the high pulsating load demand is supplied through the ESS while the relative smaller and continuous load demand is supplied by the MV distribution grid via the service transformer and cable. Thus, the investment on the transformer and cable can be considerably reduced. Besides, the BESS supply can save energy loss in transmission because of the relatively shorter supply length than the MV grid. Moreover, the study in [49], where a simplified method is proposed to extract the optimized capacity of the BESS, concludes that the BESS can help to reduce the charging cost of the FCS. The control strategy for BESS is critical to make it function properly. In [51], where the flywheel is used to compensate the high impulsive load demand. The flywheel is controlled to maintain the DC link voltage of the DCFC, so that the pulsating power naturally is taken from the flywheel, and the impact on the grid is mitigated. In [50], the control strategy for the hybrid energy storage system is proposed so that the BESS can satisfy the demand of fast response and high energy capacity simultaneously.

Besides, the BESS can be integrated either inside the DCFC with multiport converters [105, 106] or directly in the LV distribution network with its own AC/DC and DC/DC converters. On the one hand, the former approach can reduce the AC/DC converter's power rating in the DCFC and provide a controllable operating point of the AC/DC converter without influencing the EV charging course. On the other hand, distributing BESS to DCFC might increase difficulty when coordinating the distributed BESS for high-level grid control, e.g., providing reserves for the grid.

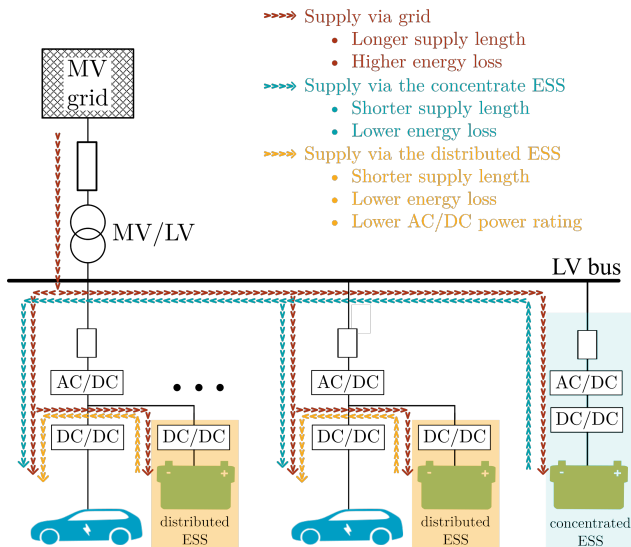


Figure 2.17: The BESS used in the FCSs can not only reduce the investment on the service transformer and cable but also the supply length and energy loss in transmission [49, 51]



### 2.5.3 IMPEDANCE BASED APPROACH

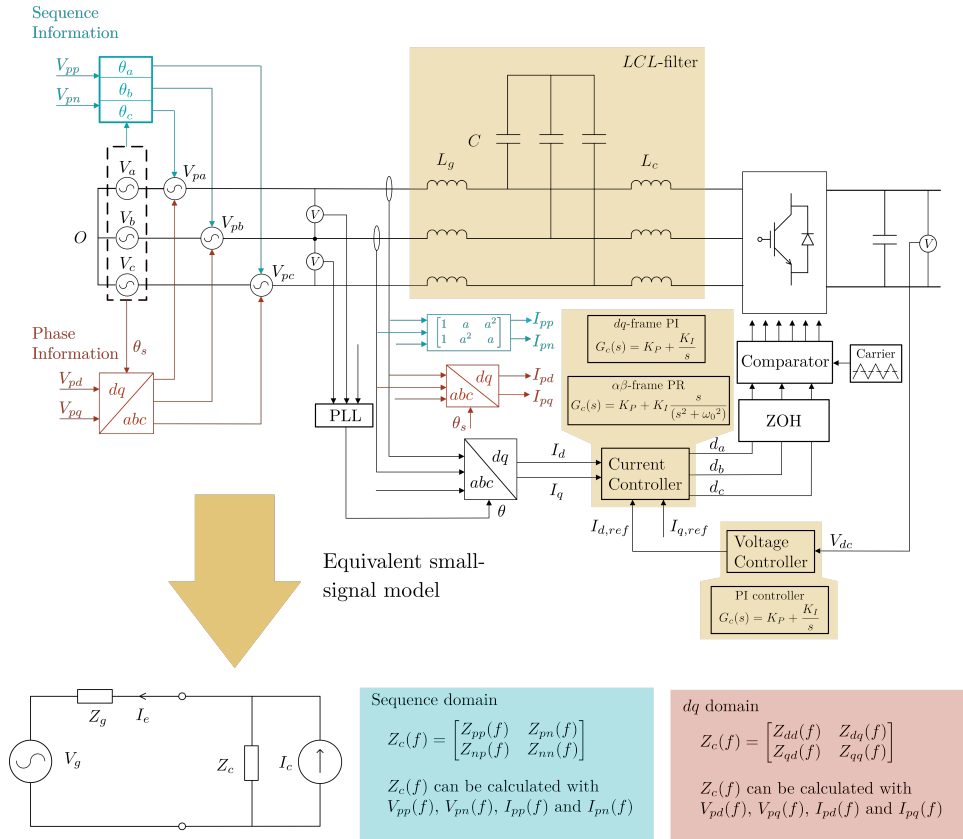


Figure 2.18: The input impedance of a typical DCFC using LCL-filter can be obtained in either the  $dq$  domain or sequence domain by injecting harmonic voltage at the frequency of interest and measure the response harmonic current at the same frequency of the injected harmonic voltage [57, 107]

The harmonic mitigation measures of the grid-tied converters typically include power filter design and control. The switching frequency noise is normally tackled with power filter design (L-, LCL-filter, etc.) together with modulation strategies [108] (SPWM, SVPWM, DPWM, SHE, interleaving, etc.). The low-frequency harmonics (e.g., up to 1/10 of switching frequency) are more affected by control. Several advanced control strategies have been proposed to handle them, including multiple resonant controllers, repetitive controller, active damping [52] etc. These approaches work well when the grid is clean. But in weak grid conditions, especially when several grid-tied converters are connected to the same weak grid (FCS is in such a condition), they start to interact with each other and get harmonics amplified and create resonances, or even instability. In that scenario, the impedance-based approach can show the mechanism more clearly.

### IMPEDANCE MODELLING OF DCFC

Many impedance modeling studies of 2-level-3-phase VSC can be found in the literature. Although the small-signal modeling and control of the Vienna rectifier (which is the main-stream front-end of DCFCs) are different from the 2-level-3-phase VSC, the difference can be neglected if the zero-sequence impedance is not of interest [109]. Thus, the impedance modeling method for general VSCs can also be used for DCFCs.

In [57], the converter small-signal model is developed in  $dq$  domain. Hence, the actual grid phase is necessary. The resulting converter impedance  $Z_c$  is a two-by-two matrix due to the coupling between the d-axis and q-axis. For stability analysis, the generalized Nyquist Criterion (GNC) [59] can be used. To verify the developed model in  $dq$  domain, small harmonic voltage perturbation at a certain frequency aligned with the d-axis and q-axis, i.e.,  $V_{pd}$  and  $V_{pq}$ , can be injected at the input terminal of the DCFC in two separate steps. In each step, the harmonic currents aligned with the d-axis and q-axis at the frequency of the injected harmonic voltage, i.e.  $I_{pd}$  and  $I_{pq}$  when  $V_{pd}$  is injected and  $I'_{pd}$  and  $I'_{pq}$  when  $V_{pq}$  is injected, are measured. Based on the measurement, the frequency related impedance can be derived by solving the equations in (2.3)

$$\begin{cases} V_{pd}(f) = Z_{dd}(f)I_{pd}(f) + Z_{dq}(f)I_{pq}(f) \\ 0 = Z_{dq}(f)I_{pd}(f) + Z_{qq}(f)I_{pq}(f) \\ 0 = Z_{dd}(f)I'_{pd}(f) + Z_{dq}(f)I'_{pq}(f) \\ V_{pq}(f) = Z_{dq}(f)I'_{pd}(f) + Z_{qq}(f)I'_{pq}(f) \end{cases} \quad (2.3)$$

The alternative approach is developing the impedance model in the sequence domain [107]. It is further improved in [110] by considering the frequency-coupling dynamics, which also results in a two-by-two matrix for the converter impedance  $Z_c$  due to the coupling between the positive sequence and negative sequence. For the model verification, the same approach used for verifying the  $dq$  domain impedance model can be used. The difference is that the injected harmonic voltage and the measured harmonic current are in the sequence domain. The methods to obtain the impedance model of a typical DCFC are illustrated in Fig. 2.18.

To ensure the accuracy of the impedance model in the  $dq$  domain, the phase of the grid voltage needs to be measured precisely, which is difficult to satisfy. However, such phase information is not necessary when implementing the impedance model in the sequence domain. Thus, the latter is easier to implement.

### IMPEDANCE SHAPING OF DCFC

As aforementioned, the input impedance of the DCFC is crucial for: a) ensuring the stability of the charger-grid system, b) low harmonic current emission. Fig. 2.19 [61] shows the frequency response of a VSC impedance  $Z_c$ , grid impedance  $Z_g$ , and the sum of them. The magnitude of  $Z_c$  and  $Z_g$  intersect at frequency  $f_i$ , where a series resonance will happen if their phase difference  $\Delta\theta = \theta(Z_g) - \theta(Z_c)$  approaches  $180^\circ$ . To improve the system stability and decrease the harmonic emission, it is crucial to shape the impedance  $Z_c$  so that the magnitude of  $Z_c$  at all frequencies is increased and the phase difference  $\Delta\theta$  at  $f_i$  is decreased[61].

Based on the developed impedance model, the factors that influence the input impedance  $Z_c$  of a DCFC are shown in Fig. 2.20 [52, 55, 57, 60, 61]. The  $Z_c$  is mainly influenced by the

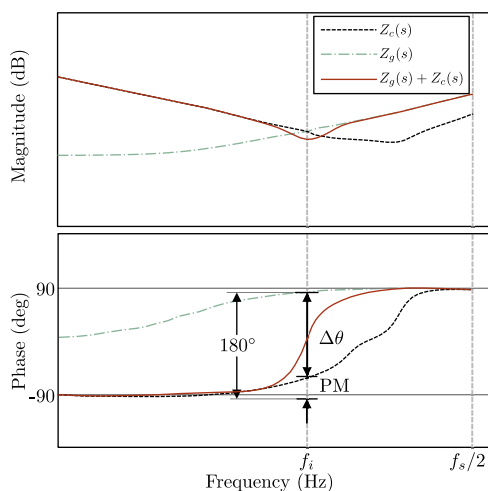


Figure 2.19: The frequency response of VSC impedance  $Z_c$ , grid impedance  $Z_g$  and the sum of them[61]

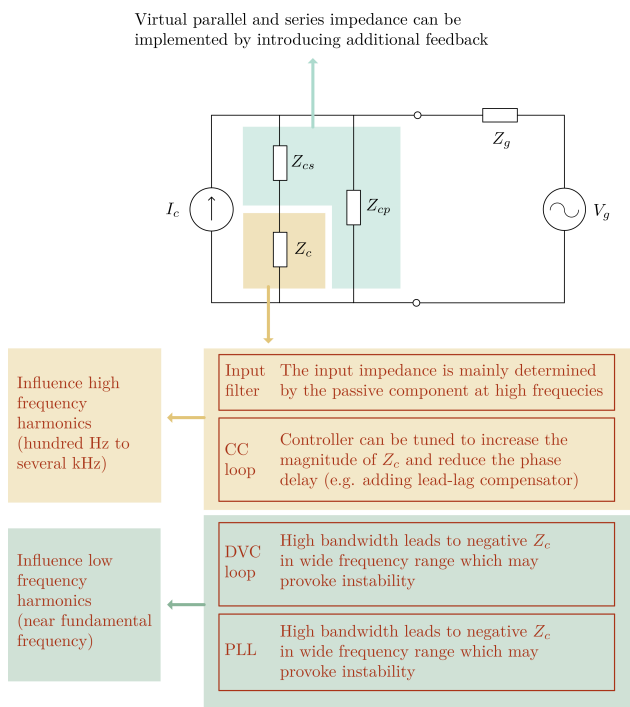


Figure 2.20: The factors that have influence on the input impedance of the DCFC [52, 55, 57, 60, 61]

outer loop, i.e., the direct voltage control (DVC) loop and the phase lock loop (PLL), at the low-frequency range due to their low bandwidth [60]. The outer loop will introduce the

additional phase delay in their bandwidth [57, 111] and decrease the magnitude of  $Z_c$  [111].

The inner loop, i.e., current control (CC) loop, has relatively higher bandwidth and influences till a higher frequency. [111] shows that the system’s harmonic stability can be increased by adding a lead-lag compensator, which decreases the phase difference  $\Delta\theta$ , in the current controller. Moreover, the input impedance can also be shaped by introducing the virtual parallel and series impedance, which is implemented by introducing additional feedback [61]. Beyond the CC loop, the input impedance is also influenced by the input filter, especially in the high-frequency range beyond the bandwidth of the CC loop.

Furthermore, it is worth noting that the VSC input impedance depends on the operation point, or more specifically, the output (or input) power. Compared with the other type of VSC, DCFCs have more dynamic input power and a wider range of operation points related to the battery’s SoC. This feature, together with unpredictable charging behaviour, introduces new challenges on maintaining the system’s harmonic stability, and further research is needed.

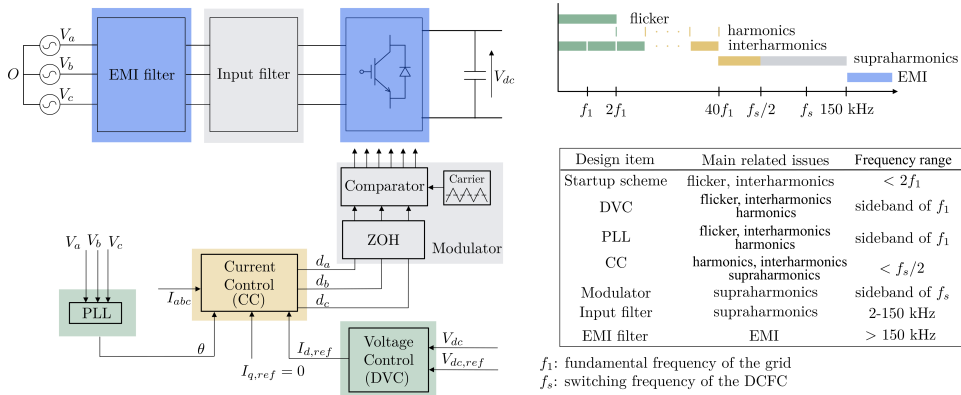


Figure 2.21: Relation between the specific charger design and the power quality issues

### 2.5.4 DESIGN OF DC FAST CHARGERS

As presented in Section 2.3, the main power quality issues induced by DCFCs are the degraded grid voltage profile and harmonic issues. To mitigate the power quality issues, it is essential to analysis the influence of the DCFCs’ design on the power quality issues. A typical DCFC’s design is illustrated in Fig. 2.21, where the relation between a specific design and the power quality issues that are most likely induced by the specific design is also shown. Analysis on each specific design is outlined as below:

1. Startup scheme; For a high-power DCFC, its startup has a significant influence on the grid voltage profile, which might lead to severe voltage fluctuation leading to flicker as shown in Fig. 2.7. The ramp startup can be applied to reduce the DCFC’s startup’s impact on the grid voltage profile. For instance, the maximum power rate of the DCFC is limited based on the distribution system operator’s command [51]. Instead of rising as a step, the DCFC’s input current ramps up slowly. However,

without a BESS integrated inside the DCFC, this approach fails to fully utilize the DCFC's power capacity.

2. PLL; As aforementioned, the PLL influences the converter impedance  $Z_c$  in the low-frequency range (near the grid's fundamental frequency) because of its bandwidth  $Z_c$ . The PLL introduces negative resistance at some frequencies, which introduces negative damping. Any harmonics and interharmonics, either preexisting in the grid or generated by the DCFC, will have increases in their amplitude due to weakening damping at the frequencies influenced by the negative resistance. In the worst case, harmonic instability might occur if the system shows negative damping at these frequencies. The PLL's bandwidth should be limited to low frequency, e.g., 20 Hz [112], to reduce the risk of the negative resistance induced by the PLL. The reason is, as found in [57, 112], the frequency range of the negative resistance has a positive relationship with the PLL's bandwidth. Besides, the PLL's dynamics induce frequency coupling, as the PLL usually tracks only the  $q$ -axis grid voltage [112]. Assuming a 450 Hz harmonic voltage exists in the background voltage, both - 350 Hz and 450 Hz harmonic current will be measured in the DCFC's input current. The minus sign indicates a negative sequence component [110]. Such a coupling effect introduces more challenges to DCFC's design. Besides, it is worth noting that the interharmonics with frequencies below  $2f_1$  is related to flicker, which is also influenced by PLL design.
3. DVC; Like PLL, the bandwidth of the DVC loop is relatively lower than the other design items in the system. The DVC loop's stability is investigated, revealing that the DVC's stability is decreased by weaker grid conditions, increasing input power of VSC, or DCFC in the case here, and bandwidth closer to the PLL's bandwidth [113]. It is further revealed that the DVC introduces negative damping in the low-frequency range [55]. Hence, the flicker, harmonics, and interharmonics are influenced by DVC. To ensure stability and prevent severe power quality issues, the DVC should be designed considering the weak grid condition, the complete DCFC's operation point, and the possible interaction with the other control loops in the system.
4. CC; As illustrated in Fig. 2.21, the CC loop influences higher frequencies. Several design aspects should be considered to ensure DCFC's stable operation and low harmonic emission when several DCFCs are connected in parallel. First of all, it is revealed in [114, 115], instability can be provoked by the interaction between the PLL and CC loop. The risk of stability can be reduced by reducing the PLL's bandwidth [114]. It is also revealed in [114] that the  $\alpha\beta$ -frame PR controller is more robust than the  $dq$ -frame PI controller against the PLL dynamics. Besides, as mentioned in [52], multiple resonant controllers can be implemented in the current control loop to null the harmonic with a certain order, e.g., 5th harmonic, in the DCFC's grid current. Besides, the CC loops of several DCFC in parallel have interaction between them, which might lead to instability, as shown in Fig. 2.9c. It is a challenge for the designers to guarantee system stability with a fixed design in this scenario, which needs to be investigated more. Finally, as aforementioned in Subsection 2.5.3, the DCFC's input impedance  $Z_c$  can be shaped with several approaches to reduce the harmonic emission in the charger-grid system.

5. Input filter; The input filter is used to attenuate the switching frequency ripple injection into the grid in the range of 2-150 kHz [116]. As aforementioned, L-, LCL-filter, and the most used two for DCFCs. Compared with L-filter, LCL-filter shows better performance when the total inductance used is the same as the L-filter's inductance [116]. However, it also has two more zeros and two more poles [116], which introduces additional challenges on the system stability. However, the design of LCL-filter is well studied in [53] to ensure system stability. Besides, there is a challenge for designing an LCL-filter, with which the DCFC is stable, in various grid impedance conditions. For instance, the LCL-filter's resonance peak would change accordingly when the DCFC is connected to a grid having a different grid impedance. In this case, a proper designed stable CC loop with high bandwidth might become unstable [52]. To solve this issue, a control, namely active damping [52], is proposed for shaping the resonance peak of the LCL-filter without compromising the bandwidth of the CC loop.
6. Modulator; The PWM modulator can induce sideband ( $f_s$ ) oscillations [55], which is normally in the range of 2-150kHz. When connecting several DCFCs with the same design in parallel, it is better to synchronize their PWM to prevent sideband-harmonic instability, which is presented in [55].
7. EMI filter; EMI filter is used to attenuate the components in the range above 150 kHz in the DCFC's grid current. However, as EMI is out of the scope of power quality issues, it is not elaborated.

## 2.6 CONCLUSION

This chapter has reviewed the state-of-the-art technology and standards for EV fast charging, which clearly show the development towards UFC. Afterwards, the PQ issues introduced by FCSs and DCFCs are thoroughly reviewed. It shows that the main PQ problems brought by FCSs and DCFCs comprises the deteriorated voltage profile and excessive harmonic emission and amplification. Since PQ standards dedicated to FCSs do not exist yet, referring to the PQ standards for general installations is a feasible approach for FCS's PQ assessment. To fulfill these PQ standards, the mitigation measures are summarized with an emphasis on the impedance-based approach. In the end, it can be concluded the barrier for large adoption of FCSs with PQ issue free is the lack of the following, which needs much effort.

1. The dedicated PQ standards for evaluating the performance of FCSs. The existing standards might be too conservative for FCSs and DCFCs, especially for the harmonic emission.
2. Study on the coordination of several parallel DCFCs considering the interaction between them to maintain the PQ. At present, the analytical impedance model of the FCS by aggregating the DCFC model has not been proposed. More study is needed on either the impedance model or another approach to model the FCS for the system analysis.

- 
- 
3. The control strategy for the FCS operator that can compromise between decreasing the impact on the grid PQ and the customers' demand on the fast charging.

## 3

## MODELLING OF ELECTRIC VEHICLE CHARGER FOR POWER QUALITY STUDY

*Extracting an electric vehicle (EV) charger's input impedance with the analytical model (white-box approach) or the frequency sweep (black-box approach) is limited by the parameter confidentiality or the measurement noise, respectively. To overcome these challenges, a Gradient-Descent (GD) optimization based gray-box modeling approach is proposed. To start with, a sensitivity study on the analytical impedance model of an EV charger with a typical controller is carried out to identify the influential frequency range per controller and circuit parameter. On top of that, given an EV charger with unknown control and circuit information, a GD optimization based algorithm for multiple parameter estimation is designed to identify the unknown controller and circuit parameters based on the measured impedance, by assuming the EV charger is using the typical controller. Then, an analytical input impedance of the black-box EV charger can be obtained. Moreover, the low accuracy issue commonly encountered when estimating multiple parameters with GD optimization is mitigated with the proposed algorithm. Compared to pure frequency sweep, the proposed approach achieves a higher accuracy for the coupling impedance and a comparable accuracy for the diagonal impedance. The effectiveness of the proposed approach is validated by experimental results.*



### 3.1 INTRODUCTION

With the electrification process of transportation systems, massive installations of DCFCs are approaching. As grid-connected power electronic converters, the impacts of DCFCs on the harmonic compatibility and the stability of power grids are inevitable [19]. Such impacts of power electronic converters have caused issues in EV charging stations [117, 118], as well as other power electronic converters based systems, e.g., PV farms and wind farms [7, 119].

The impedance-based approach is promising in analyzing the stability [54, 56, 120], and harmonic emission [121] of power electronic converter based systems, e.g., EV charging stations. Extracting the input impedance of a DCFC is indispensable to apply this approach. The input impedance can be obtained with the analytical impedance model, which is known as the white-box approach. However, a charger's analytical impedance model is not always provided by every vendor. Alternatively, the user of the charger, i.e., a charging station operator, can establish their own analytical model using the approaches in [8, 57, 112]. However, the charger's design details are required, which are confidential and concealed by the manufacturers. Here, the design details include the circuit topology, control strategy, and the parameters of the passive components and the tuned controllers. Compared to the unknown circuit topology and control strategy, which are less problematic because industrial companies follow some mainstream designs, the unknown controller and circuit parameters can vary a lot from one charger to another. Thus, extracting the input impedance with the white-box approach might be difficult in practice.

One may argue that the impedance measured with a black-box approach, namely frequency sweep, can be used instead for the stability analysis and the harmonic emission evaluation. However, the measured impedance can have significant errors [8, 122]. Furthermore, DCFCs' input impedance is also dependent on their charging power. Therefore, measuring the chargers' input impedance at all power and frequencies of interest to obtain adequate impedance information is too time-consuming.

To overcome the challenges encountered with the white-box and black-box modeling approaches, the gray-box modeling approaches [123] can be used. A gray-box impedance model has the same structure as the white-box impedance model, which is derived through the physics regulating a DCFC. The unknown parameters needed to analytically extract the input impedance can be estimated by updating the unknown parameters iteratively to minimize the mean square error, i.e., the average squared difference between the estimated impedance and the measured impedance. Therefore, the multiple-parameter estimation problem is an optimization problem. Such a problem can be solved by gradient-descent (GD) optimization, which is widely used in parameter estimation problems [124–128]. The aforementioned approaches are compared in Table 3.1 to clarify the advantages of gray-box modeling approaches.

However, one issue can arise in the parameter estimation, which leads to the low accuracy of the obtained gray-box model. Since the aforementioned parameter estimation approach generally results in a non-convex optimization problem [125], the evaluated multiple parameters can converge to wrong values which do not minimize the mean square error. Thus, the estimation results are inaccurate. Such an issue has been reported in [126], where the power transformer parameters need to be estimated. The issue can be solved by adding constraints determined by the physics in an application. For instance, in

Table 3.1: Comparison of different approaches obtaining a charger's input impedance

	Analytical model	Measured model	Normal GD optimization based gray-box model	Proposed gray-box model
How does it look like?	$Z_o = f_k(x_1, x_2, \dots, x_n)$ $f_k$ is shaped by different control of the charger, $x_i$ include both control and hardware parameters.	$Z_o = \Delta v(f) / \Delta i(f)$ $\Delta v(f)$ and $\Delta i(f)$ are small perturbations for impedance measurement.	$\hat{Z}_o = f_k(\hat{x}_1, \hat{x}_2, \dots, \hat{x}_n)$ $\hat{x}_i$ are estimated parameters of the charger by using GD optimization based on measured data.	
Need to know the control strategy $f_k$ of the charger?	Yes, but usually there are only a few typical variations of $f_k$ in EV charger, which can easily be covered.	N.A.	Yes, but usually there are only a few typical variations of $f_k$ in EV charger, which can easily be covered.	
Need to know the parameters $\hat{x}_i$ of the charger?	Yes, and the parameters are usually difficult to obtain, especially the control parameters.	N.A.	No, the parameters $x_i$ of the charger are estimated.	
Is sensitive to measured noise?	N.A.	Yes	A little, by GD optimization, the impact of the measured noise is minimized.	
Can have significant errors when the measured perturbation is small? (i.e., $< 0.1 A$ )	N.A.	Yes	No, the immeasurable points can be eliminated, since this is essentially an analytical model. Only sparse measurements are needed to identify $\hat{x}_i$ .	
Requiring of large amount of measurement data to reflect the charger's impedance in different operation conditions?	No	Yes	No, only small amount of measurement data is needed to identify $\hat{x}_i$ .	
Others	N.A.		The chance that the GD optimization converges wrongly increases as the number of $\hat{x}_i$ increases, which leads to wrong estimation. GD optimization is more effective when the number of $\hat{x}_i$ is small.	By analyzing the influential frequency range of different $\hat{x}_i$ , it is found that in some frequency ranges, $\hat{Z}_o$ is only shaped by one or several $\hat{x}_i$ . On top of that, the sequence of $\hat{x}_i$ for identification is defined. As a result, the GD optimization can converge correctly, even there are several $\hat{x}_i$ coupled together.

[127], the initial parameter estimates and constraints for power transformers are studied to help the estimated transformer parameters converge correctly to improve the accuracy of the gray-box model. However, the study on how to solve the wrong convergence issue when estimating a DCFC's parameters with their input impedance is not found in the literature. A similar concept is found in [129], where a gray-box impedance modeling approach for wind turbine inverters is proposed. However, the details on how to solve the wrong convergence issue are overlooked. Overall, the issue stems from the parameters' scaling difference and the influence of saddle points [130].

### 3

This chapter proposes a gray-box modeling approach for DCFC. The issue of low accuracy of the estimated values is addressed by a proposed estimation approach. We start with deriving the mathematical expressions of the elements in the input impedance matrix of a typical DCFC. On top of that, a sensitivity study is carried out to clarify how the input impedance is influenced by the parameters, namely the inductance of the power filter, the capacitance of the DC-link capacitor, and the controller parameters. It is found that the impedance is sensitive to the variation of different parameters in different frequency ranges. Besides, each element in the input impedance matrix is only influenced by one or several of the parameters to be estimated. Therefore, the parameters can be evaluated one by one in a designed sequence instead of together. In this way, a customized learning rate can be used for each parameter during the optimization, which ensures a fast and stable convergence. Besides, each parameter can be estimated with the impedance segment sensitive to it, which improves the estimation accuracy. The implementation of the proposed approach is elaborated and compared with a normal GD optimization-based approach. The results show that the proposed estimation approach has significantly higher accuracy and is more time efficient. Finally, the evaluated DCFC's input impedance through the proposed approach is compared with the measured one to show the effectiveness of the established gray-box model.

The rest of this chapter is organized as follows. Section 3.2 introduces the impedance modeling of a typical charger's front-end converter. Section 3.3 discusses the influence of the design parameters on the charger's input impedance. Section 3.4 discusses the challenges in a normal GD optimization-based approach and how they are addressed with the proposed approach. The implementation of the proposed parameter estimation algorithm is also presented. Section 3.5 shows the experiment carried out to verify the effectiveness of the proposed method. Finally, the chapter concludes in Section 3.6.

## 3.2 OVERVIEW AND IMPEDANCE MODELING

### 3.2.1 SYSTEM DESCRIPTION

A DCFC usually consists of several parallel power modules with smaller power rating [131]. Each power module comprises a rectifier for the AC/DC conversion and a DC/DC converter [18]. The rectifier dominates the DCFC's input impedance of EV chargers since the DC/DC converter is decoupled by a large DC-link capacitor. The mainstream designs for the DCFC's rectifier adopt either the Vienna rectifier or conventional active front end (AFE) [132]. Compared with the AFE, the Vienna rectifier has the same average model and normally has the same control strategy [109], except for an additional mid-point voltage balancing control. The balancing control is used to control the common mode current.

Therefore, it does not change the input impedance that influences the differential mode current. Here, an AFE with a typical control shown in Fig. 3.1 is assumed to elaborate on the proposed approach. As seen, the control of the AFE consists of three loops, namely the synchronous reference frame PLL for the grid synchronization, the grid current control loop in the synchronous reference frame, and the DC-link voltage control loop. Proportional-integral (PI) controllers are used as the regulators for all loops. The DC/DC converter after the AFE is simplified as an impedance  $Z_{dc}$ . For clarity, the symbols with the subscripts  $d$  and  $q$  denote the variables in the  $d$ - $q$  frame synchronous to the grid voltage. In contrast, the symbols with the subscripts  $\gamma$  and  $\delta$  denote the variables in the  $\gamma$ - $\delta$  frame synchronous to the PLL angle  $\theta_{pll}$ . The capital letters, e.g.  $E_d$ , denote the constants.

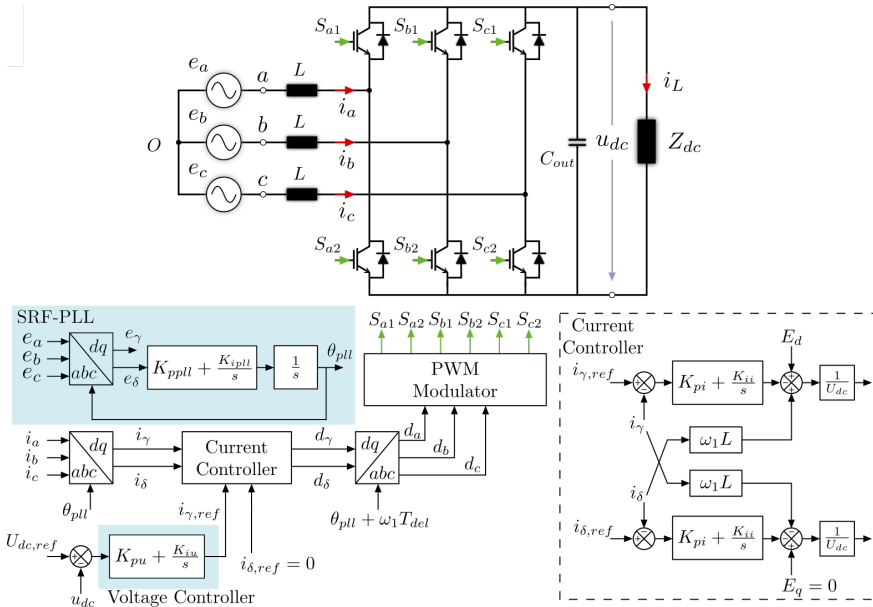


Figure 3.1: Typical active front-end converter of EV charger with the control block diagram.

The analytical modeling of the AFE’s input impedance has been well documented in the literature [57, 107, 112, 133], which, however, requires the values of the design parameters. Among the required parameters, the amplitude of the grid voltage  $E_g$ , the DC-link voltage  $u_{dc}$ , and the switching frequency  $f_{sw}$  of the AFE can be easily measured. However, due to confidentiality, the controller parameters, namely  $K_{ppll}$ ,  $K_{ipll}$ ,  $K_{pu}$ ,  $K_{iu}$ ,  $K_{pi}$ , and  $K_{ii}$ , and the circuit parameters, namely  $L$  and  $C_{out}$  are unknown and cannot be measured directly. To extract the impedance in practice with confidential parameters, purely relying on measurement is unreliable because of the influence of measurement noises. Even when accurate measurement results are reachable, tremendous effort is still needed for measurements to obtain the impedance at different frequencies and operating points. Thus, a gray-box approach requiring less effort on measurement is proposed to extract the input impedance when the controller and circuit parameters shown in Fig. 3.1 are unknown.

### 3.2.2 OVERVIEW OF THE PROPOSED APPROACH

The flowchart of the proposed gray-box modeling approach is illustrated in Fig. 3.2. As seen, the whole approach consists of two stages, namely the parameter estimation stage and the impedance extraction stage. To estimate the controller and circuit parameters, the necessary information consists of the analytical impedance model, the measured impedance at sparse frequency points, and the measured  $E_g$ ,  $u_{dc}$ , and  $f_{sw}$ . The controller and circuit parameters can be estimated by iteratively reducing the difference between the measured impedance  $Z_{meas}$  and the estimated impedance  $Z_{est}$  through a GD optimization. To ensure accurate estimation results, a parameter estimation algorithm is proposed, which requires the impedance measured when the input active power  $P$  and the reactive power  $Q$  of the AFE are both zero. As elaborated in Section 3.3, when  $P = Q = 0$ , the impedance is shaped by the parameters to be estimated in different frequency ranges so that the proposed estimation algorithm can be applied. Once the unknown parameters are estimated, the impedance at any operating points of interest can be easily extracted by using the analytical model.

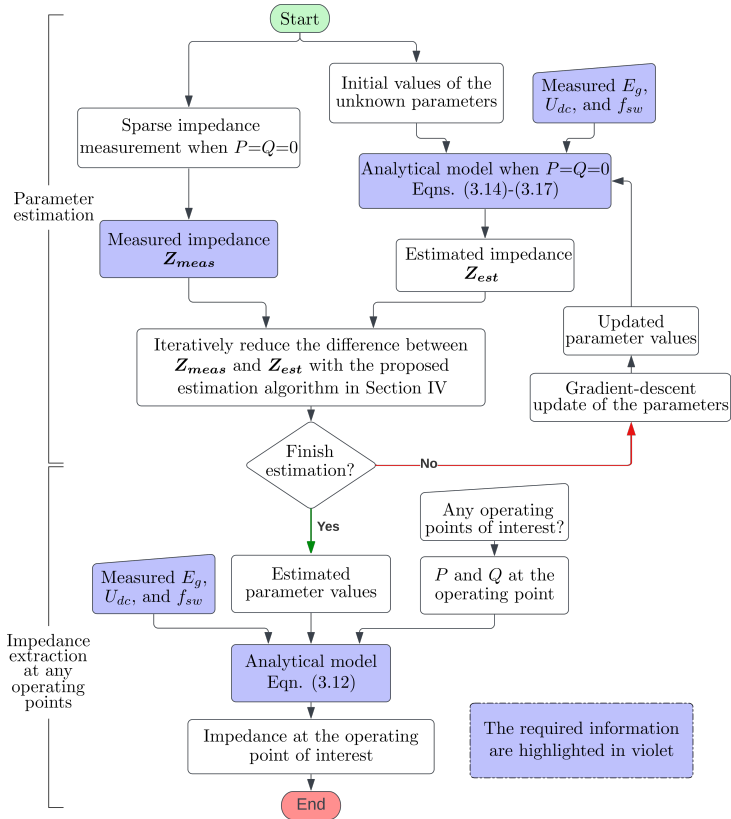


Figure 3.2: Flowchart of the proposed gray-box modeling approach.

Although the approach in Fig. 3.2 is proposed assuming the control system is the

same as the one in Fig. 3.1, the proposed approach could still be effective when another control strategy is adopted if changing the analytical model to the corresponding one. As mentioned in [129], the impedance frequency response would be different if a different control method is used. Therefore, even though the exact control method is unknown in practice, the typical control strategies can be tried to find the one that results in the best match between  $Z_{meas}$  and  $Z_{est}$ . Besides, as detailed in Section 3.4, an algorithm to obtain accurate estimation results is designed and implemented in the proposed gray-box modeling approach. When designing the estimation algorithm, one assumption used is that the multiple control loops are designed by following the well-known bandwidth selection design rule, which is choosing a higher bandwidth for the inner current loop with a lower bandwidth for the outer voltage loop. Although the design rule might not be adopted in every design, it is still followed by the majority in the industry because following the design rule saves much effort to properly design the control of an AFE. If the control of an AFE is designed without following the bandwidth selection rule, another estimation algorithm designed specifically is needed to identify the unknown parameters. However, this chapter focuses on the majority and the proposed estimation algorithm aims to be suitable for most AFEs.

### 3.2.3 SMALL-SIGNAL MODELING

Based on the average model of the AFE and the control block diagram in Fig. 3.1, the block diagram of the small-signal model of the AFE in the synchronous  $d$ - $q$  frame can be obtained. As shown in Fig. 3.3a, the small signals are denoted by the symbols with a tilde,  $G_{del}(s)$  is the delay induced by the digital control and PWM,  $Y(s)$  is the admittance of the input L-filter,  $G_v(s)$  is the DC-link voltage controller,  $G_i(s)$  is the grid current controller without the  $d$ - $q$  current decoupling,  $T_{pll}(s)$  is the transfer matrix of the synchronous reference frame PLL [112],  $J$  is the equivalent matrix of the imaginary unit  $j$  [134],  $J\omega_1 L$  represents the  $d$ - $q$  current decoupling of the grid current controller. The details of the aforementioned transfer matrices are given below

$$G_i(s) = \begin{bmatrix} K_{pi} + \frac{K_{ji}}{s} & 0 \\ 0 & K_{pi} + \frac{K_{ji}}{s} \end{bmatrix}, \quad G_v(s) = \begin{bmatrix} K_{pu} + \frac{K_{iu}}{s} \\ 0 \end{bmatrix}, \quad T_{pll}(s) = \begin{bmatrix} 0 & \frac{K_{ppll}s + K_{ipll}}{(K_{ppll}s + K_{ipll})E_d + s^2} \end{bmatrix}$$

$$G_{del}(s) = \begin{bmatrix} e^{-sT_{del}} & 0 \\ 0 & e^{-sT_{del}} \end{bmatrix}, \quad Y(s) = \begin{bmatrix} Ls + R & -\omega_1 L \\ \omega_1 L & Ls + R \end{bmatrix}^{-1}, \quad J = \begin{bmatrix} 0 & -1 \\ 1 & 0 \end{bmatrix}$$

where  $T_{del}$ , which is the time delay caused by the digital control and PWM, equals one and a half of the switching cycle period.

Additionally, in Fig. 3.3a, an element denoted with the subscripts  $dq$  represents a vector consisting of the corresponding  $d$ -axis and  $q$ -axis variables, which applies to those with the subscripts  $\gamma\delta$  as well. For example, (3.1) shows the details of the vector  $D_{\gamma\delta}$  and  $\tilde{u}_{dq}$  in Fig. 3.3a.

$$D_{\gamma\delta} = \begin{bmatrix} D_\gamma \\ D_\delta \end{bmatrix}, \quad \tilde{u}_{dq} = \begin{bmatrix} \tilde{u}_d \\ \tilde{u}_q \end{bmatrix} \quad (3.1)$$

The model shown in Fig. 3.3a can be transformed into Fig. 3.3b. The expressions of  $G_{d2dc}(s)$ ,  $G_{d2v}(s)$ ,  $G_{i2dc}(s)$ , and  $Z_{pas}(s)$  are given by

$$G_{d2v}(s) = U_{dc} \mathbf{I} + K(s) D_{dq} \mathbf{I}_{dq}^T \quad (3.2)$$

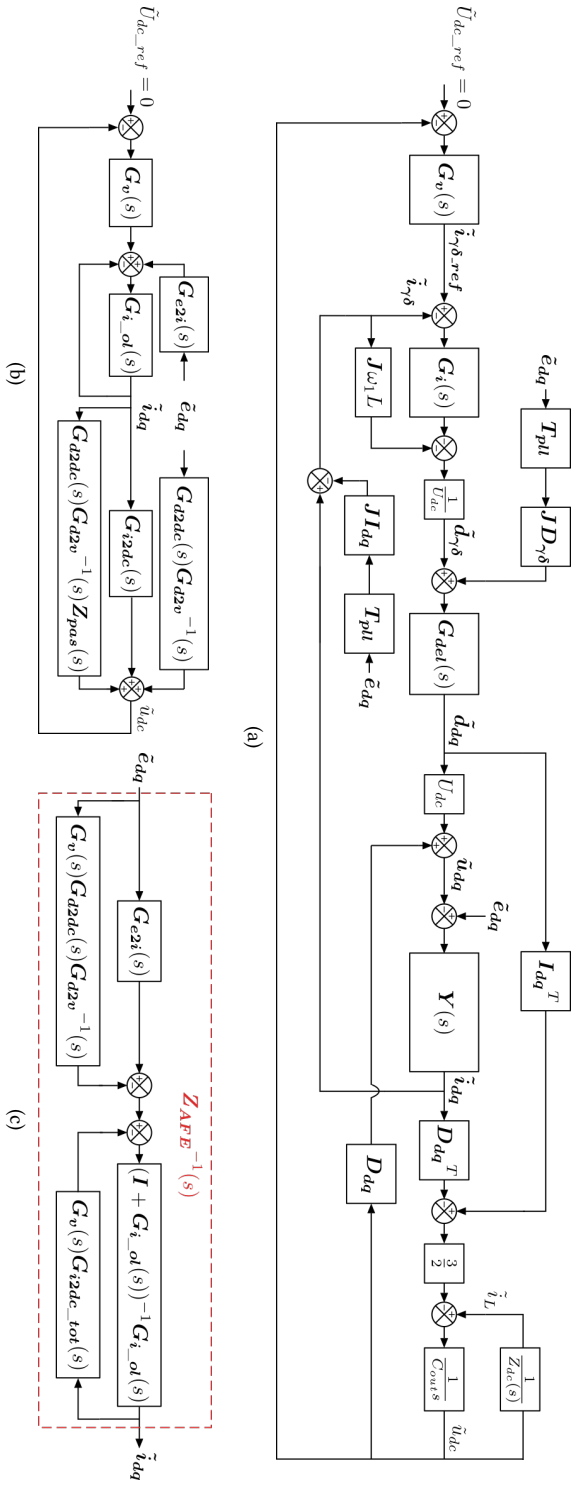


Figure 3.3: (a) Small-signal model of the system (b) equivalent transformation I, (c) equivalent transformation II.

$$G_{i2dc}(s) = K(s)D_{dq}^T \quad (3.3)$$

$$G_{d2dc}(s) = K(s)I_{dq}^T \quad (3.4)$$

$$Z_{pas}(s) = Y_{pas}^{-1}(s) = Y^{-1}(s) + K(s)D_{dq}D_{dq}^T \quad (3.5)$$

where the expressions of  $K(s)$  and  $I$  are

$$K(s) = \frac{3}{2(C_{out}s + 1/Z_{dc}(s))}$$

$$I = \begin{bmatrix} 1 & 0 \\ 0 & 1 \end{bmatrix}$$

where  $Z_{dc}(s)$  is the impedance of the load connected to the dc output of the converter.

The transfer matrix  $G_{e2i}(s)$  and the transfer matrix  $G_{i_{ol}}(s)$  can be derived as

$$G_{e2i}(s) = G_i^{-1}(s)[U_{dc}G_{del}^{-1}(s)G_{d2v}^{-1}(s) + (G_i(s) - J\omega_1L)Y_{pll}(s) - U_{dc}H_{pll}(s)] \quad (3.6)$$

$$G_{i_{ol}}(s) = (I - H(s)J\omega_1L)^{-1}H(s)G_i(s) \quad (3.7)$$

where

$$Y_{pll}(s) = JI_{dq}T_{pll}(s) \quad (3.8)$$

$$H_{pll}(s) = JD_{\gamma\delta}T_{pll}(s) \quad (3.9)$$

$$H(s) = \frac{1}{U_{dc}}Y_{pas}(s)G_{d2v}(s)G_{del}(s). \quad (3.10)$$

The equivalent block diagram can be further transformed, as shown in Fig. 3.3c. The expression of  $G_{i2dc\_tot}(s)$  is given by

$$G_{i2dc\_tot}(s) = G_{i2dc}(s) + G_{d2dc}(s)G_{d2v}^{-1}(s)Z_{pas}(s). \quad (3.11)$$

Finally, the impedance of the AFE can be written as

$$Z_{AFE}(s) = (G_{e2i}(s) + G_v(s)G_{d2dc}(s)G_{d2v}^{-1}(s))^{-1} \times (I + G_{i_{ol}}^{-1}(s) + G_v(s)G_{i2dc\_tot}(s)). \quad (3.12)$$

### 3.2.4 ELEMENTS IN THE IMPEDANCE MATRIX

The impedance is a two-by-two matrix, which is given by

$$Z_{AFE}(s) = \begin{bmatrix} Z_{dd}(s) & Z_{dq}(s) \\ Z_{qd}(s) & Z_{qq}(s) \end{bmatrix}. \quad (3.13)$$

To prepare for the sensitivity study in Section 3.3, the expressions of the  $Z_{dd}(s)$ ,  $Z_{dq}(s)$ ,  $Z_{qd}(s)$ , and  $Z_{qq}(s)$  in (3.13) are derived. However, without simplification, the expressions of the four elements in the matrix  $Z_{AFE}(s)$  are too complicated. Nevertheless, from Fig. 3.3a, it is noted that the expression can be significantly simplified when  $I_d = I_q = D_q = 0$ , i.e.,



$P = Q = 0$ . When  $P = Q = 0$ , the simplified expressions of the four elements are given by (3.14)-(3.17)

$$Z_{dd\_0}(s) = (Ls + R + \frac{3D_d^2}{2C_{out}s}) \cdot (1 + G_{i\_ol\_siso}(s)) \cdot (1 + G_{v\_ol\_siso}(s)) \quad (3.14)$$

$$Z_{dq\_0}(s) = -\omega_1 L (1 - e^{-sT_{del}}) \quad (3.15)$$

$$Z_{qd\_0}(s) = \frac{\omega_1 L (1 - e^{-sT_{del}})}{1 - G_{pll\_cl}(s) \cdot e^{-sT_{del}}} \quad (3.16)$$

$$Z_{qq\_0}(s) = (Ls + R) \cdot \frac{1 + G_{i\_ol\_siso}(s)}{1 - G_{pll\_cl}(s) \cdot e^{-sT_{del}}} \quad (3.17)$$

where  $G_{i\_ol\_siso}(s)$  and  $G_{v\_ol\_siso}(s)$  are the open-loop transfer function of the current loop after the dq-axis decoupling [135] and the voltage loop, respectively.  $G_{pll\_cl}$  is the close-loop transfer function of the PLL [136]. The expressions of  $G_{i\_ol\_siso}(s)$ ,  $G_{v\_ol\_siso}(s)$ , and  $G_{pll\_cl}$  are given by

$$G_{i\_ol\_siso}(s) = \frac{(K_{pi}s + K_{ii})e^{-sT_{del}}}{s(Ls + R)} \quad (3.18)$$

$$\begin{aligned} G_{v\_ol\_siso}(s) &= \frac{(K_{pu}s + K_{iu})}{s} \cdot \frac{3D_d}{2C_{out}s} \cdot G_{i\_cl\_siso}(s) \\ &= \frac{(K_{pu}s + K_{iu})}{s} \cdot \frac{3D_d}{2C_{out}s} \cdot \frac{G_{i\_ol\_siso}(s)}{1 + G_{i\_ol\_siso}(s)} \end{aligned} \quad (3.19)$$

$$\begin{aligned} G_{pll\_cl}(s) &= \frac{U_{dc}D_\gamma(K_{ppll}s + K_{ipll})}{E_d(K_{ppll}s + K_{ipll}) + s^2} \\ &\approx \frac{2\zeta\omega_{n\_pll}s + \omega_{n\_pll}^2}{s^2 + 2\zeta\omega_{n\_pll}s + \omega_{n\_pll}^2} \end{aligned} \quad (3.20)$$

where  $K_{ppll} = 2\zeta\omega_{n\_pll}/E_d$ ,  $K_{ipll} = \omega_{n\_pll}^2/E_d$ , and  $U_{dc}D_\gamma \approx E_d$ .

### 3.3 IMPEDANCE SENSITIVITY STUDY

#### 3.3.1 PRE-CONDITIONING

The previous section shows that the expression of  $Z_{AFE\_0}(s)$ , which is the impedance of the AFE when  $P = Q = 0$ , is a function given by

$$Z_{AFE\_0}(s) = f(R, L, K_{pi}, K_{ii}, K_{ppll}, K_{ipll}, K_{pu}, K_{iu}, f_{sw}, E_d, U_{dc}, C_{out}) \quad (3.21)$$

As mentioned in Section 3.2.1,  $f_{sw}$ ,  $E_d$ , and  $U_{dc}$  can be easily measured. Thus, the estimation of the three parameters is unnecessary, and their influence on the impedance will be not discussed. Besides, the impact of  $R$ , i.e., the equivalent loss resistance of the AFE, to  $Z_{AFE}(s)$  is found negligible in the typical range, i.e.,  $< 500 \text{ m}\Omega$ . Thus,  $R$  is also not estimated. Instead, a typical value, i.e.,  $200 \text{ m}\Omega$ , is assumed for  $R$  in the gray-box modeling of an AFE, which leads to minor errors.

The remaining eight parameters, i.e.,  $L$ ,  $C_{out}$ , and the controller parameters, will be estimated. As aforementioned, a multi-parameter estimation problem generally results in a non-convex optimization problem, which can suffer from low accuracy of the estimation because of the existence of saddle points.

Thus, we analyze the sensitivity of the impedance to the variation of each parameter to be estimated. As shown later, the sensitivity study reveals that different parameters can shape the impedance until different frequencies. Therefore, an estimation sequence for the eight parameters can be defined. In this way, the multi-parameter estimation problem can be cast into several one-parameter estimation problems to improve accuracy.

### 3.3.2 INFLUENTIAL FREQUENCY RANGE PER PARAMETER

According to (3.14)-(3.17), except for  $Z_{dq_0}$ , the impedance elements  $Z_{dd_0}$ ,  $Z_{qd_0}$ , and  $Z_{qq_0}$  are shaped by not only the passive components but also the control loop of the AFE.

However, the influence of the control loop is limited to a frequency that is positively related to the corresponding loop bandwidth. For instance, in (3.14), the item  $1 + G_{v_{ol\_siso}}$  can be approximated as 1 when  $|G_{v_{ol\_siso}}| \ll 1$  at frequencies far above the bandwidth of the VL. Similarly,  $G_{i_{ol\_siso}}$  can also be neglected when  $|G_{i_{ol\_siso}}| \ll 1$ . As for  $Z_{qd_0}$  and  $Z_{qq_0}$ , they are shaped only by the PLL regulator parameters. As the same, the close loop transfer function  $G_{pll\_cl}$  of the PLL can be ignored at high frequencies where  $|G_{pll\_cl}| \ll 1$ .

To reduce the effort of designing the control loops, some standard rules [53, 135] are followed to obtain satisfying dynamic performances, a stable system with enough margin, and a narrow frequency region of the negative input impedance [57, 112, 137], which leads to enough gain and phase margin for stability but limited loop bandwidths. Typically, for an AFE, a bandwidth above 200 Hz is used for the CL so that the current response is fast [52]. Furthermore, the bandwidth of the outer VL is generally ten to twenty times lower than the bandwidth of the inner CL, which generally results in a VL bandwidth below 100 Hz [53, 138, 139]. Such a bandwidth selection makes the tuning of the control easier by decoupling the inner loop and outer loop [53]. Further, a bandwidth below 100 Hz is generally used for PLLs to prevent instabilities and attenuate the grid voltage noise [136, 140]. As long as the bandwidth of the CL, VL, and PLL is selected as aforementioned, the influential frequency range of each parameter will not change or have only marginal change. Such stems from the fact that the influence of the parameters on the impedance is determined by the bandwidth of the corresponding control loops, which is revealed by (3.14)-(3.17).

A case study is carried out to elaborate on the influential frequency range of the parameters. The parameters of the AFE in the case study are given in Table 3.2.

Fig. 3.4 shows the absolute value of the partial derivative of  $|Z_x|$  and  $\angle Z_x$  w.r.t. each parameter, where  $x$  represents  $dd_0, dq_0, qd_0, qq_0$ . Note that the results are normalized for each parameter. With a darker blue, it indicates that  $|Z_x|$  and  $\angle Z_x$  are influenced by a parameter more at these frequencies than at the other frequencies. On the contrary, a zero partial derivative means no influence on  $|Z_x|$  and  $\angle Z_x$ . Note that similar results with marginal differences can be obtained when the parameters are different as long as the bandwidths of the control loops are designed reasonably as aforementioned.

Clearly,  $|Z_{dd_0}|$  and  $|Z_{qq_0}|$  above the CL bandwidth are mainly shaped by  $L$ .  $|Z_{dq_0}|$  is only determined by  $L$  but not by other parameters, which confirms (3.15).  $C_{out}$  has influence

Table 3.2: Parameters of charger's active front-end (AFE)

Symbol	Description	Value
$U_{dc}$	AFE output DC voltage	385 V
$E_g$	Grid line-neutral peak voltage	$110 \sqrt{2}$ V
$\omega_1$	Grid frequency	$2\pi \times 50$ rad/s
$f_{sw}$	Switching frequency of AFE	20 kHz
$C_{out}$	Output capacitance of AFE	1.67 mF
$L$	Inductance of AFE	2.5 mH
$K_{pi}$	Proportional gain of current controller	9
$K_{ii}$	Integral gain of current controller	1000
$K_{ppll}$	Proportional gain of PLL	1.21
$K_{ipll}$	Integral gain of PLL	228.40
$K_{pu}$	Proportional gain of voltage controller	0.2
$K_{iu}$	Integral gain of voltage controller	2
$BW_{CL}$	Bandwidth of current control loop	1 kHz
$BW_{PLL}$	Bandwidth of PLL	50 Hz
$BW_{VL}$	Bandwidth of voltage control loop	30 Hz

on  $\angle Z_{dd_0}$  and  $|Z_{dd_0}|$  mainly below the VL bandwidth. As for the controller parameters, it is noted that the proportional gains shape the impedance in broader frequency ranges than their corresponding integral gains, which is reasonable for PI controllers. Besides, their influences on the impedance elements  $Z_{dd_0, dq_0, qd_0, qq_0}$  are limited by their corresponding loop bandwidth.

The observation in Fig. 3.4 matches the analytical expressions given by (3.14)-(3.17). The analysis indicates that the impedance is sensitive to the variation of a parameter only in a frequency range, which is determined by the corresponding loop bandwidth. Besides, Fig. 3.4 and (3.14)-(3.17) both reveals that  $Z_{dd_0}$  is not shaped by  $K_{ppll}$  and  $K_{ipll}$ . Besides,  $Z_{dq_0}$  is only influenced by  $L$ . Finally,  $Z_{qq_0}$  is not shaped by  $K_{pu}$ ,  $K_{iu}$ , and  $C_{out}$ .

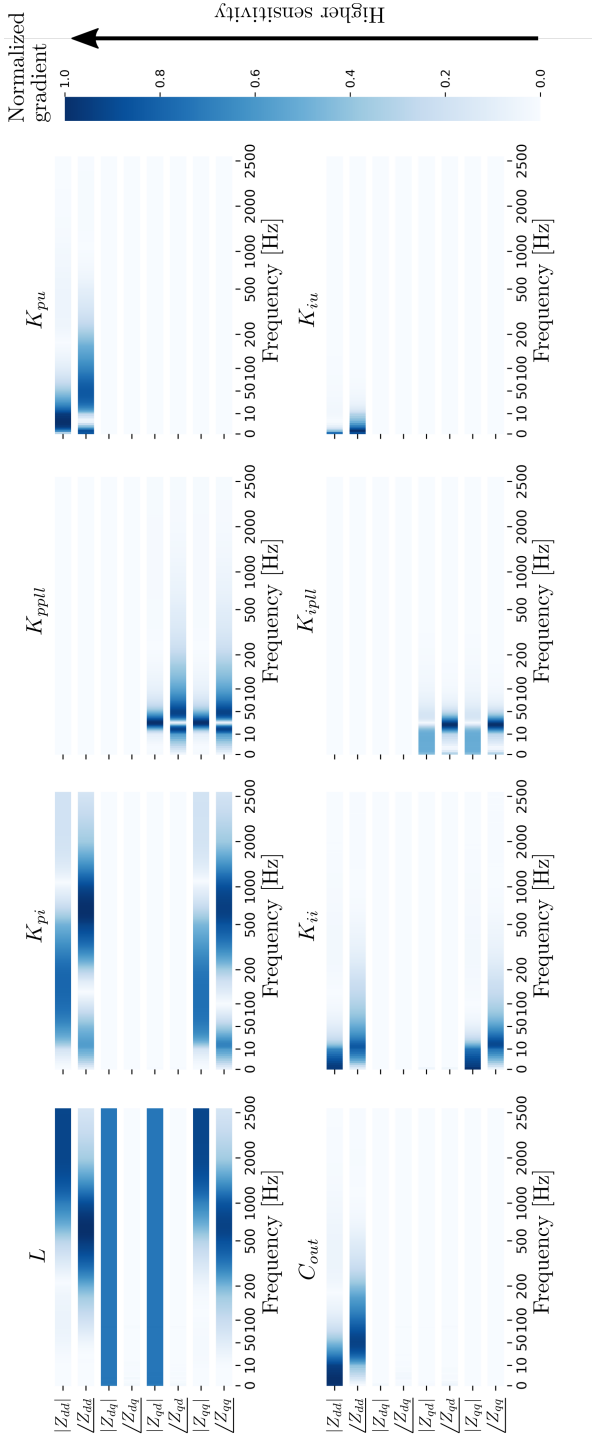


Figure 3.4: The partial derivative of the magnitude and phase of  $Z_{ddl}$ ,  $Z_{adt}$ ,  $Z_{dq}$ ,  $Z_{qd}$ ,  $Z_{qi}$  w.r.t each parameter at the value given in Table 3.2. Note that the frequency is given in the synchronous dq-frame.

### 3.4 MULTIPLE PARAMETER ESTIMATION

As aforementioned, the parameter estimation problem is essentially an optimization problem, which can be solved with GD methods. When the parameters are correctly estimated, the magnitude and phase of the estimated impedance  $Z_{AFE\_est}(s)$  should optimally match with the measured impedance  $Z_{AFE\_meas}(s)$ . Therefore, the loss function is given by

$$f_{loss} = \frac{1}{2M} \sum \left[ \frac{1}{N} \sum_{i=1}^N [ (|Z_{e\_est}(f_i)| - |Z_{e\_meas}(f_i)|)^2 + (\angle Z_{e\_est}(f_i) - \angle Z_{e\_meas}(f_i))^2 ] \right] \quad (3.22)$$

where  $e$  represents  $dd, dq, qd, qq$ ,  $f_i$  is the  $i^{th}$  frequency point of the impedance measurement,  $N$  is the total number of the frequency points in the impedance measurement,  $M$  is the number, which is maximally four, of the impedance elements composing the loss function. During the optimization process, a learning rate is decided for the optimizer to update all parameters under estimation iteratively. The loss value will decrease because a gradient descent direction is calculated to update the parameters.

#### 3.4.1 CHALLENGES IN A NORMAL GRADIENT DESCENT OPTIMIZATION BASED APPROACH

Two challenges, namely low accuracy of the estimated values and high time cost, can arise when using GD optimization to estimate the parameters. These issues are caused by two reasons.

The first reason is the significant difference in the scaling of the parameters, because of their different unit. Different scaling indicates that each parameter requires a different learning rate to achieve fast and stable convergence. If the learning rate is too small for a parameter, the loss value will converge too slowly. If the learning rate is too big, the loss value will bounce between the minima. Therefore, due to the scaling difference, using the same learning rate for all parameters can result in either a huge time cost for the estimation or an inaccurate estimation result, or both.

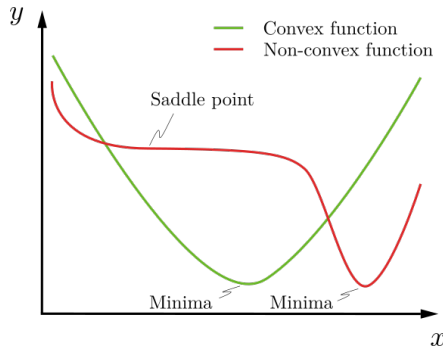


Figure 3.5: Saddle points in an non-convex function

The second reason is the loss function given by (3.22) is non-convex since its Hessian matrix is not positive semi-definite. Such increases the difficulties in converging to the minima because of the existence of the saddle points [130]. As depicted in Fig. 3.5, when

the loss function is non-convex, there are saddle points in the function. Because of the zero gradients there, these saddle points will slow down the optimization and get the optimization stuck in the worst cases. The existence of saddle points increases the time needed for converging to the minima tremendously and decreases the estimation accuracy, if the optimization gets stuck [130, 141].

### 3.4.2 PROPOSED ESTIMATION APPROACH

The challenges faced by the normal GD optimization-based estimation can be addressed by estimating the parameters separately. In this way, a multi-parameter estimation problem is cast as several one-parameter estimation problems, which reduces the dimension of the optimization problem. Thus, the customized learning rate can be used for the estimation of different parameters.

However, since the impedance is determined by all parameters together, if one parameter stays at an incorrect value, the others cannot be estimated correctly. Updating the parameters iteratively to approach the correct values may solve the problem. Nevertheless, it increases the time cost tremendously.

A more efficient estimation approach is needed. As the sensitivity study in Section 3.3 reveals, although the impedance is determined by all of the eight parameters to be estimated at low frequencies, the impedance is influenced by only one or several of them at higher frequencies. Besides, as both Fig. 3.4 and (3.14)-(3.17) reveal, instead of all of the eight parameters, only one or several of them have influences, for each impedance element among  $Z_{dd\_0}$ - $Z_{qq\_0}$ . Therefore, an estimation sequence of the parameters can be defined to effectively evaluate the eight parameters one by one.

Besides, as discussed in Section 3.3 and shown in Fig. 3.4, for a certain parameter, the impedance is more sensitive to its variation at some frequencies. When estimating the parameter, if the corresponding sensitive segment of impedance is used to compose the loss function, the saddle point issue can be avoided. At saddle points, the gradient of the loss function is zero but the loss value is still high. However, if the sensitive segment of impedance is used to compose the loss function, the gradient is zero only when the loss value is zero. For clarity, the gradient of the loss function (3.22) w.r.t. a parameter  $x$  is derived, which is obtain as

$$\begin{aligned} \frac{\partial f_{loss}}{\partial x} = & \frac{1}{M} \sum \left[ \frac{1}{N} \sum_{i=1}^N [ (|Z_{e\_est}(f_i)| - |Z_{e\_meas}(f_i)|) \frac{\partial |Z_{e\_est}(f_i)|}{\partial x} \right. \\ & \left. + (\angle Z_{e\_est}(f_i) - \angle Z_{e\_meas}(f_i)) \frac{\partial \angle Z_{e\_est}(f_i)}{\partial x} \right] \end{aligned} \quad (3.23)$$

As seen, when the sensitive impedance segment is selected,

$$\partial |Z_{e\_est}(f_i)| / \partial x \neq 0$$

and

$$\partial \angle Z_{e\_est}(f_i) / \partial x \neq 0.$$

Thus,  $\partial f_{loss} / \partial x = 0$  only when  $|Z_{e\_est}(f_i)| = |Z_{e\_meas}(f_i)|$  and  $\angle Z_{e\_est}(f_i) = \angle Z_{e\_meas}(f_i)$ , which means the loss value is zero.

Based on the analysis above and the sensitivity study in Section 3.3, a time-efficient estimation algorithm, which also improves the estimation accuracy, is proposed. The flowchart of the algorithm is illustrated in Fig. 3.6. As shown in Fig. 3.6a, the impedance measured at  $P = Q = 0$  is used for the parameter estimation, and the parameters are estimated in sequence.

The reasoning for why the algorithm is designed as such is as follows. To start with, (3.15) reveals that  $Z_{dq_0}$  is only influenced by  $L$ . So,  $L$  can be estimated first using  $|Z_{dq_0}|$  to compose its loss function. However, only the  $|Z_{dq_0}|$  above 2 kHz is used because the measured  $|Z_{dq_0}|$  at low frequency is inaccurate. Because of the higher bandwidth of the CL than the VL and PLL bandwidth,  $K_{pi}$  shapes the impedance until higher frequencies compared with the rest parameters. Thus,  $K_{pi}$  is identified next. Since the CL bandwidth is typically higher than 200 Hz, the measured  $|Z_{dd}|$ ,  $|Z_{qq}|$ ,  $\angle Z_{dd}$ , and  $\angle Z_{qq}$  above 200 Hz should be used to identify  $K_{pi}$ . Here, the impedance measured between 200-1000 Hz is used for the  $K_{pi}$  estimation.

Furthermore, as revealed by (3.17) and visualized in Fig. 3.4,  $Z_{qq_0}$  is only influenced by  $K_{ii}$ ,  $K_{ppll}$ , and  $K_{ipll}$ . Their influential frequency range is typically within 100 Hz, which is determined by the commonly followed design rules, e.g., bandwidth and phase margin selections for the PLL and the CL. Thus,  $Z_{qq_0}$  measured below 100 Hz is used to identify the three parameters. However, their influential frequency ranges are similar to each other. When identifying one of the three, e.g.,  $K_{ppll}$ , the estimated value could be far away from the exact one when  $K_{ii}$  and  $K_{ipll}$  stay at the wrong values. Thus, a loop is created to identify them iteratively. In this way, the three parameters can approach the correct values gradually and which parameter is estimated first does not make a difference. After several cycles, which is 5 cycles in our case, the loop is ended because the values of the three parameters do not change significantly. Although the cycle number that should be used in another scenario could be different, it can be easily decided by observing if the three parameters' values change significantly or not after a certain number of cycles.

Finally,  $K_{pu}$ ,  $K_{iu}$ , and  $C_{out}$  can be estimated with  $Z_{dd_0}$  measured below 100 Hz, which is determined by the VL bandwidth. Further, as revealed by Fig. 3.4 and discussed in Section 3.3,  $K_{iu}$  can shape  $Z_{dd_0}$  until a lower frequency than the  $K_{pu}$  and  $C_{out}$ . Thus,  $K_{iu}$  is identified after  $K_{pu}$  and  $C_{out}$ . As for  $K_{pu}$  and  $C_{out}$ , their influential frequency ranges are similar to each other. Any one of the two can be estimated first as long as the measured impedance at relatively higher frequencies is used to identify the parameter. For instance,  $C_{out}$  can be estimated first by using the measured impedance between 50 Hz to 100 Hz. Afterward,  $K_{pu}$  can be estimated with the measured impedance between 10 Hz to 50 Hz. However, the estimation results do not change significantly if  $K_{pu}$  is estimated first by using the measured impedance between 50 Hz to 100 Hz.

In summary, the impedance elements and the frequency ranges of the impedance segment selected to compose the loss function for the estimation of each parameter are shown in Table 3.3. Additionally, several points as follows are worth mentioning.

- $L$  and  $C_{out}$  can be initialized randomly;
- The proportional gain and the integral gain for all controllers should be initially low so that they can be estimated with the designed order;

- The GD optimizer Adam [142] is utilized to update the parameter iteratively, which leads to a fast and stable convergence;
- The magnitude and phase of the measured impedance element should be normalized, and the same transformation should be applied to the estimated impedance elements.

Table 3.3: Elements and frequency range of the impedance data used to compose the loss functions

Parameter	Elements	Frequency range
$L$	$ Z_{dq} $	(2-2.5 kHz)
$K_{pi}$	$ Z_{dd} ,  Z_{qq} , \angle Z_{dd},$ and $\angle Z_{qq}$	(0.2-1 kHz)
$K_{ppll}$	$ Z_{qq} $ and $\angle Z_{qq}$	(0-100 Hz)
$K_{ii}$	$ Z_{qq} $ and $\angle Z_{qq}$	(0-100 Hz)
$K_{ipll}$	$ Z_{qq} $ and $\angle Z_{qq}$	(0-100 Hz)
$C_{out}$	$ Z_{dd} $ and $\angle Z_{dd}$	(50-100 Hz)
$K_{pu}$	$ Z_{dd} $ and $\angle Z_{dd}$	(10-50 Hz)
$K_{iu}$	$ Z_{dd} $ and $\angle Z_{dd}$	(0-10 Hz)

In Fig. 3.6b, the flowchart of the estimation for each parameter is shown. As seen, a variable  $f_l$  is calculated to determine when the estimation of the parameter should stop. The expression of  $f_l$  is given by

$$f_l = \Delta f_{loss}[-1] - \Delta f_{loss}[0]/10 \quad (3.24)$$

where  $\Delta f_{loss}[-1]$  is the loss reduction in the last twenty epochs, whereas  $\Delta f_{loss}[0]$  is the loss reduction in the first twenty epochs. The reason for using  $f_l$  instead of a defined loss value limit to stop the estimation is as follows. Since Adam optimizer is used for the optimization, an adaptive learning rate is used when updating the parameter's value, which results in a slow reduction of the loss value when approaching the minimum. Therefore, it requires a proper loss value limit with which a balance between the estimation accuracy and the time cost is achieved. However, such a proper loss value limit changes from case to case, which is dependent on the measurement errors and the impedance data used to compose the loss function. Thus,  $f_l$  is calculated to determine whether the loss value reduction is too slow. As aforementioned, when the loss value reduction is slow, it indicates that the loss value is close to the minimum. Therefore, as illustrated in Fig. 3.6b, the estimation of the parameter stops when  $f_l < 0$ , which achieves the trade-off between the estimation accuracy and the time cost.



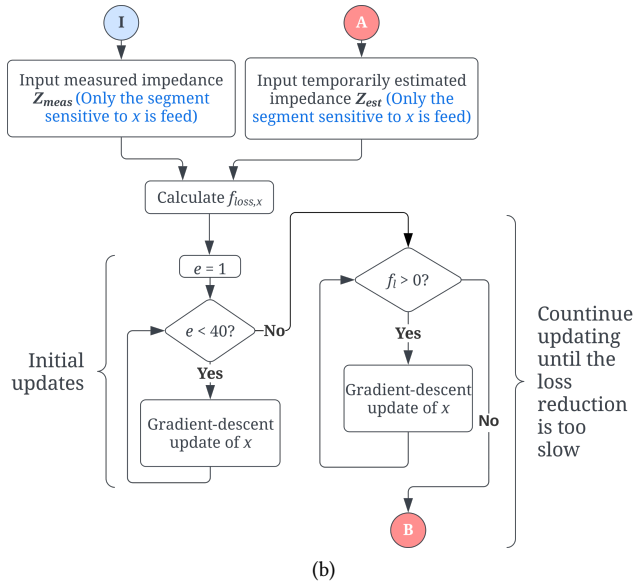
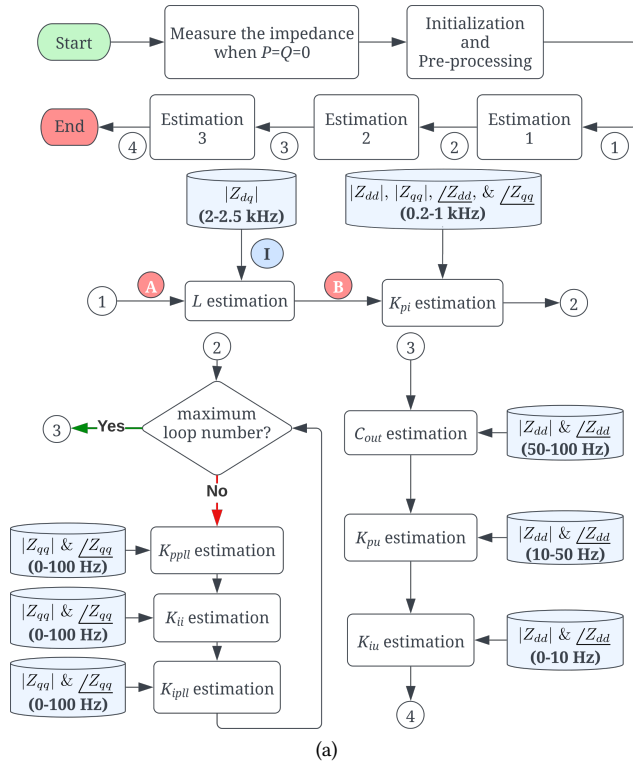


Figure 3.6: (a) Flowchart of the estimation algorithm (b) Flowchart of the estimation of the parameter  $x$ , where  $e$  represents the number of epochs, and the expression of  $f_i$  is given by (3.24).

## 3.5 EXPERIMENTAL RESULTS

### 3.5.1 EXPERIMENTS AND MEASUREMENT SETUP

The experiment setup is shown in Fig. 3.7. As seen, a Cinergia grid emulator is used to generate the grid voltage and inject harmonic voltages. An imperix power test bench is used to mimic an AFE. The imperix power test bench has a programmable controller, six 2.5 mH inductors, and six power modules. Thus, much flexibility is provided to change the AFE's design specifications. The adjustable DC load is connected to the output of the emulated AFE for different operating power.

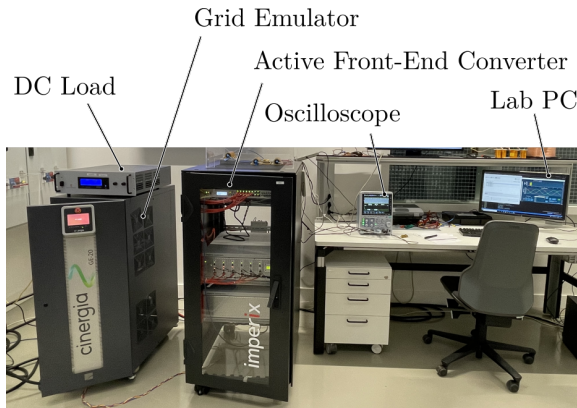


Figure 3.7: Impedance measurement setup

The current probes, the voltage probes, and the scope used in the experiments are Yokogawa 701933, Keysight N2791A, and Yokogawa DLM2034, respectively. The specifications are of the scope and probes are shown in Table 3.4. With the measurement devices, the current measurement resolution is 20 mA and the voltage measurement resolution is 0.2 V.

Table 3.4: Specifications of the current probe, voltage probe, and oscilloscope

Device	Type	Maximum Range	Bandwidth	Resolution	Accuracy
Yokogawa 701933	Current Probe	30 A	50 MHz	N.A.	$\pm 1\%$
Keysight N2791A	Differential Voltage Probe	700 V	25 MHz	N.A.	$\pm 2\%$
Yokogawa DLM2034	Digital Oscilloscope	N.A.	350 MHz	2mV/div	$\pm 1.5\%$

As shown in Table 3.5, three groups of immeasurable parameters are used in the experiment to account for parameter uncertainty. As for the measurable parameters  $U_{dc}$ ,  $E_g$ , and  $f_{sw}$ , they are the same for the three designs and given in Table 3.2.

Table 3.5: Three designs used in the experiment

Parameter	Design 1	Design 2	Design 3
$L$ [mH]	2.5	2.5	1.25
$K_{pi}$	9	15.7	1.57
$K_{ppll}$	1.21	4	2.42
$K_{ii}$	1000	15297	306
$K_{ipll}$	228	634	914
$C_{out}$ [mF]	1.67	1.67	3.21
$K_{pu}$	0.2	0.43	0.33
$K_{iu}$	2	10.47	4.66
$U_{dc}$ [V]	385		
$f_{sw}$ [kHz]	20		
$E_g$ [V]	$110 \sqrt{2}$		

### 3.5.2 ANALYTICAL MODEL VERIFICATION

In Fig. 3.8, the measured impedance of the AFE with Design 2 specifications at two operating points is compared with the analytical model. As seen, for  $Z_{dd}$  and  $Z_{qq}$ , the measurement results match the analytical calculation results. For the coupling impedance  $Z_{dq}$  and  $Z_{qd}$ , there are significant mismatches. The mismatches are caused by measurement errors that stem from the low magnitude of the coupling impedance. When the magnitude of the coupling impedance is enough high to be comparable to  $|Z_{dd}|$  and  $|Z_{qq}|$ , the analytical results match the measurement results. As seen in Fig. 3.8, when the power factor is lower,  $|Z_{dq}|$  is higher. Further, for both  $|Z_{dq}|$  and  $|Z_{qd}|$ , the analytical results match the measured ones. To further explain why the mismatches exist when  $|Z_{dq}|$  and  $|Z_{qd}|$  are low, the reasoning is as follows. When measuring the input impedance, grid voltage perturbations at  $f_p$  are injected. Then, input voltages  $u_{abc}(t)$  and currents  $i_{abc}(t)$  of the AFE are measured. Further,  $u_{abc}(t)$  and  $i_{abc}(t)$  are rotated to the same dq-frame resulting in  $u_{dq}(t)$  and  $i_{dq}(t)$ , respectively. The grid frequency is  $f_1$ . By applying Fast Fourier Transform (FFT), the  $f_p - f_1$  frequency component in  $u_{dq}(t)$  and  $i_{dq}(t)$  can be extracted resulting in  $U_{dq}(f_p - f_1) = U_d e^{j\phi_{dv}} + jU_q e^{j\phi_{qv}}$  and  $I_{dq}(f_p - f_1) = I_d e^{j\phi_{di}} + jI_q e^{j\phi_{qi}}$ , respectively. Therefore, (3.25) is satisfied. Similarly, grid voltage perturbations at  $2f_1 - f_p$  are injected to obtain  $U'_d e^{j\phi'_{dv}}$ ,  $U'_q e^{j\phi'_{qv}}$ ,  $I'_d e^{j\phi'_{di}}$ , and  $I'_q e^{j\phi'_{qi}}$ , which satisfy (3.26). Finally, the impedance at  $f_p - f_1$  can be calculated from (3.25) and (3.26), because  $Z_{AFE}(f) = Z_{AFE}^*(-f)$  [112], where the superscript \* indicates the conjugate complex form of the original variable.

$$\begin{cases} U_d e^{j\phi_{dv}} = Z_{dd}(f)I_d e^{j\phi_{di}} + Z_{dq}(f)I_q e^{j\phi_{qi}}, f = f_p - f_1 \\ U_q e^{j\phi_{qv}} = Z_{qd}(f)I_d e^{j\phi_{di}} + Z_{qq}(f)I_q e^{j\phi_{qi}}, f = f_p - f_1 \end{cases} \quad (3.25)$$

$$\begin{cases} U'_d e^{j\phi'_{dv}} = Z_{dd}(f)I'_d e^{j\phi'_{di}} + Z_{dq}(f)I'_q e^{j\phi'_{qi}}, f = f_1 - f_p \\ U'_q e^{j\phi'_{qv}} = Z_{qd}(f)I'_d e^{j\phi'_{di}} + Z_{qq}(f)I'_q e^{j\phi'_{qi}}, f = f_1 - f_p \end{cases} \quad (3.26)$$

However, when  $|Z_{dq}(f)| \ll |Z_{dd}(f)|$  and  $|Z_{qd}(f)| \ll |Z_{qq}(f)|$ , the  $Z_{dq}(f)$  and  $Z_{qd}(f)$  calculated from the measured voltages and currents are extremely sensitive to measurement

noises. As seen from the first equation in (3.25), when  $|Z_{dd}(f)| \gg |Z_{dq}(f)|$ ,  $Z_{dd}(f)I_d e^{j\phi_{di}} \gg Z_{dq}(f)I_q e^{j\phi_{qi}}$  because  $I_d$  and  $I_q$  have comparable scaling. Therefore, any tiny measurement errors of  $U_d e^{j\phi_{dv}}$ ,  $I_d e^{j\phi_{di}}$ , and  $I_q e^{j\phi_{qi}}$ , e.g., 10 mV or 10 mA, can result in a significant error in the calculated  $Z_{dq}(f)$ . Similarly, when  $|Z_{qq}(f)| \gg |Z_{qd}(f)|$ ,  $Z_{qq}(f)$  calculated from the measured voltages and currents also has significant errors. Thus, when  $|Z_{dq}(f)|$  and  $|Z_{qd}(f)|$  are much smaller than  $|Z_{dd}(f)|$  and  $|Z_{qq}(f)|$ , the measured coupling impedance is unreliable. As revealed later, such an issue of inaccurate measurement can be addressed by the proposed gray-box modeling approach.

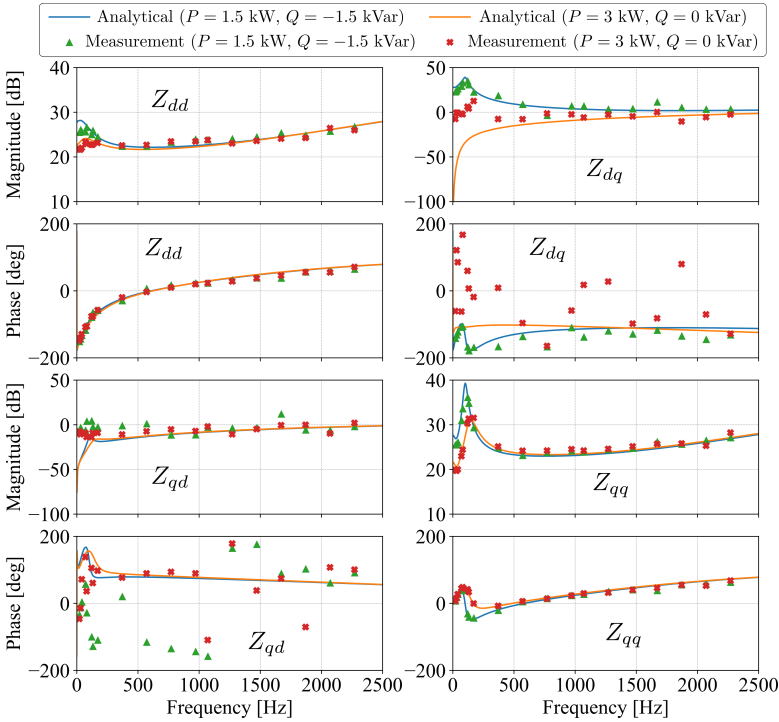


Figure 3.8: Measured impedance of the AFE with Design 2 specifications at two operating points. The analytical results are also shown for a comparison to verify the correctness of the derived analytical model.

### 3.5.3 ESTIMATION RESULTS

Following the flow in Fig. 3.2, the input impedance of the charger at  $P = Q = 0$  should be measured firstly for the parameter estimation. The data used for the parameter estimation for the three designs are visualized in Fig. 3.9. As seen, the analytical calculation results are also shown for comparison. In total, 54 frequency points are measured for each design to estimate the unknown parameters.

Fig. 3.10 shows the loss values and parameter updates during the evaluation progress. For all designs and all parameters, the loss value decreases during the estimation. Besides, the estimated parameter values approach the exact one gradually. The final estimation

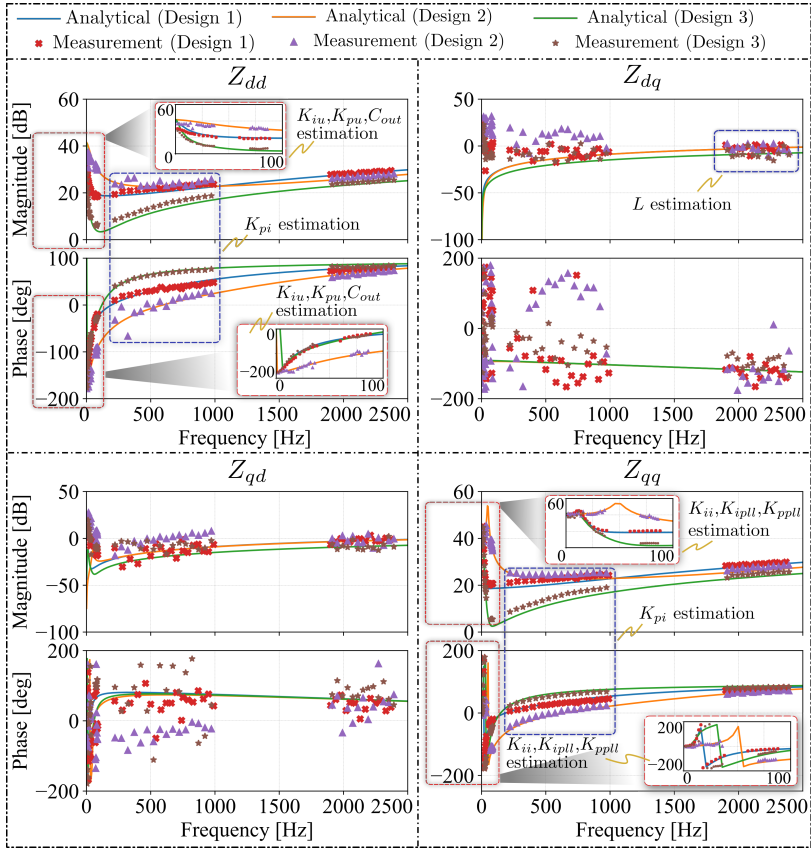


Figure 3.9: The impedance measured at  $P = Q = 0$ , which is used for parameter estimation. The analytical calculation results are shown for comparison.

results are provided in Table 3.6. Besides, Table 3.6 compares the performance of the proposed method with the performance of the normal GD optimization-based approach. In the normal approach, all parameters are estimated simultaneously with the same data set, the same GD optimizer, the same number of total epochs for the estimation, and the same initialization values as those in the proposed approach. However, without the proposed estimation algorithm in the normal approach, the optimization easily gets stuck at saddle points resulting in high errors in the identified parameter values. Moreover, the time to finish the same number of epochs is about three times higher than the one needed in the proposed approach. This is because the whole data set is used in the normal approach, whereas in the proposed approach only the sensitive impedance segment is used for the optimization. Therefore, the proposed approach has less amount of data for calculation in each epoch resulting in less time cost.

In both Fig. 3.10 and Table 3.6, it is noted that some identified parameter values have high errors. Such errors are caused by the insensitivity of the impedance to those parameters. Depending on the design specifications, the impedance could become less

sensitive to one or several parameters, and thereby low accuracy is seen for the estimated values of those parameters. For instance, in Table 3.6, for Design 1,  $K_{iu}$  has the highest estimation error whereas  $K_{ii}$  has the highest error for Design 3. However, since the impedance is less sensitive to these parameters, their high estimation errors would not result in significant errors in the estimated impedance and thereby are not problematic. The analytical impedance calculated with the estimation results shown in Table 3.6 is illustrated in Fig. 3.11. As seen, despite some errors in the identified parameter values, the estimated impedance has high accuracy. However, significant errors are noticed in the impedance estimated via the normal GD optimization-based approach.

Table 3.6: Estimation results comparison between the proposed approach and the normal GD optimization approach

Design 1			
	Exact	Proposed approach (error %)	Normal approach (error %)
$L$ [mH]	2.5	2.4 (4%)	12.6 (404%)
$K_{pi}$	9	9.7 (8%)	0.39 (96%)
$K_{ppll}$	1.21	1.2 (1%)	0.43 (64%)
$K_{ii}$	1000	1264 (26%)	0.62 (100%)
$K_{ipll}$	228	166 (27%)	0.74 (100%)
$C_{out}$ [mF]	1.67	1.62 (3%)	0.2 (88%)
$K_{pu}$	0.2	0.14 (30%)	0.37 (85%)
$K_{iu}$	2	3.63 (82%)	1.53 (24%)
Estimation time	N.A.	8 min.	24 min.
Design 2			
	Exact	Proposed approach (error %)	Normal approach (error %)
$L$ [mH]	2.5	2.39 (4%)	12.9 (416%)
$K_{pi}$	15.7	14.69 (6%)	0.81 (95%)
$K_{ppll}$	4	5.04 (26%)	0.83 (79%)
$K_{ii}$	15297	13144 (14%)	1.86 (100%)
$K_{ipll}$	634	579 (9%)	1.7 (100%)
$C_{out}$ [mF]	1.67	1.42 (15%)	0 (100%)
$K_{pu}$	0.43	0.25 (42%)	0.4 (7%)
$K_{iu}$	10.47	10.58 (1%)	2.34 (78%)
Estimation time	N.A.	17 min.	46 min.
Design 3			
	Exact	Proposed approach (error %)	Normal approach (error %)
$L$ [mH]	1.25	1.16 (7%)	8.06 (545%)
$K_{pi}$	1.57	2.1 (34%)	0.47 (70%)
$K_{ppll}$	2.42	2.02 (17%)	0.44 (82%)
$K_{ii}$	306	558 (82%)	0.6 (100%)
$K_{ipll}$	914	453 (50%)	1.37 (100%)
$C_{out}$ [mF]	3.21	4.08 (27%)	0.4 (88%)
$K_{pu}$	0.33	0.19 (42%)	0.61 (85%)
$K_{iu}$	4.66	3.45 (26%)	1.59 (66%)
Estimation time	N.A.	11 min.	30 min.

Fig. 3.12 illustrates the accuracy of the impedance estimated with the proposed approach at different operating points. As seen, at three different operating points, the estimated impedance is compared with the measured impedance and the exact impedance. Note that the exact impedance is obtained analytically by using the exact parameter values because the analytical model is verified in Section 3.5.2. Fig. 3.12 shows that the estimated impedance matches the exact one at all operating points rather than only at  $P = Q = 0$ . Thus, it is verified that despite some errors in the identified parameter values, the estimated impedance has high accuracy. Further, compared with the measured impedance, the estimated impedance shows similar accuracy for  $Z_{dd}$  and  $Z_{qq}$ . Nonetheless, for the coupling impedance, the estimated impedance is more accurate than the measured impedance when  $|Z_{dq}|$  and  $|Z_{qd}|$  are too small.

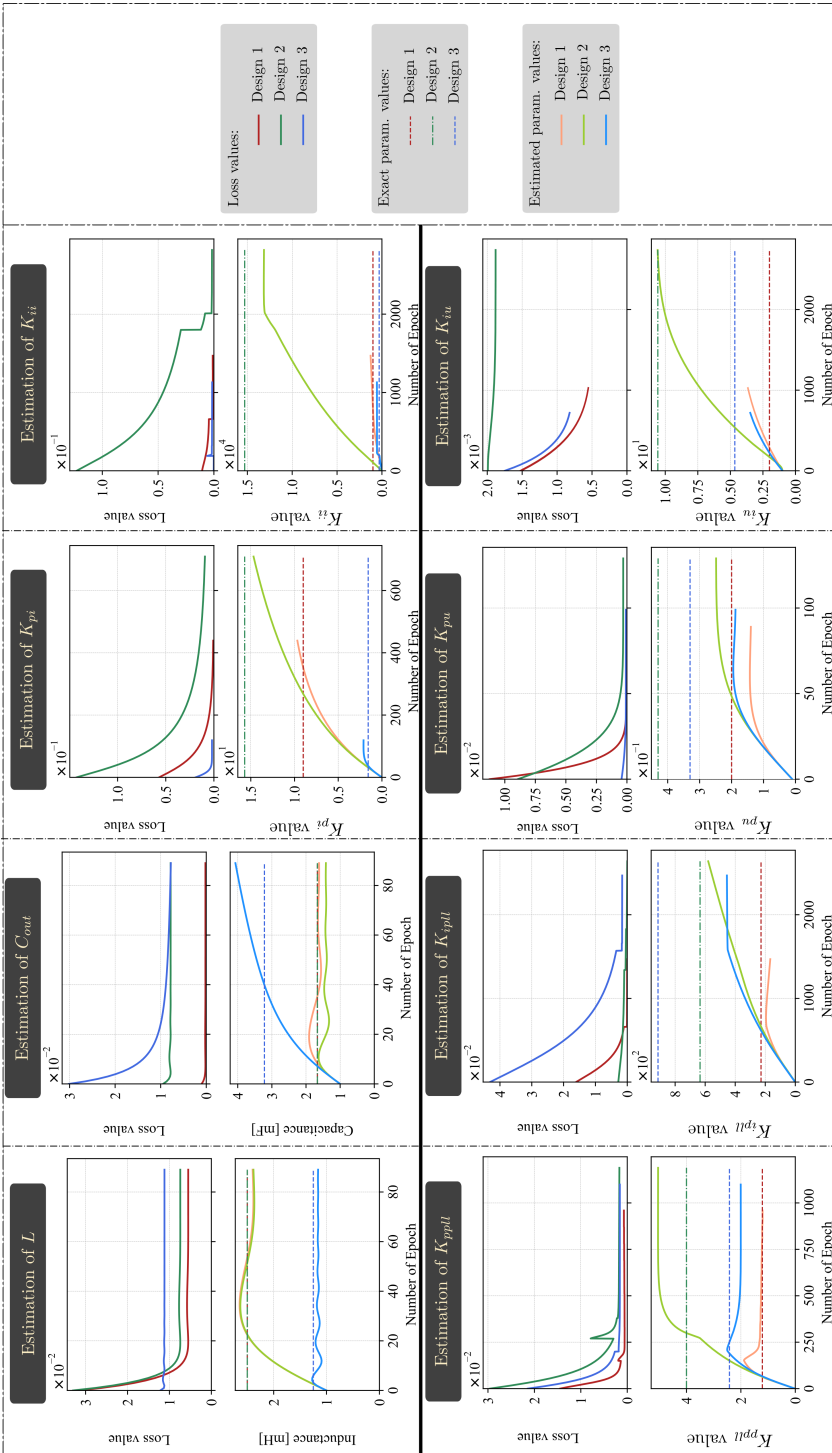


Figure 3.10: Loss values during the optimization iteration and the estimated parameter values compared with the exact parameter values.



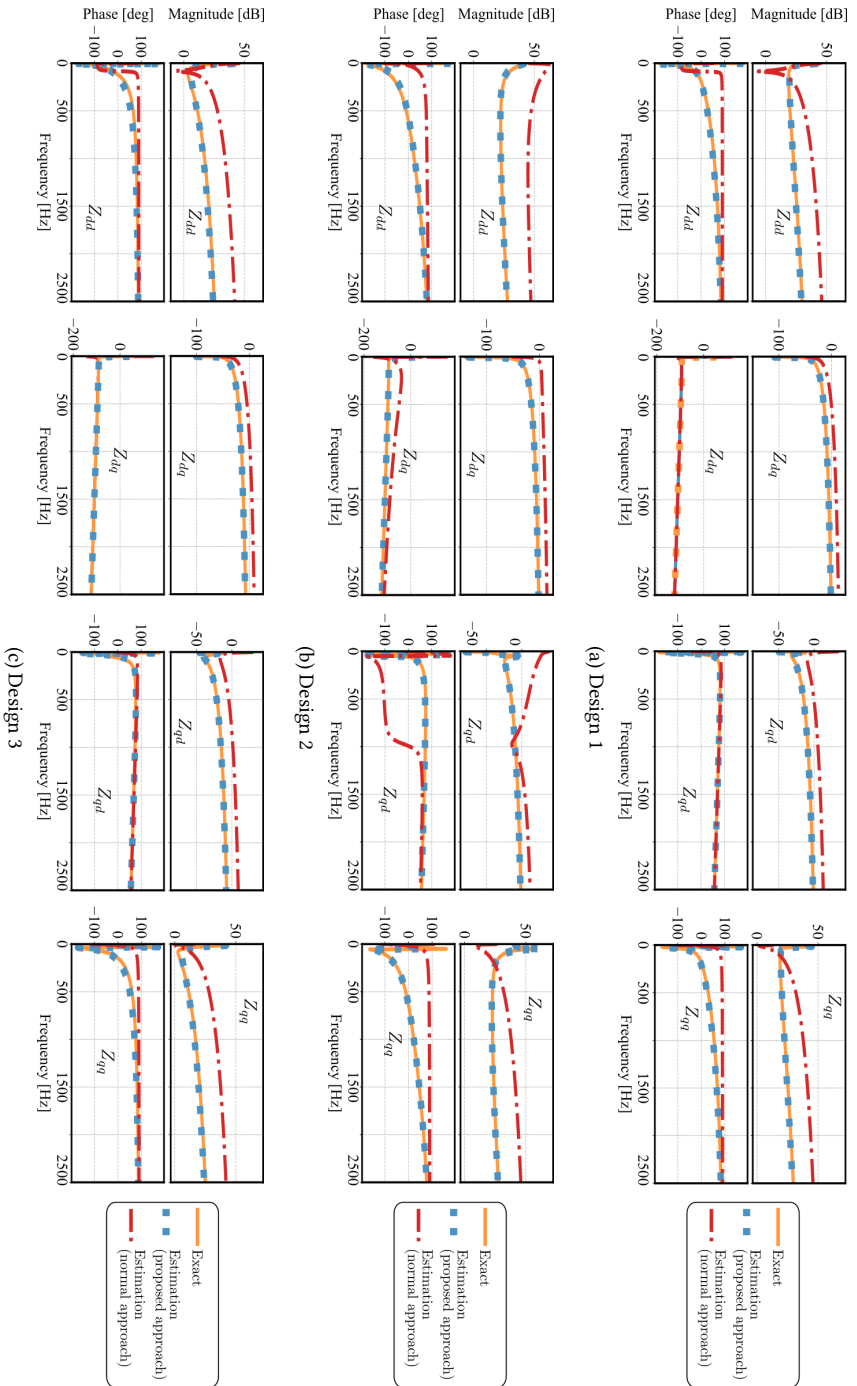


Figure 3.11: Estimated impedance via the proposed approach compared with the exact impedance and the impedance estimated with the normal GD optimization-based approach when  $P = \bar{Q} = 0$  for the three designs.

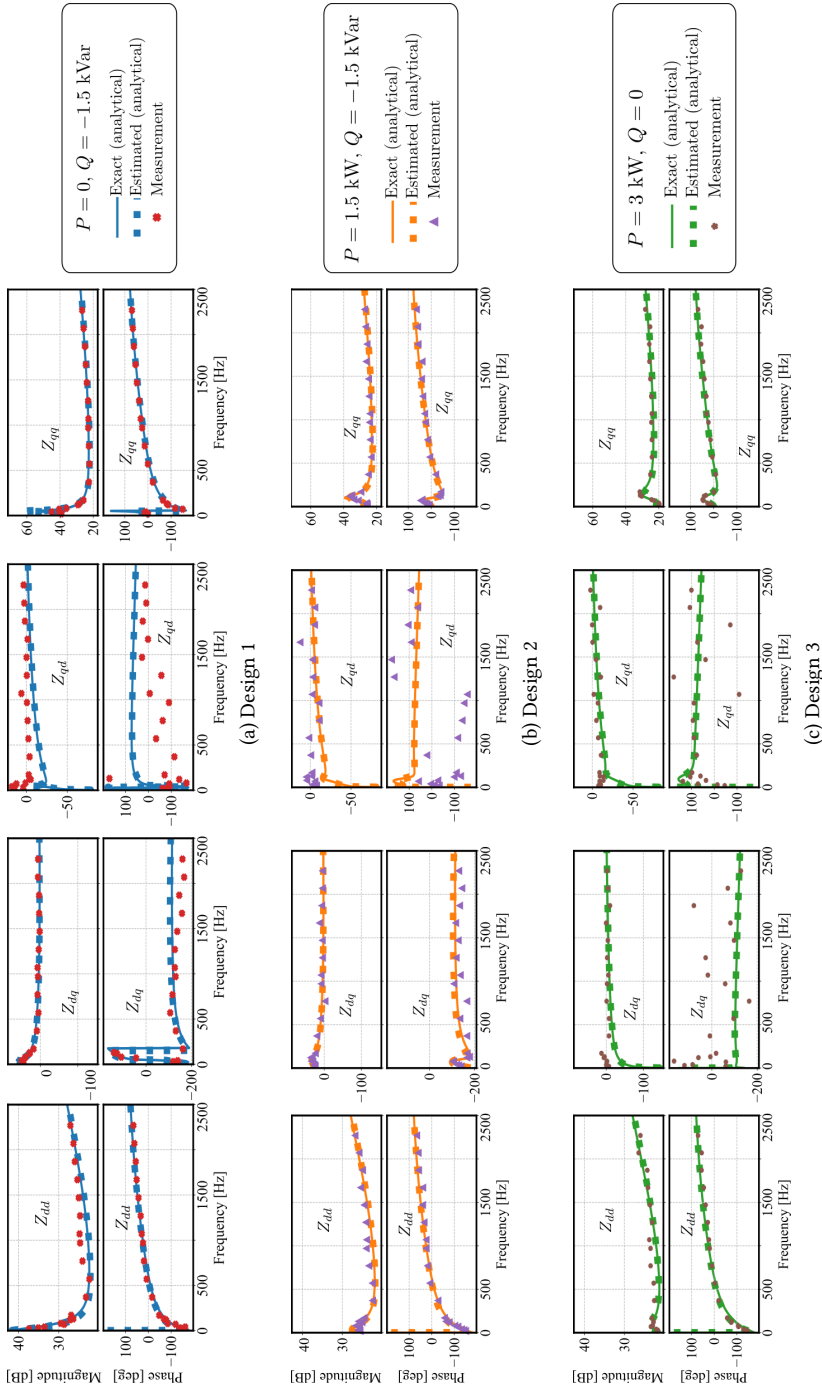


Figure 3.12: At three different operating points, the measured impedance of the AFE (Design 2) is compared with the exact impedance (analytical) and the estimated impedance (analytical).

### 3.6 CONCLUSION

This chapter proposes a GD optimization-based gray-box approach to obtain the DCFC's input impedance. The simplified expression of the impedance elements  $Z_{dd,dq,qd,qq}$  at the no-load condition is derived, which analytically reveals how the controller and circuit parameters shape the impedance. Furthermore, the influential frequency ranges of the eight parameters to be identified are analyzed. Based on the revealed influential frequency range of the parameters, a GD optimization based estimation algorithm is proposed to identify the parameters in sequence. Only the sensitive impedance segment for each parameter is selected for the estimation. As a result, the proposed estimation algorithm can achieve higher estimation accuracy and less time cost compared to a conventional counterpart, which is validated by experiment tests. Finally, the proposed gray-box modeling approach is validated with experimental tests. Compared to the measured impedance, the impedance extracted with the proposed approach has a higher accuracy for the coupling elements, namely,  $Z_{dq}$  and  $Z_{qd}$ , especially when the power factor is higher, and a comparable accuracy for the diagonal elements, namely,  $Z_{dd}$  and  $Z_{qq}$ . Moreover, the performance of the approach is evaluated with three designs with different controller and circuit parameters, evincing the effectiveness of the approach in different situations.

# 4

## MODELLING OF ELECTRIC VEHICLE CHARGING STATION FOR POWER QUALITY STUDY

*To accurately simulate electric vehicle DC fast chargers' (DCFCs') harmonic emission, a small time step, i.e., typically smaller than  $10\ \mu\text{s}$ , is required owing to switching dynamics. However, in practice, harmonics should be continuously assessed for a long duration, e.g., a day. A trade-off between accuracy and time efficiency thus exists. To address this issue, a multi-time scale modeling framework of fast-charging stations (FCSs) is proposed. In the presented framework, the DCFCs' input impedance and harmonic current emission in the ideal grid condition, that is, zero grid impedance and no background harmonic voltage, are obtained based on a converter switching model with a small timescale simulation. Since a DCFC's input impedance and harmonic current source are functions of the DCFC's load, the input impedance, harmonic emission at different loads are obtained. Thereafter, they are used in fast-charging charging station modeling, where the DCFCs are simplified as Norton equivalent circuits. In the station-level simulation, a large time step, i.e., one minute, is used because the DCFCs' operating power can be assumed as a constant over a minute. With this co-simulation, the FCSs' long-term power quality performance can be assessed time-efficiently, without losing much accuracy.*

## 4.1 INTRODUCTION

For widespread electric vehicle (EV) adoption, fast-charging stations (FCSs) are being built along highways as crucial infrastructures that can alleviate EV customers' range anxiety for long-distance trips [70, 79, 143]. The potential power quality influences of EV chargers are introduced in Chapter 2. As shown in Fig. 2.3, a typical FCS is connected to the medium-voltage (MV) distribution grid with an MV/LV transformer and equipped with several high-power DC fast chargers (DCFCs) and a battery energy storage system (BESS) [70, 79]. The DCFCs and BESS are connected to the distribution grid with power converters that comprise power electronics and power filters. Hence, an FCS is essentially a power-electronics-based system, which is the same as a wind farm or photovoltaic (PV) farm. Harmonic emission noncompliance, which have been reported in wind farms, PV farms, and other power-electronic-based systems [7, 32, 120, 144, 145], can be expected to happen in FCSs.

4

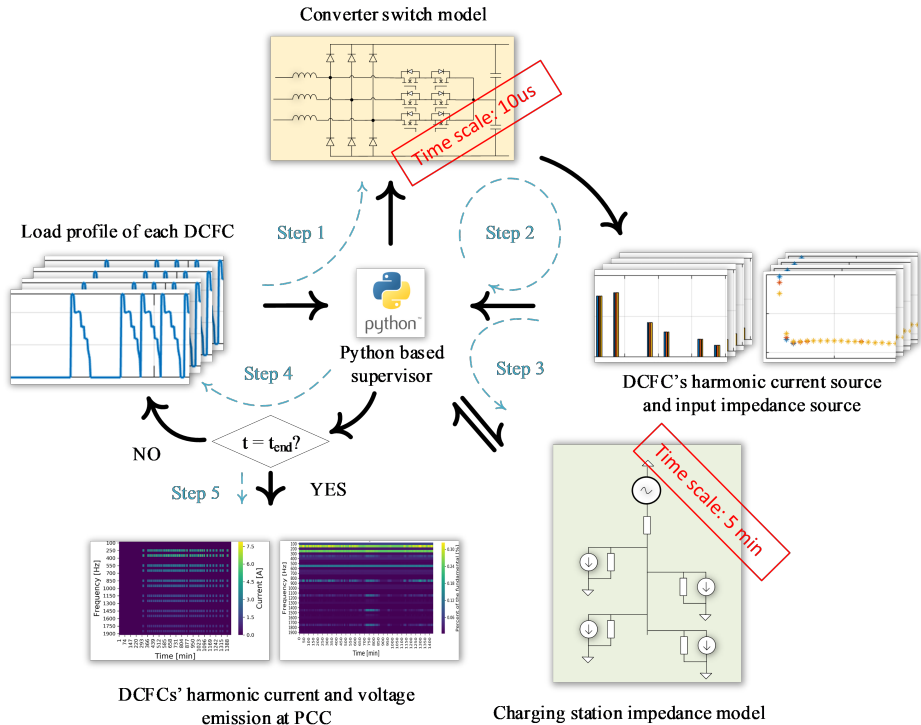


Figure 4.1: Python supervised co-simulation for a day-long harmonic emission evaluation of EV charging.

To study the impact of FCS on grid power quality, modeling and simulation of the FCS's harmonic emissions are critical. However, making this simulation both accurate and time-efficient is quite challenging. On the one hand, a small time step ( $<10 \mu\text{s}$ ) is needed for accurate simulation of the switching frequency dynamics because a typical DCFC's switching frequency is normally above 20 kHz. On the other hand, according

to the grid code, a one-day or even longer and continuous evaluation of harmonics is needed for the power quality assessment [146]. A simulation with a small time step for a day-long harmonic evaluation is not feasible due to either long simulation time or high computational cost.

To address this simulation challenge, a co-simulation is proposed, as illustrated in Fig. 4.1. Two simulation models operate simultaneously. One has a small time step (10  $\mu\text{s}$  is chosen in this study) and sits in a circuit simulation environment (PLECS in this study). The switching dynamics, current controller, and phase lock loop (PLL) of the DCFC are all modeled in detail. Based on this simulation model, the DCFC's input impedance and harmonic current source at a certain operating power can be obtained. The other model has a large time step (one minute is chosen in this study) and sits in a system simulation environment (PowerFactory in this study). In the system model, all the DCFCs are simplified as Norton equivalent circuits, where the current sources and impedances are from the small time step simulation model, as mentioned above. Consequently, the current sources and impedances are updated every minute, which is reasonable, because the charging power changes during one charging event but usually with a time step longer than one minute. For a certain charger, its Norton equivalent current source and input impedance only change when the charging power (operation point) changes. Consequently, because the harmonic evaluation is based on the Norton equivalent model, the simulation is quick. Meanwhile, the Norton equivalent model is obtained from the switching model of the charger and is updated in real time. Thus, the impact of a time-variant charging profile is considered, and the evaluation accuracy is ensured. The co-simulation is implemented using a Python supervisor. More details are as follows.

- Step 1: the operating power  $P_x(t_i)$  of each DCFC is obtained, where  $P_x(t_i)$  denotes the operating power of the DCFC  $x$  at time  $t_i$ .
- Step 2: the DCFCs' input impedance  $Z_x(t_i, f_h)$  and harmonic current source  $H_x(t_i, f_h)$  at time  $t_i$  and harmonic frequencies  $f_h$  are estimated with the small timescale simulation. Here, the harmonic frequency denotes the frequency that is the integral multiple of the fundamental frequency in the range of 0–2 kHz.
- Step 3: for the harmonic load flow simulation at  $t_i$ , each DCFC's input impedance and harmonic source in PowerFactory are updated to  $Z_x(t_i, f_h)$  and  $H_x(t_i, f_h)$ , respectively, by the Python supervisor. The simulation result of PowerFactory at  $t_i$  is sent to the Python supervisor and recorded.
- Step 4: the time step is updated to  $t_i+1$ , and the simulations are repeated. The iteration continues until all time steps in the load profile are finished. During the final step, the simulation results are visualized.

In the following sections, the modeling of DCFC and FCS is presented first. Afterward, the simulation results of the DCFC's input impedance and harmonic current source are presented. Thereafter, a one-day load profile simulation with a time resolution of one minute is performed to specify the DCFCs' operating points for that day. Later, based on the developed FCS model and load profile, the FCS's long-term harmonic performance can be simulated by updating the DCFCs' input impedance and harmonic current source per minute.

## 4.2 MODELLING OF THE DC FAST CHARGER

### 4.2.1 DESIGN OF THE DC FAST CHARGER

As aforementioned, a typical DCFC comprises two power conversion stages, a front-end AC/DC stage and a DC/DC stage. The two stages are buffered with a DC-link where high-capacitance capacitors are used for a stable DC voltage level. Hence, the DCFC's impact on power quality is mainly determined by the front-end converter.

The Vienna rectifier is a mainstream topology used for the DCFC's front-end converter because of its superior performance regarding reliability, power density, and efficiency. Thus, it is selected when modelling the DCFC. Additionally, modular design is typical for DCFCs, especially for those with high-power ratings, because of (1) the wide battery voltage range, (2) less stress on the power electronic components, (3) less design pressure on the cooling system, and (4) flexible compatibility with different EVs with different rated charging powers. Based on the selected circuit topology and modular design concept, a 360-kW DCFC comprising twelve 30-kW parallel power modules was designed. The DCFC's 30-kW power module design is illustrated in Fig. 4.2. In Table 4.1, the key parameters of the design are listed.

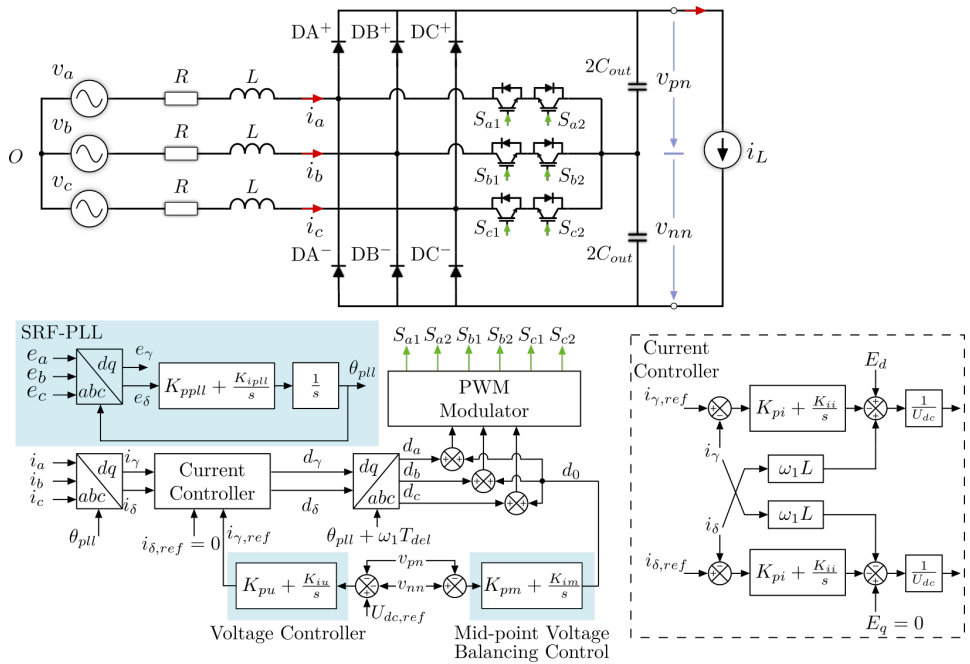


Figure 4.2: Design of a typical 30-kW power module of the modeled DC fast charger.

As shown in Fig. 4.2, the feedback control of the Vienna rectifier consists of current control, voltage control, and mid-point voltage balancing control that ensures a small difference between  $V_{pn}$  and  $V_{nn}$ . The synchronous d-q frame PI controller is used for current control. Additionally, the synchronous reference frame PLL (SRF-PLL) is used to track the grid voltage phase. As digital control is used, a calculation delay of one switching

cycle is considered in the model. The PWM signal is obtained with the symmetrical modulation method, which induces a delay of half the switching cycle. Therefore, the whole delay caused by the control roughly equals  $1.5 T_{sw}$ , where  $T_{sw}$  is one switching cycle period.

Table 4.1: Design parameters of the DCFC's power module

Symbol	Description	Value
$U_{dc}$	DC-link voltage output DC voltage	800 V
$E_g$	Grid line-neutral RMS voltage	230 V
$f_1$	Grid frequency	50 Hz
$f_{sw}$	Switching frequency	20 kHz
$C_{out}$	Output capacitance	1.5 mF
$L$	Filter Inductance	250 $\mu$ H
$R$	Filter Resistance	20 m $\Omega$
$BW_{CL}$	Bandwidth of current control loop	1 kHz
$BW_{PLL}$	Bandwidth of PLL	100 Hz
$BW_{VL}$	Bandwidth of voltage control loop	40 Hz

#### 4.2.2 INPUT IMPEDANCE MODELING

Based on the DCFC's model shown in Fig. 4.2, the input impedance can be estimated analytically. However, since the analytical model is based on an assumption that may lead to errors, a more accurate method is needed to obtain the input impedance via frequency sweep using either the switch model or real hardware.

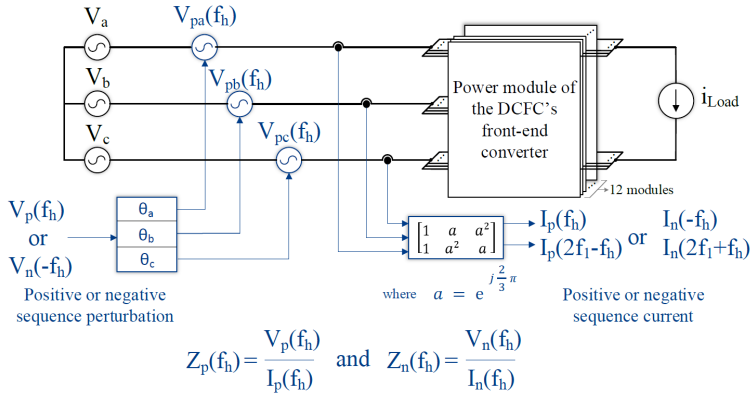


Figure 4.3: Illustration of the frequency sweep for estimating the input impedance of the DC fast charger through numerical simulation.

As illustrated in Fig. 4.3, the input impedance can be measured by injecting a small voltage perturbation  $V_h$  at frequency  $f_h$  into the input 3-phase voltages. By measuring the harmonic component  $I_h$  at  $f_h$  of the input current, the input impedance at  $f_h$  can be calculated. Notably, depending on the sequence of injected voltage perturbation, the



measured input impedance is in the corresponding sequence domain, namely the positive or negative-sequence domain. Since the frequency coupling impedances are much higher compared to their counterparts at  $f_h$  [107], they are neglected for simplicity.

## 4.3 MODELLING OF THE FAST-CHARGING STATION

### 4.3.1 CONFIGURATION OF THE FAST-CHARGING STATION

As illustrated in Fig. 4.4, an FCS with four 360-kW DCFCs was modeled. To fulfill the peak power demand with a certain safety factor, the service transformer has a capacity of 1.6 MVA. Additionally, to simulate a severe condition, a scenario where a long distance between a substation and FCS is considered. Therefore, it is assumed that the FCS is connected to the external grid with a low short circuit ratio (SCR). A transmission grid of an SCR below 6-10 is considered weak [147, 148]. Although such a low SCR has not been founded for a distribution grid, it is highly expected to happen because of the transition of power systems towards more distributed generations [149]. Therefore, an SCR of 5 is assumed in the simulation model.

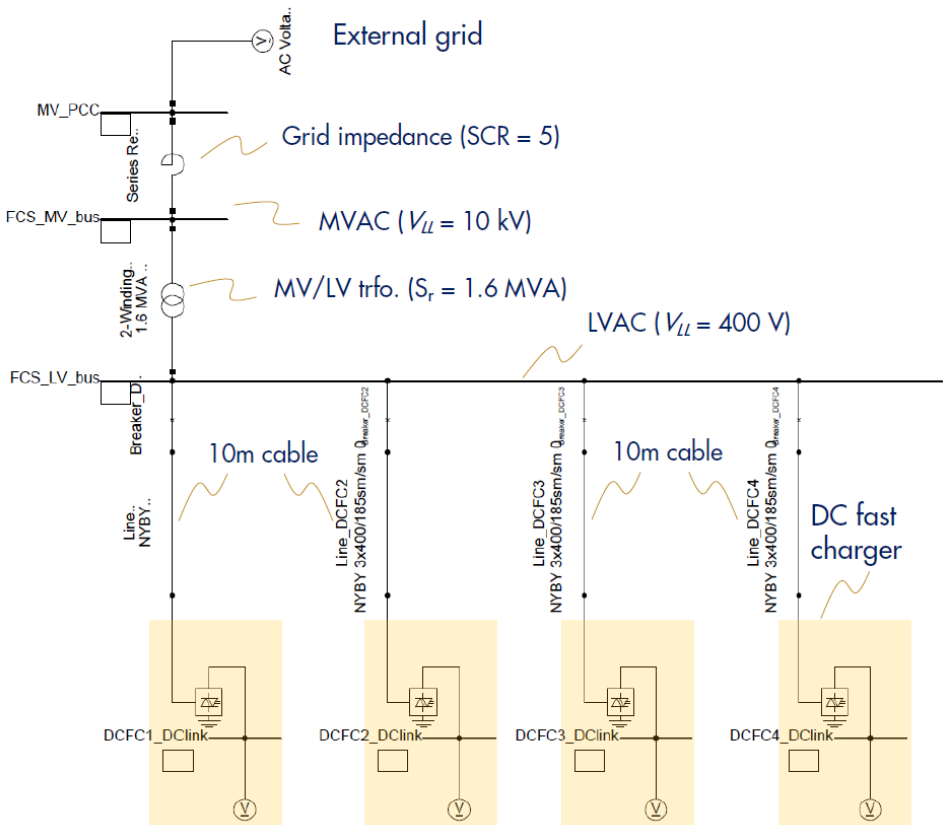


Figure 4.4: Model of the fast-charging station with four 360-kW DCFCs in PowerFactory. Note that the chargers are simplified as their Norton equivalent circuit in the simulation.

### 4.3.2 MODELING OF THE EXTERNAL GRID

In the whole year of 2023, the median of the THD of Dutch MV grid voltage 2%, more than 75% is below 3%, and the worst case value is about 7.5% [150]. Thus, to evaluate the harmonic compliance of an FCS in severe conditions, the THD for the grid voltage is assumed to be 4%. The spectrum and time-domain waveform of the grid voltage is shown in Fig. 4.5. Notably, the harmonics of the assumed grid voltage are smaller than the recommended planning level in IEC 61000-2-12 [40].

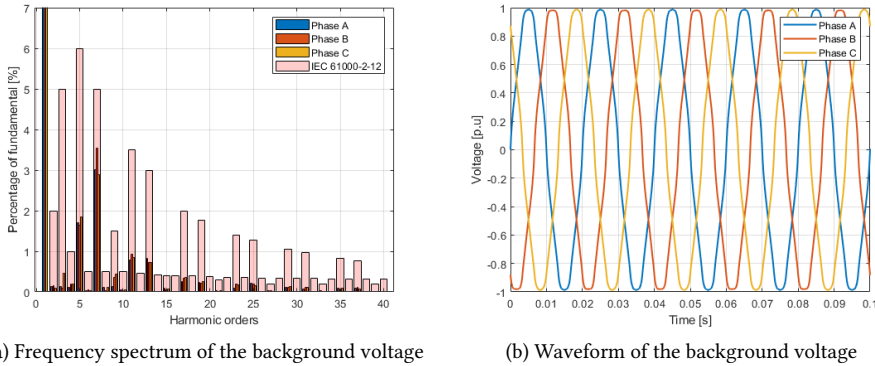


Figure 4.5: Assumed harmonic voltages in the voltage of the grid to which the fast-charging station is connected.

### 4.3.3 MODELLING OF THE CHARGING LOAD PROFILE

Based on the arrival time distribution of cars at a gasoline station in a day [95], and the charging profile of Porsche Tyacan, which is one of the model with the highest charging power, the load profile is generated by assuming that the state of charge of each car equals 10% before charging and reaches 80% after finishing charging. The time resolution of the generated load profile is reduced to one minute by assuming the arrival time of cars has an even hourly distribution. The resultant load profile is shown in Fig. 4.6.

At each simulation time step, the four DCFCs' input impedance and harmonic current source are updated according to their operating power. Thereafter, the harmonic load flow simulation in PowerFactory is conducted to evaluate the voltage harmonic at the low-voltage and MV bus bars.

Such a modeling method is also called quasi-dynamic modeling because the system dynamics within the simulation time step, i.e., one minute here, are ignored.

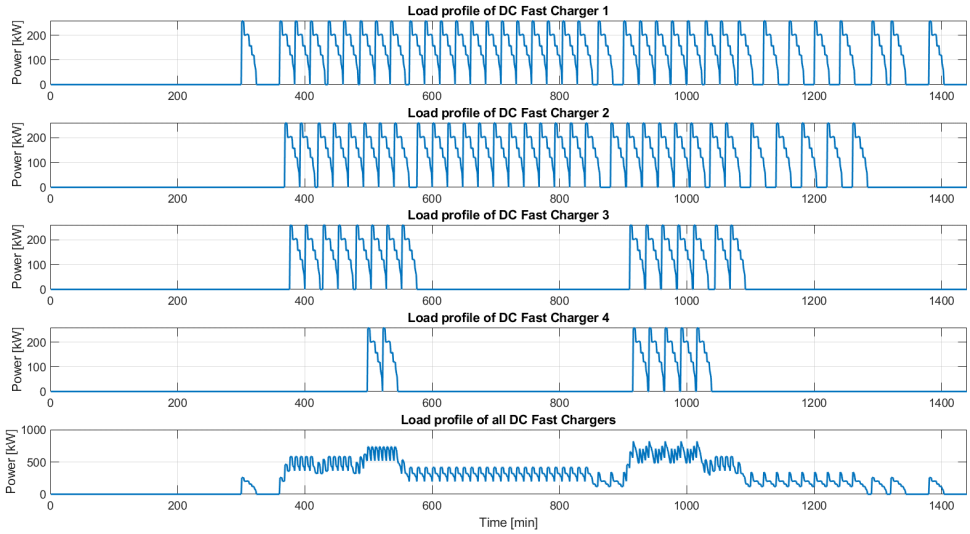


Figure 4.6: Load profile of each charger and the fast-charging station.

## 4.4 SIMULATION RESULTS AND DISCUSSION

### 4.4.1 INPUT IMPEDANCE OF THE DCFC

Based on the DCFC's model presented in Fig. 4.2 and the input impedance measurement method presented in Fig. 4.3, the DCFC's input impedance and harmonic current source at different operating powers (obtained from the load profile) are simulated. To show that the charger's impedance is influenced by the charging power, the simulation result shown in Fig. 4.7 compares the positive and negative-sequence impedances of the DCFC at 260 kW, 120 kW, and 58 kW, which are randomly selected operating powers in the load profile.

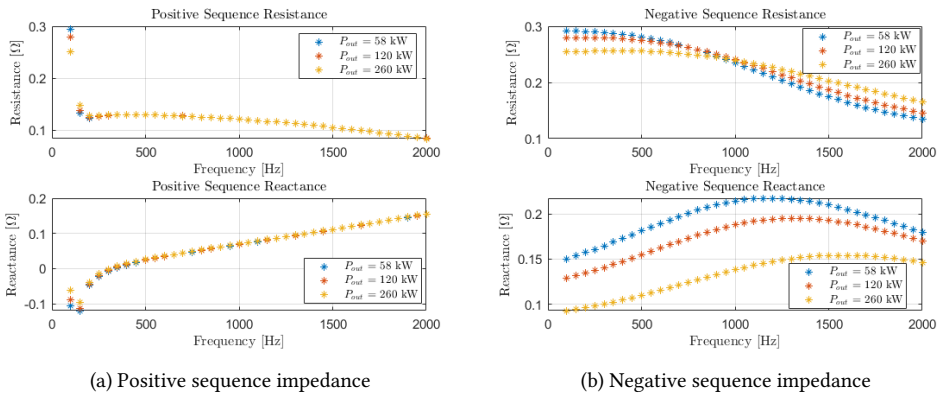


Figure 4.7: Input impedance of the DCFC at three charging power.

Fig. 4.7 shows that the operating power influences the positive sequence impedance only for frequencies smaller than 500 Hz. However, for the negative-sequence impedance, the operating power influences the entire range of 100 Hz to 2 kHz. Owing to the high switching frequency and subsequent low delay induced by digital control, the negative resistance region in the impedance reported in Ref. [107] is not observed in the presented frequency range.

Additionally, the DCFC’s input impedance is low because of the use of modular design. Since the power modules of a DCFC are connected parallel, the input impedance of the DCFC is reduced.

### 4.4.2 HARMONIC CURRENT SOURCE OF THE DCFC

In Fig. 4.8, the input current waveform and its spectrum of the DCFC at 58, 120, and 260 kW are shown. When estimating the harmonic current source of the charger, the grid to which the charger is connected is assumed ideal. The results show that the difference among the DCFC’s harmonic current source at different operating points is significant. The harmonic current is higher when the DCFC operates at low power because the charger is designed to guarantee its harmonic compliance at nominal power. When the fundamental current is low with a comparable harmonic current component, the control performance worsens.

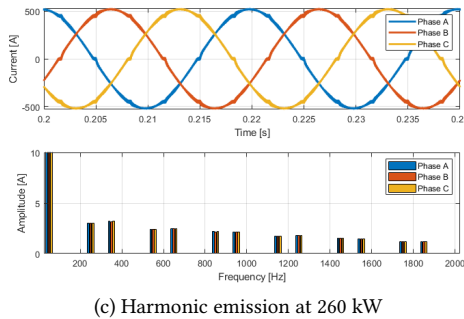
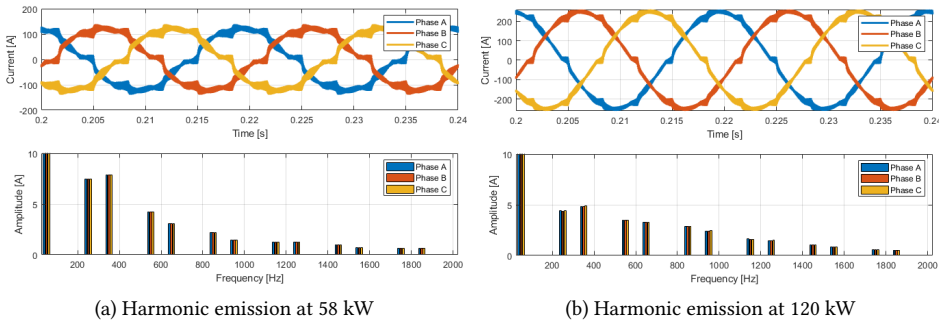


Figure 4.8: Variant harmonic current source of the DCFC at three charging power.

### 4.4.3 DAILY HARMONIC EMISSION OF THE DCFCs

After the simulation iterations of all time steps, the harmonic current emission of the DCFCs in a day can be evaluated. The whole simulation takes roughly 2 hours, which is much faster compared to the switching model. Moreover, given a load profile, the simulation can output the daily profile of the chargers' harmonic emission. Compared to the conventional approach, which only assesses the harmonic emission at several operating points of the charger, the proposed approach is more comprehensive.

The simulation results of the harmonic current emission of each DCFC are presented in Fig. 4.9. As shown, the harmonic emissions of the charger contain notably the fifth and seventh harmonic component. Compared to the harmonic emission of the charger when the grid is clean in Fig. 4.8, the fifth and seventh harmonic component increases. Such results from the significant the fifth and seventh harmonic components in the background voltages.

4

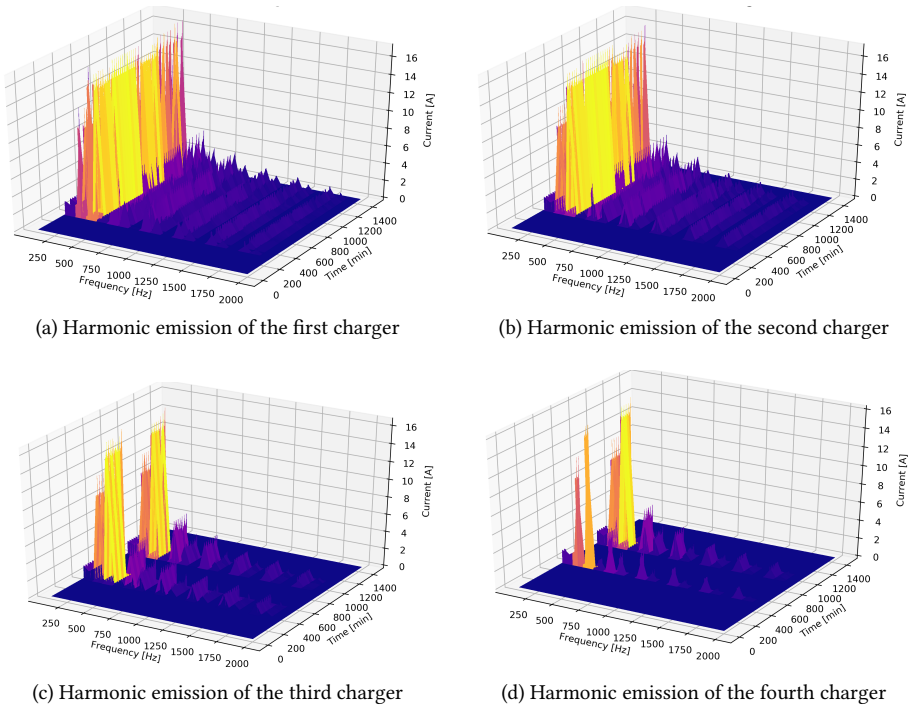


Figure 4.9: Harmonic current emission of the four DCFCs in a day. Note that only one phase current is shown since the grid is assumed to be balanced.

In Fig. 4.10, the main harmonics, namely the fifth and seventh harmonics, and total demand distortion (TDD) of the four chargers in a day are illustrated and compared to the limits in the grid code IEEE 519. As shown, the TDD, fifth, and seventh harmonic currents are all below the limits described in IEEE 519. Fig. 4.10a shows that when all the chargers are operating, e.g.,  $t = 1000$  min, the harmonic emission of a charger is slightly lower than

that when only the certain one charger is operating, e.g.,  $t = 300$  min. One possible reason is that the harmonic emission from the other chargers compensates for that induced by the distorted background voltage. To clarify the summation law of the harmonic emission from different chargers, more studies need to be conducted.

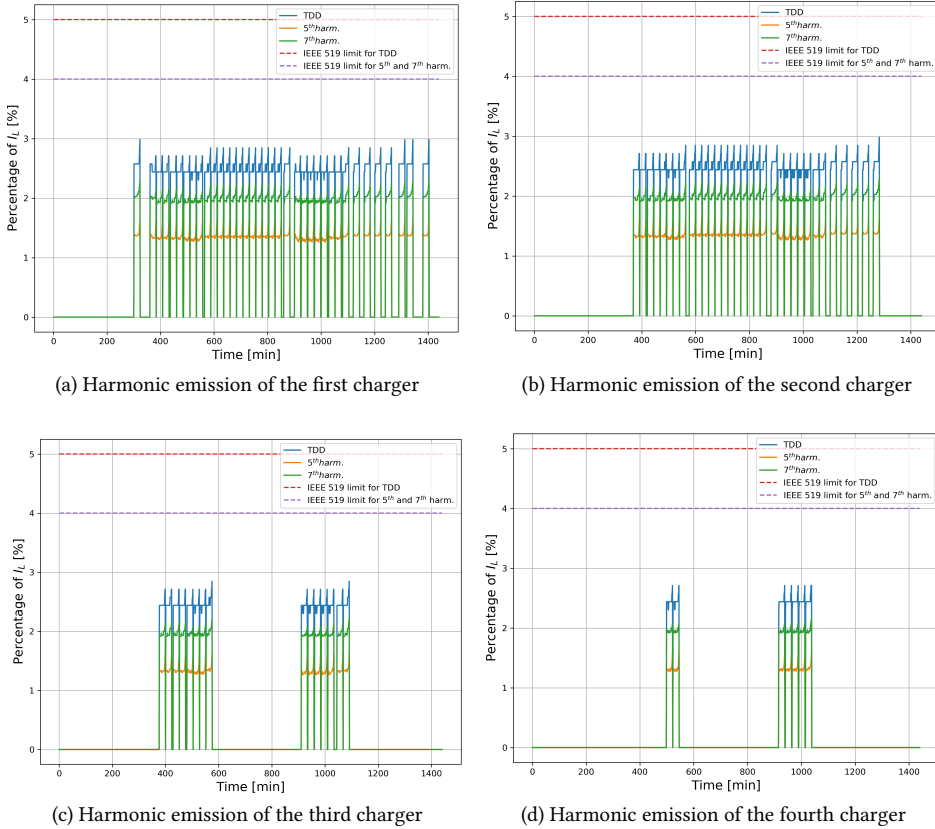


Figure 4.10: Main harmonic current emission and the total demand distortion (TDD) of the four DCFCs in a day. Note that only one phase current is shown since the grid is assumed to be balanced. Note that  $I_L$  is the rated current.

### 4.5 CONCLUSION

In this study, a python-supervised co-simulation for a day-long harmonic evaluation of EV charging is proposed and elaborated. The co-simulation consists of a switching model of the EV charger with a time step at the microsecond level, and a Norton equivalent model of the chargers with a time step at the minute level. The harmonic current source and impedance in the Norton equivalent model are updated in real time based on the information from the switching model. With such a co-simulation, a good balance between the accuracy and computational cost of the harmonic evaluation is achieved. For instance,

a day-long harmonic evaluation can be completed in two hours using a normal computer with the proposed co-simulation method. The simulation time can be further reduced if a more advanced computer is utilized. The effectiveness of the proposed co-simulation is verified by a case study, where the harmonic emission of a charging station is evaluated with a day-long charging profile.

# 5

## DESIGN GUIDELINES OF CHARGER CONTROL FOR POWER QUALITY IMPACT MITIGATION

5

*This chapter proposes an analytic approach to design the typical power factor correction (PFC) control of an electric vehicle (EV) charger to ensure small signal stability in weak grid conditions. Compared to the previous works, the proposed method considers the dynamics of all the control loops, i.e., phase-locked loop (PLL), voltage loop (VL), and current loop (CL). The impacts of key influential parameters on stability are analyzed. Furthermore, the upper limits of the PLL and voltage loop bandwidth to ensure small signal stability are derived. Accordingly, the influences of the CL bandwidth, short circuit ratio (SCR), and the filter inductance on the upper limit of the PLL bandwidth and the VL bandwidth are quantified. Consequently, a design procedure that eliminates the need to model the input impedance for tuning the controller to prevent small signal instability is proposed. Simulations and experiments validate the analysis.*



## 5.1 INTRODUCTION

Amid the rollout of electric vehicles (EVs), more EV chargers will be connected to the power grid. However, connecting an EV charger to a grid may result in small signal instability [54, 118]. The situation could become worse if the grid weakens.

The problem is mainly caused by the AC/DC converter of the EV charger [70]. Typically, this AC/DC converter has the power factor correction (PFC) ability that attempts to control the power factor to one. So, the AC/DC converter is called PFC for simplicity. A widely adopted PFC control for EV chargers is using a phase-lock loop (PLL) for grid synchronization. A voltage loop (VL) is implemented to stabilize the DC-link voltage. Inside the VL, a current loop (CL) is implemented to provide a fast current response. Such a PFC control can lead to small signal instability, especially with a weak grid connection.

The root cause of the small signal instability by adopting such control is well studied via the impedance-based approach [57, 70, 107, 120, 133, 151]. In brief, due to the PFC control, the real part of the charger's input impedance becomes negative at low frequencies, which is thereby called a non-passive region (NPR). Small signal instability appears if the resonance between the grid impedance and the charger's input impedance has a resonant frequency located inside the NPR [60, 152]. Otherwise, small signal instability happens because the negative resistance will energize the resonance between the grid and the charger leading to unbounded responses.

To address the issue, many studies have been carried out to analyze the influence of controller parameters on the input impedance to give design recommendations. An early work [137] revealed that the bandwidth of the PLL and VL should be kept low to narrow the NPR of the input impedance. It was further recommended to limit the bandwidth of the PLL and VL to one-tenth of the CL bandwidth. However, the recommendation is given regardless of the difference in short-circuit ratio (SCR), which can be too conservative or too aggressive since the SCR influences the system stability [153]. The influence of the SCR on stability was considered in [113] and the suggestion on the selection of the PLL bandwidth was given. However, a design procedure to prevent the small signal instability was not given. A more recent work regarding the selection of PLL gain to prevent instability was presented in [154]. Nonetheless, to follow the approach and design the converter control is not intuitive, as the converter impedance needs to be first modeled. Besides, the dynamic of the VL is not relevant in inverter control and thus is not considered, which is not the case for EV chargers. The VL dynamics were considered in [155] and the influence of the VL gain on stability was discussed. However, no design recommendations are given. A more recent work [156] proposed an analytic approach to design the VL bandwidth. However, the relation between the VL bandwidth and the CL bandwidth was overlooked, which easily leads to a either conservative or aggressive design. An analytic approach for the controller gain selection considering the influence of the SCR and all PLL, VL, and CL dynamics can hardly be found in the literature. Without such an analytic design, the controller gains have to be selected by trial and error, which hardly gives an accurate design.

The main contribution of the chapter is the proposed analytic gain selection method aiming to optimize the PLL bandwidth and the VL bandwidth while keeping the stability of an EV charger, or a PFC more broadly, with a weak grid connection. To that end, after clarifying the background in Section 5.2, in Section 5.3 the NPR maximum frequencies and the resonant frequencies expressed as the loop bandwidth are derived, which reveals the

influences of the grid impedance, the filter inductance, and the bandwidth of the PLL, CL, and VL on stability. Further, the upper limits of the PLL and the VL bandwidths are derived analytically, which is presented in Section 5.4. Intriguingly, the analytically derived upper limits reveal that, with the same SCR, the bandwidth of the PLL and VL can be higher by increasing the CL bandwidth and the filter inductance. Simulations and experiments for validations are presented in Section 5.5.

## 5.2 FUNDAMENTALS

### 5.2.1 SYSTEM DESCRIPTION

The prevalent design of an EV charger's PFC [131, 132] is already introduced in Chapters 3 and 4. Here, we choose the design shown in Fig. 3.1 to elaborate on the proposed analytic controller design approach. However, since the average model of a Vienna rectifier and a two-level active rectifier is the same, the proposed approach can be applied to both regardless of the topology difference. Fig. 5.1 depicts the system again for convenience.

It is worth mentioning that an L-filter is assumed for the analysis. However, the proposed approach can be extended to a design with the LC filter. Since the LC-resonant frequency is far above the NPR caused by the control, when the L-filter has the same inductance as the LC-filter, the difference between the input impedance of the PFC with the L-filter and the input impedance of the PFC with the LC-filter is negligible, which makes the obtained conclusion suitable for both. The grid impedance is assumed purely inductive because it is the worst case for the small signal stability [157].

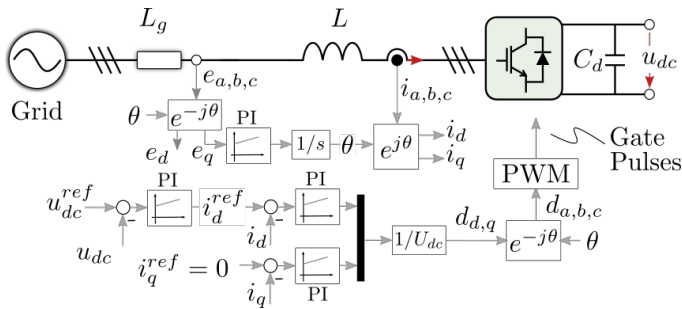


Figure 5.1: Typical design of an EV charger's PFC.

### 5.2.2 SMALL SIGNAL STABILITY CRITERION FOR A CHARGING SYSTEM

The small signal stability of a charging system can be evaluated with the impedance-based analysis [54, 118]. For a system with a high power factor, e.g. a charger's PFC, the coupling impedance is low and the stability is dominated by the diagonal impedance. Consequently, the stability of the system can be analyzed with the two single-input single-output systems on the d-axis and the q-axis [158]. Briefly, for both the d-axis and q-axis systems, the resonant frequency, where the magnitude of the grid impedance equals the converter's input impedance, should be located outside the NPR [137].

Such a stability criterion should be satisfied during the whole charging course despite the change in the charging power. Since the charger's input impedance changes at different

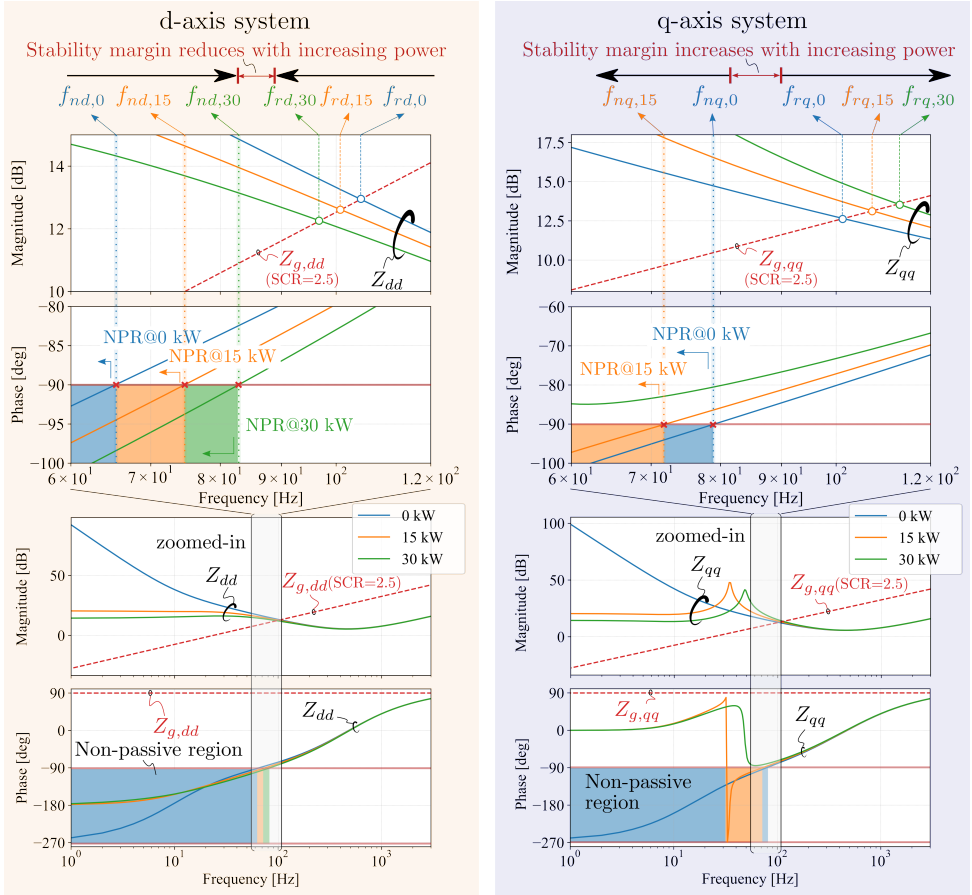


Figure 5.2: The change of the maximum NPR frequency, the resonant frequency, and the small signal stability margin of the d-axis system and the q-axis system of a charger's PFC with different charging power levels.

charging powers, the worst-case scenario should be analyzed to ensure stability during the entire charging process.

Fig. 5.2 illustrates the influence of the charging power on the stability margin. As seen, it shows the input impedance of a charger's PFC whose specifications are given as Design 1 in Table 5.1. The charger's d-axis and q-axis input impedance are denoted as  $Z_{dd}(s)$  and  $Z_{qq}(s)$ , respectively. The d-axis and q-axis grid impedance are denoted as  $Z_{g,dd}(s)$  and  $Z_{g,qq}(s)$ , respectively. The acronym  $f_{nx,y}$ , where  $x$  is  $d$  or  $q$  and  $y$  is 0 or 15 or 30, denotes the maximum x-axis NPR frequency, where the real part of the x-axis impedance changes from negative to zero and the phase of the x-axis impedance crosses  $-90^\circ$  when the charging power is  $y$  in kilowatt. For example,  $f_{nd,15}$  denotes the maximum d-axis NPR frequency when the charging power is 15 kW. The acronym  $f_{rx,y}$ , where  $x$  is  $d$  or  $q$  and  $y$  is 0 or 15 or 30, denotes the x-axis resonant frequency, where the magnitude of the x-axis input impedance equals the magnitude of the x-axis grid impedance when the charging power is

y in kilowatt. For example,  $f_{rd,15}$  denotes the maximum d-axis NPR frequency when the charging power is 15 kW.

Table 5.1: Specifications of the PFC in all studies carried out in this chapter

Param.	Description	Value		
		Design 1	Design 2	Design 3
$E_g$	Grid RMS voltage	230 V	230 V	230 V
$U_{dc}$	DC-link voltage	800 V	800 V	700 V
$f_1$	Grid frequency	50 Hz	50 Hz	50 Hz
$f_{sw}$	Switching frequency	20 kHz	20 kHz	20 kHz
$L$	Power filter inductance	0.4 mH	2.5 mH	2.5 mH
$C_f$	Power filter capacitance (if applicable)	-	10 $\mu$ F	5 $\mu$ F
$C_d$	PFC output capacitance	1.5 mF	1.5 mF	0.83 mF
$f_{cpll}$	PLL bandwidth	30 Hz	77 Hz	50 Hz
$\delta_{pll}$	PLL damping ratio	0.707	0.707	0.707
$f_{ci}$	CL bandwidth	800 Hz	800 Hz	500 Hz
$\delta_i$	CL damping ratio	0.707	0.707	0.707
$f_{cv}$	VL bandwidth	20 Hz	41 Hz	20 Hz
$\delta_v$	VL damping ratio	0.707	0.707	0.707
$P_{max}$	Nominal power	30 kW	-	10 kW

Clearly, with a higher charging power, the NPR of the  $Z_{dd}(s)$  expands, and the magnitude  $|Z_{dd}(s)|$  decreases. Consequently, the resonant frequency  $f_{rd}$  decreases from  $f_{rd,0}$  to  $f_{rd,30}$  whereas the maximum d-axis NPR frequency  $f_{nd}$  increases from  $f_{nd,0}$  to  $f_{nd,30}$ . However, with increasing power, the resonant frequency  $f_{rq}$  increases from  $f_{rq,0}$  to  $f_{rq,30}$  whereas the maximum q-axis NPR frequency  $f_{nq}$  decreases from  $f_{nd,0}$  to  $f_{nd,15}$  and completely vanishes when the charging power is 30 kW.

As a result, for the d-axis system, the margin between the  $f_{rd}$  and the  $f_{nd}$ , which is referred to as the stability margin, is the smallest when the charging power reaches the maximum. On the contrary, the stability margin of the q-axis system is the lowest when the charging power is zero. Therefore, the criterion for ensuring small signal stability during the entire charging process is

$$f_{nd,P_{max}} < f_{rd,P_{max}} \quad \text{and} \quad f_{nq,P_0} < f_{rq,P_0}, \quad (5.1)$$

where the subscript  $P_0$  denotes zero charging power and  $P_{max}$  denotes the maximum charging power. The frequencies denoted with  $f$  in (5.1) can be changed to the angular frequencies denoted with  $\omega$ . For convenience, both of the two kinds of expressions will be used. With an analytical expression of (5.1), the control parameters can be designed analytically instead of by trial and error, which is the main focus of this chapter.

## 5.3 STABILITY CRITERION BREAKDOWN

### 5.3.1 FULL-ORDER MODEL

The full-order impedance model of a PFC has already been derived in [70, 153]. Accordingly, the expression of  $Z_{dd}(s)$  and  $Z_{qq}(s)$  when the power factor is unity can be obtained as

$$Z_{dd}(s) = (Ls + R + \frac{3E_g^2}{2C_d U_{dc}^2 s})(1 + G_{oi,dd}(s))(1 + G_{ov}(s)) \frac{1}{1 - T(s)}, \quad (5.2)$$

$$Z_{qq}(s) = \frac{(Ls + R)(1 + G_{oi,qq}(s))}{1 - G_{cpll}(s)(1 - (k_{pi} + \frac{k_{ii}}{s})\frac{I_d}{E_g})}, \quad (5.3)$$

where  $E_g$  and  $U_{dc}$  denote the grid voltage amplitude and the dc-link voltage, respectively.  $I_d$  denotes the d-axis current at a steady state.  $L$  and  $R$  denote the inductance and the resistance of the power filter, respectively.  $C_d$  denotes the output capacitance of the PFC.  $G_{oi,dd}(s)$ ,  $G_{oi,qq}(s)$ ,  $G_{ov}(s)$ ,  $T(s)$ , and  $G_{cpll}(s)$  are functions of  $s$ , whose expressions are given by

$$G_{oi,qq}(s) = \frac{k_{pi} + k_{ii}/s}{Ls + R} e^{-sT_{del}}, \quad (5.4)$$

$$G_{cpll}(s) = \frac{E_g(k_{ppll}s + k_{ipll})}{s^2 + E_g(k_{ppll}s + k_{ipll})}, \quad (5.5)$$

$$G_{oi,dd}(s) = \frac{(1 + \frac{3E_g I_d}{2C_d U_{dc}^2 s})(k_{pi} + \frac{k_{ii}}{s})}{Ls + R + \frac{3E_g^2}{2C_d U_{dc}^2 s}} e^{-sT_{del}}, \quad (5.6)$$

$$T(s) = \frac{3E_g}{2C_d U_{dc} s} (k_{pv} + \frac{k_{iv}}{s})(k_{pi} + \frac{k_{ii}}{s}) \frac{I_d}{E_g}, \quad (5.7)$$

$$G_{ov}(s) = \frac{3E_g}{2C_d U_{dc} s} (k_{pv} + \frac{k_{iv}}{s}) \frac{G_{oi,dd}(s)}{1 + G_{oi,dd}(s)}, \quad (5.8)$$

where  $T_{del}$  is the delay caused by pulse wave modulation and control.  $k_{pi}$ ,  $k_{pv}$ , and  $k_{ppll}$  are the proportional gain of the current controller, the voltage controller, and the PLL controller, respectively.  $k_{ii}$ ,  $k_{iv}$ , and  $k_{ipll}$  denote the integral gain of the current controller, the voltage controller, and the PLL controller, respectively.

### 5.3.2 REDUCED-ORDER MODEL

To obtain concise expressions of the  $f_{nd,P_{max}}$ ,  $f_{rd,P_{max}}$ ,  $f_{nq,P_0}$ , and  $f_{rq,P_0}$  in (5.1), replacing the controller parameters in (5.2) and (5.3) with the cut-off frequencies and damping ratios of the control loops is beneficial.

Considering the CL bandwidth is much smaller than the switching frequency, the CL can be simplified as the model shown in Fig. 5.3.

Accordingly, the CL cut-off frequency  $\omega_{ci}$  can be approximated by neglecting the low-order term of  $s$  in the open-loop TF because of their small value about  $\omega_{ci}$ . Then,  $\omega_{ci}$  can be obtained as

$$\omega_{ci} = \frac{k_{pi}}{L}. \quad (5.9)$$

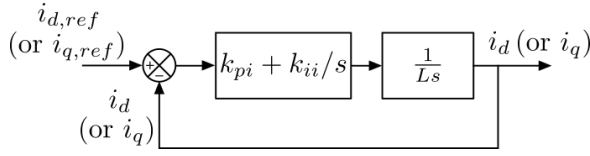


Figure 5.3: Block diagram of the simplified current loop

The closed loop of the CL is a second-order system whose damping ratio  $\delta_i$  can be derived as

$$\delta_i = \sqrt{\frac{k_{pi}^2}{4 \cdot L \cdot k_{ii}}} \quad (5.10)$$

The block diagram of the VL is depicted in Fig. 5.4. The TF of the inner CL is denoted as  $G_{ci}(s)$ , which can be approximated as a gain of one because the CL bandwidth is much higher than the VL bandwidth.

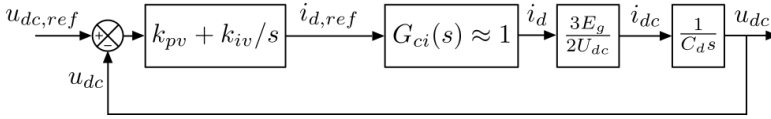


Figure 5.4: Block diagram of the simplified voltage loop

Similarly, the VL cut-off frequency  $\omega_{cv}$  can be approximated by neglecting the low-order term of  $s$  in the open-loop TF, which is obtained as

$$\omega_{cv} = \frac{3 \cdot E_g \cdot k_{pv}}{2 \cdot U_{dc} \cdot C_d} \quad (5.11)$$

Clearly, the closed loop of the VL is also a second-order system whose damping ratio  $\delta_v$  can be obtained as

$$\delta_v = \sqrt{\frac{3 \cdot E_g \cdot k_{pv}^2}{8 \cdot U_{dc} \cdot C_d \cdot k_{iv}}} \quad (5.12)$$

As for the PLL, its block diagram is illustrated in Fig. 5.5, where  $\theta_s$  is the grid voltage angle. Since the difference between the PLL output angle  $\theta$  and  $\theta_s$  is small,  $\sin(\theta_s - \theta)$  can be approximated as  $\theta_s - \theta$ .

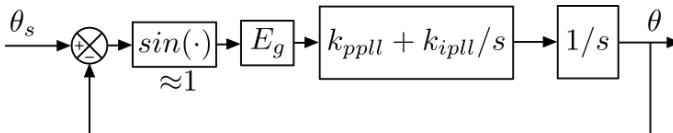


Figure 5.5: Block diagram of the phase-locked loop.

The cut-off frequency  $\omega_{cpll}$  of the PLL can be obtained as

$$\omega_{cpll} = k_{ppll} \cdot E_g \quad (5.13)$$

The closed loop of the PLL is, again, a second-order system whose damping ratio is derived as

$$\delta_{pll} = \sqrt{\frac{E_g \cdot k_{ppll}^2}{4 \cdot k_{ipll}}}. \quad (5.14)$$

According to (5.9)-(5.14), the controller parameters, e.g.,  $k_{pi}$  and  $k_{ii}$ , can be expressed with the cut-off frequencies and damping ratios of the corresponding control loops, e.g.,  $\omega_{ci}$  and  $\delta_i$ . Substituting these expressions of the controller parameters into (5.2) and (5.3), the full-order impedance model is then expressed with the cut-off frequencies and damping ratios of the CL, VL, and PLL. Then, based on the full-order impedance model and the practical conditions, several assumptions are made to obtain a reduced-order model.

**Assumption 1:** the delay  $T_{del}$ , which equals  $1.5/f_{sw}$ , where  $f_{sw}$  is the switching frequency, can be neglected. This is reasonable because the NPR of the input impedance is at low frequencies. The effect of the control delay inside the NPR is negligible since  $f_{sw}$  is far beyond the NPR.

**Assumption 2:** the resistance of the power filter is negligible. This is reasonable because the influence of the resistance on the input impedance is small [137].

**Assumption 3:** the cut-off frequency  $\omega_{cv}$  of the VL, and the cut-off frequency  $\omega_{cpll}$  of the PLL, are much lower than the cut-off frequency  $\omega_{ci}$  of the CL. Thus,  $\omega_{cv} + \omega_{ci} \approx \omega_{ci}$  and  $\omega_{cpll} + \omega_{ci} \approx \omega_{ci}$ .

After simplifying the expressions in MAPLE, the reduced-order model of  $Z_{dd}(s)$  when the power factor is unity is obtained as

$$Z_{dd}(s) = L \cdot \frac{s^4 + \omega_{ci} \cdot s^3 + a_2 \cdot \omega_{ci} \cdot s^2 + a_1 \cdot \omega_{ci} \cdot s + a_0}{s^3 - I_d \cdot b_2 \cdot [\omega_{ci} \cdot s^2 + b_1 \cdot \omega_{ci} \cdot s + a_0 / \omega_{cv}]}, \quad (5.15)$$

where the  $a_2$ ,  $a_1$ ,  $a_0$ ,  $b_2$ , and  $b_1$  are given by

$$\begin{aligned} b_2 &= \frac{L \cdot \omega_{cv}}{E_g}, & a_0 &= \frac{\omega_{ci}^2}{4 \cdot \delta_i^2} \cdot \frac{\omega_{cv}^2}{4 \cdot \delta_v^2}, \\ b_1 &= \frac{\omega_{ci}}{4 \cdot \delta_i^2} + \frac{\omega_{cv}}{4 \cdot \delta_v^2}, & a_1 &= b_1 \cdot \omega_{cv} + \frac{\omega_{ci}}{4 \cdot \delta_i^2} \cdot \frac{3 \cdot E_g \cdot I_d}{2 \cdot C_d \cdot U_{dc}^2}, \\ a_2 &= \omega_{cv} + \frac{3 \cdot E_g \cdot I_d}{2 \cdot C_d \cdot U_{dc}^2} + \frac{3 \cdot E_g^2}{2 \cdot C_d \cdot L \cdot \omega_{ci} \cdot U_{dc}^4} + \frac{\omega_{ci}}{4 \cdot \delta_i^2}. \end{aligned} \quad (5.16)$$

Similarly, the reduced-order model of  $Z_{qq}$  when the power factor is unity is obtained as

$$Z_{qq}(s) = L \cdot \frac{s^4 + \omega_{ci} \cdot s^3 + c_2 \cdot \omega_{ci} \cdot s^2 + c_1 \cdot \omega_{ci} \cdot s + c_0}{s^3 + I_d \cdot d_2 \cdot [\omega_{ci} \cdot s^2 + d_1 \cdot \omega_{ci} \cdot s + c_0 / \omega_{cpll}]}, \quad (5.17)$$

where the  $c_2$ ,  $c_1$ ,  $c_0$ ,  $d_2$ , and  $d_1$  are given by

$$\begin{aligned} d_2 &= \frac{L \cdot \omega_{cpll}}{E_g}, & d_1 &= \frac{\omega_{ci}}{4 \cdot \delta_i^2}, \\ c_2 &= \omega_{cpll} + \frac{\omega_{ci}}{4 \cdot \delta_i^2}, & c_1 &= d_1 \cdot \omega_{cpll}, & c_0 &= \frac{\omega_{ci}^2}{4 \cdot \delta_i^2} \cdot \frac{\omega_{cpll}^2}{4 \cdot \delta_{pll}^2}. \end{aligned} \quad (5.18)$$

Practically speaking, the optimum damping ratio is 0.707 [159]. Thus, the damping ratio is fixed at 0.707 for the CL, the PLL, and the VL in the following discussion. In this case, the bandwidth is about the cut-off frequency. Thus, the cut-off frequencies are referred to as the bandwidth, which are to be designed to ensure stability.

### 5.3.3 EXPRESSIONS OF THE MAXIMUM NPR FREQUENCIES

At the maximum NPR frequency  $\omega_{nd,P_{max}}$ , the real part of  $Z_{dd}(j\omega)$  equals zero. Therefore, the analytical expression of  $\omega_{nd,P_{max}}$  can be obtained by solving

$$Re(Z_{dd}(j\omega)) = \omega_{ci} \cdot \frac{4 \cdot \omega^4 - 2 \cdot \omega_{ci} \cdot k_1 \cdot \omega^2 - k_1 \cdot k_2 \cdot \omega_{ci}^3}{(2 \cdot \omega^2 + \omega_{ci} \cdot k_2)^2 + 4 \cdot k_2^2 \cdot \omega^2} = 0, \quad (5.19)$$

where

$$k_1 = \omega_{cv} + \underbrace{\frac{3 \cdot E_g}{2 \cdot C_d \cdot U_{dc}^2} \cdot I_m}_{\omega_r}, \quad k_2 = \underbrace{\frac{L}{E_g} \cdot I_m}_{h} \cdot \omega_{cv}. \quad (5.20)$$

$I_m$  denotes the steady-state current  $I_d$  at the maximum charging power. The term  $\omega_r$  can be regarded as a frequency whose value is much smaller than  $\omega_{ci}$ . Since  $\omega_{nd,P_{max}}$  is positive, the only valid solution (5.19) is obtained as

$$\omega_{nd,P_{max}} = \sqrt{\frac{\omega_{ci}}{2} \cdot \frac{k_1 + \sqrt{k_1 \cdot (k_1 + 4 \cdot k_2 \cdot \omega_{ci})}}{2}}, \quad (5.21)$$

Similarly, the maximum NPR frequency  $\omega_{nq,P_0}$  can be obtained by solving

$$Re(Z_{qq}(j\omega)) = L \cdot \omega_{ci} - L \cdot \frac{\omega_{ci}^2 \cdot \omega_{cpll}}{2 \cdot \omega^2} = 0 \quad (5.22)$$

Since (5.22) has only one reasonable solution, the  $\omega_{nq,P_0}$  is obtained as

$$\omega_{nq,P_0} = \sqrt{\frac{\omega_{cpll} \cdot \omega_{ci}}{2}}. \quad (5.23)$$

### 5.3.4 EXPRESSIONS OF THE RESONANT FREQUENCIES

Given that  $k_1 < \omega_{ci}/2$  and  $k_2$  is always positive, the expression of the  $\omega_{nd,P_{max}}$ , namely (5.21), indicates a lower boundary of  $k_1$  and an upper boundary of  $\omega_{ci}/2$  of the  $\omega_{nd,P_{max}}$ . Therefore, if the  $\omega_{rd,P_{max}}$  is smaller than  $k_1$ , the system is unstable because the  $\omega_{rd,P_{max}}$  is smaller than the  $\omega_{nd,P_{max}}$  in this case. On the contrary, when the  $\omega_{rd,P_{max}}$  is located in the frequency range beyond  $\omega_{ci}/2$ , the system is stable because the  $\omega_{rd,P_{max}}$  is larger than the  $\omega_{nd,P_{max}}$  in this case.

To simplify the expression of  $\omega_{rd,P_{max}}$ , three frequency ranges, namely low-frequency range, medium frequency range, and high-frequency range, are defined according to the lower and upper boundary of the  $\omega_{nd,P_{max}}$ . The magnitude  $|Z_{dd}(j\omega)|$  is approximated by



ignoring the small items in the different frequency ranges, which is obtained as

$$|Z_{dd}(j\omega)| \approx \begin{cases} \left| \frac{L}{k_2} \cdot \frac{2 \cdot k_1 \cdot j\omega + \omega_{cv}^2}{2 \cdot j\omega + \omega_{cv}} \right| & (\omega \leq k_1) \\ \frac{L \cdot \omega_{ci}^2 \cdot j\omega}{-2 \cdot \omega^2 - 2 \cdot k_2 \cdot \omega_{ci} \cdot j\omega - k_2 \cdot \omega_{ci}^2} & (k_1 < \omega \leq \frac{\omega_{ci}}{2}) \\ \left| \frac{-L \cdot \omega^2 + \omega_{ci} \cdot j\omega}{j\omega - k_2 \cdot \omega_{ci}} \right| & (\omega > \frac{\omega_{ci}}{2}) \end{cases} \quad (5.24)$$

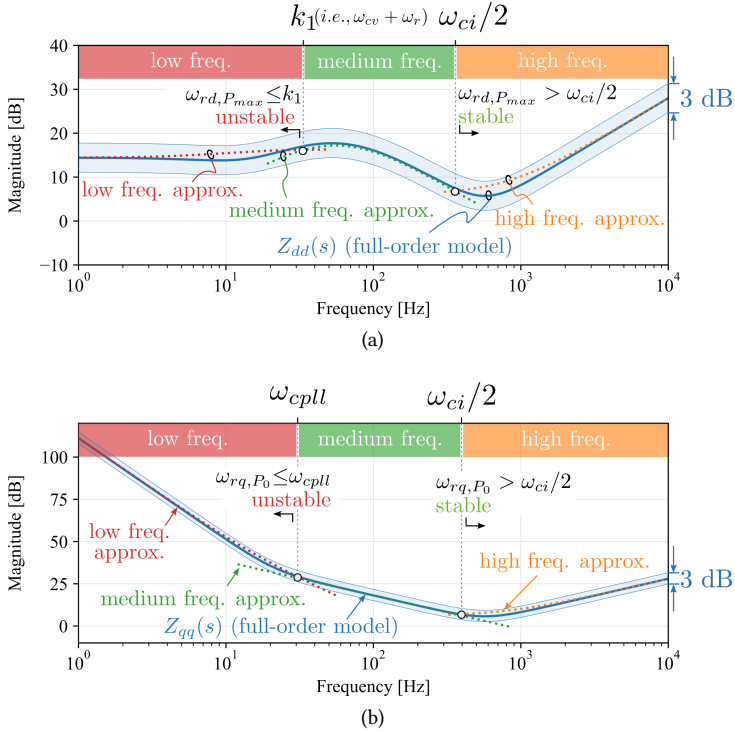


Figure 5.6: (a) compares the approximation of  $|Z_{dd}(j\omega)|$  using (5.24) to the full-order model in the different frequency ranges evincing the approximation is accurate. (b) compares the approximation of  $|Z_{qq}(s)|$  using (5.26) with the full-order model in the different frequency ranges evincing the approximation is accurate.

Fig. 5.6a illustrates the accuracy of the magnitude approximation given by (5.24) using Design 1 specifications in Table 5.1. As aforementioned, only the math expression of the  $\omega_{rd,P_{max}}$  in the medium frequency range is of interest. Substituting the expression of  $|Z_{dd}(j\omega)|$  in the medium frequency range into  $|Z_{dd}(j\omega_{rd,P_{max}})| = |L_g \cdot \omega_{rd,P_{max}}|$ , the expression of  $\omega_{rd,P_{max}}$  is obtained as

$$\omega_{rd,P_{max}} = \frac{\omega_{ci}}{\sqrt{2}} \cdot \sqrt{\frac{L}{L_g} - \frac{L}{E_g} \cdot I_m \cdot \omega_{cv}}. \quad (5.25)$$

Similarly, given that  $\omega_{cpll} < \omega_{ci}/2$ , (5.26) indicates that the lower boundary and the high boundary of the  $\omega_{nq,P_0}$  are  $\omega_{cpll}$  and  $\omega_{ci}/2$ , respectively. Accordingly, the low, medium, and high frequency ranges are defined to simplify the expression of  $|Z_{qq}(j\omega)|$  in the different frequency ranges, which is beneficial for obtaining a concise expression of the  $\omega_{rq,P_0}$ . As a result, the magnitude  $|Z_{qq}(j\omega)|$  at zero charging power is approximated by ignoring the small items in the different frequency ranges, which results in

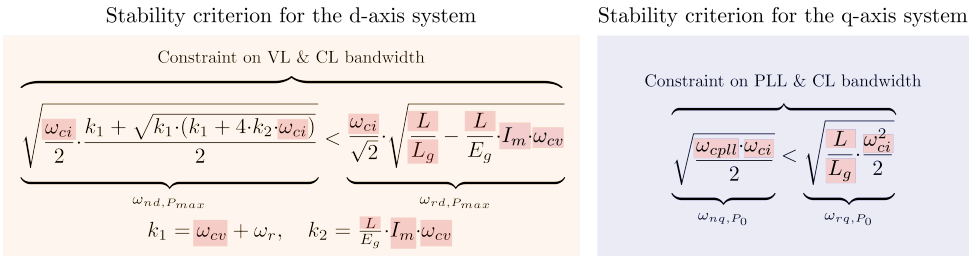
$$|Z_{qq}(j\omega)| \approx \begin{cases} \left| \frac{L \cdot c_1 \cdot \omega_{ci} \cdot j\omega + L \cdot c_0}{\omega^3} \right| & (\omega \leq \omega_{cpll}) \\ \left| \frac{L \cdot \omega_{ci}^2}{2 \cdot \omega} \right| & (\omega_{cpll} < \omega \leq \frac{\omega_{ci}}{2}) \\ |L \cdot (\omega + \omega_{ci})| & (\omega > \frac{\omega_{ci}}{2}) \end{cases} \quad (5.26)$$

The approximation results are illustrated in Fig. 5.6b evincing the error caused by the approximation within 3 dB. Similarly, only the expression of the  $\omega_{rq,P_0}$  in the medium frequency range is of interest. Substituting (5.26) in the medium frequency range into  $|Z_{qq}(j\omega_{rq,P_0})| = |L_g \cdot \omega_{rq,P_0}|$  gives

$$\omega_{rq,P_0} = \sqrt{\frac{L}{L_g} \cdot \frac{\omega_{ci}^2}{2}} \quad (5.27)$$

### 5.3.5 IMPACT OF INFLUENTIAL PARAMETERS ON STABILITY

The sufficient and necessary conditions to maintain small signal stability can be obtained by substituting (5.21), (5.25), (5.23), and (5.27) into (5.1), which are illustrated in Fig.5.7. It is revealed that the stability criterion for the d-axis system actually poses a constraint on the selection of the VL and CL bandwidth whereas the stability criterion for the q-axis system poses a constraint on the selection of the PLL and CL bandwidth. For maintaining stability, reducing the maximum NPR frequency and increasing the resonant frequency are preferred, since it enlarges the stability margin. Based on (5.21), (5.25), (5.23), and (5.27), the impact of the influential parameters on stability are summarized in Table 5.2.



The influential parameters are highlighted in red.

$E_g$  and  $\omega_r$  are considered as constants because their variations are small, which very marginally influence the value of  $\omega_{nd,Pmax}$  and  $\omega_{rd,Pmax}$

Figure 5.7: Sufficient and necessary conditions for stability expressed with the design parameters obtained by substituting (5.21), (5.25), (5.23), and (5.27) into (5.1).

Table 5.2: Impact of the influential parameters on the critical frequencies and stability as indicated by (5.21), (5.25), (5.23), and (5.27)

Action	Consequences				Stability impact
	$\omega_{nd,P_{max}}$	$\omega_{rd,P_{max}}$	$\omega_{nq,P_0}$	$\omega_{rq,P_0}$	
$\omega_{ci} \uparrow$	$\uparrow$	$\uparrow$	$\uparrow$	$\uparrow$	–
$\omega_{cv} \uparrow$	$\uparrow$	$\downarrow$	N.A.	N.A.	Negative
$\omega_{cpll} \uparrow$	N.A.	N.A.	$\uparrow$	N.A.	Negative
$L \uparrow$	$\uparrow$	$\uparrow$	N.A.	$\uparrow$	–
$L_g \uparrow$	N.A.	$\downarrow$	N.A.	$\downarrow$	Negative
Denotation meaning					
$\uparrow$	Increase. E.g., increasing $\omega_{ci}$ leads to the increase of $\omega_{nd,P_{max}}$ .				
$\downarrow$	Decrease. E.g., increasing $\omega_{cv}$ leads to the decrease of $\omega_{rd,P_{max}}$ .				
N.A.	Not related.				
–	Unclear. Further analysis will be given in Section 5.4.				

## 5

## 5.4 ANALYTIC DESIGN OF THE CONTROLLER

### 5.4.1 UPPER LIMIT OF THE PLL AND VL BANDWIDTH

Based on Fig.5.7, the boundary constraining the selection of the PLL bandwidth is obtained as

$$\omega_{cpll} < \frac{L}{L_g} \cdot \omega_{ci} \quad (5.28)$$

The definition of the SCR is given in [60, 160],

$$\text{SCR} = \frac{S_{SC}}{S_{equ}} = \frac{3 \cdot E_g^2}{|Z_g| \cdot P_{max}} = \frac{3 \cdot E_g^2}{\omega_1 \cdot L_g \cdot P_{max}} \quad (5.29)$$

where  $S_{SC}$  is the short-circuit power at the PCC and  $S_{equ}$  is the rated power of the equipment and equals to  $P_{max}$  for a PFC converter whose power factor is unity. Accordingly, (5.28) can be rewritten as

$$\omega_{cpll} < \underbrace{\frac{2 \cdot P_{max} \cdot \omega_1}{3 \cdot E_g^2}}_g \cdot \text{SCR} \cdot L \cdot \omega_{ci} \quad (5.30)$$

where  $\omega_1$  is the grid angular frequency, and  $P_{max}$  is the maximum charging power. Note that satisfying (5.30) is a sufficient condition for the existence of the solution of (5.27).

Further, based on Fig.5.7, the boundary constraining the selection of the VL bandwidth is obtained as

$$\begin{aligned} \omega_{cv} &< \frac{g}{h} - \frac{\sqrt{g^2 + 4 \cdot g \cdot h \cdot \omega_{ci} \cdot (g + h \cdot \omega_r)} - g}{2 \cdot h^2 \cdot \omega_{ci}} \\ \Rightarrow \omega_{cv} &< \omega_1 \cdot \text{SCR} \cdot \left(1 - \frac{\sqrt{1 + 4 \cdot h \cdot \omega_{ci} \cdot \left(1 + \frac{\omega_r}{\omega_1 \cdot \text{SCR}}\right)} - 1}{2 \cdot h \cdot \omega_{ci}}\right) \end{aligned} \quad (5.31)$$

It is worth mentioning that satisfying (5.31) is a sufficient condition for the existence of the solution of (5.25).

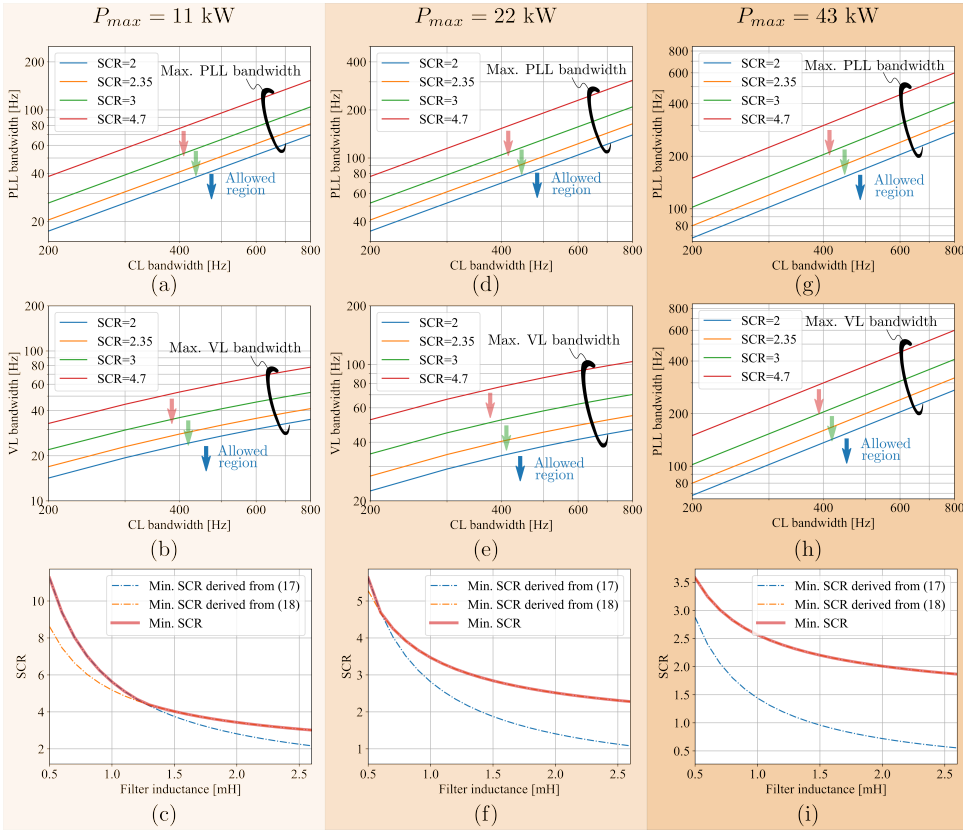


Figure 5.8: Visualization of the observations from (5.30) and (5.31) with an example PFC whose specifications are given by Design 2 in Table 5.1 with three different typical power rating levels of EV chargers. (a,b,d,e,g,h) show the upper limits of the PLL and VL bandwidth increase with a higher CL bandwidth. (c,f,i) show the minimum allowed SCR can be reduced by increasing the filter inductance. Comparing (a,b,c) to (d,e,f) or (g,h,i) indicates that without changing the control and filter design, a PFC with a higher power rating can stably operate in a lower SCR case.

### 5.4.2 DISCUSSION

Based on (5.30) and (5.31), the following can be observed.

1. (5.30) indicates that the maximum allowed PLL bandwidth  $\omega_{cpll}$  decreases with the reduction of the SCR. However, it can be increased by increasing the CL bandwidth  $\omega_{ci}$  and the filter inductance.
2. (5.31) indicates that the maximum allowed VL bandwidth  $\omega_{cpll}$  decreases with the reduction of the SCR. However, it can be increased by increasing the CL bandwidth  $\omega_{ci}$  and the filter inductance.
3. Increasing the filter inductance increases the maximum allowed PLL and VL bandwidth. Inversely, keeping the PLL, VL, and CL bandwidth unchanged, using a higher filter inductance allows the PFC of a charger stably operate with a lower SCR.

- Without changing the control and filter design, the charger PFC with a higher charging power can stably operate in a lower SCR case. The reason is that a higher charging power indicates a smaller grid impedance  $L_g$  if the SCR is unchanged, as seen from (5.29). Such increases the resonant frequency and the stability margin since the charger input impedance does not significantly change with different charging power. Thus, a lower SCR is allowed.

To showcase the observations above, an example PFC with the specifications shown in Design 2 in Table 5.1 is given. The calculated  $f_{cpll}$  and  $f_{cv}$  upper limit when selecting different  $f_{ci}$  and the minimum SCR for the stable operation when choosing different filter inductance are illustrated in Fig. 5.8 for three standard power rating levels of EV chargers.

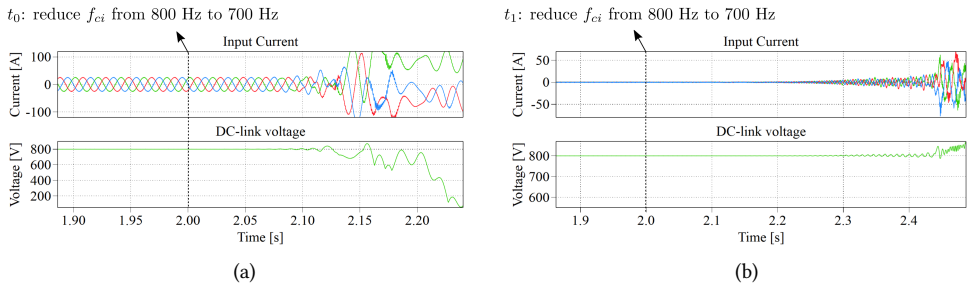


Figure 5.9: The influence of the CL bandwidth on (a) the upper limit of the VL bandwidth and (b) the upper limit of the PLL bandwidth.

The calculations shown in Fig. 5.8 are verified with simulations. Specifically, assuming the SCR is 2.35 and the  $P_{max}$  is 11 kW, when  $f_{ci}$  is 800 Hz, the calculated upper limit of the  $f_{cv}$  and  $f_{cpll}$ , as seen in Fig. 5.8a,b, is about 41 Hz and 77 Hz, respectively. In the simulation shown in Fig. 5.9a, the PFC is operating at the maximum power and it has the same design as Design 2 but with a  $f_{cpll}$  reduced to 10 Hz to be far below its upper limit. As seen, once reducing the  $f_{ci}$  at  $t_0$ , the system becomes unstable. It happens because the upper limit of the  $f_{cv}$  reduces after decreasing the  $f_{ci}$ , and the 41-Hz  $f_{cv}$  exceeds the reduced upper limit of the  $f_{cv}$ .

With the same PFC and SCR, another simulation shown in Fig. 5.9b is carried out in no load condition since it is the worst case for the PLL-related stability. This time, the  $f_{cpll}$  is changed to its upper limit of 77 Hz while the  $f_{cv}$  is reduced to 10 Hz to be much smaller than its upper limit. As seen, instability appears once reducing the  $f_{ci}$ , which happens because the  $f_{cpll}$  exceeds the reduced upper limit after decreasing the  $f_{ci}$ .

### 5.4.3 DESIGN STEPS

Based on the analysis and obtained upper limits for the PLL bandwidth and the VL bandwidth, a design method illustrated in Fig. 5.10 is concluded to prevent the small signal instability caused by improper controller gain selections.

As seen, the CL bandwidth can be selected firstly, which is typically below one-twentieth of the switching frequency to sufficiently attenuate the switching noises [52]. Then, after knowing the hardware specifications and the lowest possible SCR, the upper limits of

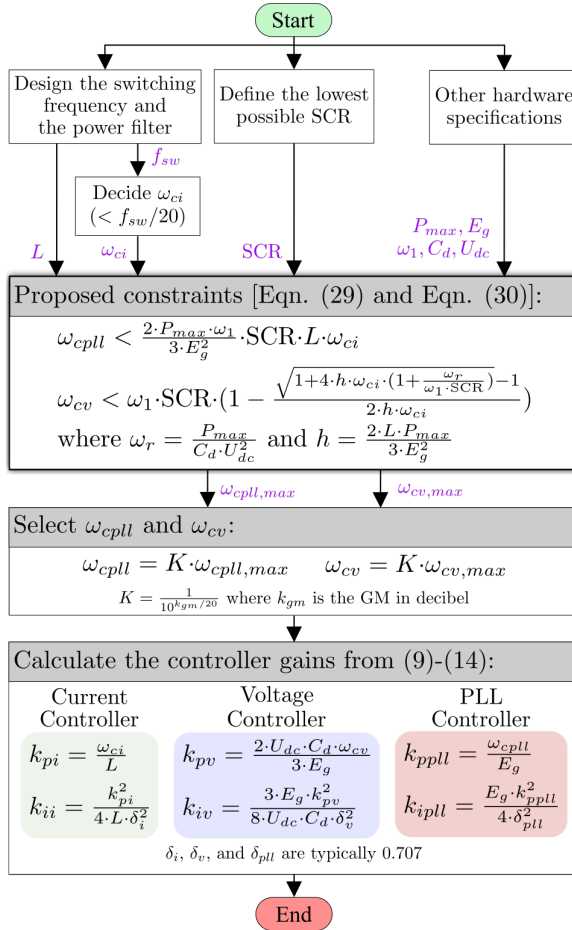


Figure 5.10: Flowchart of the proposed approach to tuning the controllers.

the PLL and VL bandwidth can be calculated. Accordingly, after leaving a proper gain margin (GM) of 3-6 dB [154, 156], as shown in Fig. 5.11, all controller gains can be selected directly without trials and errors. However, without the proposed approach, one needs to establish the input impedance model of the EV charger. Then, the controller gains are obtained through trials and errors by plotting the characteristic loci of the return ratio matrix [153] and check if any characteristic loci encircle the point of  $-1+j0$ . Such a process might take many rounds of iterations to find proper controller gains, which is prevented by applying the proposed approach. Hence, the proposed approach reduces the effort and time of properly tuning the controller in practice.

#### 5.4.4 INFLUENCES OF NEGLECTING THE COUPLING EFFECTS

It is worth mentioning that the influences of the coupling effects on stability are neglected when applying (5.1) as the stability criteria for simplicity. Such a simplification can influence

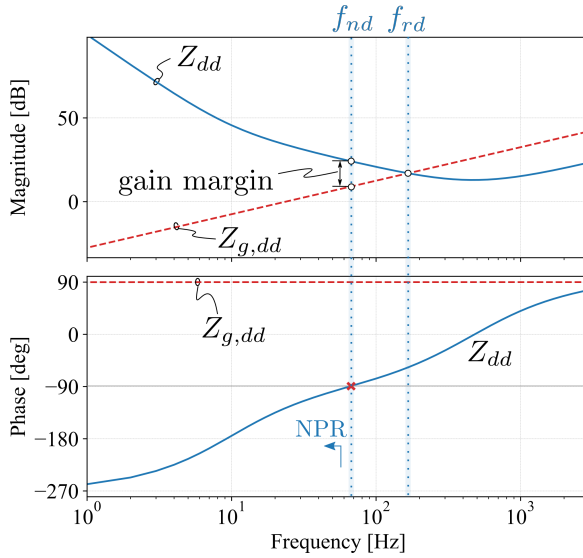


Figure 5.11: Gain margin of the d-axis system of a grid-charger system.

the accuracy of the upper limits of the PLL bandwidth and the VL bandwidth obtained from (5.30) and (5.31). However, since a charger’s PFC has a unity power factor, the coupling impedance is small, which leads to practically trivial influences of neglecting the coupling effects on stability analysis. Hence, the errors of the obtained bandwidth upper limits are small. With leaving a GM of 3-6 dB, the errors caused by neglecting the coupling effects are unproblematic for stability.

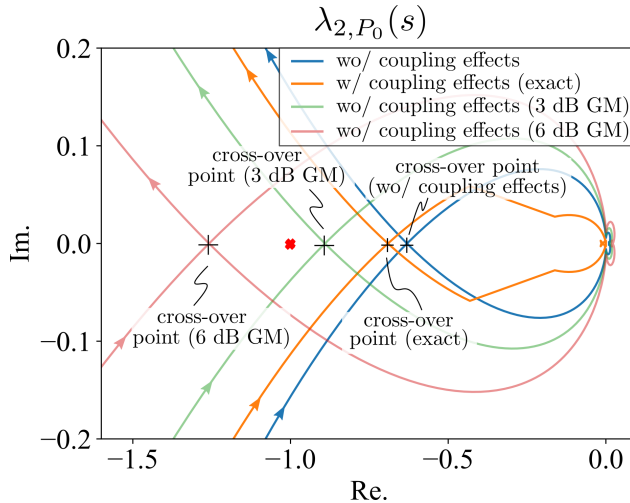


Figure 5.12: Influences of neglecting the coupling effects on the characteristic loci of the return ratio matrix when the charging power is zero.

Specifically, for the PFC in Fig. 5.8, the influences of neglecting the coupling effects on the characteristic loci of the return ratio matrix [133] when the SCR is 4.5 are depicted in Fig. 5.12 and Fig. 5.13. According to the general Nyquist stability criterion (GNC), none of the characteristic loci should encircle the point of  $-1+j0$  for the sake of stability [133]. In the two characteristic loci of the return ratio matrix, namely  $\lambda_1(s)$  and  $\lambda_2(s)$ , only  $\lambda_2(s)$  presents the risk of encircling the point of  $-1+j0$  in the worst case for the q-axis system stability, i.e., when the charging power is zero. Therefore, Fig. 5.12 compares the locus of the  $\lambda_{2,P_0}(s)$ , i.e.,  $\lambda_2(s)$  when the charging power is zero, in the cases with and without considering the coupling effects. It can be seen that the differences between the two are minor. When leaving a GM of 3-6 dB, the point of  $-1+j0$  is located between the cross-over point of the locus with a 3-dB GM and the cross-over point of the one with a 6-dB GM. In this case, there is no risk of encircling the point of  $-1+j0$  for the loci both with and without the coupling effects.

When the charging power is maximum, which is the worst case for the d-axis system stability, only the  $\lambda_1(s)$  presents the risk of encircling the point of  $-1+j0$ . Hence, Fig. 5.13 depicts the locus of the  $\lambda_{1,P_{max}}(s)$ , which represents the  $\lambda_1(s)$  when the charging power is the maximum, in the cases with and without considering the coupling effects. Similarly, after leaving a GM of 3-6 dB, the point of  $-1+j0$  is located between the cross-over point of the locus with a 3-dB GM and the cross-over point of the one with a 6-dB GM. Consequently, the errors caused by ignoring the coupling effects are unproblematic for stability.

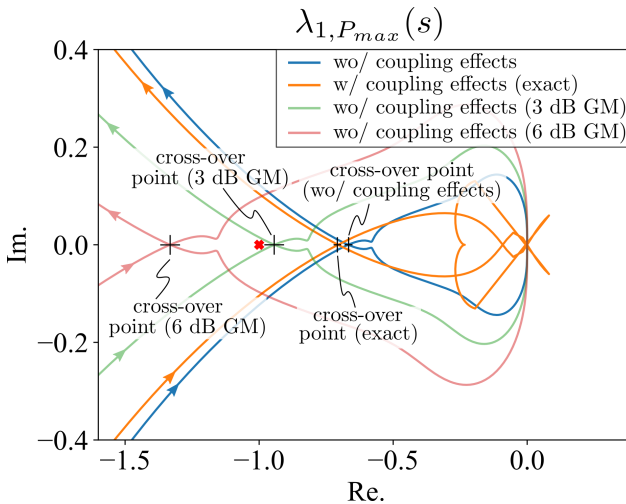


Figure 5.13: Influences of neglecting the coupling effects on the characteristic loci of the return ratio matrix when the charging power is maximum.

### 5.4.5 COMPARISON WITH THE EXISTING METHODS

In [137], design recommendations for the control of voltage source converters, which include PFC, are given to shape their input impedance to prevent small signal instability. It concluded that the maximum allowed VL bandwidth and the PLL bandwidth are one-tenth



of the CL bandwidth. However, following the recommendation may lead to instability in an extremely weak grid condition.

As an example, two simulations are carried out. The PFC in the simulation has the parameters of Design 2 in Table 5.1 and the maximum power of 11 kW. In the first simulation, the VL bandwidth is increased from 41 Hz to 80 Hz, i.e., one-tenth of the CL bandwidth. And, the charger is operating at the maximum power. As seen in Fig. 5.14a, at  $t_1=6$  s, the SCR starts decreasing from 10. When the SCR is decreased to 4.7, the PFC loses stability. The simulation result complies with the analytical result shown in Fig. 5.8b since when SCR is 4.7, a VL bandwidth of 80 Hz is just outside the allowed region.

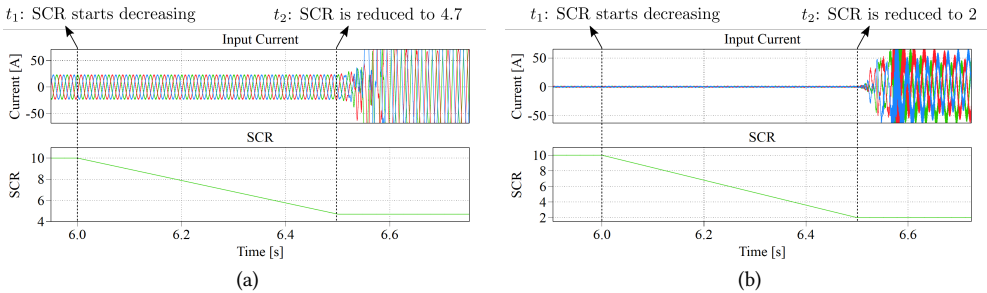


Figure 5.14: Influence of short circuit ratio on the upper limit of (a) the VL bandwidth and (b) the PLL bandwidth.

In the second simulation, the PLL bandwidth is increased to 80 Hz while the VL bandwidth is reduced to the original 41 Hz. The charger is operating at no-load condition since, for a PFC, it is the worst case for the PLL-related instability. Similarly, at  $t_1=6$  s, the SCR starts decreasing from 10. When SCR is decreased to 2, the PLL bandwidth of 80 Hz is just over the upper limit, as shown in Fig. 5.8a. Thus, the PFC becomes unstable.

The influence of the SCR on small signal stability is considered in two more recent works [154, 156]. However, the influence of the CL bandwidth on the upper limit of the PLL bandwidth or the VL bandwidth was not revealed. Specifically, Ref. [154] proposed a method to derive the maximum allowed PLL bandwidth for grid-tied inverters. The proposed method is also valid for the case when the power factor is not unity. However, the method still requires modeling the input impedance, and the influence of the CL bandwidth on the upper limit of the PLL bandwidth was not revealed and quantified. Ref. [156] proposed an approach to select the maximum allowed VL bandwidth for PFCs. It was noticed that with a smaller SCR, the maximum allowed VL bandwidth is decreased, which is also revealed by (5.31). However, the influence of the CL bandwidth on the maximum allowed VL bandwidth was overlooked. Such an influence of the CL bandwidth on the upper limit of the PLL bandwidth and the VL bandwidth can be seen in the simulation shown in Fig. 5.9 since the PFC loses stability once the CL bandwidth is reduced.

## 5.5 VALIDATIONS

The analytically derived upper limits of the PLL bandwidth and VL bandwidth are validated by experiments using the setup shown in Fig. 5.15. The Cinergia grid emulator is used to

generate the three-phase grid voltage. The Imperix power test bench mimics a 10-kW EV charger PFC whose power filter is an LC filter. After the PFC, a DC load is connected to emulate the load. The specifications of the PFC in the experiment are given in Table 5.1 as Design 3. Three 14.4-mH inductors are used to emulate a grid with an SCR of 3.5.

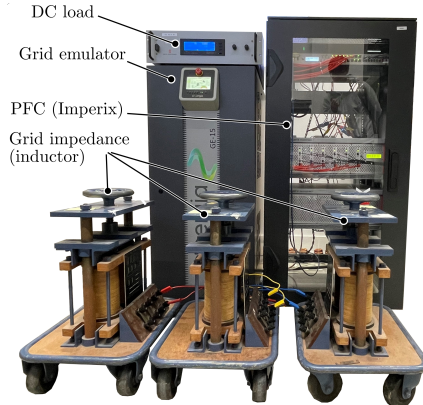


Figure 5.15: Setup for the experimental verification.

During the experiment, the CL bandwidth is fixed at a certain frequency. Then, the PLL bandwidth and the VL bandwidth are increased by 5 Hz each time until instability happens to verify the calculated upper limit. To demonstrate how instability happens once the bandwidth reaches its upper limit, the transient of increasing the PLL bandwidth to its upper limit is shown in Fig. 5.16. As seen, before  $t_0$ , the CL, PLL, and VL bandwidth are 500 Hz, 50 Hz, and 20 Hz, respectively. At  $t_0$ , only the PLL bandwidth  $f_{cpll}$  is increased from 50 Hz to 105 Hz. Then, the PFC loses stability and eventually trips at  $t_1$ , which can be seen from the unregulated  $u_{dc}$  and ripple-free current waveform. Again, note the experiment is conducted at zero operating power because it is the worst case for the PLL-related stability.

In the experiment shown in Fig. 5.16b, the bandwidth of the control loops is kept the same as those in the first example. However, this time, the operating power is at the maximum, namely 10 kW, which is the worst case for the VL-related stability. Similarly, at  $t_0$ , only the VL bandwidth  $f_{cv}$  is increased from 20 Hz to 40 Hz. Then, the PFC loses stability and eventually trips at  $t_1$ , which can be seen from the unregulated  $u_{dc}$ .

The upper limits of the PLL and VL bandwidth in cases of different CL bandwidths are summarized in Fig. 5.17. The measured results show a good match with the calculations. The errors of the analytical calculations are not problematic for stability after leaving a 3-6 dB GM as explained in Section 5.4.3. However, if the control of the EV charger is not the mainstream cascade control method shown in Fig. 5.1 so that the impedance model of the PFC is different, the obtained upper limits might be invalid. In this case, one should establish the impedance model and apply GNC to analyze if the controllers are properly tuned.

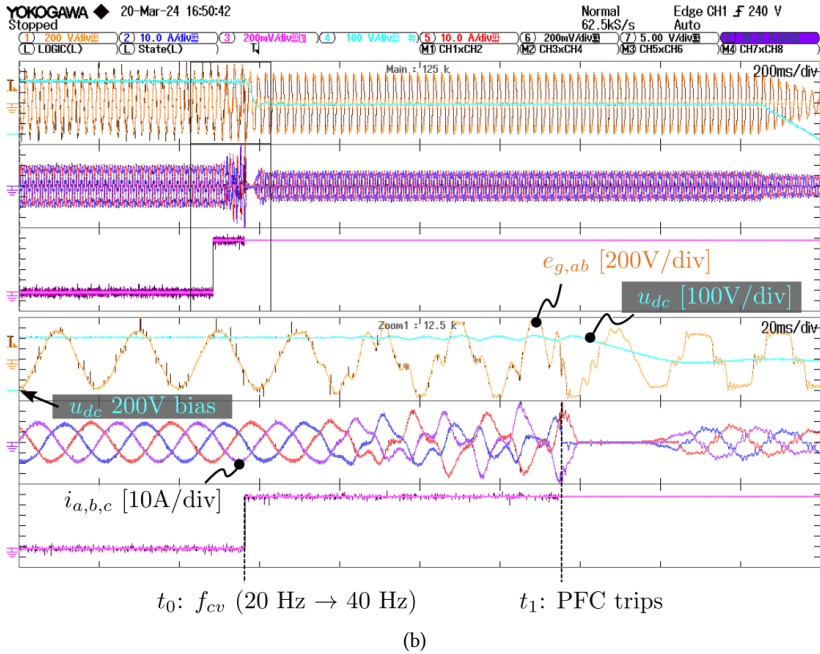
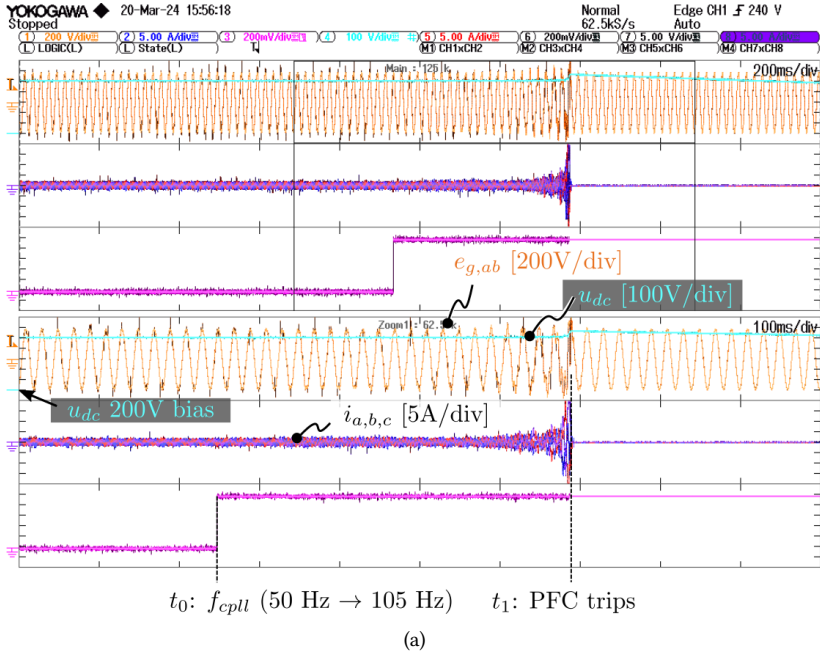


Figure 5.16: Experimental validation of (a) the upper limit of the PLL bandwidth calculated with (5.30) and (b) the upper limit of the VL bandwidth calculated with (5.31).

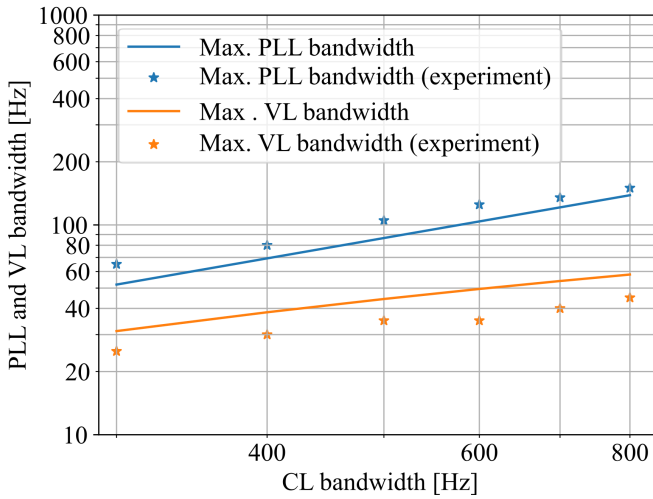


Figure 5.17: Validation of the upper limit of the PLL and VL bandwidth

## 5.6 CONCLUSION

An analytic design approach for the typical PFC control of an EV charger with a weak grid connection was presented. Based on the simplified impedance model, the upper limits of the PLL bandwidth and VL bandwidth, which ensure small signal stability in the whole charging session, were derived analytically and validated with the simulations and experiments. Accordingly, the influences of the CL bandwidth, the filter inductance, and the SCR, on the maximum allowed PLL bandwidth and VL bandwidth, are quantified. Based on the obtained upper limits, a design procedure is proposed, which ensures small signal stability without excessively compromising the PLL bandwidth and the VL bandwidth. The proposed design procedure prevents tuning by trials and errors and does not require establishing the impedance model, which makes the controller tuning much easier.



# 6

## ONSITE BESS FOR ENHANCING SYSTEM INERTIA

*A BESS is typically installed inside an EV fast charging station to shave the pulsating load profile of the fast charging. To maximize the usage of the installed BESS, enabling its multi-functionalities is crucial. As one of the important functionalities, using BESS to provide frequency control service is deemed a promising solution for maintaining the grid frequency of a more power-electronics-based system in the future. Thus, this chapter discusses leveraging the BESS to provide frequency control service for the grid. Especially, the focus is on using BESS to provide synthetic inertia (SI). After discussing the essence of SI, how to control BESS to provide SI better is revealed. Simulations with an IEEE 14 bus system are carried out to verify the analysis.*

## 6.1 INTRODUCTION

The charging power of a high-power charger shows an extremely uneven distribution on time. For example, the charging profile of the Tesla V3 supercharger is shown in Fig. 6.1 [6]. On top of that, the charging event is highly random making it difficult for grid operators to predict every single charging event. These characteristics of EV charging make the grid frequency very likely to be influenced if massive EV chargers are connected to grids.

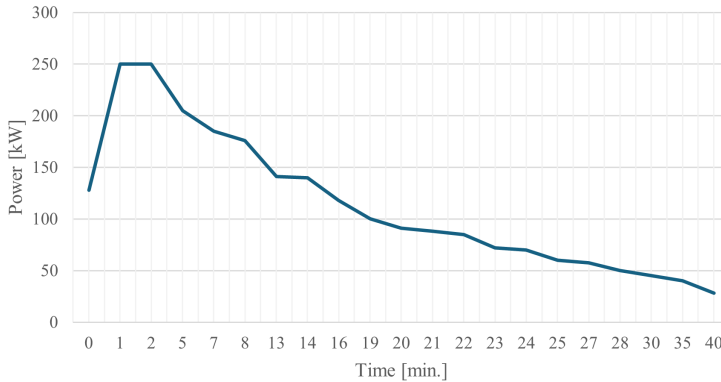


Figure 6.1: Charging profile of a Tesla model 3 when using V3 supercharger [6].

One promising solution to reduce the impacts of EV charging on the grid frequency is installing a battery energy storage system (BESS) in the EV fast charging station. Besides, the BESS can also prevent upgrading the costly grid infrastructure and increasing the revenues of the fast charging station[161]. How to control BESS to provide different ancillary services to support the grid frequency is widely discussed in the literature [162]. Among the different ancillary services, providing inertia is a crucial one since a BESS, which does not have a rotating mass as the one of a synchronous generator (SG), lacks it fundamentally. As system inertia plays an important role in limiting the rate of change of frequency (RoCoF) and the nadir frequency after a contingency event, such as the loss of a generator, replacing the SGs that have physical inertia with the BESS that does not have physical inertia poses a risk of reducing the system inertia and less ability to maintain the grid frequency. However, amid the increasing penetration of CBRs including BESSs, more and more SGs are replaced by power electronics converters, which is deemed a threat to system inertia and frequency stability. Concerns about decreasing system inertia are pervasive.

The solution lies in the problem. Given the fast response speed of CBRs, they can be controlled to mimic the inertia of SGs. For example, among different approaches, one of the widely adopted control strategies is the virtual synchronous machine (VSM) whose control block diagram is illustrated in Fig. 6.2. The inertia mimicked by CBRs is thereby called synthetic inertia (SI).

Although the concept of SI has existed for a while, how to quantify the contribution of the SI to system inertia is still unclear. The problem lies in the unclear definition of SI. Although the controller parameters  $H$  in Fig. 6.2 are normally treated equally to the SI

provided by the converter, it is hard to be convincing because the controller parameters are inherently virtual and adjustable. A method to quantify the SI based on a generator’s input and output power is needed.

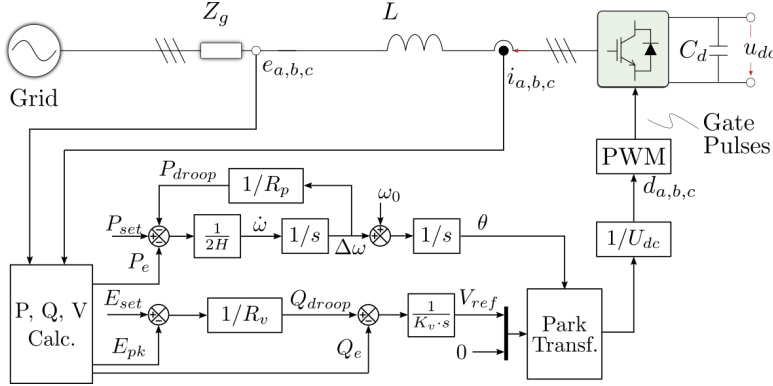


Figure 6.2: Virtual synchronous machine control block diagram.

To fill in the gap, this chapter provides a definition of SI from a power and energy perspective. It is aimed to reveal the essence of SI. Besides, an approach to quantify the SI from the power and energy perspective is proposed. On top of that, how to modify the conventional VSM control to leverage an CBR to provide SI is discussed.

## 6.2 REVISIT SYNCHRONOUS GENERATOR INERTIA

In this section, we will revisit the model of a conventional generation unit including a synchronous generator and its governor. On top of that, the importance of inertia in frequency regulation will be discussed.

### 6.2.1 MODEL OF A SYNCHRONOUS GENERATOR

Despite the differences in the type of turbine system, the frequency control system of an SG-based generation unit can be modeled generally as the one shown in Fig. 6.3 [163].  $P_{set}$  is the active power set-point or the dispatch active power of the SG,  $R$  is the  $P - f$  droop coefficient,  $H_{sg}$  is the inertia constant of the SG whose unit is in second,  $\omega_0$  is the nominal grid angular frequency,  $P_m$  is the mechanical power from the governor,  $P_e$  is the electrical power of the SG,  $\theta$  is the electrical angle of the SG, and  $G_{gov}(s)$  is the transfer function of the governor response [163].

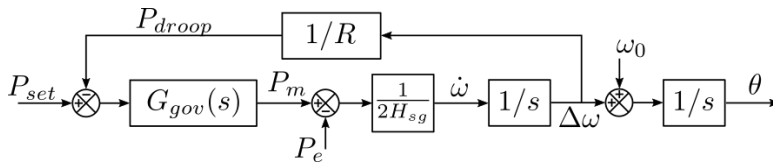


Figure 6.3: Frequency control block diagram of a synchronous-generator-based generation unit.



Depending on the type of the turbine system, e.g., reheat steam turbine and hydraulic turbine,  $G_{gov}(s)$  can be modeled differently. The response speed of the turbine output power is dominated by the most sluggish process in the control loop. According to the widely adopted governor and turbine model [163],  $G_{gov}(s)$  can be generally approximated as a lead-lag filter for all types of governor, which is given by

$$G_{gov}(s) = \frac{kT_r s + 1}{T_r s + 1}, \quad (6.1)$$

where  $k$  is a coefficient smaller than one and  $T_r$  is the time constant of the lead-lag filter.

### 6.2.2 FREQUENCY RESPONSE OF SYNCHRONOUS GENERATORS

The importance of an SG's inertia to maintaining power system frequency is reflected in a typical contingency event as illustrated in Fig. 6.4. Due to unexpected load increases and generation losses at  $t_0$ , the SG's electrical frequency starts decreasing and reaches the nadir at  $t_1$  when the SG's mechanical power  $P_m$  reaches its electrical power  $P_e$  for the first time. Because of the slow response of the governor, the additional mechanical power  $\Delta P_m$  brought by the primary frequency control increases slowly. The gap  $\Delta P$  between the  $P_m$  and the  $P_e$  is filled by the inertia power on the price of decreasing the electrical frequency.

6

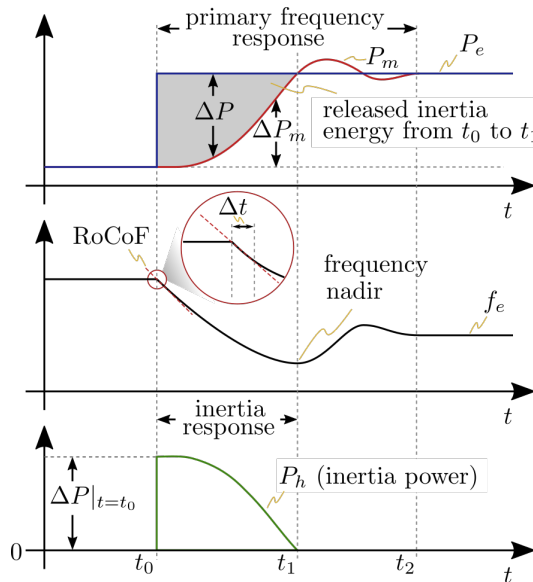


Figure 6.4: Frequency response of an SG after a contingency event.

The frequency response depicted in Fig. 6.4 can be the frequency response of either one SG or a power system with many SGs. In the case of the latter, the  $P_m$  is the total mechanical power of all generation units,  $P_e$  is the total change of the electrical power, the frequency  $f_e$  is the frequency of the center of inertia (COI) [164], and the inertia of the

system  $H_{sys}$  is the sum of the inertia of all SGs, which is given by

$$H_{sys} = \frac{\sum_i^N S_i \cdot H_{sg,i}}{S_{sys}}, \quad (6.2)$$

where  $S_{sys}$  is the summation of the apparent power of all SGs,  $S_i$  is the apparent power of the  $i$ -th SG, and  $H_{sg,i}$  is the inertia constant of the  $i$ -th SG rated to  $S_i$ . Similarly, the block diagram shown in Fig. 6.3 can be either the model of one SG or the model of a power system with many SGs. In the case of the latter,  $G_{gov}(s)$  is the governor response of the system, which is the averaged summation of the governor response of each SG in the system.  $H_{sg}$  shall be replaced by  $H_{sys}$  and the frequency in the block diagram is the frequency of the COI, namely  $\omega_{COI}$ .

To reveal the influence of system inertia on the nadir frequency, the transfer function from the electrical power change  $\Delta P_e$  to the frequency change  $\Delta\omega$  is derived according to the block diagram in Fig. 6.3, which is obtained as

$$\frac{\Delta\omega_{COI}}{\Delta P_e} = -\frac{1}{s + \frac{1}{2RH_{sys}}G_{gov}(s)} \cdot R. \quad (6.3)$$

Assuming  $T = \frac{1}{2RH_{sys}}$  and substituting (6.1) into (6.3), we obtain

$$\frac{\Delta\omega_{COI}}{\Delta P_e} = -R \cdot \frac{Ts + \frac{T}{T_r}}{s^2 + (\frac{1}{T_r} + kT)s + \frac{T}{T_r}}. \quad (6.4)$$

The above equation can be transformed to a standard transfer function of a second-order system by defining

$$\zeta = \frac{1 + kTT_r}{2\sqrt{TT_r}} = \frac{2RH_{sys} + kT_r}{2\sqrt{2RH_{sys}T_r}}, \quad (6.5)$$

$$\omega_n = \sqrt{\frac{T}{T_r}} = \sqrt{\frac{1}{2RH_{sys}T_r}}. \quad (6.6)$$

As a result, (6.4) can be rewritten as

$$\frac{\Delta\omega_{COI}}{\Delta P_e} = -T \cdot R \cdot \frac{s + \frac{\omega_n^2}{T}}{s^2 + 2\zeta\omega_n s + \omega_n^2}. \quad (6.7)$$

When a contingency event happens, the power system is subjected to a step change in electrical power  $\Delta P_e$ , and the response of  $\Delta\omega_{COI}$  is obtained as

$$\Delta\omega_{COI}(s) = -T \cdot R \cdot \frac{s + \frac{\omega_n^2}{T}}{s^2 + 2\zeta\omega_n s + \omega_n^2} \cdot \frac{\Delta P_e}{s}. \quad (6.8)$$

Equation (6.8) can be rearranged as

$$\Delta\omega_{COI}(s) = -R \cdot \Delta P_e \cdot \left( \frac{1}{s} - \frac{s + \zeta\omega_n}{s^2 + 2\zeta\omega_n s + \omega_n^2} - \frac{\zeta\omega_n - T}{s^2 + 2\zeta\omega_n s + \omega_n^2} \right). \quad (6.9)$$

According to the typical values of the parameters of a governor and turbine system [163], the following inequalities exist

$$\zeta < 1, \quad k \cdot T_r > 1. \quad (6.10)$$

Therefore, the frequency response of an SG-based power system is typically an under-damped system, which has a nadir. Assuming the damped frequency is  $\omega_d = \omega_n \cdot \sqrt{1 - \zeta^2}$  and applying the inverse Laplace transform to (6.9), the time domain response of  $\Delta\omega_{COI}$  can be obtained as

$$\begin{aligned} \Delta\omega_{COI}(t) &= -R \cdot \Delta P_e \cdot [1 - e^{-\zeta\omega_n t} \cdot (\cos(\omega_d t) - \underbrace{\frac{T_r\omega_n - \zeta}{\sqrt{1 - \zeta^2}}}_m \cdot \sin(\omega_d t))] \\ &= -R \cdot \Delta P_e \cdot [1 - e^{-\zeta\omega_n t} \cdot \sqrt{1 + m^2} \cdot \sin(\omega_d t + \pi - \tan^{-1} \frac{1}{m})] \end{aligned} \quad (6.11)$$

Given the typical parameter values [163] listed in Table 6.1, the response curve given by (6.11) assuming a load step  $\Delta P_e = 0.1$  at  $t = 0$  is illustrated in Fig. 6.5

Table 6.1: Typical parameter values of an SG-based generation unit [163]

k	$T_r$	R	H
0.3	7	0.05	5

6

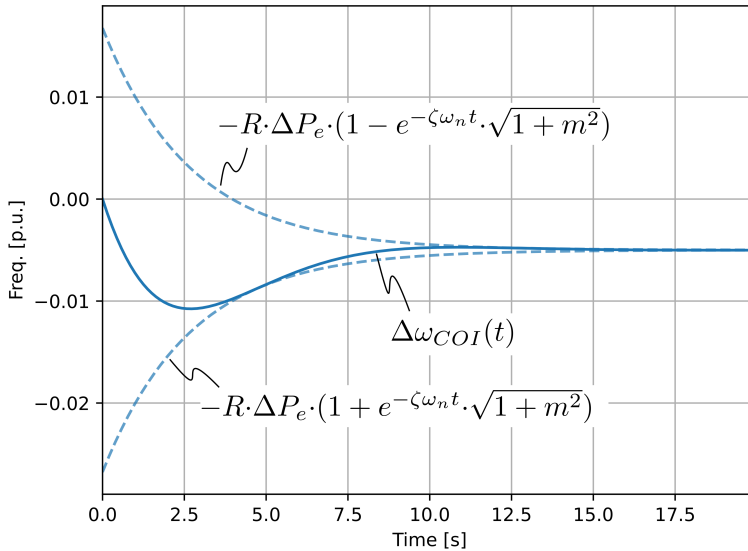


Figure 6.5: Response of  $\Delta\omega_{COI}(t)$  given by (6.11) based on the typical values of an SG-based generation unit in Table 6.1.

The derivative of  $\Delta\omega_{COI}(t)$  can be derived from (6.11), which is obtained as

$$\begin{aligned} \frac{d\Delta\omega_{COI}(t)}{dt} &= -R\cdot\Delta P_e\cdot\zeta\cdot\omega_n\cdot e^{-\zeta\omega_n t}\cdot(\cos(\omega_d t) - m\cdot\sin(\omega_d t)) \\ &\quad - R\cdot\Delta P_e\cdot e^{-\zeta\omega_n t}\cdot(\omega_d\cdot\sin(\omega_d t) + m\cdot\omega_d\cdot\cos(\omega_d t)) \end{aligned} \quad (6.12)$$

Substituting the expression of  $m$  into the equation above, the final simplified result of (6.12) is obtained as

$$\begin{aligned} \frac{d\Delta\omega_{COI}(t)}{dt} &= -R\cdot\Delta P_e\cdot e^{-\zeta\omega_n t}\cdot\left[T\cdot\cos(\omega_d t) - \underbrace{\frac{T\zeta - \omega_n}{\sqrt{1-\zeta^2}}}_{a}\cdot\sin(\omega_d t)\right] \\ &= -R\cdot\Delta P_e\cdot e^{-\zeta\omega_n t}\cdot\sqrt{a^2 + T^2}\cdot\sin(\omega_d t + \pi - \tan^{-1}\frac{T}{a}) \end{aligned} \quad (6.13)$$

Thus, the derivative of  $\Delta\omega_{COI}(t)$  equals zero when

$$\omega_d t + \pi - \tan^{-1}\frac{T}{a} = 0, \pi, 2\pi, \dots \quad (6.14)$$

Since the nadir frequency is the first peak undershoot of  $\Delta\omega_{COI}(t)$ , the time point  $t_{nadir}$  when the frequency reaches the nadir can be obtained as

$$t_{nadir} = \frac{\tan^{-1}\frac{T}{a}}{\omega_d} \quad (6.15)$$

Substituting the expression of  $a$  and  $\omega_d$  into (6.15), it is noted that  $t_{nadir}$  can be expressed as a function of  $T$ , which is obtained as

$$t_{nadir}(T) = \frac{2\cdot T_r\cdot\tan^{-1}\frac{\sqrt{4T\cdot T_r - (1+k\cdot T\cdot T_r)^2}}{k\cdot T\cdot T_r - 1}}{\sqrt{4T\cdot T_r - (1+k\cdot T\cdot T_r)^2}} \quad (6.16)$$

The derivative of  $t_{nadir}(T)$  is obtained as

$$\begin{aligned} \frac{dt_{nadir}(T)}{dT} &= -\frac{T_r}{T\cdot(4T\cdot T_r - (1+k\cdot T\cdot T_r)^2)^2}\cdot\left[(4T\cdot T_r - (1+k\cdot T\cdot T_r)^2)\cdot(k\cdot T\cdot T_r + 1) \right. \\ &\quad \left. + 2\cdot T\cdot T_r\cdot\underbrace{(2-k\cdot(k\cdot T\cdot T_r + 1))}_n\cdot\sqrt{4T\cdot T_r - (1+k\cdot T\cdot T_r)^2}\cdot\tan^{-1}\frac{\sqrt{4T\cdot T_r - (1+k\cdot T\cdot T_r)^2}}{k\cdot T\cdot T_r - 1}\right]. \end{aligned} \quad (6.17)$$

It can be seen that the derivative of  $t_{nadir}(T)$  is negative if  $n \geq 0$ . When  $n < 0$ , according to  $\tan^{-1}(x) \leq x$  ( $x > 0$ ), we have

$$\begin{aligned} \frac{dt_{nadir}(T)}{dT} &\leq -\frac{T_r}{T\cdot(4T\cdot T_r - (1+k\cdot T\cdot T_r)^2)^2}\cdot\left[(4T\cdot T_r - (1+k\cdot T\cdot T_r)^2)\cdot(k\cdot T\cdot T_r + 1) \right. \\ &\quad \left. + 2\cdot T\cdot T_r\cdot(2-k\cdot(k\cdot T\cdot T_r + 1))\cdot\sqrt{4T\cdot T_r - (1+k\cdot T\cdot T_r)^2}\cdot\frac{\sqrt{4T\cdot T_r - (1+k\cdot T\cdot T_r)^2}}{k\cdot T\cdot T_r - 1}\right] \\ \implies \frac{dt_{nadir}(T)}{dT} &\leq -\frac{T_r}{T\cdot(k\cdot T\cdot T_r - 1)} < 0. \end{aligned} \quad (6.18)$$

Therefore, the derivative of  $t_{nadir}(T)$  is strictly negative when the condition of (6.10) is satisfied. Hence, for a typical power system, the higher the system inertia  $H_{sys}$  is, the smaller the  $T$  is and the larger the  $t_{nadir}$  is, which indicates that it takes a longer time to reach the nadir frequency. Hence, a higher  $H_{sys}$  is preferred since it leaves more time for the primary frequency control to react.

Then, substituting (6.15) into (6.11), the nadir frequency is calculated as

$$\Delta\omega_{COI}|_{t=t_{nadir}} = -R \cdot \Delta P_e \cdot \left[ 1 - e^{-\zeta \cdot \omega_n \cdot t_{nadir}} \cdot \frac{a - m \cdot T}{\sqrt{a^2 + T^2}} \right]. \quad (6.19)$$

Substituting the expression of  $a$  and  $m$  into (6.19), it can be derived that

$$\Delta\omega_{COI}|_{t=t_{nadir}} = -R \cdot \Delta P_e \cdot \left[ 1 + e^{-\zeta \cdot \omega_n \cdot t_{nadir}} \cdot \sqrt{T \cdot T_r \cdot (1 - k)} \right]. \quad (6.20)$$

(6.20) indicates  $\Delta\omega_{COI,lev}|_{t=t_{nadir}}$  can be expressed as a function of  $T$ , whose derivative is obtained as

$$\begin{aligned} \frac{d\Delta\omega_{COI,lev}|_{t=t_{nadir}}(T)}{dT} &= R \cdot \Delta P_e \cdot e^{-\zeta \omega_n t} \cdot \sqrt{T \cdot T_r \cdot (1 - k)} \\ &\quad \cdot \left( \omega_n \cdot t_{nadir} \cdot \frac{d\zeta}{dT} + \zeta \cdot t_{nadir} \cdot \frac{d\omega_n}{dT} + \omega_n \cdot \zeta \cdot \frac{dt_{nadir}}{dT} - \frac{1}{2 \cdot T} \right). \end{aligned} \quad (6.21)$$

(6.21) can be finally simplified as

$$\frac{d\Delta\omega_{COI,lev}|_{t=t_{nadir}}(T)}{dT} = R \cdot \Delta P_e \cdot e^{-\zeta \omega_n t} \cdot \frac{\sqrt{T \cdot T_r \cdot (1 - k)}}{4 \cdot T \cdot T_r - (1 + k \cdot T \cdot T_r)^2} \cdot [(k \cdot T \cdot T_r - 1) \cdot t_{nadir} - 2 \cdot T_r]. \quad (6.22)$$

According to (6.16) and  $\tan^{-1}(x) \leq x$  ( $x > 0$ ), it can be obtained that

$$\begin{aligned} \frac{d\Delta\omega_{COI,lev}|_{t=t_{nadir}}(T)}{dT} &\leq R \cdot \Delta P_e \cdot e^{-\zeta \omega_n t} \cdot \frac{\sqrt{T \cdot T_r \cdot (1 - k)}}{4 \cdot T \cdot T_r - (1 + k \cdot T \cdot T_r)^2} \cdot \underbrace{[(k \cdot T \cdot T_r - 1) \cdot \frac{2 \cdot T_r}{k \cdot T \cdot T_r - 1} - 2 \cdot T_r]}_{=0} \\ &= 0. \end{aligned} \quad (6.23)$$

Hence, (6.23) strictly proves that increasing  $H_{sys}$  can decrease the  $T$  and increase the nadir frequency. Based on the example given in Fig. 6.5, the influence of  $H_{sys}$  on the frequency response is illustrated in Fig. 6.6, which proves that a higher  $H_{sys}$  leads to a higher nadir frequency and a larger  $t_{nadir}$ .

The RoCoF at the instance  $t = t_0$  when the load step  $\Delta P_e$  happens can be simply obtained by assuming  $P_m$  does not change at  $t = t_0$ . Therefore, it can be obtained that

$$\text{RoCoF} = \frac{d\Delta\omega_{COI}|_{t=t_0}}{dt} = \frac{\Delta P_e}{2 \cdot H_{sys}}. \quad (6.24)$$

Hence, increasing the system inertia  $H_{sys}$  can also reduce the RoCoF.

In summary, the discussion presented in this sub-section reveals that increasing the system inertia can increase the nadir frequency and reduce the RoCoF during a contingency event. It is worth mentioning that the obtained conclusion is also applicable to an individual SG since the models used for an SG and a power system with many SGs are interchangeable.

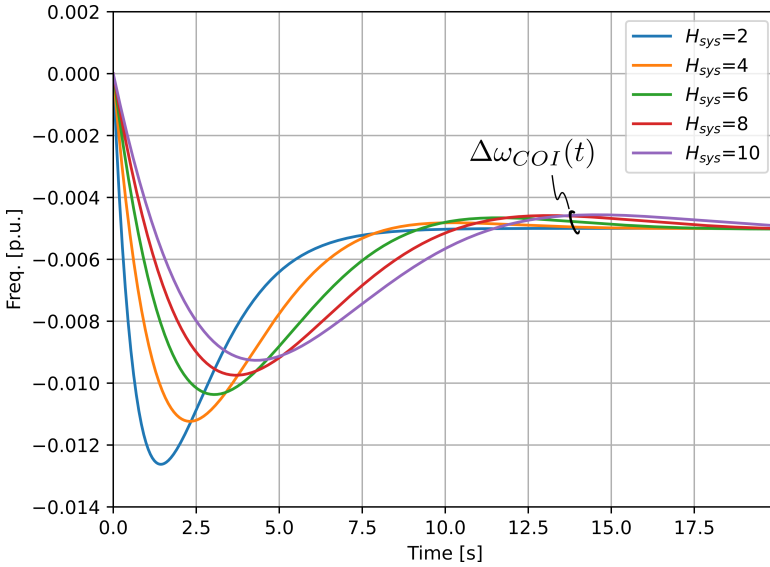


Figure 6.6: Influence of the system inertia  $H_{sys}$  on the frequency response.

### 6.2.3 APPROACHES TO ESTIMATING THE INERTIA OF A SYNCHRONOUS GENERATOR

6

According to the influence of the inertia of an SG on its frequency response during a contingency event, the inertia can be estimated via the frequency response curve in two different approaches. The first one is based on the RoCoF. Since the RoCoF is not directly measurable, it is approximated with the frequency change within a short period after the contingency event. Thus, assuming the frequency response of the SG is the one depicted in Fig. 6.4, the  $H$  of the SG is practically approximated as

$$H = \frac{f_n}{2 \cdot S_n} \cdot \frac{\Delta \bar{P}_e|_{t=t_0}^{t=t_0+\Delta t}}{f_e|_{t=t_0} - f_e|_{t=t_0+\Delta t}} \cdot \Delta t, \quad (6.25)$$

where  $f_e|_{t=t_0}$  is the electrical frequency at  $t_0$ ,  $H$  is the SG's inertia constant in s,  $f_n$  is the SG's nominal electrical frequency in Hz, and  $S_n$  is the SG's nominal apparent power in VA [163].  $\Delta t$  is a small time step.  $\Delta \bar{P}_e|_{t=t_0}^{t=t_0+\Delta t}$  is the average of  $\Delta P_e$  within  $\Delta t$  after the contingency event. The time window width  $\Delta t$  to calculate the RoCoF and the  $H$  should not be too large otherwise the increase of  $P_m$  within  $\Delta t$  cannot be neglected, which may lead to a bigger estimated  $H$  than the exact one. However,  $\Delta t$  should also be not too small to properly filter measurement noises. Currently, the selection of  $\Delta t$  is different from approximately 0.1-0.5 seconds in different grid codes.

Alternatively, the inertia can also be calculated from an energy perspective. Based on the example shown in Fig. 6.4, the released inertia energy from  $t_0$  to  $t_1$  is represented by the shadow region in Fig. 6.4. Accordingly, the  $H$  can be obtained as

$$H = \frac{f_n^2}{S_n} \cdot \frac{\int_{t_0}^{t_1} (P_e(t) - P_m(t)) dt}{f_e^2|_{t=t_0} - f_e^2|_{t=t_1}} \quad (6.26)$$

For an SG with a rotating mass, (6.25) and (6.26) are equivalent to each other. However, the former one given by (6.25) focuses more on limiting RoCoF whereas the latter one focuses more on increasing the nadir frequency. Such a difference between the two leads to two different measurables to estimate the inertia of a generation unit. Considering a fixed frequency response profile after a contingency event, the measurables for both approaches are given in Table 6.2.

Table 6.2: Measurables of inertia in the two estimation approaches

Name	Method	Measurable
Approach 1	Equation (6.25)	The total energy released to fill the gap between the electrical energy and the mechanical energy within $\Delta t$ after $t_0$ .
Approach 2	Equation (6.26)	The total energy released to fill the gap between the electrical energy and the mechanical energy between $t_0$ and $t_1$ .

Note: The statement is based on assuming the frequency response profile is fixed.

As seen, the two measurables are both related to the energy released by the inertia. However, their time scale is different. Besides, different challenges are encountered when applying the two approaches in practice. For the first one, the challenge comes from how to properly select the time window  $\Delta t$  to calculate the RoCoF. As for the second one, the difficulty stems from that it requires measuring the output mechanical power of the turbine, which, however, is normally not measured.

In order to compare the differences between the two approaches to estimating the inertia of a generation unit, a simulation based on an IEEE 14-bus system is carried out. The structure of the system is illustrated in Fig. 6.7.

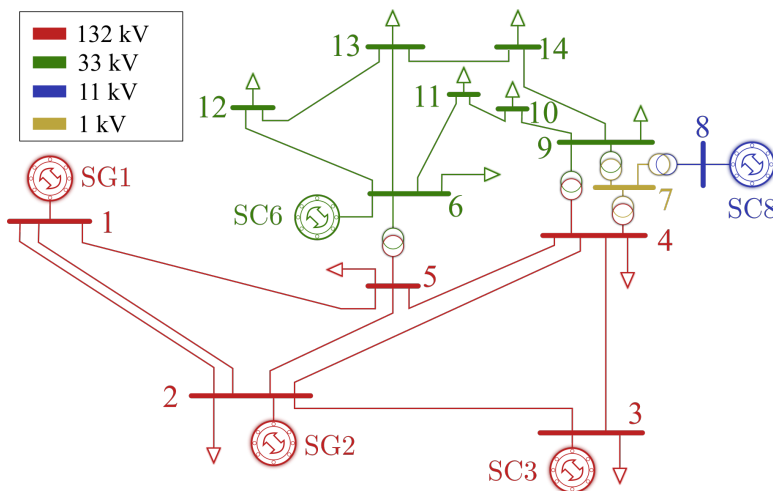


Figure 6.7: IEEE 14 bus benchmark system.

As seen, in the system, there are two SGs connected to Bus 1 and Bus 2. Besides, three synchronous condensers (SCs) are connected to Bus 3, Bus 6, and Bus 8, respectively. The ratings, dispatch, and inertia of the SGs and the SC3 are summarized in Table 6.3.

Table 6.3: Information of the SGs and SCs in the simulation

	Apparent Power (MVA)	Power Factor	Inertia Constant (s)	Dispatch $P$ (MW)	Dispatch $Q$ (Mvar)	Bus Voltage (p.u.)
SG1	400	0.8	4	190.5	-7.7	1.06
SG2	200	0.8	4	80	27	1.04
SC3	100	1	5	0	23.3	1.01
SC6	28	1	5	0	12.2	1.07
SC8	100	1	5	0	17.3	1.09

In the simulation, SG2 trips at  $t = 70$  s. The response of the  $f_{COI}$  and the responses of the SG1, SC3, SC6, and SC8 are depicted in Fig. 6.8.

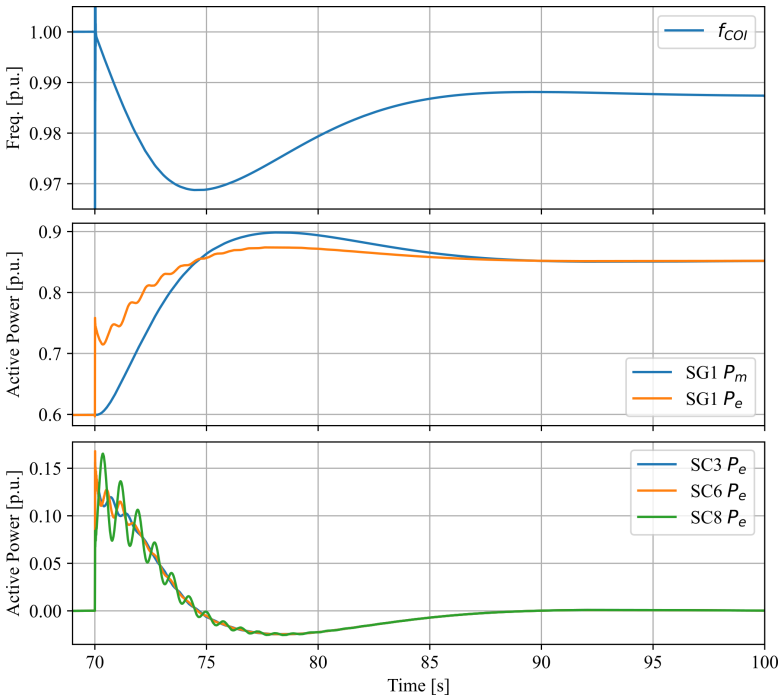


Figure 6.8: Frequency response of the system and the active power responses of the SG1 and the three SC3 after losing the SG2 at  $t = 70$  s.

Since after losing the SG2 the SG1 is the only SG in the system, the frequency  $f_{COI}$  reaches its nadir when the  $P_m$  of the SG1 increases enough to supply the total loads in the system. According to the active power responses shown in Fig. 6.8, the inertia of the SG1, the SC3, the SC6, and the SC8 can be estimated using Approach 1 and Approach 2. The results are compared in Table 6.4. Generally, the results obtained from Approach 2 are



more accurate since it is less influenced by the fluctuation in the responding active power. However, when the mechanical power of the turbine is not measured, namely without knowing the curve of  $P_m$ , Approach 2 cannot be applied.

Table 6.4: Comparison of the accuracy of the two approaches to estimating the inertia

	Exact	Approach 1 Estimation	Approach 2 Estimation
SG1	4	4.001	3.988
SG3	5	4.871	5.006
SG6	5	4.915	5.005
SG8	5	5.3	5.006

Despite the difference between the two approaches, there are no significant differences between the two estimated inertia constants in this case study. However, both of them encounter challenges when estimating the synthetic inertia provided by a grid-tied power electronic converter. The first one only evaluates the output power of the generation unit within a short period  $\Delta t$  after the contingency event. It will not bring problems when evaluating the inertia of an SG because the inertia of the rotating mass cannot be changed. However, for a converter, the controller parameters dominate how much inertia the converter provides and can be time-variant. Therefore, it is not sufficient to use the output power only within  $\Delta t$  after the contingency event to evaluate the synthetic inertia the converter provides. As for the second approach, the challenge stems from the fact that the converter naturally does not have mechanical power. Hence, the second approach cannot be applied when evaluating the inertia provided by a converter.

## 6

### 6.3 PROPOSED SYNTHETIC INERTIA ESTIMATION APPROACH

#### 6.3.1 APPROXIMATE INERTIA POWER WITHOUT MEASURING MECHANICAL POWER

The previous discussion reveals that inertia power is needed to reduce the frequency deviation caused by the active power imbalance because the mechanical power of SGs cannot immediately follow the change in the electrical power. The released inertia power shows a pattern related to the frequency responding profile after a contingency event. For example, as seen from the inertia power released by SC3, SC6, and SC8 depicted in Fig. 6.8, the inertia power reaches the maximum just after the contingency event and becomes zero when the frequency reaches the nadir. This pattern is also reflected by the formula to calculate the inertia power, which is given by

$$P_{inertia} = J \cdot \dot{\omega} \cdot \omega, \quad (6.27)$$

where  $J$  is the rotational inertia of the generator,  $\dot{\omega}$  is the rate of change of angular frequency, and  $\omega$  is the angular frequency. Clearly,  $\omega$  and  $\dot{\omega}$  are both the highest just after the contingency event. Considering the change in  $\omega$  is not significant, the inertia power can be approximated by changing the exact  $\omega$  to the nominal one  $\omega_n$ . Consequently, the inertia power is obtained as

$$P_{inertia} = \frac{2 \cdot H \cdot S_n}{\omega_n} \cdot \dot{\omega}. \quad (6.28)$$

Therefore, once the inertia constant  $H$  and the apparent power capacity are fixed, the inertia power released by the generator is only determined by  $\dot{\omega}$ . Considering that  $\dot{\omega}$  is calculated with the frequency change in a time window  $\Delta t$  in practice to filter out the fluctuations, the averaged inertia power in each  $\Delta t$  time window can be approximated as

$$\bar{P}_{inertia}|_{t_i}^{t_i+\Delta t} = \frac{2 \cdot H \cdot S_n}{\omega_n} \cdot \frac{\omega(t_i + \Delta t) - \omega(t_i)}{\Delta t}, \quad (6.29)$$

where  $t_i$  is the start point of the  $i$ -th time window.

Based on (6.29), the inertia power released by a generator with a rotating mass can be approximated without knowing the mechanical power once knowing the profile of the frequency and the electrical power. The inertia constant  $H$  can be estimated from (6.25). Then, the inertia power pattern before reaching the nadir frequency can be approximated. For example, considering a case where the RoCoF is calculated using a 0.5-s time window, the exact average inertia power profile of SG1 within each 0.5-s time window in the case study in Fig. 6.8 is depicted in Fig. 6.9. Besides, the approximated average inertia power by (6.29) is also depicted. Clearly, the approximated inertia power is highly accurate.

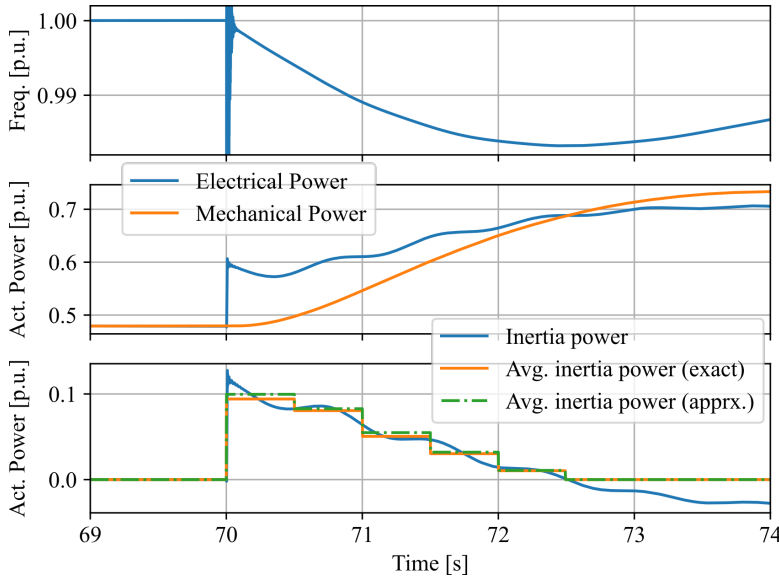


Figure 6.9: Accuracy of the approximated inertia power of the synchronous generator 1 in the IEEE 14 bus system using a 0.5s time window.

### 6.3.2 PROPOSED APPROACH TO ESTIMATING SYNTHETIC INERTIA

The approach to estimating inertia without knowing mechanical power can also be applied to estimate the synthetic inertia of a generation unit without mechanical power, such as a CBR. Specifically, based on the obtained responding frequency curve and the output electrical power curve, the inertia constant  $H$  can be first estimated with (6.25). Then, the inertia power pattern before the nadir frequency can be calculated by using (6.29). The

electrical power released by the CBR cannot be lower than the calculated inertia power. Otherwise, the mimicked synthetic inertia is not equivalent to a real inertia with an inertia constant of  $H$ . A flow chart of the proposed estimation approach is depicted in Fig. 6.10.

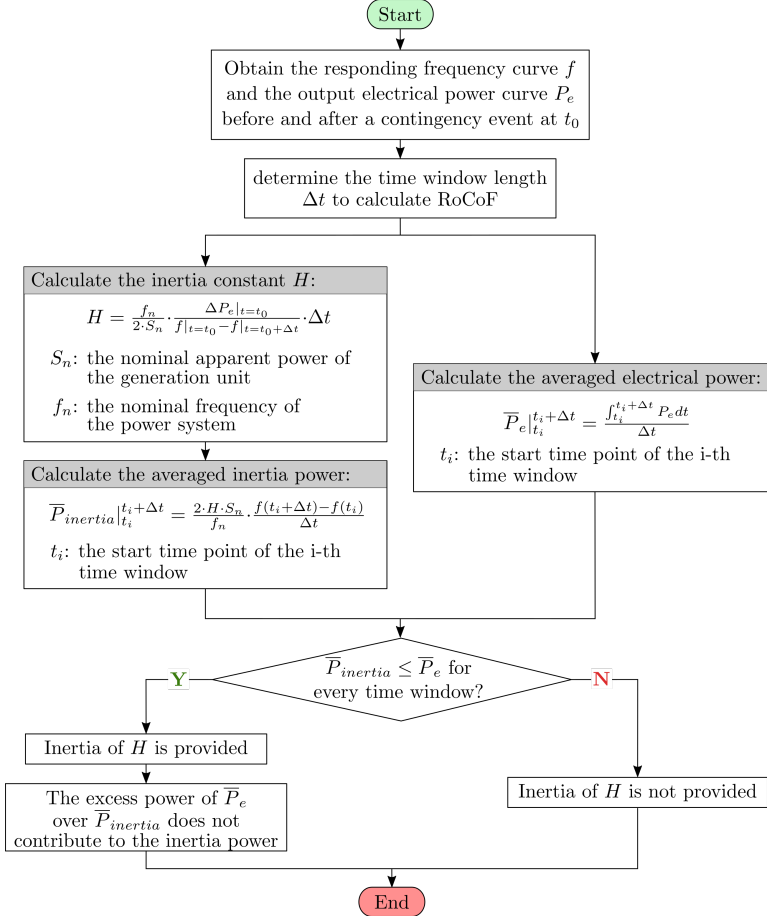


Figure 6.10: Flow chart of the proposed approach to estimating total inertia, namely the summation of physical inertia and synthetic inertia, of a generation unit without knowing or without mechanical power.

It is worth mentioning that an SG can also provide synthetic inertia if the governor response speed of an SG is fast enough so that the mechanical power significantly increases in  $\Delta t$  after the contingency event. A case study is given for clarification. In the case study of the IEEE 14 bus system, the SC6 is changed to an SG by adding a governor and turbine system. For simplicity, the governor and turbine systems of different SGs are all assumed to be the reheat steam type [163] whose block diagram is illustrated in Fig. 6.11.

The specifications of the governor and turbine system of SG1 and SG6 are listed in Table 6.5. The case when the governor of SG6 is inactive is called Case 1 whereas the counterpart is called Case 2. Compared to SG1 whose power capacity is much higher,

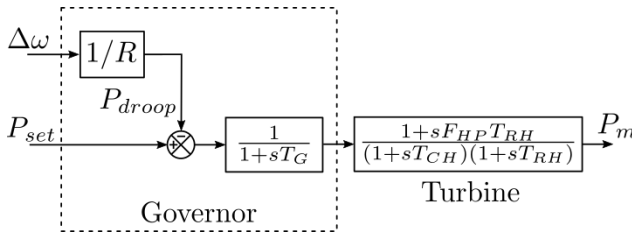


Figure 6.11: Block diagram of the governor and turbine system of a reheat steam type generator.

SG6 has a lower reheat time constant and a larger high-pressure time constant to mimic a governor and turbine system with faster response. In Case 1, the droop coefficient  $R$  of SG6 is zero so the governor is not activated and SG6 is simply an SC. Besides, it is worth mentioning that the droop coefficients are designed to ensure the system has the same frequency containment reserve (FCR). After the tripping of SG2, the system frequency can go back to 49.6 Hz without the secondary frequency control in both cases.

Table 6.5: Specifications of the governor and turbine systems of the synchronous generators in the IEEE 14 bus system study

	$T_G$	$T_{CH}$	$T_{RH}$	$F_{HP}$	$R$	
					Case 1	Case 2
SG1	0.2	0.3	15	0.2	1.6%	2%
SG6	0.2	0.3	5	0.5	0	0.7%

The responses of the frequency of Bus 6 and the active power responses of SG6 in Case 2 are shown in Fig. 6.12. As seen, different from SG1 shown in Fig. 6.9, the estimated average inertia power is larger than the exact one for SG6. This is caused by the fast response speed of the governor of SG6. Within 0.5 seconds after the contingency event at  $t = 70$  s, the governor of SG6 is fast enough to react so that the output electrical power, which is the summation of the inertia power and the mechanical power, is more than the inertia power. Mechanical power, which also contributes to reducing RoCoF, should be counted as synthetic inertia power. Therefore, the total inertia provided by SG6 is the summation of the real inertia and the synthetic inertia. However, it is worth mentioning that the time window length  $\Delta t$  to calculate RoCoF is assumed to be 0.5 seconds in this case, which can be different depending on the need of the grid operator to ensure the system's stability. In the case of a different time window length used, the synthetic inertia provided by the same generation unit is different.

Based on the estimation approach, the total inertia including the physical inertia and the synthetic inertia of SG6 in two cases is shown in Table 6.6, where the physical inertia, RoCoF, and nadir frequency of the measured at the local bus, namely Bus 6, are also shown. As seen, because of the additional synthetic inertia in Case 2, the RoCoF is reduced. However, since the synthetic inertia is not high, the decrease in the RoCoF is not significant. A more significant change is noticed in the nadir frequency. It is increased in Case 2 not only because of the additional synthetic inertia but also because of the fast frequency

response power of SG6, which will be elaborated on in the following subsection.

Table 6.6: Total inertia and physical inertia of SG6, RoCoF, and nadir frequency in Case 1 and Case 2

	Total inertia [s]	Physical inertia [s]	RoCoF [Hz/s]	Nadir frequency [Hz]
Case 1	4.99	5	0.611	49.16
Case 2	5.63	5	0.603	49.23

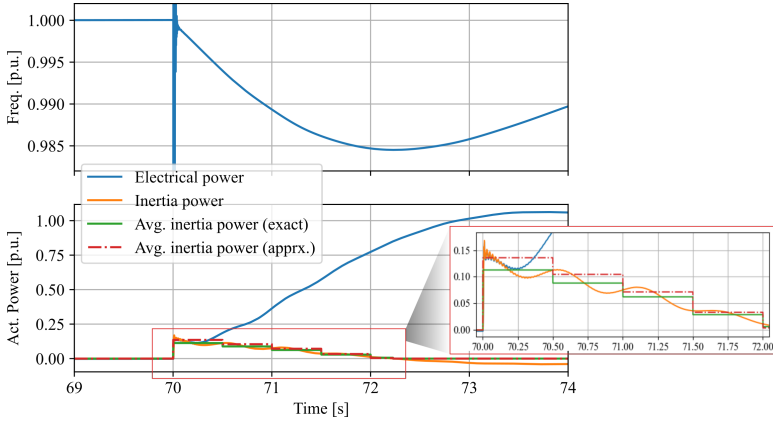


Figure 6.12: Total average power released by both synthetic inertia and physical inertia of SG6 compared to the power released by physical inertia of SG6 in Case 2.

### 6.3.3 DISCUSSION OVER FAST FREQUENCY RESPONSE POWER

The previous study reveals that for an SG the inertia power can be quantified by the difference between the mechanical power and the electrical power before the frequency reaches the nadir. When the mechanical power cannot be directly measured, the inertia power can be estimated with the method illustrated in Fig. 6.10.

Following the same principles, the inertia of a system with many SGs can be estimated. Specifically, the total inertia power of the system equals the difference between the total mechanical power of all SGs in the system and the total electrical power of all SGs in the system. Then, the system inertia can be estimated accordingly, which is obtained as

$$\hat{H}_{sys} = \frac{f_n}{2 \cdot \sum_i^N S_i} \cdot \frac{\sum_i^N \Delta \bar{P}_{e,i}|_{t_0}^{t_0+\Delta t}}{f_{coi}|_{t=t_0} - f_{coi}|_{t=t_0+\Delta t}} \cdot \Delta t, \quad (6.30)$$

where the subscription  $i$  denotes the  $i$ -th SG or SC in the system.  $f_{coi}$  denotes the frequency of the COI. In practice,  $f_{coi}$  can be approximated by the frequency of the bus to which an SG with a big  $H$  is connected. The selected bus frequency should not have significant small oscillations after a contingency event.

The estimated inertia  $H_{sys}$  of the system in Case 1 and Case 2 are 4.47 s and 4.48 s, respectively. Due to the small apparent power capacity of SG 6, the small additional

synthetic inertia provided by SG 6 in Case 2 does not bring a noticeable increase in the system inertia. However, the fast primary frequency control of SG 6 did increase the nadir frequency. A comparison of Bus 1 frequency, the total electrical power, and the total mechanical power in the two cases is shown in Fig. 6.13. Here, the COI frequency is approximated by Bus 1 frequency since the inertia of SG 1 is dominant.

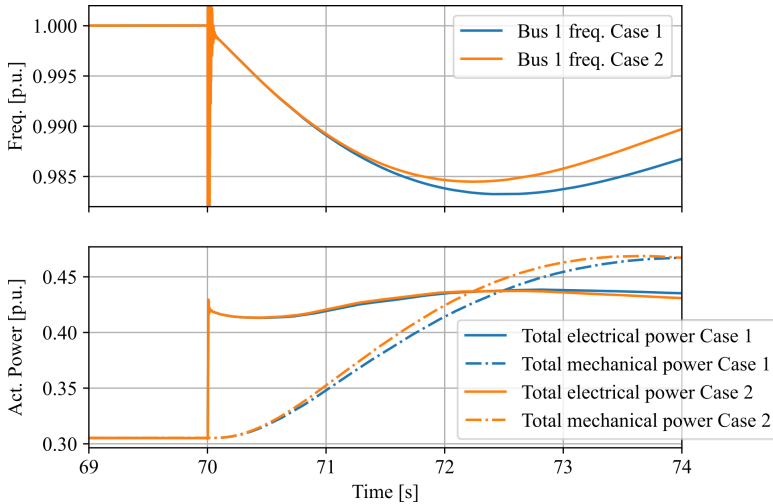


Figure 6.13: Comparison between the frequency response of the system in Case 1 and Case 2.

It can be seen that the total mechanical power in Case 2 increases slightly faster than in Case 1. This happens because the governor response speed of SG 6 is faster than that of SG 1. However, the response speed of SG 6 is not fast enough to change the RoCoF. As a result, the inertia of the system is unchanged but the nadir frequency in Case 2 is higher than that in Case 1. Therefore, it is beneficial to encourage a generation unit to maximize its response speed even if the generation unit is not fast enough to respond to reduce the RoCoF.

A comparison between the response speed of SG 1, SG 6, and their average is illustrated in Fig. 6.14. For clarity, the electrical power and mechanical power of an SG are expressed in the percentage of its steady-state value that is determined by its droop coefficient.

As seen, the mechanical power of SG 6 increases much faster than that of SG 1. Considering the response speed of the mechanical power of SG 1 is the baseline of the primary frequency response (PFR), the excess mechanical power provided by SG 6 over the baseline of the PFR power can be referred to as the fast frequency response (FFR) power. In summary, the FFR power has the following characteristics:

- it does not help to reduce the RoCoF,
- it has a faster response speed than the PFR power and thereby helps to increase the nadir frequency.

Fig. 6.15 illustrates the separation of the output electrical energy of SG 6 from the inertial power, the FFR power, and the PFR power. As seen,  $E_{inertia}$  is the area enclosed by

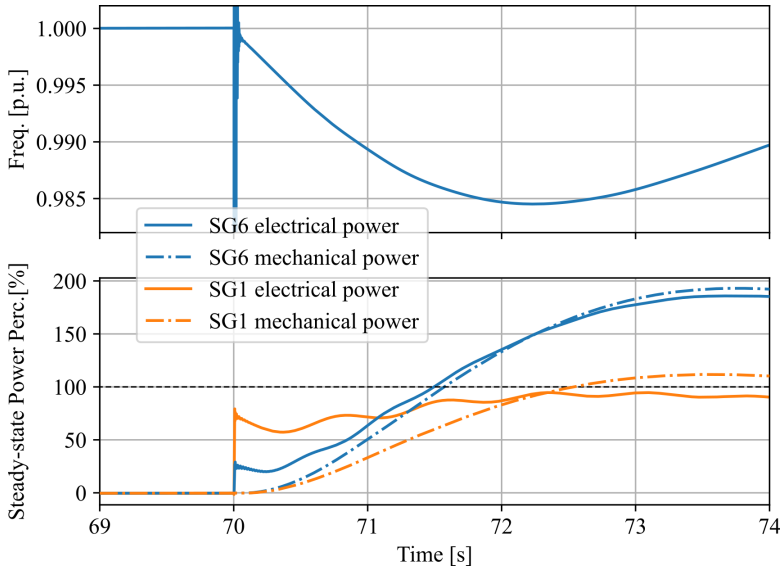


Figure 6.14: Comparison between the response speed of SG 1 and SG 6 in Case 2.

6

the response curve of  $P_{e,SG6}$  and that of  $P_{m,SG6}$ . When  $P_{m,SG6} = P_{e,SG6}$ , the frequency reaches its nadir and the inertia power becomes zero. The energy  $E_{FFR}$  contributed by the FFR power is colored in blue. The part, namely  $E_{PFR}$ , counted as the energy from the PFR power is colored in orange. It is worth mentioning that the electrical power of SG 6 consists of mechanical power and inertia power. The electrical power from the mechanical power is further divided into FFR power and PFR power depending on the response speed. As noticed, the quantification of the FFR power and the PFR power is highly dependent on how the response speed of the PFR power is defined. Luckily, the definition of PFR power already exists in many countries.

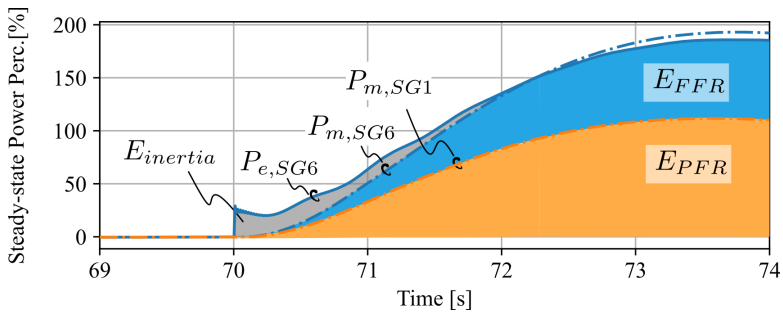


Figure 6.15: Categorization of the output power of SG 6 in Case 2.

For example, the slowest PFR power response speed is standardized by ENTSO-e as the requirement for response speed of the generation units providing the FCR, which is illustrated in Fig. 6.16.

Based on the existing requirements, an additional response curve inside the allowed region and the acceptable region of the PFR power can be set as the slowest FFR power response curve. For example, Fig. 6.17 depicts one possible requirement for the response speed of FFR. It is worth mentioning that with the transition of the power system towards a more power electronics-based system, the response speed of the generation units can have significant changes. Therefore, the requirements for the response speed of PFR should be updated accordingly and so does the requirements for the response speed of FFR if they exist.

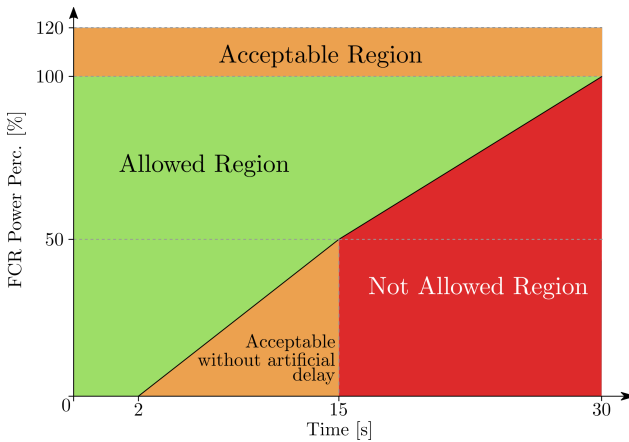


Figure 6.16: Requirement on the response speed of the generator providing frequency containment reserve.

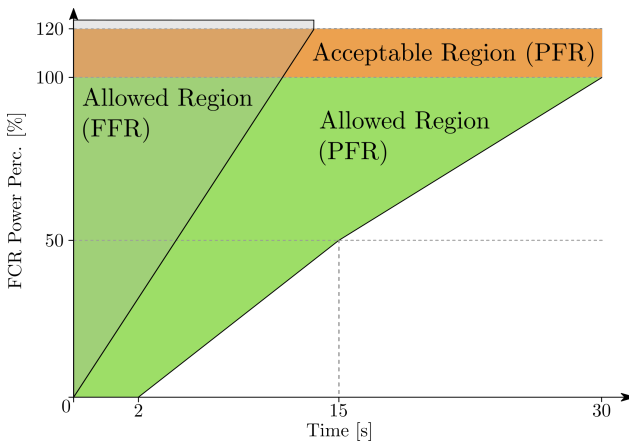


Figure 6.17: Example of fast frequency response requirement based on the existing frequency containment reserve standard.



## 6.4 CASE STUDY

The previous discussions reveal the difference between inertia power, FFR power, and PFR power. Moreover, a method to quantify the inertia power without measuring the mechanical power is clarified. Since the quantification of FFR power and PFR power is dependent on the specific standard that is different from one country to another, it will not be studied here. All the output electrical power other than the inertia power will be treated equally.

To evaluate the performance of the proposed synthetic inertia estimation method, the first case study is carried out based on the IEEE 14-bus system while the SG 6 is replaced by a grid forming converter whose apparent power capacity is the same as that of SG 6. The block diagram of the control is depicted in Fig. 6.2. The droop coefficient  $R_p$  is set to zero so that the grid forming converter mimics only an SC that only provides inertia power. The parameter  $H$  is ten in the first case. Since there is no mechanical power nor rotating mass for a converter, the synthetic inertia power has to be estimated by the proposed approach shown in Fig. 6.10. As a result, the estimated average synthetic inertia power is illustrated in Fig. 6.18. The estimated inertia constant of the converter is 9.5, which is close to the value of the controller parameter  $H$ . Since the converter in this case is mimicking an SC with a time-invariant inertia constant, the effective inertia constant is close to the setting value of  $H$ .

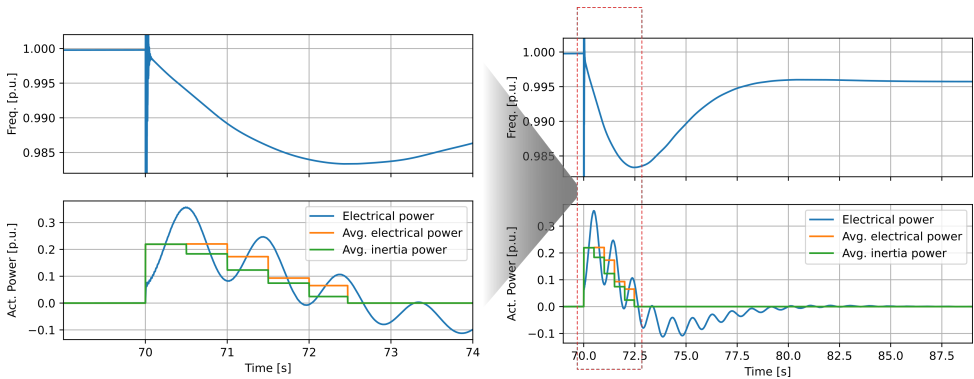


Figure 6.18: Estimated average inertia power of the converter. A 0.5-s time window is used to calculate the RoCoF.

However, the effective synthetic inertia constant of the grid forming converter is not necessarily the same as the value of the controller parameter  $H$ . In the second case, the parameter  $H$  is five, which is half of that in the first case. Meanwhile, the droop coefficient  $R_p$  is set to 0.7%. The responses of Bus 1 frequency, the output electrical power of the converter, and the estimated synthetic inertia power of the converter are illustrated in Fig. 6.19. For comparison, the responses of Bus 1 frequency, the output electrical power of the converter, and the estimated synthetic inertia power of the converter in the first case are also shown. Clearly, despite the parameter  $H$  being smaller in the second case, the synthetic inertia power of the converter is higher and the RoCoF is slightly lower in the second case. The estimated synthetic inertia constant is 11.2 which is higher than 9.5 in the first case.

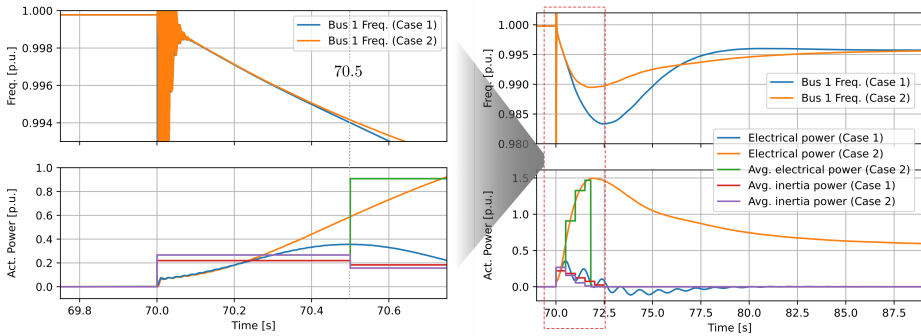


Figure 6.19: Example of fast frequency response requirement based on the existing frequency containment reserve standard.

Such a result is caused by the fast response of the converter. Without the delay of the governor and turbine system, the power  $P_{droop}$  of the converter can immediately respond to the frequency drop. Therefore, due to the additional  $P_{droop}$ , the output electrical power of the converter within 0.5-s after the contingency event in the second case is higher than that in the first case, which leads to a higher synthetic inertia constant.

## 6.5 RETHINKING VSM CONTROL FOR PROVIDING SYNTHETIC INERTIA

The previous case studies indicate the controller parameter  $H$  of a VSM converter does not necessarily equal the synthetic inertia constant of the converter. Although the VSM control is invented to let a converter mimic the behavior of an SG, the two show significant differences in overcurrent ability and response speed [165–167], as shown in Table 6.7.

Table 6.7: Differences between a VSM converter and an SG [165–167]

	VSM converter	Synchronous generator
Overloading capability	1.2 - 1.3 p.u.	3 - 10 p.u.
Response speed	milliseconds	seconds

Although increasing the parameter  $H$  can increase the synthetic inertia constant of the grid forming converter, it is not the best approach because a high  $H$  can lead to active power oscillation which easily makes the converter overloaded. As seen from the control block diagram in Fig. 6.2, when there is a sudden change in the output electrical power of the converter because of the load or generation changes in the external system, using a higher  $H$  makes the frequency of the converter’s AC voltages less changed, which leads to the increasing of the converter’s output electrical power. This is desired before the output electrical power reaches the maximum allowed power. When the converter is about to be overloaded, the phase angle of the converter should change fast to follow the phase angle of the external power system to prevent damaging the converter due to excessively

overloading it. In this case, a high  $H$  prevents the fast change of the converter's phase angle and is not desired.

Considering the overloading capability of a converter, the active power control loop shown in Fig. 6.2 is modified as that shown in Fig. 6.20. The structure of the modified control does not have significant change except that a limiter and an extra feedback  $P_{comp}$  is added. Note a low pass filter is added before the gain  $D_c$  so that  $P_{comp}$  becomes zero in the steady state and the frequency droop power is not changed. A saturation block is used to ensure  $P'_{set}$  is not bigger than the active power capacity of the converter. When  $P_{set} - P_{comp} - P_{droop} \leq P_{max}$ , where  $P_{max}$  is the activate power capacity of the converter, the transfer function from the difference between  $\Delta P$ , where  $\Delta P = P_{set} - P_e$ , to  $\dot{\omega}$  is obtained as

$$\frac{\dot{\omega}}{\Delta P} = \frac{1}{2H + \frac{1}{R_p} \cdot \frac{1}{s} + \frac{D_c}{T_d s + 1}}. \quad (6.31)$$

Considering the RoCoF is calculated with a small time window after the contingency event, the two items, namely  $\frac{1}{R_p} \cdot \frac{1}{s}$  and  $\frac{D_c}{T_d s + 1}$ , both have contributions and cannot be dropped out. The steady-state droop power requirement determines the value of  $R_p$ . However,  $D_c$  does not influence the steady state and can be increased to have the similar effect of increasing  $H$ . Therefore, choosing a small  $H$  while a big  $D_c$  will not lead to a high value of RoCoF. Besides, the benefits of such a choice are obvious when the converter is about to be overloaded. When the sum of  $P_{set}$ ,  $P_{comp}$ , and  $P_{droop}$  is higher than  $P_{max}$ ,  $P'_{set}$  is clamped to  $P_{max}$ , the frequency  $\omega$  need to be changed rapidly to follow the grid voltage so that  $P_e$  can also be clamped to  $P_{max}$ . Such requires a small value of  $H$ . Hence, a better parameter tuning is selecting a small  $H$  to reduce the risk of overloading and selecting a high  $D_c$  to provide enough inertia power.

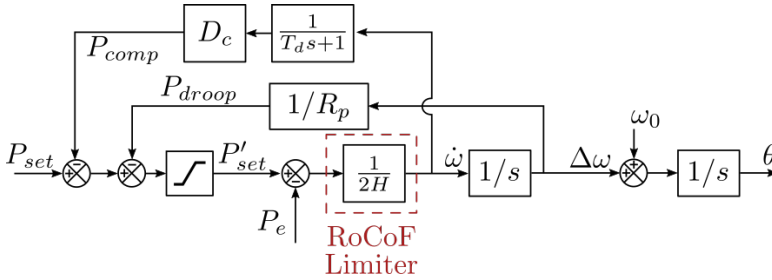


Figure 6.20: Modified VSM control to prevent overloading of the grid-tied converter.

To elaborate on the tuning suggestion, two case studies are carried out. Both case studies are carried out based on the IEEE 14 bus system and a 28-MW CBR is connected to Bus 6. However, in the first case, the active power control loop is the same as that shown in Fig. 6.20. In the second case the feedback loop of  $P_{comp}$  is not added, which is the same as a conventional VSM control. The values of  $R_p$  are the same in the two case studies to ensure the same steady state and a saturation block is also used in both cases. However, in the first case, a small  $H$  and a high  $D_c$  are used. In the second case, only a high  $H$  is used and  $D_c$  is deemed zero since the feedback loop of  $P_{comp}$  is not added.

The output electrical power of the converter in the two cases is compared in Fig. 6.21. The exact selections of  $H$ ,  $D_c$ , and  $T_d$  are also shown. The RoCoF calculated with a time window length of 0.5 seconds is the same in the two cases. Besides, the output electrical power of the converter within 0.5 seconds after the tripping of SG 2 at  $t = 70$  s is also the same in the two cases, which indicates that the synthetic inertia of the converter in both cases is the same as each other.

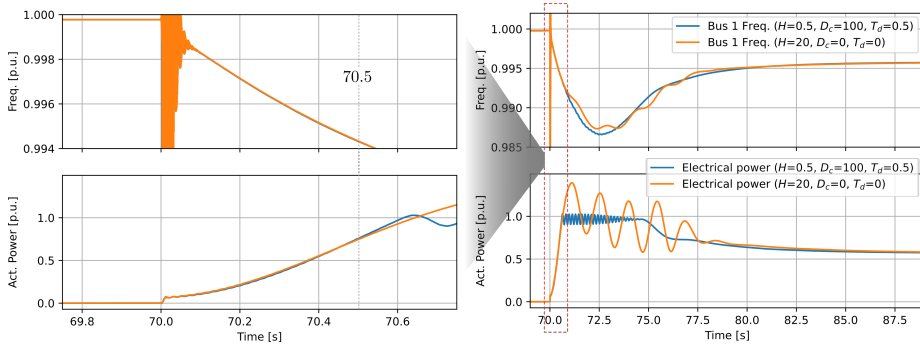


Figure 6.21: Comparison between the two different parameter tuning for a VSM control.

The differences between the two cases are seen after the converter is overloaded. In the first case, the oscillation of the active power has less amplitude since a small  $H$  is used. The converter phase angle can rapidly change to follow the grid voltage phase angle after the output active power reaches the maximum. Therefore, the risk of excessive overloading is prevented. However, in the other case when a high  $H$  is used to provide the same synthetic inertia, the amplitude of the active power oscillation is much higher. Considering an overloading capacity of 1.2-1.3 p.u., there is a risk of damaging the converter.

## 6.6 CONCLUSION

This chapter discusses the essence of the inertia of a generation unit and presents a method to quantify the synthetic inertia of CBRs from a power and energy perspective. It starts with revisiting the influences of inertia on the frequency response of a conventional SG-dominated system, which reveals that inertia can reduce the RoCoF and increase the frequency nadir in a contingency event. By analyzing the inertia power of an SG after the failure of another SG in the system, it was clarified that the electrical power released by an SG in a short period after the failure of another SG is almost purely inertia power. Together with the grid frequency profile, the inertia power can be used to estimate the inertia constant. Besides, the SG continues releasing its inertia power before the frequency reaches the nadir. The value of the inertia power is related to the profile of the grid frequency, which shows a formatted pattern.

On top of that, a more general definition of inertia power is proposed. Depending on the time window length to calculate RoCoF, any electrical power released to reduce RoCoF and has the formatted pattern of inertia power can be regarded as inertia power regardless of the source of the electrical power. As such, simulations demonstrate that an SG with a fast frequency response can also provide synthetic inertia beyond its physical inertia.

To further differentiate the differences between inertia power, FFR power, and PFR power, a case study is given, which shows that FFR power is the electrical power released by a generation unit, which has a faster response speed than PFR power but not fast enough to reduce RoCoF. Finally, based on the obtained insight, how to modify the conventional VSM control to provide synthetic inertia better is presented. With the proposed suggestion, the risk of damaging the grid-tied converter of an CBR by excessive overloading can be mitigated, which is verified by simulation.

# 7

## CONCLUSION

The thesis, as indicated by the research objective given in Chapter 1, aims to develop methods to model EV chargers' power quality disturbances emission and mitigation measures to reduce EV chargers' impacts on power quality. To that end, the thesis starts with reviewing the concept of power quality and introducing the power quality issues that might be or already brought about by EV chargers. On top of that, the thesis focuses on harmonic modelling and improving the small-signal stability of EV chargers. Besides, how to control the BESS that is typically installed to shave the pulsating load profile of EV chargers to provide synthetic inertia is also discussed. Specifically, as an important approach to analyzing harmonic emission and small-signal stability of grid-tied converters, the impedance based stability analysis approach and the impedance modelling in the literature are validated. Moreover, a novel gray-box impedance modelling approach is proposed to extract the input impedance of an EV charger, or more broadly, a PFC converter without knowing the controller parameters and circuit parameters. Furthermore, a multi-timescale co-simulation method is proposed to evaluate the harmonic compliance of an FCS where several high power chargers are connected in parallel. The demonstrated co-simulation method can simulate a day-long harmonic profile in about 2 hours without neglecting the small dynamics that are essential for accuracy. Additionally, the tuning of controller parameters to shape the input impedance of an EV charger is also discussed. As a result, an analytic tuning method to prevent small-signal instability is proposed. Last but not least, the control of BESS to support grid frequency is reviewed. On top of that, the methodology of quantifying the synthetic inertia provided by a BESS from a power and energy perspective is discussed. As a result, a modified VSM control is proposed to control BESS to provide synthetic inertia better.

More specifically, the research objective of the thesis is partitioned into five research questions. Accordingly, Chapters 2-6 present the discussions and studies leading to the answers to the five research questions, respectively. In summary, the main conclusions obtained for each research question are reviewed here. Further, recommendations for future work are given.

**Q1** *What power quality issues do EV chargers potentially have and what standards should be used to evaluate their power quality?*

The fast-charging standards, battery technologies, and power-electronics technologies related to EV charging are reviewed in Chapter 2. On top of that, the potential power quality issues of EV chargers are discussed. Specifically, three power quality issues are highly expected, which are excessive flicker emissions, excessive harmonic emissions, and harmonic instability also known as small-signal instability. Accordingly, the related existing power quality standards that can be used to evaluate EV chargers' power quality compliance are summarized. Specifically, international power quality standards, namely IEEE 1159, IEEE 1453, IEEE 141, IEEE 519, and IEC 61000 series, are compared. Besides, it was presented that these power quality issues are caused by the interactions between EV chargers and grids. Hence, modelling a grid-connected EV charger to study its interaction with the grid and understand the root causes of the aforementioned power quality issues is also briefly introduced. Compared to modelling an EV charger's flicker emission, modelling its harmonics emissions is more challenging because more dynamics are involved. A promising solution is the impedance based approach, which models the charger's dynamics as its input impedance. Based on the impedance modelling, both the issues of excessive harmonic emissions and small-signal instability can be analyzed. Furthermore, the presented modelling revealed that to mitigate EV chargers' power quality impacts the key is properly designing the EV charger's grid-tied converter. Accordingly, some promising mitigation measures are summarized. Chapter 2 established a foundation by introducing the preliminaries. On top of that, the advances in the following chapters are developed to tackle the challenges faced in modelling and developing mitigation measures.

**Q2** *Without knowing design details, how to model EV chargers to analyze their harmonic emission considering their interactions with grids?*

7

As discussed in Chapter 3, the impedance based method can be used to study the harmonic emission of an EV charger, which also considers chargers' interactions with the grid. However, a challenge in practice is extracting a charger's input impedance when the charger's design details are unknown. Therefore, Chapter 3 presented a gray-box method to extract the input impedance of an EV charger with the mainstream design. The proposed gray-box approach does not need to know an EV charger's confidential design details, including the control parameter values and circuit parameters, as the prerequisite. Instead, based on some sparsely measured input impedance of the charger, it estimates the unknown confidential parameters first. Then, the estimated parameter values are used to extract the input impedance model of the charger. The task of parameter estimation is essentially solving an optimization problem, which can be achieved by applying the gradient-descent optimization method. However, because multiple parameters are to be estimated, the loss function to be optimized is highly non-convex, which leads to inaccurate estimation results. Through analysis, it was revealed that the issue of estimation inaccuracy can be mitigated by preventing the creation of saddle points in the loss function. To that end, influential frequency ranges of each parameter were investigated, which is highly correlated to the bandwidth of different control loops. Then, only the impedance within the influential frequency range of a parameter is used when estimating that parameter. In this way, the parameter estimation accuracy is improved. As a result, the extracted input impedance is accurate with the proposed gray-box approach. On top of that, the interactions between an

EV charger and the grid to which it is connected can be studied to analyze the harmonic emissions of the charger and the small-signal stability of the grid-charger system.

**Q3** *How to model a fast charging station that has several EV chargers for a long term harmonic study?*

The multi-timescale co-simulation framework presented in Chapter 4 is a promising solution to simulating the long-term harmonic emissions of an FCS for its harmonic compliance study. In the simulation, the time resolution is decreased to reduce the simulation time cost. This is acceptable because the harmonic compliance study looks at the quasi-steady-state behavior of the device. The fast transient is not of interest. Therefore, the chargers' dynamics influencing their harmonic emissions at different operation points are modelled by establishing their input impedance model at the different operating points updated every minute or longer if needed. The changes in the chargers' input impedance caused by the change of charging power within a shorter time scale are ignored because they are insignificant. In this way, the trade-off between simulation accuracy and time cost is balanced, which enables the feasibility of simulating the long-term harmonic emissions of an FCS.

**Q4** *How to design an EV charger to prevent small-signal instability caused by its interactions with a grid?*

The analytic design approach presented in Chapter 5 gives rise to the answer to the research question. When connecting a grid-tied converter to a grid, e.g., installing an EV charger, small-signal instability might arise because of the interactions between the converter and the grid, which can be analyzed with the impedance based approach. Due to the coupling effect, namely frequency coupling or dq-axis coupling, the input impedance of a grid-tied converter, namely rectifier and inverter, is a two-by-two matrix. As a result, the small-signal stability of the grid-converter system can be analyzed by the general Nyquist stability criterion. However, such an approach is very complicated. Moreover, the controller parameters can only be tuned by trial and error to prevent small-signal instability. It is preferred to have an analytic design method. To that end, Chapter 5 starts with simplifying the impedance model considering the application scenario of EV chargers. Based on the simplified model, it becomes clear how the phase-locked loop, dc-voltage loop, and the current loop are related to the input impedance. Accordingly, how the input impedance is shaped by the controller parameters and circuit parameters is revealed. As a result, an upper limit of the phase-locked loop bandwidth and an upper limit of the dc-voltage loop bandwidth are derived analytically. Accordingly, a design procedure is proposed to tune a charger's controller parameters analytically to prevent small-signal instability when the charger is connected to different locations with different short-circuit ratios.

**Q5** *How to quantify the synthetic inertia provided by inverter-based resources and how to control inverters to provide synthetic inertia better?*

In Chapter 6, a method to quantify the synthetic inertia of a CBR from a power and energy perspective is presented. The synthetic inertia of a CBR should have the same functionality as physical inertia despite it is not from a physical rotating mass. Therefore, the chapter



starts by revisiting the influence of system inertia on a power system. It was revealed that, from a power system perspective, the inertia of synchronous generators can reduce RoCoF and increase nadir frequency after a contingency event by releasing inertia power at the price of decreasing the system frequency. Due to the delay of the primary frequency control, mismatches between the mechanical power and electrical power of all synchronous generators exist and can only be filled up by inertia power. Hence, if both the mechanical power and the electrical power of a device after a contingency event can be measured, it is not challenging to evaluate the inertia of the generation unit. However, a CBR does not have mechanical power making the evaluation of its synthetic inertia difficult. A further analysis found that the released inertia power by a synchronous generator shows a pattern that can be used to quantify synthetic inertia. As a result, the method to quantify synthetic inertia is proposed. Specifically, it calculates the synthetic inertia constant of a CBR based on the RoCoF during a contingency event. Additionally, the profile of the released synthetic inertia power needs to have the pattern of the power released by a physical inertia. As such, synthetic inertia has the equivalent effect as that of inertia. Based on the new understanding, the control of the VSM, a popular grid-forming control method for CBR, is revisited, which leads to a modified VSM control to prevent damaging the converter due to excessive overloading.

## RECOMMENDATIONS FOR FUTURE WORK

In this thesis, the potential power quality issues brought by EV chargers and standards to be used for EV chargers' power quality compliance evaluation are presented. Among the potential power quality issues, the thesis focuses more on the harmonic-related ones. Nevertheless, the influence of EV chargers on system voltage levels is, or is expected to be if not any, problematic. How to deal with this issue is, however, not covered by the thesis due to time constraints.

The presented gray-box modelling approach to extract an EV charger's input impedance is demonstrated based on one popular circuit topology and control method used for EV chargers. Improving this approach for the other design of EV chargers should be considered, which requires more analysis of how different control strategies shape the input impedance differently. Besides, the accuracy of the estimation results is very sensitive to the noises in the measured data. How to improve the method to increase the immunity of the estimation accuracy to measurement noises is also crucial. Hopefully, the method can be further developed to bring a tool that helps anyone who needs to extract an EV charger's input impedance but has no access to confidential design information.

Additionally, the power quality impacts of EV chargers are not only determined by the chargers themselves but also by the power grid. The grid conditions, e.g., the grid impedance and grid voltage harmonics, at the PCC, have crucial influence. To prevent problematic power quality impacts, using the worst-case condition is normally considered, which, however, makes the design conservative. Accurately estimating the power quality impacts of EV chargers and mitigating their power quality impacts requires precisely estimating the grid conditions at the PCC. Since the grid conditions are time-variable, a preferred approach is to estimate the real-time grid conditions by using the EV charger itself. Although some attempts are already seen in the literature, a reliable and accurate grid impedance estimation approach still requires more research.

Last but not least, how to evaluate the synthetic inertia of a CBR is presented in the thesis. On top of that, the VSM control is modified accordingly to improve the ability of a CBR to provide synthetic inertia. However, I believe a better control method should be developed for grid-forming type converters. Since a converter has a fast response speed but low overloading capacity, the fundamental concept of VSM control, namely using a converter to mimic a sluggish but robust synchronous machine, is questionable. Although how to modify the VSM control to prevent damaging the converter due to excessive overloading without compromising the synthetic inertia that it provides is presented in the thesis, it is still not satisfactory. Specifically, when the output electrical power of the converter reaches the maximum, oscillations in the voltage frequency and the output electrical power are seen. Although the amplitude of the oscillations is reduced, they can still be problematic. A better control method that completely prevents the oscillations and the risk of excessive overloading but is still able to maximize the synthetic inertia provided by a CBR is needed.



# BIBLIOGRAPHY

## REFERENCES

- [1] M. Steinmetz, E. van Eijk, and N. Ligterink. Real-world Fuel Consumption and Electricity Consumption of Passenger Cars and Light Commercial Vehicles - 2023. *TNO Report*, 2024.
- [2] European Commission. Road transport: Reducing CO<sub>2</sub> emissions from vehicles. Accessed: 2024. [online]. Available: [https://climate.ec.europa.eu/eu-action/transport/road-transport-reducing-co2-emissions-vehicles\\_en](https://climate.ec.europa.eu/eu-action/transport/road-transport-reducing-co2-emissions-vehicles_en).
- [3] International Energy Agency. Electric Car Sales, 2012-2024. Accessed: 2024. [online]. Available: <https://www.iea.org/data-and-statistics/charts/electric-car-sales-2012-2024>.
- [4] Electric Vehicle Database. Range of full electric vehicles. Accessed: 2024. [online]. Available: <https://ev-database.org/cheatsheet/range-electric-car>.
- [5] ABB E-mobility. ABB E-mobility's New A400 All-in-One Charger: From Chargers to Managed Assets, Accessed: 2024. [online]. Available: <https://new.abb.com/news/detail/115615/abb-e-mobilitys-new-a400-all-in-one-charger-from-chargers-to-managed-assets>.
- [6] Here is my supercharger v2 vs v3 chart. 15-80% within 24 min feels unreal, Accessed: 2024. [online]. Available: [https://www.reddit.com/r/teslamotors/comments/ayaa6g/here\\_is\\_my\\_supercharger\\_v2\\_vs\\_v3\\_chart\\_1580/](https://www.reddit.com/r/teslamotors/comments/ayaa6g/here_is_my_supercharger_v2_vs_v3_chart_1580/).
- [7] J. H. R. Enslin and P. J. M. Heskes. Harmonic interaction between a large number of distributed power inverters and the distribution network. *IEEE Transactions on Power Electronics*, 19(6):1586–1593, 2004.
- [8] L. B. Larumbe, Z. Qin, L. Wang, and P. Bauer. Impedance Modeling for Three-Phase Inverters With Double Synchronous Reference Frame Current Controller in the Presence of Imbalance. *IEEE Transactions on Power Electronics*, 37(2):1461–1475, 2022.
- [9] C. H. Dharmakeerthi, N. Mithulananthan, and T. K. Saha. Impact of Electric Vehicle Fast Charging on Power System Voltage Stability. *International Journal of Electrical Power & Energy Systems*, 57:241–249, 2014.

- [10] Idaho National Laboratory. DC Fast Charger Fact Sheet: ABB Terra 53 CJ charging a 2015 Nissan Leaf, June 2016. Available: <https://avt.inl.gov/sites/default/files/pdf/evse/ABBDCFCFactSheetJune2016.pdf>.
- [11] D. Andersson and D. Carlsson. Measurement of abb's prototype fast charging station for electric vehicles. M.sc. dissertation, Chalmers University of Technology, Gothenburg, Sweden, 2012.
- [12] A. Lucas, F. Bonavitacola, E. Kotsakis, and G. Fulli. An Experimental Approach for Assessing the Harmonic Impact of Fast Charging Electric Vehicles on the Distribution Systems. *Institute for Energy and Transport, Joint Research Centre*, 2015.
- [13] T. Slangen, T. van Wijk, V. Ćuk, and S. Cobben. The Propagation and Interaction of Supraharmonics from Electric Vehicle Chargers in a Low Voltage Grid. *Energies*, 13(15):3865, 2020.
- [14] T. Slangen. *Supraharmonics and Electric Vehicle Charging*. PhD thesis, Eindhoven University of Technology, Eindhoven, North Brabant, Netherlands, Dec. 2023.
- [15] S. M. Alshareef and W. G. Morsi. Impact of Fast Charging Stations on the Voltage Flicker in the Electric Power Distribution Systems. In *2017 IEEE Electrical Power and Energy Conference (EPEC)*, pages 1–6, 2017.
- [16] T. Thiringer and S. Haghbin. Power Quality Issues of a Battery Fast Charging Station for a Fully-Electric Public Transport System in Gothenburg City. *Batteries*, 1(1):22–33, 2015.
- [17] M. Yilmaz and P. T. Krein. Review of Battery Charger Topologies, Charging Power Levels, and Infrastructure for Plug-In Electric and Hybrid Vehicles. *IEEE Transactions on Power Electronics*, 28(5):2151–2169, 2013.
- [18] H. Tu, H. Feng, S. Srdic, and S. Lukic. Extreme Fast Charging of Electric Vehicles: A Technology Overview. *IEEE Transactions on Transportation Electrification*, 5(4):861–878, 2019.
- [19] L. Wang, Z. Qin, J. Dong, and P. Bauer. Design, Modelling and Evaluation of a GaN Based Motor Drive for a Solar Car. In *IECON 2019 - 45th Annual Conference of the IEEE Industrial Electronics Society*, volume 1, pages 5120–5125, 2019.
- [20] M. Nicholas and D. Hall. Lessons Learned on Early Electric Vehicle Fast Charging Deployments. *ICCT White Paper*, 2018. Available: [https://theicct.org/sites/default/files/publications/ZEV\\_fast\\_charging\\_white\\_paper\\_final.pdf](https://theicct.org/sites/default/files/publications/ZEV_fast_charging_white_paper_final.pdf).
- [21] International Electrotechnical Commission. Electric vehicle conductive charging system - Part 1: General Requirements, IEC 61851-1, 2017.
- [22] H. Shareef, M. M. Islam, and A. Mohamed. Review of the Stage-of-the-Art Charging Technologies, Placement Methodologies, and Impacts of Electric Vehicles. *Renewable and Sustainable Energy Reviews*, 64:403–420, 2016.

- [23] L. Pieltain Fernández, T. Gomez San Roman, R. Cossent, C. Mateo Domingo, and P. Frias. Assessment of the Impact of Plug-in Electric Vehicles on Distribution Networks. *IEEE Transactions on Power Systems*, 26(1):206–213, 2011.
- [24] A. D. Hilshey, P. D. H. Hines, P. Rezaei, and J. R. Dowds. Estimating the Impact of Electric Vehicle Smart Charging on Distribution Transformer Aging. *IEEE Transactions on Smart Grid*, 4(2):905–913, 2013.
- [25] Y. Shen, H. Wang, A. Al-Durra, Z. Qin, and F. Blaabjerg. A Bidirectional Resonant DC–DC Converter Suitable for Wide Voltage Gain Range. *IEEE Transactions on Power Electronics*, 33(4):2957–2975, 2018.
- [26] Z. Qin, Y. Shen, P. C. Loh, H. Wang, and F. Blaabjerg. A Dual Active Bridge Converter With an Extended High-Efficiency Range by DC Blocking Capacitor Voltage Control. *IEEE Transactions on Power Electronics*, 33(7):5949–5966, 2018.
- [27] Y. Ma, T. Houghton, A. Cruden, and D. Infield. Modeling the Benefits of Vehicle-to-Grid Technology to a Power System. *IEEE Transactions on Power Systems*, 27(2):1012–1020, 2012.
- [28] S. Han, S. Han, and K. Sezaki. Development of an Optimal Vehicle-to-Grid Aggregator for Frequency Regulation. *IEEE Transactions on Smart Grid*, 1(1):65–72, 2010.
- [29] J. Wang, G. R. Bharati, S. Paudyal, O. Ceylan, B. P. Bhattarai, and K. S. Myers. Coordinated Electric Vehicle Charging With Reactive Power Support to Distribution Grids. *IEEE Transactions on Industrial Informatics*, 15(1):54–63, 2019.
- [30] M. J. E. Alam, K. M. Muttaqi, and D. Sutanto. Effective Utilization of Available PEV Battery Capacity for Mitigation of Solar PV Impact and Grid Support With Integrated V2G Functionality. *IEEE Transactions on Smart Grid*, 7(3):1562–1571, 2016.
- [31] C. Suarez and W. Martinez. Fast and Ultra-Fast Charging for Battery Electric Vehicles – A Review. In *2019 IEEE Energy Conversion Congress and Exposition (ECCE)*, pages 569–575, 2019.
- [32] L. B. Larumbe, Z. Qin, and P. Bauer. Introduction to the Analysis of Harmonics and Resonances in Large Offshore Wind Power Plants. In *2018 IEEE 18th International Power Electronics and Motion Control Conference (PEMC)*, pages 393–400, 2018.
- [33] International Electrotechnical Commission. Electromagnetic compatibility (EMC) - Part 4-30: Testing and measurement techniques - Power quality measurement methods, IEC 61000-4-30, 2015.
- [34] Institute of Electrical and Electronics Engineers. IEEE Recommended Practice and Requirements for Harmonic Control in Electric Power Systems, IEEE 519, 2014.
- [35] Institute of Electrical and Electronics Engineers. IEEE Recommended Practice for Monitoring Electric Power Quality, IEEE 1159, 2019.

- [36] Institute of Electrical and Electronics Engineers. IEEE Recommended Practice for the Analysis of Fluctuating Installations on Power Systems, IEEE 1453, 2015.
- [37] Institute of Electrical and Electronics Engineers. IEEE Recommended Practice for Electric Power Distribution for Industrial Plants, IEEE 141, 1993.
- [38] International Electrotechnical Commission. Electromagnetic compatibility (EMC) - Environment - Compatibility levels for low-frequency conducted disturbances and signalling in public low-voltage power supply systems, IEC 61000-2-2, 2002.
- [39] International Electrotechnical Commission. Electromagnetic compatibility (EMC) - Part 2-4: Environment - Compatibility levels in industrial plants for low-frequency conducted disturbances, IEC 61000-2-4, 2002.
- [40] International Electrotechnical Commission. Electromagnetic compatibility (EMC) - Part 2-12: Environment - Compatibility levels for low-frequency conducted disturbances and signalling in public medium-voltage power supply systems, IEC 61000-2-12, 2003.
- [41] International Electrotechnical Commission. Electromagnetic compatibility (EMC) - Part 3-4: Limits - Limitation of emission of harmonic currents in low-voltage power supply systems for equipment with rated current greater than 16 A, IEC 61000-3-4, 1999.
- [42] International Electrotechnical Commission. Electromagnetic compatibility (EMC) - Part 3-5: Limits - Limitation of voltage fluctuations and flicker in low-voltage power supply systems for equipment with rated current greater than 75 A, IEC 61000-3-5, 2009.
- [43] International Electrotechnical Commission. Electromagnetic compatibility (EMC) - Part 3-6: Limits - Assessment of emission limits for the connection of distorting installations to MV, HV and EHV power systems, IEC 61000-3-6, 2008.
- [44] International Electrotechnical Commission. Electromagnetic compatibility (EMC) - Part 3-7: Limits - Assessment of emission limits for the connection of fluctuating installations to MV, HV and EHV power systems, IEC 61000-3-7, 2008.
- [45] International Electrotechnical Commission. Electromagnetic compatibility (EMC) - Part 3-13: Limits - Assessment of emission limits for the connection of unbalanced installations to MV, HV and EHV power systems, IEC 61000-3-13, 2008.
- [46] International Electrotechnical Commission. Electromagnetic compatibility (EMC) - Part 3-14: Assessment of emission limits for harmonics, interharmonics, voltage fluctuations and unbalance for the connection of disturbing installations to LV power systems, IEC 61000-3-14, 2011.
- [47] J. Tan and L. Wang. Real-Time Charging Navigation of Electric Vehicles to Fast Charging Stations: A Hierarchical Game Approach. *IEEE Transactions on Smart Grid*, 8(2):846–856, 2017.

- [48] T. Zhao, Y. Li, X. Pan, P. Wang, and J. Zhang. Real-Time Optimal Energy and Reserve Management of Electric Vehicle Fast Charging Station: Hierarchical Game Approach. *IEEE Transactions on Smart Grid*, 9(5):5357–5370, 2018.
- [49] H. Ding, Z. Hu, and Y. Song. Value of the energy storage system in an electric bus fast charging station. *Applied Energy*, 157:630–639, 2015.
- [50] J. Shi, Y. Liu, Y. Tang, and J. Deng. Application of a Hybrid Energy Storage System in the Fast Charging Station of Electric Vehicles. *IET Generation, Transmission & Distribution*, 10(4):1092–1097, 2016.
- [51] T. Dragičević, S. Sučić, J. C. Vasquez, and J. M. Guerrero. Flywheel-Based Distributed Bus Signalling Strategy for the Public Fast Charging Station. *IEEE Transactions on Smart Grid*, 5(6):2825–2835, 2014.
- [52] M. Liserre, R. Teodorescu, and F. Blaabjerg. Stability of Photovoltaic and Wind Turbine Grid-Connected Inverters for a Large Set of Grid Impedance Values. *IEEE Transactions on Power Electronics*, 21(1):263–272, 2006.
- [53] M. Liserre, F. Blaabjerg, and A. Dell’Aquila. Step-by-Step Design Procedure for a Grid-Connected Three-Phase PWM Voltage Source Converter. *International Journal of Electronics*, 91(8):445–460, 2004.
- [54] J. Sun. Impedance-Based Stability Criterion for Grid-Connected Inverters. *IEEE Transactions on Power Electronics*, 26(11):3075–3078, 2011.
- [55] X. Wang and F. Blaabjerg. Harmonic Stability in Power Electronic-Based Power Systems: Concept, Modeling, and Analysis. *IEEE Transactions on Smart Grid*, 10(3):2858–2870, 2019.
- [56] L. B. Larumbe, Z. Qin, and P. Bauer. On the Importance of Tracking the Negative-Sequence Phase-Angle in Three-Phase Inverters with Double Synchronous Reference Frame Current Control. In *2020 IEEE 29th International Symposium on Industrial Electronics (ISIE)*, pages 1284–1289, 2020.
- [57] B. Wen, D. Boroyevich, R. Burgos, P. Mattavelli, and Z. Shen. Analysis of D-Q Small-Signal Impedance of Grid-Tied Inverters. *IEEE Transactions on Power Electronics*, 31(1):675–687, 2016.
- [58] J. Lei, Z. Qin, W. Li, P. Bauer, and X. He. Modelling of Output Admittance Coupling Between Shunt Active Power Filters and Non-linear Loads. In *2019 4th IEEE Workshop on the Electronic Grid (eGRID)*, pages 1–5, 2019.
- [59] M. Belkhatat. *Stability Criteria for AC Power Systems with Regulated Loads*. PhD thesis, Purdue University, West Lafayette, IN, USA, Dec. 1997.
- [60] L. Harnefors, X. Wang, A. G. Yepes, and F. Blaabjerg. Passivity-Based Stability Assessment of Grid-Connected VSCs—An Overview. *IEEE Journal of Emerging and Selected Topics in Power Electronics*, 4(1):116–125, 2016.



- [61] D. Yang, X. Ruan, and H. Wu. Impedance Shaping of the Grid-Connected Inverter with LCL Filter to Improve Its Adaptability to the Weak Grid Condition. *IEEE Transactions on Power Electronics*, 29(11):5795–5805, 2014.
- [62] M. Neaimeh, S. D. Salisbury, G. A. Hill, P. T. Blytheand, D. R. Scoffield, and J. E. Francfort. Analysing the Usage and Evidencing the Importance of Fast Chargers for the Adoption of Battery Electric Vehicles. *Energy Policy*, 108:474–486, 2017.
- [63] Y. Liu and M. Yoshida. ChaoJi Standard: Faster, Safer, and Compatible to All. Accessed: 2024. [online]. Available: [chrome-extension://efaidnbmnnnibpcajpcglclefindmkaj/https://www.chademo.com/wp2016/wp-content/uploads/ChaoJi202006/ChaoJi\\_Presenataion\\_EN.pdf](chrome-extension://efaidnbmnnnibpcajpcglclefindmkaj/https://www.chademo.com/wp2016/wp-content/uploads/ChaoJi202006/ChaoJi_Presenataion_EN.pdf).
- [64] Tesla forum. V3 superchargers or V2+??, Accessed: 2019. [online]. Available: <https://forums.tesla.com/discussion/168859/v3-superchargers-or-v2>.
- [65] H. Engel, R. Hensley, S. Knupfer, and S. Sahdev. Charging ahead: Electric-Vehicle Infrastructure Demand. *McKinsey Center for Future Mobility*, 2018. Available: <https://www.mckinsey.com/~media/McKinsey/Industries/Automotive%20and%20Assembly/Our%20Insights/Charging%20ahead%20Electric-vehicle%20infrastructure%20demand/Charging-ahead-electric-vehicle-infrastructure-demand-final.pdf>.
- [66] Electric Vehicle Charging Definitions and Explanation. *Netherlands Enterprise Agency Report*, Accessed: 2020. [online]. Available: [https://www.rvo.nl/files/file/2019/01/Electric%20Vehicle%20Charging%20-%20Definitions%20and%20Explanation%20-%20january%202019\\_0.pdf](https://www.rvo.nl/files/file/2019/01/Electric%20Vehicle%20Charging%20-%20Definitions%20and%20Explanation%20-%20january%202019_0.pdf).
- [67] European Alternative Fuels Observatory. *European Commission*, Accessed: 2024. [online]. Available: <https://alternative-fuels-observatory.ec.europa.eu/transport-mode/road/european-union-eu27/infrastructure>.
- [68] ING Economics Department. Breakthrough of Electric Vehicle Threatens European Car Industry, 2017. Available: [https://www.ing.nl/media/ING\\_EBZ\\_breakthrough-of-electric-vehicle-threatens-European-car-industry\\_tcm162-128687.pdf](https://www.ing.nl/media/ING_EBZ_breakthrough-of-electric-vehicle-threatens-European-car-industry_tcm162-128687.pdf).
- [69] Electric Vehicle Database. Useable Battery Capacity of Full Electric Vehicles. Accessed: 2020. [online]. Available: <https://ev-database.org/cheatsheet/useable-battery-capacity-electric-car>.
- [70] L. Wang, Z. Qin, T. Slangen, P. Bauer, and T. van Wijk. Grid Impact of Electric Vehicle Fast Charging Stations: Trends, Standards, Issues and Mitigation Measures - An Overview. *IEEE Open Journal of Power Electronics*, 2:56–74, 2021.

- [71] CATL. Innovative Technology. Accessed: 2020. [online]. Available: <https://www.catl.com/en/research/technology/>.
- [72] Kokam. Superior Lithium-ion Battery. Accessed: 2020. [online]. Available: [https://kokam.com/data/filebox/cell\\_brochure.pdf](https://kokam.com/data/filebox/cell_brochure.pdf).
- [73] Microvast. Mpc0, Hnc0 Li-ion Battery. Accessed: 2020. [online]. Available: <https://microvast.com/solutions/transportation/>.
- [74] Enevate. Charge Faster, Go Farther with XFC-Energy Technology. Accessed: 2020. [online]. Available: <https://www.enevate.com/technology/hd-energy-technology-overview/>.
- [75] M. Keyser et al. Enabling Fast Charging—Battery Thermal Considerations. *Journal of Power Sources*, 367:228–236, 2017.
- [76] Porsche. "Porsche Turbo Charging", Accessed: 2020. Available: <https://www.porsche.com/international/models/taycan/taycan-models/taycan-turbo-s/#charging~open>.
- [77] S. Ahmed et al. Enabling Fast Charging—A Battery Technology Gap Assessment. *Journal of Power Sources*, 367:250–262, 2017.
- [78] Tesla. Map of Supercharger Stations, Accessed: 2020. [online]. Available: <https://www.tesla.com/supercharger>.
- [79] S. Srdic and S. Lukic. Toward Extreme Fast Charging: Challenges and Opportunities in Directly Connecting to Medium-Voltage Line. *IEEE Electrification Magazine*, 7(1):22–31, 2019.
- [80] M. Ahmadi, N. Mithulananthan, and R. Sharma. A Review on Topologies for Fast Charging Stations for Electric Vehicles. In *2016 IEEE International Conference on Power System Technology (POWERCON)*, pages 1–6, 2016.
- [81] S. Kalker et al. Fast-Charging Technologies, Topologies and Standards. Technical Report RWTH-CONV-242119, E.ON Energy Research Center, Aachen, Germany, 2018.
- [82] Delta Electronics. Delta Kicks Off US DOE-Sponsored Program to Develop Microgrid-Capable Solid State Transformer-Based 400kW Extreme Fast Chargers for Electric Vehicles. Accessed: 2018. [online]. Available: <https://www.delta-americas.com/news/pressDetail.aspx?secID=3&pID=1&typeID=1;&itemID=8278&tid=02&hl=en-US>.
- [83] S. Chon, M. Bhardwaj and H. Nene. Maximizing Power for Level 3 EV Charging Stations. *Texas Instruments*, June 2018. Available: [https://www.ti.com/lit/wp/sway014/sway014.pdf?ts=1609739136722&ref\\_url=https%253A%252F%252Fwww.ti.com%252Fsolution%252Fwireless-EV-charging-station](https://www.ti.com/lit/wp/sway014/sway014.pdf?ts=1609739136722&ref_url=https%253A%252F%252Fwww.ti.com%252Fsolution%252Fwireless-EV-charging-station).

- [84] P. Chatterjee and M. Hermwille. Tackling the Challenges of Electric Vehicle Fast Charging. *ATZelectronics worldwide*, 15(10):18–22, 2020.
- [85] A. Khaligh and S. Dusmez. Comprehensive Topological Analysis of Conductive and Inductive Charging Solutions for Plug-In Electric Vehicles. *IEEE Transactions on Vehicular Technology*, 61(8):3475–3489, 2012.
- [86] D. Aggeler, F. Canales, H. Zelaya-De La Parra, A. Coccia, N. Butcher, and O. Apeldoorn. Ultra-fast dc-charge infrastructures for ev-mobility and future smart grids. In *2010 IEEE PES Innovative Smart Grid Technologies Conference Europe (ISGT Europe)*, pages 1–8, 2010.
- [87] S. Dusmez, A. Cook, and A. Khaligh. Comprehensive Analysis of High Quality Power Converters for Level 3 Off-Board Chargers. In *2011 IEEE Vehicle Power and Propulsion Conference*, pages 1–10, 2011.
- [88] J. W. Kolar and F. C. Zach. A Novel Three-Phase Utility Interface Minimizing Line Current Harmonics of High-Power Telecommunications Rectifier Modules. *IEEE Transactions on Industrial Electronics*, 44(4):456–467, 1997.
- [89] B. Singh, S. Gairola, B. N. Singh, A. Chandra, and K. Al-Haddad. Multipulse AC–DC Converters for Improving Power Quality: A Review. *IEEE Transactions on Power Electronics*, 23(1):260–281, 2008.
- [90] E. Loveday. Rare Look Inside Tesla Supercharger, Accessed: 2020. [online]. Available: <https://insideevs.com/news/322486/rare-look-inside-tesla-supercharger/>.
- [91] W. Chen, X. Ruan, H. Yan, and C. K. Tse. DC/DC Conversion Systems Consisting of Multiple Converter Modules: Stability, Control, and Experimental Verifications. *IEEE Transactions on Power Electronics*, 24(6):1463–1474, 2009.
- [92] C. Wan, M. Huang, C. K. Tse, and X. Ruan. Effects of Interaction of Power Converters Coupled via Power Grid: A Design-Oriented Study. *IEEE Transactions on Power Electronics*, 30(7):3589–3600, 2015.
- [93] J. Meyer, V. Khokhlov, M. Klatt, J. Blum, C. Waniek, T. Wohlfahrt, and J. Myrzik. Overview and classification of interferences in the frequency range 2–150 khz (supraharmonics). In *2018 International Symposium on Power Electronics, Electrical Drives, Automation and Motion (SPEEDAM)*, pages 165–170, 2018.
- [94] J. Yong, V. K. Ramachandramurthy, K. Tan, and N. Mithulananthan. A Review on the State-of-the-Art Technologies of Electric Vehicle, its Impacts and Prospects. *Renewable and Sustainable Energy Reviews*, 49:365–385, 2015.
- [95] K. Yunus, H. Z. De La Parra, and M. Reza. Distribution Grid Impact of Plug-In Electric Vehicles Charging at Fast Charging Stations Using Stochastic Charging Model. In *Proceedings of the 2011 14th European Conference on Power Electronics and Applications*, pages 1–11, 2011.

- [96] R. Bass and N. Zimmerman. Impacts of Electric Vehicle Charging on Electric Power Distribution Systems. *Transportation Research and Education Center (TREC)*, 2013.
- [97] International Electrotechnical Commission. Electromagnetic compatibility (EMC) - Part 3-2: Limits - Limits for harmonic current emissions (equipment input current  $\leq 16$  A per phase), IEC 61000-3-2, 2018.
- [98] S. Rönnerberg and M. Bollen. Propagation of Supraharmonics in the Low Voltage Grid. Technical Report 2017:461, Energiforsk AB, Stockholm, Sweden, Dec. 2017.
- [99] International Electrotechnical Commission. Electromagnetic compatibility (EMC) - Part 4-30: Testing and measurement techniques – Power quality measurement methods, IEC 61000-4-30, 2015.
- [100] T. M. H. Slangen, T. van Wijk, V. Ćuk, and J. F. G. Cobben. The harmonic and supraharmonic emission of battery electric vehicles in the netherlands. In *2020 International Conference on Smart Energy Systems and Technologies (SEST)*, pages 1–6, 2020.
- [101] J. Meyer, S. Mueller, S. Ungethuen, X. Xiao, A. Collin, and S. Djokic. Harmonic and Supraharmonic Emission of On-Board Electric Vehicle Chargers. In *2016 IEEE PES Transmission Distribution Conference and Exposition-Latin America (PES T D-LA)*, pages 1–7, 2016.
- [102] J. Barros, J. J. Gutierrez, M. de Apraiz, P. Saiz, R. I. Diego, and A. Lazkano. Rapid Voltage Changes in Power System Networks and Their Effect on Flicker. *IEEE Transactions on Power Delivery*, 31(1):262–270, 2016.
- [103] N. Chuo, H. Lee, I. Seo, and S. Lee. Comparisons of IEC/TR 61000-3-6 and IEEE Std 519 in the MV Systems. In *Proc. of the 25th Int. Conf. on Electr. Distrib.*, pages 1–5, Madrid, Spain, June 2019. AIM.
- [104] A. B. Gallo, J. R. Simoes-moreira, H. K. M. Costa, M. M. Santos, and E. Moutinho. Energy Storage in the Energy Transition Context: A Technology Review. *Renewable and Sustainable Energy Reviews*, 65:800–822, 2016.
- [105] S. Bandyopadhyay, P. Purgat, Z. Qin, and P. Bauer. A Multiactive Bridge Converter With Inherently Decoupled Power Flows. *IEEE Transactions on Power Electronics*, 36(2):2231–2245, 2021.
- [106] S. Bandyopadhyay, Z. Qin, and P. Bauer. Decoupling Control of Multi-Active Bridge Converters using Linear Active Disturbance Rejection. *IEEE Transactions on Industrial Electronics*, 68(11):10688–10698, 2021.
- [107] M. Cespedes and J. Sun. Impedance Modeling and Analysis of Grid-Connected Voltage-Source Converters. *IEEE Transactions on Power Electronics*, 29(3):1254–1261, 2014.

- [108] J. Xu, J. Han, Y. Wang, S. Habib, and H. Tang. A Novel Scalar PWM Method to Reduce Leakage Current in Three-Phase Two-Level Transformerless Grid-Connected VSIs. *IEEE Transactions on Industrial Electronics*, 67(5):3788–3797, 2020.
- [109] R. Lai, F. Wang, R. Burgos, D. Boroyevich, D. Jiang, and D. Zhang. Average Modeling and Control Design for VIENNA-Type Rectifiers Considering the DC-Link Voltage Balance. *IEEE Transactions on Power Electronics*, 24(11):2509–2522, 2009.
- [110] M. K. Bakhshizadeh et al. Couplings in Phase Domain Impedance Modeling of Grid-Connected Converters. *IEEE Transactions on Power Electronics*, 31(10):6792–6796, 2016.
- [111] M. Cespedes and J. Sun. Impedance Shaping of Three-Phase Grid-Parallel Voltage-Source Converters. In *2012 Twenty-Seventh Annual IEEE Applied Power Electronics Conference and Exposition (APEC)*, pages 754–760, 2012.
- [112] X. Wang, L. Harnefors, and F. Blaabjerg. Unified Impedance Model of Grid-Connected Voltage-Source Converters. *IEEE Transactions on Power Electronics*, 33(2):1775–1787, 2018.
- [113] Y. Huang, X. Yuan, J. Hu, and P. Zhou. Modeling of VSC Connected to Weak Grid for Stability Analysis of DC-Link Voltage Control. *IEEE Journal of Emerging and Selected Topics in Power Electronics*, 3(4):1193–1204, 2015.
- [114] X. Wang, F. Blaabjerg, and W. Wu. Modeling and Analysis of Harmonic Stability in an AC Power-Electronics-Based Power System. *IEEE Transactions on Power Electronics*, 29(12):6421–6432, 2014.
- [115] T. Midtsund, J. A. Suul, and T. Undeland. Evaluation of Current Controller Performance and Stability for Voltage Source Converters Connected to a Weak Grid. In *The 2nd International Symposium on Power Electronics for Distributed Generation Systems*, pages 382–388, 2010.
- [116] M. Liserre, F. Blaabjerg, and S. Hansen. Design and Control of an LCL-Filter-Based Three-Phase Active Rectifier. *IEEE Transactions on Industry Applications*, 41(5):1281–1291, 2005.
- [117] B. Basta and W. G. Morsi. Low and High Order Harmonic Distortion in the Presence of Fast Charging Stations. *International Journal of Electrical Power & Energy Systems*, 126(106557):1–9, 2021.
- [118] Z. Qin, L. Wang, and P. Bauer. Review on Power Quality Issues in EV Charging. In *2022 IEEE 20th International Power Electronics and Motion Control Conference (PEMC)*, pages 360–366, 2022.
- [119] C. Buchhagen, C. Rauscher, A. Menze, and J. Jung. BorWin1 - First Experiences with Harmonic Interactions in Converter Dominated Grids. In *Proc. Int. ETG Congr.; Die Energiewende - Blueprints New Energy Age*, pages 1–7, 2015.

- [120] J. Lei, Z. Qin, W. Li, P. Bauer, and X. He. Stability Region Exploring of Shunt Active Power Filters Based on Output Admittance Modeling. *IEEE Transactions on Industrial Electronics*, 68(12):11696–11706, 2021.
- [121] L. Wang, Z. Qin, L. B. Larumbe, and P. Bauer. Python supervised co-simulation for a day-long harmonic evaluation of EV charging. *Chinese Journal of Electrical Engineering*, 7(4):15–24, 2021.
- [122] J. Sun. Input Impedance Analysis of Single-Phase PFC Converters. *IEEE Transactions on Power Electronics*, 20(2):308–314, 2005.
- [123] B. Sohlberg and E. W. Jacobsen. Grey Box Modelling—Branches and Experiences. In *Proc. 17th IFAC World Congr.*, pages 11415–11420, 2008.
- [124] J. Y. Hung. Parameter Estimation Using Sensitivity Points: Tutorial and Experiment. *IEEE Transactions on Industrial Electronics*, 48(6):1043–1047, 2001.
- [125] R. S. Blom and P. M. J. Van den Hof. Multivariable Frequency Domain Identification Using IV-Based Linear Regression. In *Proc. 49th IEEE Conf. Decision Control*, pages 1148–1153, 2010.
- [126] C. C. Brozio and H. J. Vermeulen. Wideband Equivalent Circuit Modelling and Parameter Estimation Methodology for Two-Winding Transformers. *IEE Proc. Gener., Transm. Distrib.*, 150(4):487–492, 2003.
- [127] S. D. Mitchell and J. S. Welsh. Initial Parameter Estimates and Constraints to Support Gray Box Modeling of Power Transformers. *IEEE Transactions on Power Delivery*, 28(4):2411–2418, 2013.
- [128] B. Long, Z. Zhu, W. Yang, K. T. Chong, J. Rodríguez, and J. M. Guerrero. Gradient Descent Optimization Based Parameter Identification for FCS-MPC Control of LCL-Type Grid Connected Converter. *IEEE Transactions on Industrial Electronics*, 69(3):2631–2643, 2022.
- [129] M. Amin and M. Molinas. A Gray-Box Method for Stability and Controller Parameter Estimation in HVDC-Connected Wind Farms Based on Nonparametric Impedance. *IEEE Transactions on Industrial Electronics*, 66(3):1872–1882, 2019.
- [130] R. Ge, F. Huang, C. Jin, and Y. Yuan. Escaping from Saddle Points—Online Stochastic Gradient for Tensor Decomposition. In *Proc. Conf. Learn. Theory*, pages 797–842, 2015.
- [131] A. Ahmad, Z. Qin, T. Wijekoon, and P. Bauer. An Overview on Medium Voltage Grid Integration of Ultra-fast Charging Stations: Current Status and Future Trends. *IEEE Open Journal of Industrial Electronics Society*, 3:420–447, 2022.
- [132] S. Rivera, S. Kouro, S. Vazquez, S. M. Goetz, R. Lizana, and E. Romero-Cadaval. Electric Vehicle Charging Infrastructure: From Grid to Battery. *IEEE Industrial Electronics Magazine*, 15(2):37–51, 2021.

- [133] B. Wen, R. Burgos, D. Boroyevich, P. Mattavelli, and Z. Shen. AC Stability Analysis and dq Frame Impedance Specifications in Power-Electronics-Based Distributed Power Systems. *IEEE Journal of Emerging Selected Topics on Power Electronics*, 5(4):1455–1465, 2017.
- [134] L. Harnefors. Modeling of Three-Phase Dynamic Systems Using Complex Transfer Functions and Transfer Matrices. *IEEE Transactions on Industrial Electronics*, 54(4):2239–2248, 2007.
- [135] M. P. Kazmierkowski, R. Krishnan, and F. Blaabjerg. *Control in Power Electronics*, volume 17. Elsevier, 2002.
- [136] S. Golestan and J. M. Guerrero. Conventional Synchronous Reference Frame Phase-Locked Loop is an Adaptive Complex Filter. *IEEE Transactions on Industrial Electronics*, 62(3):1679–1682, 2015.
- [137] L. Harnefors, M. Bongiorno, and S. Lundberg. Input-Admittance Calculation and Shaping for Controlled Voltage-Source Converters. *IEEE Transactions on Industrial Electronics*, 54(6):3323–3334, 2007.
- [138] J. Dannehl, C. Wessels, and F. W. Fuchs. Limitations of Voltage-Oriented PI Current Control of Grid-Connected PWM Rectifiers With LCL Filters. *IEEE Transactions on Industrial Electronics*, 56(2):380–388, 2009.
- [139] K. Li, A. Formentini, D. Dewar, and Pericle Zanchetta. Controller Design of an Active Front-End Converter Keeping in Consideration Grid Dynamic Interaction. *IEEE Transactions on Industrial Electronics*, 69(5):5195–5206, 2022.
- [140] D. Dong, B. Wen, D. Boroyevich, P. Mattavelli, and Y. Xue. Analysis of Phase-Locked Loop Low-Frequency Stability in Three-Phase Grid-Connected Power Converters Considering Impedance Interactions. *IEEE Transactions on Industrial Electronics*, 62(1):310–321, 2015.
- [141] Y. N. Dauphin, R. Pascanu, C. Gulcehre, K. Cho, S. Ganguli, and Y. Bengio. Identifying and Attacking the Saddle Point Problem in High-Dimensional Non-Convex Optimization. *Advances in Neural Information Processing Systems*, 27, 2014.
- [142] D. P. Kingma and J. Ba. Adam: A method for stochastic optimization. *arXiv:1412.6980*, 2014.
- [143] M. Cheng and M. Tong. Development Status and Trend of Electric Vehicles in China. *Chinese Journal of Electrical Engineering*, 3(2):1–13, 2017.
- [144] T. Wang, H. Nian, and Z. Q. Zhu. Using Inverter-Based Renewable Generators to Improve the Grid Power Quality—A Review. *Chinese Journal of Electrical Engineering*, 4(4):16–25, 2018.
- [145] J. Lin, Y. Li, S. Hu, Q. Liu, J. Zhang, S. Wang, L. Dong, and J. Ni. Resonance Mechanism Analysis of Large-Scale Photovoltaic Power Plant. *Chinese Journal of Electrical Engineering*, 7(1):47–54, 2021.



- [146] International Electrotechnical Commission. Electromagnetic compatibility (EMC) - Part 4-7: Testing and measurement techniques-General guide on harmonics and interharmonics measurements and instrumentation, for power supply systems and equipment connected thereto, IEC 61000-4-7, 2009.
- [147] Agurtzane Etxegarai, Pablo Eguia, Esther Torres, Araitx Iturregi, and Victor Valverde. Review of Grid Connection Requirements for Generation Assets in Weak Power Grids. *Renewable and Sustainable Energy Reviews*, 41:1501–1514, 2015.
- [148] G Misyris, D Ramasubramanian, M Val Escudero, T Kerci, and S Murray. Weak Grid Analysis for Interconnecting Inverter-Based Generation-Ireland Case Study. *CIGRE Sci. Eng. J. CSE*, 29:1–19, 2023.
- [149] D.Ramasubramanian. Program on Technology Innovation: Benefit of Fast Reactive Power Response from Inverters in Supporting Stability of Weak Distribution Systems. EPRI, Accessed: 2024. Available: <https://restservice.epri.com/publicdownload/000000003002020197/0/Product>.
- [150] Spanningskwaliteit in Nederland. *Netbeheer Nederland*, Accessed: 2024. Available: <https://www.netbeheernederland.nl/publicatie/rapport-spanningskwaliteit-nederland-2023>.
- [151] A. Rygg, M. Molinas, C. Zhang, and X. Cai. On the Equivalence and Impact on Stability of Impedance Modeling of Power Electronic Converters in Different Domains. *IEEE Journal of Emerging Selected Topics on Power Electronics*, 5(4):1444–1454, 2017.
- [152] Z. Zhang, W. Wu, Z. Shuai, X. Wang, A. Luo, H. S. Chung, and F. Blaabjerg. Principle and Robust Impedance-Based Design of Grid-tied Inverter with LLCL-Filter under Wide Variation of Grid-Reactance. *IEEE Transactions on Power Electronics*, 34(5):4362–4374, 2019.
- [153] B. Wen, D. Dong, D. Boroyevich, R. Burgos, P. Mattavelli, and Z. Shen. Impedance-Based Analysis of Grid-Synchronization Stability for Three-Phase Paralleled Converters. *IEEE Transactions on Power Electronics*, 31(1):26–38, 2016.
- [154] Y. Chen, X. Ruan, Z. Lin, Y. Yan, and Y. He. A Reconstructed Singular Return Ratio Matrix for Optimizing Design of the PLL in Grid-Connected Inverters. *IEEE Transactions on Industrial Electronics*, 70(12):12453–12464, 2023.
- [155] D. Lu, X. Wang, and F. Blaabjerg. Impedance-Based Analysis of DC-Link Voltage Dynamics in Voltage-Source Converters. *IEEE Transactions on Power Electronics*, 34(4):3973–3985, 2019.
- [156] K. Wang, X. Yuan, S. Li, and X. Wu. Stability-Margin-Oriented Key Parameter Design for Voltage-Source Rectifiers in Weak Power Grids With Inductive Impedance. *IEEE Open Journal of Industrial Electronics Society*, 2:511–527, 2021.
- [157] Z. Lin, X. Ruan, H. Zhang, and L. Wu. A Hybrid-Frame Control Based Impedance Shaping Method to Extend the Effective Damping Frequency Range of the Three-Phase Adaptive Active Damper. *IEEE Transactions on Industrial Electronics*, 70(1):509–521, 2022.



- [158] R. Burgos, D. Boroyevich, F. Wang, K. Karimi, and G. Francis. On the AC Stability of High Power Factor Three-Phase Rectifiers. In *2010 IEEE Energy Conversion Congress and Exposition*, pages 2047–2054, 2010.
- [159] S. M. Shahruz, G. Langari, and M. Tomizuka. Optimal Damping Ratio for Linear Second-Order Systems. *Journal of Optimization Theory and Applications*, 73:563–576, 1992.
- [160] International Electrotechnical Commission. Limits for harmonic currents produced by equipment connected to public low-voltage systems with input current  $> 16$  A and  $\leq 75$  A per phase, IEC 61000-3-12, 2011.
- [161] M. Stecca, W. Vermeer, T. B. Soeiro, L. Ramirez Elizondo, P. Bauer, and P. Palensky. Battery Storage Integration in EV Fast Charging Station for Increasing its Revenues and Reducing the Grid Impact. In *2022 IEEE Transportation Electrification Conference & Expo (ITEC)*, pages 109–113, 2022.
- [162] M. Stecca. *Battery energy storage systems: Power electronics interface and grid integration*. PhD thesis, 2023.
- [163] P. Kundur. *Power System Stability and Control*. McGraw-Hill, New York, 1994.
- [164] E. A. S. Ducoin, Y. Gu, B. Chaudhuri, and T. C. Green. Analytical Design of Contributions of Grid-Forming & Grid-Following Inverters to Frequency Stability. *IEEE Transactions on Power Systems*, 39(5):6345–6358, 2024.
- [165] Shubhangi Bhadoria, Frans Dijkhuizen, Rishabh Raj, Xiongfei Wang, Qianwen Xu, Elisa Matioli, Konstantin Kostov, and Hans-Peter Nee. Enablers for Overcurrent Capability of Silicon-Carbide-Based Power Converters: An Overview. *IEEE Transactions on Power Electronics*, 38(3):3569–3589, 2023.
- [166] Ruiqi Li, Campbell Booth, Adam Dyško, Andrew Roscoe, Helge Urdal, and Jiebei Zhu. Protection Challenges in Future Converter Dominated Power Systems: Demonstration Through Simulation and Hardware Tests. In *International Conference on Renewable Power Generation*. IET, 2015.
- [167] Nathan Baeckeland, Debjyoti Chatterjee, Minghui Lu, Brian Johnson, and Gab-Su Seo. Overcurrent Limiting in Grid-Forming Inverters: A Comprehensive Review and Discussion. *IEEE Transactions on Power Electronics*, 39(11):14493–14517, 2024.

---

## ACKNOWLEDGMENTS

PhD journey is long trip with low fault tolerance. The enemies of a PhD student include but not limited to tight time schedule, misleading publications, identifying specificity and focus in ambiguous research gaps, explosions in the lab, unexpected simulation and experiment results, drafting a manuscript, sluggish review processes, revisions, rejections ... Luckily, because many of you, I was not troubled by the difficulties for long. Therefore, I would like to gratitude to you.

Firstly, I would like to thank prof. Bauer for giving me the opportunity to join the DCE&S group, and a lot of freedom for carrying out this research. Our monthly meeting helped me in improving in both my communication skills, which let me realize that the essence of research lies not only in uncovering new insights but also in sharing those insights with others in a way engaging their interests.

I would like to thank you Zian. I still remember how excited I was four years ago when I first heard from you about the PhD position and how you guided me at the beginning on how to work as a PhD student. Undoubtedly, your research styles and tastes deeply shape mine. As my supervisor, you are my closest ally in front of all the challenges in my PhD journey. Thank you for your unwavering support, both mentally and practically.

I would like to thank Sharmila. Thank you for your always willing to help, creating a warm and welcoming atmosphere for everyone around you. I want to also thank Bart, Joris, Mladen, and Hitesh, for your valuable supports in the all my experiments in the lab.

My fellows in the group made the work place friendly and cozy. Thank you Aditya, Marco, Francesca, Wiljan, Wenli, Christian, Dhanashree, Ibra, Pierpaolo, Miad, Joel, István, Felipe, Zichen, Rohan, Heshi, Faezeh, Yongpeng, Koen, Alvaro, Margo, Bagas, Julian, Robin, Manfredo, Leila, Siddhesh, Sourabh, Darío, Shibo, Gangwei, Abdourahim.

In the four years, I was lucky to collaborate with many researchers. You helped me, taught me, and inspired me. To Lucia, thank you for the valuable discussing at the beginning of my PhD. They greatly helped me familiarize myself with my research topic. To Junjie, it is lucky to have you accompany during my PhD journey. Many times, I feel you are my mirror image because we share many of the same emotions. You will become a big name that you want to be in the future. To Yawen, thank you for working with me on your Master thesis. Although I was your supervisor, you later taught me the importance of always considering things from another's perspective. To Zhengzhao, you exemplify what it means to be a quick and effective doer. I hope our American dream can all become true in the future. To Ruijun, thank you for all the positive energy you bring. It has greatly helped me break free from my constant negative thoughts. To Fan, you have lots of questions just as I did four years ago. But I believe that you will find your own path. To Reza, I still remember our discussion about MagNet challenge on the train to Gaeta. It was so enjoyable that makes the boring time on the train fly.

My PhD friends made my PhD studying time more than work. To Yang, we emotionally support each other a lot along the journey. Thanks for being my crucial emotional trash

can. To Lyu, I enjoyed a lot talking with you about life, work, and our future. Wish we won't feel we are Sisyphus at the end. To Sachin, my bro, thank you for always taking care of me just like you carried me home when I broke my ankle in Gaeta. To Calvin, it is great to be with you from the beginning to the end. From the crazily spicy fried chicken to the all the gossips, I appreciate all the wonderful moments with you. To Farshid, my philosopher, you told me to enjoy my life on my first day in our office. But I enjoyed the most when I compliant about my life to you. To Guangyao, you are the one most dedicated and strict when it comes to your work. Life is not easy, but stay confident and try to be more tolerant of the imperfections in yourself and your work. To Yunhe, I am really happy for you for going through all the dilemma. I wish you the best for your future with Mark and Tuoba. To Tianming, please recommend me if you went to NVIDIA in the future. To Jundong, Delft may not be the best place in the world, but I hope you'll find it good enough by the time you graduate. To Carina, I know I caused you some trouble with the numerous discussions I had with others, and I'm sorry for that. I hope you will have a better new desk-mate. To Jianning, thank you for all the barbecues and interesting talks. You are more of a friend than just a former supervisor to me. I wish you a wonderful life with Yichi and your lovely sons. To Ruo Chen, it is lucky to meet you at the very end of my PhD study. I wish us all a bright future in Sweden.

My PhD studying time in Delft has been enjoyable because of the many friends that I made here. Thank you Dequan, Jiaxuan, Weiming, Aoqiao, and Keyu for all the lunches, dinners, and for sharing your experiences and emotions. We supported each other, and we will keep supporting each other.

My old friends also gave me many supports. Thank you Lichen, Minfeng, and both of your partners whose names are also Lu, for being with me since long time ago and all the important festivals that we celebrated together. Thank you, Sihang and Rob. I deeply value the friendship I share with your family. Six years ago, the four of us graduated together as master's students. Now, I graduate again, but this time alone, as a PhD. How time flies.

Lastly, I would like to thank my wife, Yu, my mom, and my dad. You are the most important people in my life. With you, I have shared all my joys and sorrows, failures and successes, tears and laughter. You are the only ones with whom I feel safe enough to share my vulnerabilities, which has been crucial in helping me find relief and navigate through dilemmas. In the future, I hope to be strong enough to take care of you and to be the back you can rely on.

## CURRICULUM VITÆ

Lu Wang was born in Sichuan, China, in 1993. He received the B.Sc. degree in electrical engineering from the Beijing Institute of Technology, Beijing, China, in 2015, the M.Sc. degree (cum laude) in electrical power engineering from the Delft University of Technology, Delft, the Netherlands, in 2018, where he pursued the Ph.D. degree with the DC Systems, Energy Conversion and Storage Group on Power Quality of EV Charing from 2020. From Dec. 2018 to Apr. 2019, he was a hardware integration engineer at United Automotive Electronic Systems Co., Ltd, Shanghai, China. From May 2019 to May 2020, he was an electronic designer at Prodrive Technologies B.V., Eindhoven, the Netherlands.



---

# LIST OF PUBLICATIONS

## PUBLICATIONS RELATED TO THE THESIS

### JOURNAL PUBLICATIONS

1. L. Wang, Z. Qin, T. Slangen, P. Bauer and T. van Wijk, "Grid Impact of Electric Vehicle Fast Charging Stations: Trends, Standards, Issues and Mitigation Measures - An Overview," in *IEEE Open Journal of Power Electronics*, vol. 2, pp. 56-74, 2021.
2. L. Wang, Z. Qin, L. B. Larumbe and P. Bauer, "Python supervised co-simulation for a day-long harmonic evaluation of EV charging," in *Chinese Journal of Electrical Engineering*, vol. 7, no. 4, pp. 15-24, Dec. 2021.
3. L. Wang, Z. Qin and P. Bauer, "A Gradient-Descent Optimization Assisted Gray-Box Impedance Modeling of EV Chargers," in *IEEE Transactions on Power Electronics*, vol. 38, no. 7, pp. 8866-8879, July 2023.
4. L. Wang, J. Xiao, P. Bauer and Z. Qin, "Analytic Design of an EV Charger Controller for Weak Grid Connection," in *IEEE Transactions on Industrial Electronics*, vol. 71, no. 12, pp. 15268-15279, Dec. 2024.

### CONFERENCE PUBLICATIONS

1. L. Wang, Z. Qin, L. B. Larumbe and P. Bauer, "Multi-timescale Modeling of Fast Charging Stations for Power Quality Analysis," 2021 23rd European Conference on Power Electronics and Applications (EPE'21 ECCE Europe), Ghent, Belgium, pp. P.1-P.9, 2021.
2. Y. Liang, L. Wang, Z. Qin and P. Bauer, "Harmonic Emission Modelling of Electric Vehicle Chargers," IECON 2022 – 48th Annual Conference of the IEEE Industrial Electronics Society, Brussels, Belgium, pp. 1-6, 2022.
3. Z. Qin, L. Wang and P. Bauer, "Review on Power Quality Issues in EV Charging," 2022 IEEE 20th International Power Electronics and Motion Control Conference (PEMC), Brasov, Romania, pp. 360-366, 2022.
4. L. Wang, Z. Qin, J. Xiao and P. Bauer, "Critical Short Circuit Ratio of an EV Charging System," 2023 25th European Conference on Power Electronics and Applications (EPE'23 ECCE Europe), Aalborg, Denmark, pp. 1-8, 2023.
5. L. Wang, Z. Qin, Y. Wu and P. Bauer, "Stability Enhanced Design of EV Chargers for Weak Grid Connection," 2023 IEEE Energy Conversion Congress and Exposition (ECCE), Nashville, TN, USA, pp. 1231-1237, 2023.

## BOOK CHAPTER

1. Z. Qin, T. B. Soeiro, J. Dong, G. R. C. Mouli, L. Wang, W. Shi, F. Grazian, Y. Yu, P. Bauer, "Electric vehicle charging technology and its control," in *Control of Power Electronic Converters and Systems*, Vol. 4, F. Blaabjerg, Academic Press, 2024, pp. 241-307.

## PUBLICATIONS COLLABORATIVE PROJECTS

### JOURNAL PUBLICATIONS

1. L. B. Larumbe, Z. Qin, L. Wang and P. Bauer, "Impedance Modeling for Three-Phase Inverters With Double Synchronous Reference Frame Current Controller in the Presence of Imbalance," in *IEEE Transactions on Power Electronics*, vol. 37, no. 2, pp. 1461-1475, Feb. 2022.
2. J. Xiao, L. Wang, Z. Qin and P. Bauer, "A Resilience Enhanced Secondary Control for AC Micro-Grids," in *IEEE Transactions on Smart Grid*, vol. 15, no. 1, pp. 810-820, Jan. 2024.
3. Z. Li et al., "A Data-Driven Model for Power Loss Estimation of Magnetic Materials Based on Multi-Objective Optimization and Transfer Learning," in *IEEE Open Journal of Power Electronics*, vol. 5, pp. 605-617, 2024.
4. J. Xiao, L. Wang, P. Bauer and Z. Qin, "Virtual Impedance Control for Load Sharing and Bus Voltage Quality Improvement in Low-Voltage AC Microgrid," in *IEEE Transactions on Smart Grid*, vol. 15, no. 3, pp. 2447-2458, May 2024.
5. J. Xiao, L. Wang, Y. Wan, P. Bauer and Z. Qin, "Distributed Model Predictive Control-Based Secondary Control for Power Regulation in AC Microgrids," in *IEEE Transactions on Smart Grid*, vol. 15, no. 6, pp. 5298-5308, Nov. 2024.
6. M. Chen et al., "MagNet Challenge for Data-Driven Power Magnetics Modeling," in *IEEE Open Journal of Power Electronics*, doi: 10.1109/OJPEL.2024.

### CONFERENCE PUBLICATIONS

1. J. Xiao, L. Wang, Z. Qin and P. Bauer, "Detection of cyber attack in smart grid: A Comparative Study," 2022 IEEE 20th International Power Electronics and Motion Control Conference (PEMC), Brasov, Romania, pp. 48-54, 2022.
2. J. Xiao, L. Wang, Z. Qin and P. Bauer, "An Adaptive Cyber Security Scheme for AC Micro-grids," 2022 IEEE Energy Conversion Congress and Exposition (ECCE), Detroit, MI, USA, pp. 1-6, 2022.
3. J. Xiao, L. Wang, Z. Qin and P. Bauer, "Virtual Impedance Control for Load Sharing and Bus Voltage Quality Improvement," 2023 25th European Conference on Power Electronics and Applications (EPE'23 ECCE Europe), Aalborg, Denmark, pp. 1-8, 2023.
4. J. Xiao, L. Wang, Z. Qin and P. Bauer, "An Adaptive Virtual Impedance Control for Reactive Power Sharing in Microgrids," 2023 IEEE Energy Conversion Congress and Exposition (ECCE), Nashville, TN, USA, pp. 584-589, 2023.
5. J. Xiao, L. Wang, P. Bauer and Z. Qin, "Cyber Secure-Oriented Communication Network Design for Microgrids," 2024 IEEE 15th International Symposium on Power Electronics for Distributed Generation Systems (PEDG), Luxembourg, Luxembourg, pp. 1-6, 2024.

- 
6. J. Xiao, L. Wang, P. Bauer and Z. Qin, "Distributed Model Predictive Control for Active Power Regulation in AC Microgrids," 2024 IEEE 10th International Power Electronics and Motion Control Conference (IPEMC2024-ECCE Asia), Chengdu, China, pp. 2756-2761, 2024.